AFRL-RZ-ED-TR-2012-0016

Contamination and Micropropulsion Technology

Andrew Ketsdever
Sergey Gimelshein
Natalia Gimelshein
Taylor Lilly

Air Force Research Laboratory
AFRL/RZSA
10 E. Saturn Blvd.
Edwards AFB CA 93524-7680

July 2012

Distribution A: To be approved for Public Release; distribution unlimited. PA# 12432

AIR FORCE RESEARCH LABORATORY
PROPULSION DIRECTORATE

■ **Air Force Materiel Command** ■ **United States Air Force** ■ **Edwards Air Force Base, CA 93524**

- STINFO COPY -
NOTICE AND SIGNATURE PAGE

Using Government drawings, specifications, or other data included in this document for any purpose other than Government procurement does not in any way obligate the U.S. Government. The fact that the Government formulated or supplied the drawings, specifications, or other data does not license the holder or any other person or corporation; or convey any rights or permission to manufacture, use, or sell any patented invention that may relate to them.

Qualified requestors may obtain copies of this report from the Defense Technical Information Center (DTIC) (http://www.dtic.mil).

AFRL-RZ-ED-TR-2012-0016 HAS BEEN REVIEWED AND IS APPROVED FOR PUBLICATION IN ACCORDANCE WITH ASSIGNED DISTRIBUTION STATEMENT.

FOR THE DIRECTOR:

//Signed//	//Signed//
ANDREW D. KETSDEVER, Ph.D. Project Manager	INGRID J. WYSONG, Ph.D. Chief, Aerophysics Branch

//Signed//

LaDONNA J. DAVIS, Lt Col, USAF
Deputy Chief – Senior Technical Advisor
Space and Missile Propulsion Division

This report is published in the interest of scientific and technical information exchange, and its publication does not constitute the Government’s approval or disapproval of its ideas or findings.

REPORT DOCUMENTATION PAGE

Form Approved
OMB No. 0704-0188

Public reporting burden for this collection of information is estimated to average 1 hour per response, including the time for reviewing instructions, searching existing data sources, gathering and maintaining the data needed, and completing and reviewing this collection of information. Send comments regarding this burden estimate or any other aspect of this collection of information, including suggestions for reducing this burden to Department of Defense, Washington Headquarters Services, Directorate for Information Operations and Reports (0704-0188), 1215 Jefferson Davis Highway, Suite 1204, Arlington, VA 22202-4302. Respondents should be aware that notwithstanding any other provision of law, no person shall be subject to any penalty for failing to comply with a collection of information if it does not display a currently valid OMB control number. **PLEASE DO NOT RETURN YOUR FORM TO THE ABOVE ADDRESS.**

1. REPORT DATE *(DD-MM-YYYY)*
27 Jul 2012

2. REPORT TYPE
Final Technical Report

3. DATES COVERED *(From - To)*
25 Oct 2004 – 28 Apr 2012

4. TITLE AND SUBTITLE
Contamination and Micropropulsion Technology

5a. CONTRACT NUMBER

5b. GRANT NUMBER

5c. PROGRAM ELEMENT NUMBER
62203F

6. AUTHOR(S)
Ketsdever, Andrew; Gimelshein, Sergey; Gimelshein, Natalia; and Lilly, Taylor

5d. PROJECT NUMBER

5e. TASK NUMBER

5f. WORK UNIT NUMBER
50260568

7. PERFORMING ORGANIZATION NAME(S) AND ADDRESS(ES)

Air Force Research Laboratory (AFMC)
AFRL/RZSA
10 E. Saturn Blvd.
Edwards AFB CA 93524-7680

8. PERFORMING ORGANIZATION REPORT NO.

9. SPONSORING / MONITORING AGENCY NAME(S) AND ADDRESS(ES)

Air Force Research Laboratory (AFMC)
AFRL/RZS
5 Pollux Drive
Edwards AFB CA 93524-7048

10. SPONSOR/MONITOR'S ACRONYM(S)

11. SPONSOR/MONITOR'S REPORT NUMBER(S)
AFRL-RZ-ED-TR-2012-0016

12. DISTRIBUTION / AVAILABILITY STATEMENT
Approved for public release; distribution unlimited. PA No. 12432.

13. SUPPLEMENTARY NOTES

14. ABSTRACT

The growing interest in the use of microspacecraft within government and industry is driving a critical need for new propulsion systems capable of fulfilling a wide range of mission requirements. The applicability of each propulsion system is highly mission dependent and subject to system constraints. The purpose of this research was to investigate the design, fabrication, and microspacecraft systems limitations associated with the scaling of micropropulsion devices.

15. SUBJECT TERMS
zero-point energy; plane wave diffraction; vacuum fluctuations; vacuum energy

16. SECURITY CLASSIFICATION OF:			**17. LIMITATION OF ABSTRACT**	**18. NUMBER OF PAGES**	**19a. NAME OF RESPONSIBLE PERSON**
					Dr. Andrew D. Ketsdever
a. REPORT	**b. ABSTRACT**	**c. THIS PAGE**	SAR	135	**19b. TELEPHONE NO** *(include area code)*
Unclassified	**Unclassified**	**Unclassified**			N/A

Standard Form 298 (Rev. 8-98)
Prescribed by ANSI Std. 239.18

TABLE OF CONTENTS

Section	Title	Page No.
1.1	Micropropulsion and MEMS Propulsion	1
1.2	Spacecraft-Thruster Interactions	2
2.0	SUMMARY	3
2.1	Micropropulsion and MEMS Propulsion	3
2.2	Spacecraft-Thruster Interactions	3
3.0	REFERENCES	4
APPENDIX	Publications and Presentations	A-1

GLOSSARY

DSMC	Direct Simulation Monte Carlo
FMMR	Free Molecule Micro-Resistojet
MEMS	microelectromechanicall systems
nNTS	nano-Newton Thrust Stand

1.0 INTRODUCTION

The growing interest in the use of microspacecraft within government and industry is driving a critical need for new propulsion systems capable of fulfilling a wide range of mission requirements. The applicability of each propulsion system is highly mission dependent and subject to system constraints. The purpose of this research was to investigate the design, fabrication, and microspacecraft systems limitations associated with the scaling of micropropulsion devices.

When in orbit, spacecraft require on-board or secondary propulsion systems to perform orbit transfer, orbit maintenance, and attitude control maneuvers. An important issue in the use of any spacecraft propulsion system involves the assessment and reduction of effects caused by the interaction between the thruster plume and spacecraft surfaces. Direct impingement of a thruster plume on surfaces can generate unwanted torques, localized surface heating, and surface contamination. Self-impingement (i.e., the impingement of a thruster plume on a host satellite surface) generally occurs for small surface angles with respect to the propulsion system's thrust vector or occurs in the thruster backflow. Cross-impingement (i.e., the impingement of one spacecraft's thruster plume onto another spacecraft) can occur at essentially any angle and is becoming increasingly important with the advent of microsatellite constellations.

1.1. Micropropulsion and MEMS Propulsion

There are many definitions as to what the term "micropropulsion" really describes. Some definitions use characteristic size while others use producible thrust level. Perhaps the most general definition of micropropulsion is any propulsion system which is applicable to a microspacecraft (mass less than 100 kg) mission. This definition allows the inclusion of a wide range of concepts from scaled down versions of existing thrusters operating at reduced power levels to completely redesigned microelectromechanical (MEMS) fabricated thrusters with micron characteristic sizes. Although this definition is rather broad, it appears to be the most widely accepted. However, the objective of this research will be to address the systems related issues and design considerations in the limit of MEMS devices, since the ultimate goal of micropropulsion systems (even for relatively large microspacecraft) lies in this direction.

Micropropulsion is an enabling technology for microspacecraft operations by making missions possible which otherwise could not be performed. For example, the formation and maintenance of platoons of microspacecraft will require a maneuvering capability to counter orbital perturbations. Microspacecraft missions involving large spacecraft resupply, repair or surveillance will also require maneuverability. The mission requirements for microspacecraft will be varied; and in some cases a large range of capability might be required on the same spacecraft. Micropropulsion systems must be extremely versatile to address these requirements. It is clear that there is a need for micropropulsion systems – from high thrust chemical engines to high specific impulse electric ion thrusters – to fulfill specific missions. Applications of micropropulsion systems for every mission need to be carefully studied to ensure that the propulsion system has sufficient benefit.

The design of micropropulsion systems is also complicated by the scaling of systems level aspects with spacecraft size, including power, mass, and volume. One systems level aspect that may not scale with spacecraft size is the expected propulsion system lifetime. Although microspacecraft will be designed to be replaceable, propulsion system failures will not be tolerated any more than on larger spacecraft. To maintain a platoon of microspacecraft, members of the platoon will need to be removed from the general platoon "neighborhood" at the end of the spacecraft's useful life or in the event of premature failure of a spacecraft subsystem. In this regard, the micropropulsion system may be required to function even after a major spacecraft failure or after several years on orbit.

In order to ensure long lifetime, micropropulsion systems will need to be robust and durable. Issues will arise from corrosive propellant usage, plugging of small orifices with contaminants, thin film degradation, MEMS component mechanical and thermal cycling, and environmental interactions. Early indications suggest that micropropulsion systems in general may experience decreased performance efficiency due to losses associated with small characteristic sizes, limitations on system mass and power, and the lagging development of adequate micromachined support hardware. In the limit of MEMS fabrication scales, simply scaled down versions of existing thrusters may not perform as expected.

Careful attention should be paid to the characteristics of propulsion systems that scale favorably with reduced size. There are several large-scale thruster characteristics that do not scale favorably with reduced size. Those characteristics that do scale favorably may hold the key in the design of efficient micropropulsion systems.

1.2 Spacecraft-Thruster Interactions

The interactions between onboard spacecraft propulsion systems and spacecraft surfaces have received considerable attention in recent years from Department of Defense, NASA, and commercial investigators. The growing popularity of electric ion propulsion systems promises renewed interest in this area of research. The impact of potential interactions on spacecraft is becoming more critical as mission life and payload sensitivity requirements are continually increased. The adsorption of propellant gases on spacecraft surfaces (often referred to as contamination) can change solar absorptivity of thermal control surfaces, alter reflectivity of optical surfaces, alter transmission through solar cell cover-glass, and induce environments that can alter scientific results. Ion electric thrusters add further complications due to material sputtering from high-energy ion (propellant) impact and the possible alteration of spacecraft potentials.

Although the space shuttle has made space-based investigations more feasible by providing a reliable space platform and the capability of returning payloads to Earth for careful examination, the cost of space-based experiments is still prohibitively high. Space-based experiments can also be extremely limited in scope due to a lack of available instrumentation, geometrical variation, accurate detail of the time-dependent space environment, and on-orbit time. It is clear that ground-based examination of thruster–spacecraft interactions is necessary to complement the sometimes limited data returned from space experiments.

2.0 SUMMARY

The detailed technical results for this in-house research project are provided in the articles in Appendix A.

2.1. Micropropulsion and MEMS Propulsion

Research into the Free Molecule Micro-Resistojet (FMMR) was performed under this in-house research program. The FMMR is a MEMS fabricated resistojet that incorporated a full systems design approach. The FMMR was designed, developed, constructed, and tested. A MEMS fabricated FMMR heater (i.e., the resistojet components without propellant) flew on ASUSat built by the Arizona State University. ASUSat was launched on the inaugural Delta IV Heavy in October 2007. Unfortunately, a flight anomaly released the satellite at an altitude too low to maintain an orbit. A complete version of the FMMR with water propellant for thrust was built for AggieSat (Texas A&M University) in 2009, but that satellite was never approved for flight.

A nano-Newton Thrust Stand (nNTS) was developed and tested to measure the low-level thrust from micropropulsion systems including the FMMR. Calibration methods were also developed for this low-thrust range. An RF plasma micro-thruster developed at Purdue University was successfully tested on the nNTS. A version of the nNTS was developed that can simultaneously measure mass flow and impulse in pulsed operation thrusters. This allows a direct, in-situ measurement of specific impulse.

2.2 Spacecraft-Thruster Interactions

The interactions between spacecraft thrusters and surfaces were investigated under this in-house research program. Gas-surface interactions were experimentally tested using the nNTS and were numerically investigated using the Direct Simulation Monte Carlo (DSMC) technique. The interactions between gases and engineering rough surfaces were quantified. A new, computationally efficient method for including surface roughness in the DSMC numerical simulations was developed and validated.

Radiometric flows were investigated experimentally and numerically to better understand the physics of gas-surface interactions. Accommodation coefficients for various gases on engineering surfaces were measured.

Charging of dielectric materials in low-Earth orbit was investigated experimentally and numerically. Liquid droplets in a vacuum were charged using an extreme ultraviolet light source. A simple diagnostic technique allowed the charge state of the droplet to be determined. These results compared favorably to numerical simulations that showed charging in the natural space environment. The results were used to assess the effect of the space environment on a notional inter-satellite propulsion system based on liquid droplet streams.

3.0 REFERENCES

1. T. Joslyn and A. Ketsdever, "Droplet Charging Effects in the Space Environment," Proceedings of the 27th International Symposium on Rarefied Gas Dynamics, ed. D. Levin, I. Wysong, and A. Garcia, (AIP, New York, 2011), pp. 1079-1084.
2. N. Selden, N. Gimelshein, S. Gimelshein, and A. Ketsdever, "Analysis of Accommodation Coefficients of Noble Gases on Aluminum Surface with an Experimental/Computational Method," **Phys. Fluids**, Vol. 21, No. 7, 073101, 2009.
3. T. Lilly, A. Ketsdever, A. Pancotti, and M. Young, "Development of a Specific Impulse Balance for a Pulsed Capillary Discharge," **J. Propulsion and Power**, Vol. 25, No. 3, pp. 823-826, 2009.
4. (INVITED) J. Olliges, A. Ketsdever, W.B. Stein, A. Alexeenko, and I. Hrbud, "Experimental and Computational Investigation of a RF Plasma Micro-Thruster," Proceedings of the 26th International Symposium on Rarefied Gas Dynamics, ed. T. Abe, (AIP, New York, 2009), pp. 863-870.
5. (INVITED) J. Olliges, T. Lilly, T. Joslyn, and A. Ketsdever, "Time Accurate Mass Flow Measurements of Solid-Fueled Systems," **Rev. Sci. Instrum**., Vol. 79, No. 10, 101301, October 2008.
6. A. Ketsdever, B. D'Souza, and R. Lee, "Thrust Stand Micromass Balance for the Direct Measurement of Specific Impulse," **J. Prop. and Power**, Vol. 26, No. 6, pp. 1376-1381, 2008.
7. R. Lee, A. Bauer, M. Killingsworth, T. Lilly, J. Duncan, and A. Ketsdever, "Free Molecule Micro-Resistojet Performance Utilizing Water Propellant for Nanosatellite Applications," **J. Spacecraft and Rockets**, Vol. 45, No. 2, pp. 264-269, 2008.
8. T. Lilly, J. Duncan, S. Nothnagel, S. Gimelshein, N. Gimelshein, A. Ketsdever, and I. Wysong, "Numerical and Experimental Investigation of Microchannel Flows with Rough Surfaces," **Phys. Fluids**, Vol. 19, 106101, 2007.
9. N. Gimelshein, T. Lilly, S. Gimelshein, A. Ketsdever, and I. Wysong, "Surface Roughness Effects in Low Reynolds Number Nozzle Flows," Proceedings of the 25th International Sympo¬sium on Rarefied Gas Dynamics, eds. M. Ivanov and A. Rebrov, (Siberian Branch of RAS, Novosibirsk, Russia, 2007), pp. 695-702.
10. C. Ngalande, T. Lilly, M. Killingsworth, S. Gimelshein, and A. Ketsdever, "Nozzle Plume Impingement on Spacecraft Surfaces: Effects on Surface Roughness," **J. Spacecraft and Rockets**, Vol. 43, No. 5, pp. 1013-1018, 2006.
11. T. Lilly, S. Gimelshein, A. Ketsdever, and G. Markelov, "Measurements and computations of mass flow and momentum flux through short tubes in rarefied gases," **Phys. Fluids**, Vol. 18, No. 9, 093601-1-11, September 2006.
12. Z. Ahmed, S. Gimelshein, and A. Ketsdever, "Numerical analysis of Free Molecule Micro-Resistojet Performance," **J. Propulsion and Power**, Vol. 22, No. 4, pp. 749-756, 2006.
13. A. Ketsdever, R. Lee, and T. Lilly, "Performance testing of a microfabricated propulsion system for nanosatellite applications," **J. of Micromechanics and Microengineering**, Vol. 15, pp. 2254-2263, 2005.
14. B. D'Souza and A. Ketsdever, "Investigation of time-dependent forces on a nano-Newton-second impulse balance," **Review of Scientific Instruments**, Vol. 76, No. 1, pp. 015105-1-10, January 2005.

15. A. Ketsdever, T. Lilly, S. Gimelshein, and A. Alexeenko, “Experimental and Numerical Study of Nozzle Plume Impingement on Spacecraft Surfaces,” Proceedings of the 24th International Symposium on Rarefied Gas Dynamics, ed. M. Capitelli, (AIP, New York, 2005), pp. 367-372.

This Page Intentionally Left Blank

APPENDIX

PUBLICATIONS AND PRESENTATIONS

This Page Intentionally Left Blank

AIP | Conference Proceedings

Droplet Charging Effects in the Space Environment

Thomas B. Joslyn and Andrew D. Ketsdever

Citation: AIP Conf. Proc. **1333**, 1079 (2011); doi: 10.1063/1.3562788

View online: http://dx.doi.org/10.1063/1.3562788

View Table of Contents: http://proceedings.aip.org/dbt/dbt.jsp?KEY=APCPCS&Volume=1333&Issue=1

Published by the American Institute of Physics.

Related Articles

Band alignment of HfO2 on SiO2/Si structure
Appl. Phys. Lett. 100, 122907 (2012)

Impact of high temperature annealing on La diffusion and flatband voltage (Vfb) modulation in TiN/LaOx/HfSiON/SiON/Si gate stacks
J. Appl. Phys. 111, 054110 (2012)

The band alignment of Cu2O/ZnO and Cu2O/GaN heterostructures
Appl. Phys. Lett. 100, 094102 (2012)

Effects of Cu diffusion-doping on structural, optical, and magnetic properties of ZnO nanorod arrays grown by vapor phase transport method
J. Appl. Phys. 111, 013903 (2012)

Bias application hard x-ray photoelectron spectroscopy study of forming process of Cu/HfO2/Pt resistive random access memory structure
Appl. Phys. Lett. 99, 223517 (2011)

Additional information on AIP Conf. Proc.

Journal Homepage: http://proceedings.aip.org/

Journal Information: http://proceedings.aip.org/about/about_the_proceedings

Top downloads: http://proceedings.aip.org/dbt/most_downloaded.jsp?KEY=APCPCS

Information for Authors: http://proceedings.aip.org/authors/information_for_authors

ADVERTISEMENT

AIPAdvances

Explore AIP's new open-access journal

- Article-level metrics now available
- Join the conversation! Rate & comment on articles

Submit Now

Downloaded 11 Apr 2012 to 129.198.241.47. Redistribution subject to AIP license or copyright; see http://proceedings.aip.org/about/rights_permissions

Droplet Charging Effects in the Space Environment

Thomas B. Joslyn[a] and Andrew D. Ketsdever[b]

[a]United States Air Force Academy, Department of Astronautics, USAF Academy, CO 80840
[b]University of Colorado at Colorado Springs, Department of Mechanical and Aerospace Engineering, Colorado Springs, CO 80918

Abstract. Several applications exist for transiting liquid droplets through the near-Earth space environment. Numerical results are presented for the charging of liquid droplets of trimethyl pentaphenyl siloxane (DC705) in three different plasma environments: ionosphere, auroral, and geosynchronous Earth orbit (GEO). Nominal and high geomagnetic activity cases are investigated. In general, high levels of droplet charging (>100V) exist only in GEO during periods of high geomagnetic or solar activity. An experiment was conducted to assess the charging of silicon-oil droplets due to photoemission. The photoemission yield in the 120-200nm wavelength range was found to be approximately 0.06.

Keywords: liquid droplet charging, plasma environment.
PACS: 52.65.-y, 94.05.Sd

INTRODUCTION

The idea of propagating liquid droplet streams through the space environment was first put forth in the 1980s as a means of spacecraft thermal control.[1] These liquid droplet radiator concepts release multiple liquid droplet streams into space where the droplets radiate heat. The cooled liquid droplets are collected on the same spacecraft after a short distance, pumped throughout the spacecraft to remove heat from various components, and released back into space to cool again.. A subsequent study has alluded to other potential applications for liquid droplets transiting the near-Earth space environment.[2] For the application of interest in this study, a liquid droplet stream of low-vapor-pressure, silicon-based oil is being proposed as a potential spacecraft propulsion system.[3] In this concept, liquid droplets are constantly passed between two (or multiple) spacecraft flying in formation. The receiving satellite collects the liquid droplet stream from the originating satellite and returns the liquid droplets back to the original satellite. This "pitch and catch" scenario allows a constant momentum exchange between the two satellites allowing a constant spacing to be maintained between the spacecraft. Large arrays of satellites can be envisioned using this concept where the relative spacing between individual satellite members of the array can be constantly controlled.

Trimethyl pentaphenyl siloxane (better known by its trade name of DC 705) was selected as the liquid of choice due to its low-vapor-pressure and viscosity. Obviously, the low-vapor-pressure is required for the liquid droplet to be appropriate for a space application. The low viscosity allows the fluid to be transported throughout the spacecraft at relatively little pumping power.

An object in near-Earth space is subject to many interactions with the ambient environment at a given altitude such as exposure to atomic oxygen, radiation, and charged particles.[4] This study investigates the interactions between the ambient, near-Earth plasma environment and DC 705 liquid droplets. Charging of the DC 705 can cause operational concerns for all of the space related applications discussed above. Since DC 705 is a dielectric material, differential charging can cause a droplet to breakup if the Coulomb repulsive force is greater than the surface tension force holding the droplet together. Also, for this particular application, a stream of charged droplets in close proximity can begin to produce Coulomb-type forces between individual droplets potentially leading them off course.

This study assesses the charging potential of DC 705 in three general near-Earth environments as a function of geomagnetic and solar activity using a numerical approach. An experiment was designed to quantify the amount of droplet charging due to solar extreme ultraviolet (EUV) radiation exposure, one of several mechanisms that can cause droplet charging in space.

27th International Symposium on Rarefied Gas Dynamics, 2010
AIP Conf. Proc. 1333, 1079-1084 (2011); doi: 10.1063/1.3562788

© 2011 American Institute of Physics 978-0-7354-0888-0/$30.00

Downloaded 11 Apr 2012 to 129.198.241.47. Redistribution subject to AIP license or copyright; see http://proceedings.aip.org/about/rights_permissions

THEORY

As objects move through space, they come into contact with ambient ions and electrons that constitute the Earth's plasma environment. Several different mechanisms are responsible for adding or removing electrons (charge) from an object exposed to a plasma environment. Quantifying the net current of an object immersed in a plasma is generally an iterative (i.e. numerical) process since the charge of the object is highly coupled to the plasma interaction mechanisms. The current balance for an object floating at an electrostatic potential, V, is given by

$$I_{net}(V) = I_e(V) - \{I_i(V) + I_{se}(V) + I_{si}(V) + I_{bse}(V) + I_{ph}(V)\} \tag{1}$$

where I_{net} is the net current flow to the object, I_e is the incident electron current, I_i is the incident ion current, I_{se} is the secondary electron current caused by the incident electrons, I_{si} is the secondary electron current caused by the incident ions, I_{bse} is the current caused by backscattered incident electrons, and I_{ph} is the secondary electron current caused by incident solar photons. In order to assess the charging of an object in a plasma environment, characteristics of the plasma environment (e.g. species, density and energy) and active plasma-surface interaction mechanisms must be understood.

Characteristics of the Plasma Environment

In general, the Earth's plasma environment can be separated into three main categories based on the characteristics (e.g. density and energy) of the ambient plasma species: ionosphere, auroral, and geosynchronous Earth orbit (GEO). The ionosphere ranges from an altitude of 100 km to approximately 1000 km. It is characterized by a relatively dense number density of heavy ion species dominated by O^+ between 150 and 900 km. Ion and electron number densities vary from approximately 7×10^5 to 10^4 cm^{-3} over this altitude range. There is a reasonable degree of non-equilibrium in the ionosphere between neutral species, ions and electrons where the neutral temperature is essentially constant at approximately 1000K, the ion temperature varies from 1000 to 2000K, and the electron temperature varies from 1600 to 3200K.[4]

The auroral plasma environment is characterized by the high energy electrons precipitating down the Earth's magnetic field lines at high latitudes where solar wind electrons can readily access the upper atmosphere. The electron energy distribution in the auroral region is highly non-equilibrium as described by Fontheim et al.[5] The energy generally ranges from 0.1 to 10keV with higher energy particles generally having a lower flux. The electron density and energy in this region can be highly variable and can be influenced by solar and geomagnetic storms.[4] The GEO plasma environment is characterized by low density ($\sim 1 cm^{-3}$), high energy (0.6 to 20keV) electrons and protons. The GEO plasma environment is also highly variable.

Space Charging Mechanisms

The general charging mechanisms for an object in a moderate energy (<20keV) plasma environment are shown in Fig. 1. Secondary electrons formed from the interaction of ions, electrons, or photons on the surface may escape the material, be conducted through the material, or be re-adsorbed by the material. As can be deduced from Eq. 1, determining the total number of secondary electrons produced and accurately assessing the relative number that escape the material is critical in quantifying the material's charge state. In general, secondary electron yield (the average number of secondary electrons produced per incident collider) is a function of the incident collider (ion, electron, neutral, photon), the relative energy, and the material substrate. Secondary electron yields for DC 705 for electron and photon colliders have been experimentally determined by Ishikawa and Goto[6] and Koizumi et al.[7] respectively. Plots of the secondary electron yields for both electron and photon colliders with DC 705 are shown in Fig. 2 as a function of incident energy.

NASCAP MODEL

The NASA Charging Analyzer Program (NASCAP)[8] was used to quantify the charging of a DC 705 droplet exposed to the three space plasma environments described in the previous section. The potential in the plasma near a charged surface with potential V is given by the Poisson equation as

Downloaded 11 Apr 2012 to 129.198.241.47. Redistribution subject to AIP license or copyright; see http://proceedings.aip.org/about/rights_permissions

$$\epsilon_o \nabla^2 V = q(n_i - n_e) \qquad (2)$$

where ϵ_o is the permittivity of free space, q is the elemental charge, and n_i and n_e are the number density of ions and electrons, respectively. NASCAP solves Eq. 2 by applying the specified environmental flux distribution of ions, electrons, and photons in an iterative process alternating the development of a plasma sheath at the surface and the recalculation of the near-surface plasma densities. NASCAP employs the Boundary Element Method which relates the electric fields in the surrounding plasma to sources at the surface. This method allows rapid determination of changes in plasma densities, current flow to and from the surface, and a new solution to Poisson's equation to determine changes in electrostatic potential that occur during the time step.

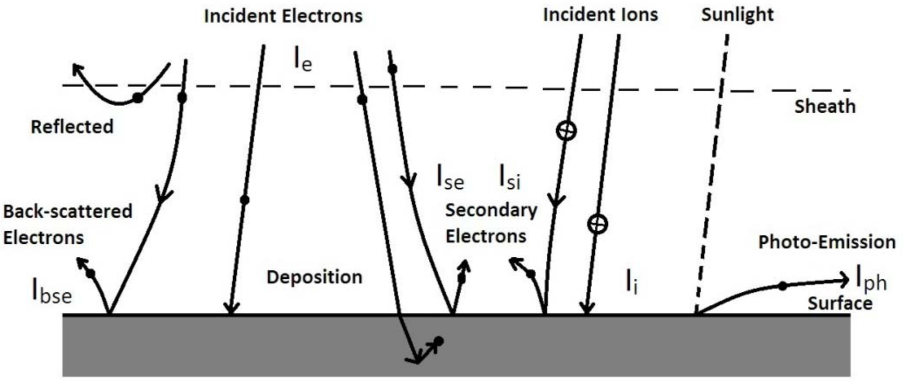

FIGURE 1. Charging Processes Near the Surface of a Dielectric Material.

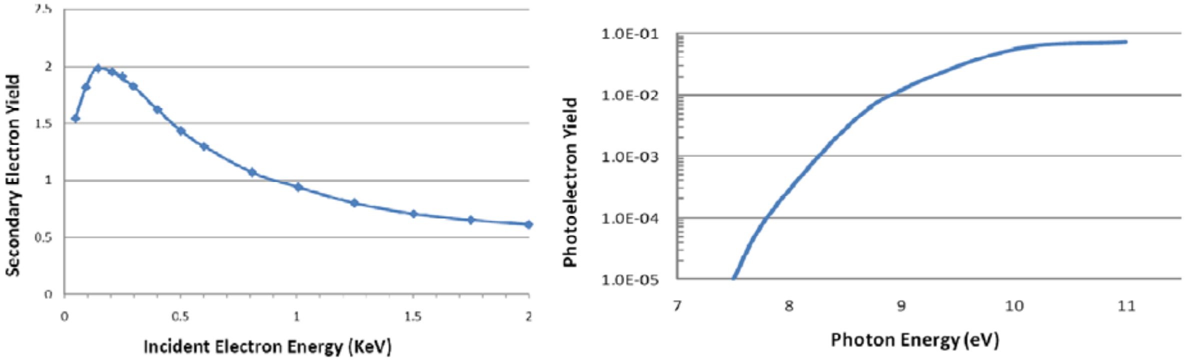

(A) **(B)**

FIGURE 2. Secondary Electron Yield as a Function of Energy for **(A)** Electron[6] and **(B)** Photon[7] Colliders at Normal Incidence.

Ionospheric environmental conditions are derived from data in the International Reference Ionosphere (IRI) model.[9] Auroral environmental conditions based on data from the Defense Meteorological Satellite Program (DMSP) were used.[5] Nominal and worst-case environments are derived from over 35 years of DMSP measurements orbiting at altitudes between 500 and 800km. The GEO environmental conditions are modeled after data from the Applications Technology Satellite (ATS) and the Spacecraft Charging at High Altitude (SCATHA) spacecraft.[10] Nominal and worst-case conditions are both modeled.

EXPERIMENTAL SET UP

An experiment was constructed to quantify DC704 charging due to photon colliders. DC704 is expected to have the same charging characteristics of DC705.[6] A continuous stream of DC704 droplets were produced in a small vacuum chamber and exposed to a 30W EUV lamp made by the Hamamatsu Corporation. The lamp, which was used to simulate the EUV output from the sun, emits photons in the wavelength range of 120 to 200nm using a deuterium plasma source. The spectral profile of the lamp can be found in ref. 3. The lamp position was varied relative to the droplet stream to change the irradiance at the droplet. After illumination by the solar simulator, the droplets passed through a parallel plate capacitor. The amount of deflection of the droplets in the parallel plate

Downloaded 11 Apr 2012 to 129.198.241.47. Redistribution subject to AIP license or copyright; see http://proceedings.aip.org/about/rights_permissions

capacitor is proportional to their charge. By measuring the deflection for a known droplet diameter (i.e. mass), the droplet charge due to secondary electrons produced by photon colliders was determined. The experimental set up is shown in Fig. 3.

In this set up, the droplets are only exposed to the EUV radiation as they fall through the opening of the cylindrical shield. Because the amount of charge built up on the droplets is a function of exposure time to the EUV radiation, the shield is meant to block the EUV from the droplet stream except for a well quantified amount of time. In these experiments, the exposure time is 0.065 sec.

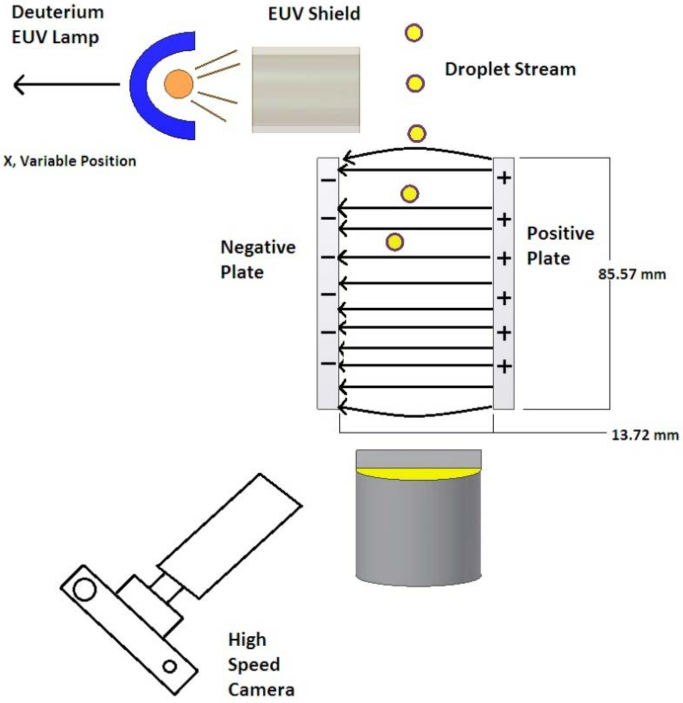

FIGURE 3. Photoemission Experimental Set Up.

RESULTS

Numerical

In general, differences in the charging in all three plasma environments considered are seen between droplets in the sun and those in eclipse. There are two main reasons for these differences. First, in eclipse, photoemission of secondary electrons from a surface is not an active mechanism for charge production. Second, there can be differences in the plasma environment between regions in the sun and those in eclipse. For example, the production of charged particles in the ionosphere is dominated by photo-ionization of neutral species. Diffusion and induced drifts cause the charged particles to be present in the eclipse region; however, there is a strong diurnal variation in density where some ionospheric layers (e.g. the D and F1 regions) completely disappear at night.[4] A summary of the charging on DC 705 droplets exposed to the three plasma environments is shown in Table 1. Values are given for both sunlit and eclipsed regions. The maximum charge found in the NASCAP simulations for any surface exposed to the sun is shown along with the minimum charge found on any surface during eclipse.

The nominal and high geomagnetic activity environments for the ionosphere show very benign charging characteristics for DC 705. For the nominal environment in sunlight, DC 705 reached a very small, nearly uniform negative charge potential of -0.01V relative to the ambient plasma potential. In eclipse, the surface potential was approximately -0.05V. These results are consistent with the idea that in a quasi-neutral plasma, a floating surface will charge slightly negative due to the fact that at the same energy the mean electron speed is higher (i.e. higher flux of electrons to the surface). The high geomagnetic environment in the ionosphere was also found to be fairly benign. Because of the relatively high density of both positively and negatively charged particles in the ionosphere,

Downloaded 11 Apr 2012 to 129.198.241.47. Redistribution subject to AIP license or copyright; see http://proceedings.aip.org/about/rights_permissions

any large potential built up on the droplet is quickly neutralized by collecting oppositely charged particles from the plasma.

The auroral environment simulations are highly dependent on the assumed plasma densities and energy distributions. At orbital speeds, the leading surface of a droplet (RAM direction) collects both ions and electrons. However, the trailing surface (anti-velocity vector or wake) only collects the much faster electrons (i.e. the speed of the droplet is much larger than the average thermal speed of the ions). Therefore, there are some slight differences in the charging of RAM and wake surfaces. At altitudes below 800km, the plasma densities are still relatively high and the sheath is fully developed within 0.5 sec.

Simulations for GEO are highly dependent on geomagnetic activity and photoemission. The strong dependence on droplet charge of photoemission can be seen in the difference of potential in the sunlight case versus the eclipse case in Table 1. In GEO, the orbital speed is such that it is less than the mean speed of both the electrons and ions. Because the ambient plasma density in GEO is extremely small ($n \sim 1 cm^{-3}$), the droplet can charge to extremely high negative potentials due to the increase in electron density during high geomagnetic or solar activity. In nominal environmental conditions, photoemission is the dominant charge mechanism which can lead to relatively high positive potentials.

TABLE (1). Summary of equilibrium charging results from NASCAP for various plasma environments. Maximum sunlit surface and minimum eclipsed surface values are given.

Environment	Ionosphere	Auroral (<800km)	GEO
Nominal Geomagnetic	0V, -1V	+4V, -16V	+18V, +1.5V
High Geomagnetic	+2V, -2V	+21V, -26V	-2kV, -13kV

Experimental

Figure 4 shows the average droplet charge potential as a function of the EUV lamp irradiance (normalized by the solar irradiance). The droplet potential is seen to vary linearly with the irradiance as expected. The experiment did not include an ambient plasma environment. Therefore, the droplets charge to relatively high positive potentials due to photoemission of secondary electrons without the opportunity to collect electrons from an ambient plasma to help neutralize the droplet charge. NASCAP simulations were run where the only active charging mechanism was photoemission (i.e. the background plasma was turned off). A study was conducted with the photoemission yield as the only parametric variable. Figure 5 shows the comparison of the transient NASCAP simulations with the experimental results. The numerical results show excellent agreement for a photoemission yield of 0.06. The empirical results for photoemission yield from DC704 and DC705 of Koizumi et al.[7] is shown in Fig. 6 along with the solar spectra and the assumed (i.e. provided by the manufacturer) spectra from the EUV lamp. The total irradiance is taken as the area under each spectra. As shown in Fig. 6, the EUV lamp used in this study should produce a photoemission yield somewhere between 0.03 and 0.06 of its range of transmission wavelengths which is consistent with the NASCAP results from Fig. 5.

CONCLUSIONS

In general, high levels of droplet charging (>100V) were only found in GEO during periods of high geomagnetic activity. Nominal GEO conditions along with conditions in the ionosphere and auroral environments tend to lead to levels of charging between +20V and -30V. The ambient plasma plays a dominant role in both the ionosphere and auroral environments. Generally, solar EUV radiation plays a dominant role in GEO during nominal environmental conditions. The effects of charging on DC705 droplets were found to be negligible in all cases except the high geomagnetic activity GEO scenario. The photoemission yield of approximately 0.06 found through a combination of experimental and numerical studies is consistent with the yields found in the literature for EUV wavelengths between 120 and 200nm.

ACKNOWLEDGMENTS

The authors wish to thank the United States Air Force Research Laboratory, Propulsion Directorate (Edwards AFB, California) for their support of this research. The figure-making skills of Mr. Ryan Bosworth are appreciated.

Downloaded 11 Apr 2012 to 129.198.241.47. Redistribution subject to AIP license or copyright; see http://proceedings.aip.org/about/rights_permissions

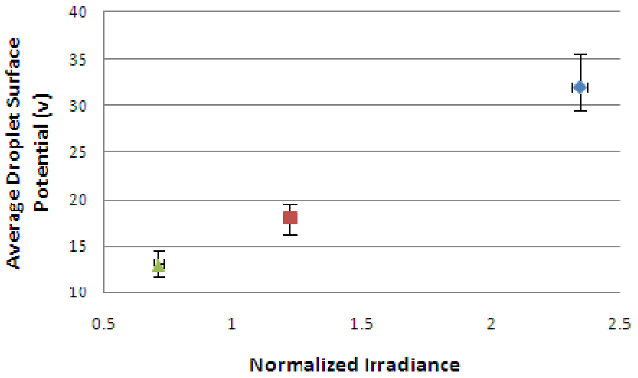

FIGURE 4. DC704 Droplet Potential as a Function of Normalized Irradiance (1=Solar Irradiance).

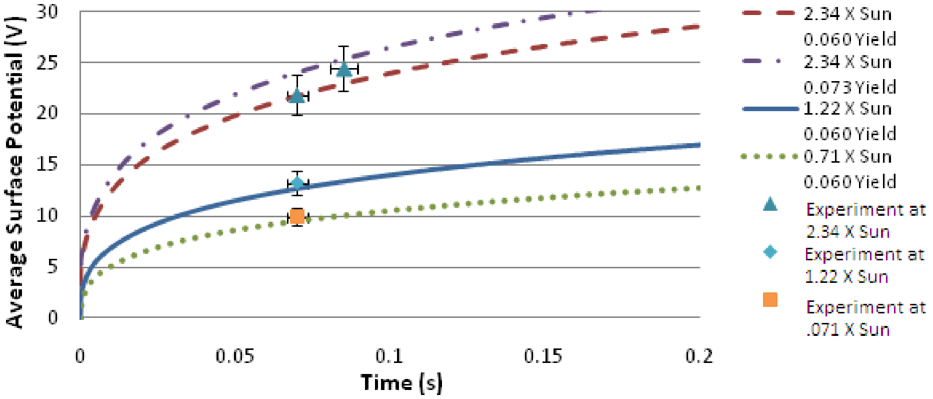

FIGURE 5. Comparison of NASCAP and Experimental Charging Results.

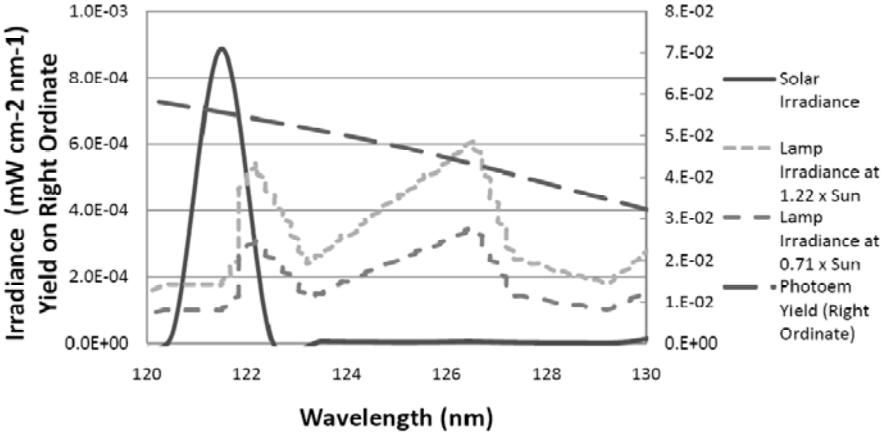

FIGURE 6. Typical Solar and EUV Lamp Irradiance with Corresponding Photoemission Yield (right ordinate).

REFERENCES

1. A. Mattick and A. Hertzberg. *J. Energy*, **5**, 387-393 (1981).
2. E.P. Muntz and M. Dixon, *J. Spacecraft Rockets*, 23, 411-419 (1986).
3. T. Joslyn, “Charging Effects on Fluid Stream Droplets for Momentum Exchange Between Spacecraft,” Ph.D. Thesis, University of Colorado at Colorado Springs, 2009.
4. T. Gombosi, Physics of the Space Environment, Cambridge UK, Cambridge University Press, 1998.
5. E. Fontheim, K. Stasiewicz, and M. Chandler. *J. Geophys. Res.*, **87**, 3469-3480 (1982).
6. K. Ishikawa and K. Goto, *Jpn. J. Appl. Phys.*, **6**, 1329-1335 (1967).
7. H. Koizumi, K. Lacmann, and W. Schmidt. *IEEE Trans. Dielect. and Elect. Insul.*, **3**, 233-236 (1996).
8. M. Mandell, I. Katz, J. Hilton, J. Minor, and D. Cooke. *AIAA paper 2001-0957*, 39th Aerospace Sciences Meeting (2001).
9. C. Purvis, H. Garrett, A. Whittlesey, and N. Stevens. *NASA Technical Paper 2361* (1984).

Downloaded 11 Apr 2012 to 129.198.241.47. Redistribution subject to AIP license or copyright; see http://proceedings.aip.org/about/rights_permissions

AIP | Physics of Fluids

Analysis of accommodation coefficients of noble gases on aluminum surface with an experimental/computational method

Nathaniel Selden, Natalia Gimelshein, Sergey Gimelshein, and Andrew Ketsdever

Citation: Phys. Fluids **21**, 073101 (2009); doi: 10.1063/1.3187932

View online: http://dx.doi.org/10.1063/1.3187932

View Table of Contents: http://pof.aip.org/resource/1/PHFLE6/v21/i7

Published by the American Institute of Physics.

Related Articles

Spectrum of position fluctuations of a Brownian particle bound in a harmonic trap near a plane wall
J. Chem. Phys. 136, 144701 (2012)

Effect of slippage on the thermocapillary migration of a small droplet
Biomicrofluidics 6, 012809 (2012)

Nonlinearity and slip behavior of n-hexadecane in large amplitude oscillatory shear flow via nonequilibrium molecular dynamic simulation
J. Chem. Phys. 136, 104904 (2012)

Parabolic temperature profile and second-order temperature jump of a slightly rarefied gas in an unsteady two-surface problem
Phys. Fluids 24, 032002 (2012)

Instability of a transverse liquid rivulet on an inclined plane
Phys. Fluids 24, 032104 (2012)

Additional information on Phys. Fluids

Journal Homepage: http://pof.aip.org/

Journal Information: http://pof.aip.org/about/about_the_journal

Top downloads: http://pof.aip.org/features/most_downloaded

Information for Authors: http://pof.aip.org/authors

ADVERTISEMENT

Running in Circles Looking for the Best Science Job?
Search hundreds of exciting new jobs each month!
http://careers.physicstoday.org/jobs
physicstoday JOBS

PHYSICS OF FLUIDS **21**, 073101 (2009)

Analysis of accommodation coefficients of noble gases on aluminum surface with an experimental/computational method

Nathaniel Selden,[1] Natalia Gimelshein,[2] Sergey Gimelshein,[2] and Andrew Ketsdever[3]
[1]*University of Southern California, Los Angeles, California 90089, USA*
[2]*ERC, Inc., Edwards AFB, California 93524, USA*
[3]*Propulsion Directorate, Edwards AFB, California 93524, USA*

(Received 2 February 2009; accepted 12 June 2009; published online 22 July 2009)

A method that connects measurements of radiometric forces on a heated vane in the transitional flow regime with the kinetic modeling of the flow, and derives the accommodation coefficients through the successive analysis of measured and computed results, is proposed. The method utilizes the fact that radiometric forces exerted on heated objects immersed in rarefied gases are governed by the interaction of gas molecules with the surface. Experimental results on radiometric forces on a 0.11 m diameter circular vane are obtained on a nano-Newton thrust stand in a 3 m long vacuum chamber for pressures ranging from approximately 0.01 to 1 Pa. The vane was heated to 419 K on the hot side and 396 K on the cold side. The numerical modeling is conducted using a combined ellipsoidal statistical Bhatnagar–Gross–Krook/direct simulation Monte Carlo approach that allows accurate and time efficient analysis of radiometric forces on a vane in large vacuum chambers filled with rarefied gas. Accommodation coefficients for the Maxwell model are estimated for argon, xenon, and helium on a machined aluminum surface, and found to be 0.81, 0.86, and 0.53, respectively. © *2009 American Institute of Physics*. [DOI: 10.1063/1.3187932]

I. INTRODUCTION

The history of accommodation coefficients of energy and momentum of gas molecules colliding with solid surfaces spans well over a century.[1] Its beginning dates to the work of Kundt and Warburg[2] who studied the effect of gas density change in the damping of a vibrating disk. The viscosity appeared to decrease with density, which seemed unexplainable at the time. The authors suggested an incomplete interaction, or accommodation, of gas molecules at the surface, where a low density gas slips over a surface. Following that work, Maxwell[3] showed that the slip phenomenon has roots in kinetic theory, and he treated the solid wall as something intermediate between a perfectly reflecting and a perfectly absorbing surface. He proposed that "of every unit of area a portion α absorbs all the incident molecules, and afterwards allows them to evaporate with velocities corresponding to those in still gas at the temperature of the solid, while a portion 1-α perfectly reflects all the molecules incident upon it."[3]

The model proposed by Maxwell is in fact the first theoretical model that describes gas-surface interaction, and it is still widely used today both in experiment and numerical simulation. According to the Maxwell model, the velocity distribution function of reflected molecules may be written as a function of the accommodation coefficient α (see, for example, Ref. 4),

$$f_r(t,\mathbf{x},\mathbf{v}_r) = (1-\alpha)f_i(t,\mathbf{x},\mathbf{v}_r - 2(\mathbf{v}_r\cdot\mathbf{n})\mathbf{n}) + \alpha\left(\frac{\beta_r^2}{\pi}\right)^{3/2} e^{-\beta^2\mathbf{v}_r^2}, \quad (1)$$

where f is the distribution function, t is time, $\mathbf{x}$ and $\mathbf{v}$ are molecular position and velocity vectors, respectively, and $\mathbf{n}$ denotes the surface normal. Subscripts i and r refer to incident and reflected molecules, respectively, and $\beta=\sqrt{m/2kT_r}$. The first term in Eq. (1) refers to specular reflection and the second term refers to diffuse reflection. The reflected temperature, T_r, is the wall temperature, T_w, according to the original Maxwell's idea, but may generally be a free parameter of the model.

The tangential momentum transferred to the surface by the incident molecules may be written as[4]

$$\mathbf{P}_{i\tau} = -m\int_{\mathbf{v}\cdot\mathbf{n}<0} f_i\mathbf{v}_{i\tau}(\mathbf{v}_i\cdot\mathbf{n})d\mathbf{v}_i, \quad (2)$$

where the subscript τ refers to the tangential to the surface components of molecular velocity, and the tangential momentum of reflected molecules is then

$$\mathbf{P}_{r\tau} = -m\int_{\mathbf{v}\cdot\mathbf{n}>0} f_r\mathbf{v}_{r\tau}(\mathbf{v}_r\cdot\mathbf{n})d\mathbf{v}_r = (1-\alpha)\mathbf{P}_{i\tau}. \quad (3)$$

These equations show that the accommodation coefficient used in Eq. (1) may be considered as the coefficient of accommodation of the tangential momentum, and may be written as

$$\alpha \equiv \alpha_\tau = \frac{P_{i\tau}-P_{r\tau}}{P_{i\tau}}. \quad (4)$$

The accommodation coefficients for the normal momentum and energy may be introduced similar to Eq. (4) as

© 2009 American Institute of Physics

$$\alpha_n = \frac{P_{i\tau} - P_{r\tau}}{P_{i\tau} - P_w}, \quad \alpha_E = \frac{E_{i\tau} - E_{r\tau}}{E_{i\tau} - E_w}, \tag{5}$$

where the subscript w refers to the surface properties or the properties that would have had a gas at equilibrium with the wall.

Although the Maxwell model is still the most widely used model of gas-surface interaction, other models have also been proposed. Here we mention only a two-parameter Cercignani–Lampis model[5] that uses two accommodation coefficients, α_τ and α_n, and a multiparametric Nocilla model[6] in which the velocity of reflected molecules is simulated by the function

$$f = n_r \pi^{-3/2} c_r^{-3} \exp\{-c_r^{-2}[\vec{\xi} - c_r \vec{S}_r]^2\},$$

$$c_c = \sqrt{2k/mT_r},$$

$$\vec{S}_r = \vec{\xi}/c_r.$$

The four parameters $\vec{S}_r \equiv (S_{nr}, S_{\tau r})$, T_r, n_r of this function are determined from experimental data.

The development and utilization of different gas-surface interaction models is related to various application areas where such interactions are important. One area of interest is the high altitude aerodynamics, and, in particular, free molecular aerodynamics of satellites (see, for example, Ref. 7). For the latter application, the Nocilla model is often used. The importance of the gas-surface interaction model in this case is obvious since the collisions of molecules with the spacecraft surface are the dominant process that influences drag, lift, and heat loads.

Another area where the gas-surface processes are important is gas flows in micro- and nanoscale devices. In such devices, the gas mean free path is comparable to characteristic flow dimensions, and the consideration of kinetic effects is essential for accurate prediction of device performance and peculiarities. The large surface-to-volume ratio further increases the influence of the wall. Note that for microscale flows, the preservation of the detailed balance in collisions of gas molecules with solid interfaces is critical. Therefore, the Nocilla model, which does not satisfy this requirement, is not a good choice, and the Maxwell and Cercignani–Lampis models are better suited for the description of low speed flows in microdevices. Beside these two areas, gas-surface interaction is important, if not determining, in many other applications. Near-continuum supersonic flows over sharp leading edges, contamination problems, and two-phase flows[8] are just a few examples of such applications.

Accurate prediction of the above flows requires the researcher not only to select an appropriate gas-surface interaction model, but also to specify the parameters of this model for each type of gas species-solid wall interface. Two principal approaches are used to determine parameters of the model, theoretical and experimental. The theoretical approach is usually based on the detailed studies of molecular interactions using classical or quasiclassical trajectory calculations in the framework of the molecular dynamics method.[9] In the experimental approach, parameters of the selected interaction model are estimated directly from the measurement. The parameters for the Nocilla model, for example, are usually obtained from molecular beam experiments or flight experiments (see, for example, Refs. 10 and 11 and references therein). In Ref. 12, a connection between the exit velocity distribution described by the Nocilla model and the classical momentum and energy accommodation coefficients was given.

The advantage of the molecular beam technique is that it may provide detailed information on the velocity distributions of reflected molecules. There are many situations, however, when such detailed information is not necessary, and the knowledge of accommodation coefficients, either momentum or energy, would suffice. Examples include the force estimate of spacecraft at high altitudes, or the evaluation of heat loads in microdevices. Over the past three decades, molecular beam experiments have been used extensively to determine both the normal and tangential momentum and energy accommodation coefficients[13–15] for various gas-surface pairs. For the energy (thermal) accommodation coefficient, parallel plates, coaxial cylinders, and hot-wire methods have been widely used. A comprehensive review of different approaches to the thermal accommodation coefficient measurements may be found in Ref. 16. A wide range of results for accommodation coefficients have been reported for the three gases studied here (argon, xenon, and helium). In view of this, the results of Ref. 17 are particularly important; these are state-of-the-art measurements of energy accommodation coefficients for argon and helium at temperatures similar to those for the present work, and thus provide the most useful comparison with the present results. Various experimental techniques used in the past to measure tangential momentum accommodation coefficient, such as the rotating cylinder method, the spinning rotor gage method, the flow through microchannel approach, as well as the molecular beam technique, are discussed in recent review article.[18]

In contrast to high-enthalpy flows around space vehicles, gas-driven flows in microscale devices are characterized by relatively low gradients in gas velocity and temperature, and the velocity distribution function in these flows is often close to Maxwellian. As a result, prediction of gas-driven flows in such devices typically requires knowledge of momentum and/or energy accommodation coefficients as a function of gas and surface temperature. The use of molecular beam technique may be quite difficult in this case since the after-collision velocities need to be analyzed for a large number of precollisional energies. On the other hand, standard techniques for the accommodation measurement may not be applicable when information on momentum accommodation, normal, or tangential is needed.

One major issue with the need of gas-surface interaction parameters to predict complicated flow interactions is the range of experimental data for similar flows. For example, various experiments can have different, and in some cases conflicting, results. Take, for instance, the measurement of the energy accommodation of helium on a platinum surface. References 19–21 present results which vary by more than 30%. Thus there is a need to reinvestigate these data sets in order to study the effects of gas temperature, surface temperature, surface preparation, gas adsorption on surfaces, and gas pressure.

The objective of this work is to evaluate the feasibility of using a new method for measurements of momentum accommodation coefficients, based on the comparing experimental and computational results on radiometric forces on heated plates. Radiometric forces are typically exerted on nonuniformly heated objects immersed in rarefied gases, and tend to move these objects in the direction from the cold to the hot side. The authors of Ref. 22 have recently remarked that the measurement of radiometric forces may yield data on gas-surface interaction. However, there are two problems that make the direct use of such measurements to infer momentum accommodation coefficients extremely difficult. First, there are usually molecular collisions present in radiometric flows, and these collisions do not allow simple and accurate analytic evaluation of accommodation coefficients from force measurements beyond the free molecular regime. Second, while the availability of force measurements in free molecular regime would offer the benefit of accommodation coefficient evaluation, there is a physical limitation in the accuracy of such measurements. The fewer gas-surface collisions a radiometer vane experiences, the greater the experimental error. To avoid these difficulties, it is suggested in the present work to measure radiometric forces in the transitional regime, and then use kinetic modeling of radiometric flows to infer the momentum accommodation coefficients.

II. RADIOMETRIC APPROACH TO MOMENTUM ACCOMMODATION STUDY

The radiometric forces on a heated plate may be described analytically only in a free molecular regime; the presence of even relatively small number of molecular collisions in the transition regime complicates the flow to the point where accurate analytical description is not possible, and a numerical approach has to be used to address the problem. Even for a free molecule flow, some model needs to be used for the gas-surface accommodation in order to make analytical treatment possible.

Generally, for a plate with its opposite sides heated uniformly to different temperatures T_h and T_c, the forces in the direction normal to the plate, created by molecules reflected from the hot and the cold sides of the plate, may be written as

$$F_h = n_h m \int_{\mathbf{v}\cdot\mathbf{n}} f_h \mathbf{v}_{r\tau}(\mathbf{v}_r\cdot\mathbf{n})d\mathbf{v}_r \quad \text{and}$$

$$F_c = n_c m \int_{\mathbf{v}\cdot\mathbf{n}} f_c \mathbf{v}_{r\tau}(\mathbf{v}_r\cdot\mathbf{n})d\mathbf{v}_r, \qquad (6)$$

where subscripts h and c refer to the hot and cold sides, respectively. The number density that describes the flux of reflected molecules may be obtained from the assumption of the equality of the incident and reflected mass flux (i.e., no sticking on the surface),

$$n_{h,c}\int_{\mathbf{v}\cdot\mathbf{n}} f_{h,c}(\mathbf{v}_r\cdot\mathbf{n})d\mathbf{v}_r = n_g\int_{\mathbf{v}\cdot\mathbf{n}} f_g(\mathbf{v}_r\cdot\mathbf{n})d\mathbf{v}_r, \qquad (7)$$

where subscript g refers to the incident gas molecules. In a free molecular flow, the Maxwellian distribution function of f_g may be reasonably assumed. For fully diffuse accommodation, the number density of reflected molecules is obtained by integrating Eq. (7) over equilibrium distribution functions to give

$$n_{h,c} = n_g\sqrt{\frac{T_g}{T_{h,c}}}, \qquad (8)$$

where indices h and c refer to either hot or cold side of the plate. The force on the side of the plate will be

$$F_{h,c} = \frac{p_g}{2} + \frac{p_g}{2}\sqrt{\left(\frac{T_{h,c}}{T_g}\right)}, \qquad (9)$$

where p_g is the gas pressure. The first term in Eq. (9) is for the incident molecules and the second term accounts for the contribution from the reflected molecules. If the accommodation coefficient is introduced according to the expression suggested by Knudsen,[23]

$$\alpha_K = \frac{T_g - T_r}{T_g - T_w}, \qquad (10)$$

then assuming the same accommodation coefficient on the hot and cold sides of the plate (a small temperature difference between the plates), and using T_w from Eq. (10) instead of T_h and T_c in Eq. (9), one can obtain the expression for the total radiometric force on the plate,

$$F_K = \frac{p_g}{2}\left(\sqrt{\frac{(1-\alpha_K)T_g + \alpha_K T_h}{T_h}} - \sqrt{\frac{(1-\alpha_K)T_g + \alpha_K T_c}{T_c}}\right). \qquad (11)$$

Note that the contributions from the incident molecules cancel out in the free molecular flow; the force is directed from the hot to the cold surface.

If the Maxwell model of gas-surface interaction is used, then, substituting Eq. (1) into Eq. (6) and making use of Eq. (7), one can obtain for the free molecular force

$$F_M = \alpha\frac{p_g}{2}\left(\sqrt{\frac{T_h}{T_g}} - \sqrt{\frac{T_c}{T_g}}\right). \qquad (12)$$

Therefore, the free molecular radiometric force calculated using the Maxwell model is linearly dependent on the tangential momentum accommodation coefficient. If the momentum accommodation coefficient in the Maxwell model, α, is close to the energy accommodation coefficient in the Knudsen model, α_K, then the force predictions obtained with Eqs. (11) and (12) are similar for small temperature differences. The difference between them becomes significant when the surface temperatures are not similar. Equation (12) allows one to easily calculate the accommodation coefficients when the radiometric force in the free molecular regime can be measured.

In reality, however, it is difficult to accurately measure the radiometric force in free molecular regime. Such measurements are possible for a transitional regime, for which the above analytic expressions are not applicable. Therefore, it is reasonable to infer the accommodation coefficients from a numerical simulation performed for a given gas-surface interaction model with varying parameters of the model. It is clear that the conventional continuum approaches of the computational fluid dynamics, such as those based on the solution of the full Navier–Stokes equations or boundary layer equations, cannot be used to compute radiometric forces in the transitional flow regime. In these approaches, developed for modeling gas flows close to equilibrium, the effects of rarefaction are typically accounted for through the boundary conditions of slip velocity and temperature jump on the surface. The assumption of small deviation from equilibrium makes them inapplicable for modeling radiometric flows and calculating radiometric forces. In this case, a kinetic approach based on the solution of the Boltzmann equation has to be used. For a kinetic approach, a kinetic model of gas-surface interaction needs to be used, such as the Maxwell model, and the approach naturally gives the velocity distribution functions for the incident and reflected molecules.

Thus, in order to obtain the accommodation coefficients for a given gas-surface interaction model, numerical results need to be obtained by comparing results from a kinetic approach for a computational setup that closely reproduces the experimental one. The details on the present experimental setup are given in Sec. III.

III. EXPERIMENTAL SETUP

As radiometric phenomena occur in rarefied conditions, there are only two ways to study them experimentally. The first is to build extremely small devices on the order of nanometers and test them under atmospheric conditions. The second way is to build a larger device and modify the background pressure such that the local Knudsen number is large enough for the flow to be considered transitional (i.e., Kn >0.01). In this work the latter method has been chosen, and all the experimental results that follow have been achieved under low pressure conditions in a large 3.0 m diameter vacuum chamber. The use of such a large chamber is critical to avoid the effect of chamber walls that was found to strongly impact the radiometric force in smaller chambers.[24]

To accurately measure the impact of various accommodation coefficients, and to be practical to model using an axisymmetric code, a circular radiometer vane with a diameter of 11.13 cm was used. The vane consisted of a Teflon insulator sandwiched between two aluminum plates with a resistive heater located between one of the plates and the insulator. The temperature of one side of the device was maintained by varying the power input to the heater, while the temperature of the opposite side was not actively maintained and was allowed to float. Each of the three pieces of the radiometer vane had a thickness of 0.32 cm, and when assembled yield a total device thickness of 0.96 cm.

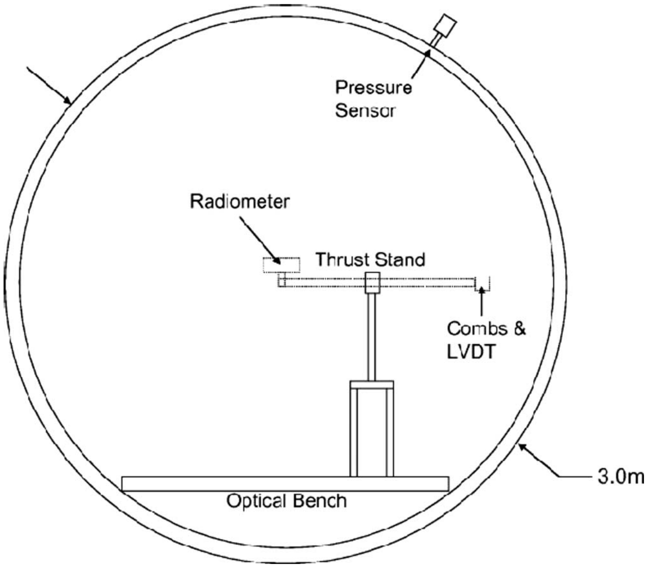

FIG. 1. Setup of the radiometric experiment.

One motivation for this particular configuration of radiometer vane comes from historical work[25] where rudimentary temperature measurements of the vanes suggested that a significant temperature drop occurred at the outermost edges. This same work made it quite clear that to accurately deduce a theory for the operation of the radiometer, it would be necessary to discover exactly what effect the temperature variations at the edges had. For the sake of clarity it should be noted here that there are two gradients important to the flow: The first of these shall be referred to as the radial gradient and will refer to the temperature profile of a plate from the center to the periphery, while the second will be called the axial gradient and will refer to temperature profile along an axis normal to the face. In an ideal experiment, the axial gradient would be large and the radial gradient would be nonexistent such that the experiment and simulation share nearly identical temperature profiles. It is for these reasons that the particular aluminum "sandwich" design was chosen; not only does the high thermal conductivity maximize the surface temperature of the hot plate (and thus the axial temperature gradient), but it also minimizes the radial temperature gradients near the edges of the device.

To measure the force produced by this device, it was mounted on a modified nano-Newton Thrust Stand[26] (nNTS) located inside the vacuum chamber. A schematics of the experimental setup is shown in Fig. 1. Here, every effort was made to minimize the impact of the thrust stand arm and attachment mechanism by using 6.35 mm tubing coupled with a 2×40 mm^2 threaded rod. When calibrated using a pair of electrostatic combs,[27] the nNTS provides very accurate and repeatable data with typical force resolution of approximately 0.1 μN and statistical scatter of about 1%. For the preliminary experiment, the experimental error based on standard deviation ranges from a few percent at the lowest pressures to less than 1% through most of the curve. However, due to the normalization by experimental temperature measurements and the small uncertainty of the calibration method, the total absolute experimental uncertainty is $\approx$4%.

Day-to-day variation of multiple data sets has been observed to be $\approx 1\%$.

The experimental data were obtained by evacuating the vacuum chamber to a base pressure below 10^{-3} Pa. This low pressure was required to minimize the impact of the background gas to a level low enough as to be inconsequential to the measurements being made. While the evacuation of the chamber was taking place, a constant voltage was applied to the heater. This resulted in the main radiometer surfaces reaching temperatures of approximately 419 K (hot) and 394 K (cold), although the exact values fluctuated depending on both the species and pressure of the background gas. Force measurements were made by varying the background pressure of the gas in the chamber, where argon, helium, and xenon were all used. The highest background pressure achieved was approximately 1.6 Pa, but varied depending on the molecular weight of the background gas.

IV. NUMERICAL MODELING OF RADIOMETRIC FLOWS: A COMBINED KINETIC APPROACH

In this work, a combined ellipsoidal statistical Bhatnagar–Gross–Krook/direct simulation Monte Carlo (ES-BGK/DSMC) approach, where the final solution is obtained in two successive steps. First, an ES-BGK modeling is conducted in a large computational domain that includes both the radiometer vane and the chamber walls. The solution of this first step is used to set the boundary conditions for the second step. At the second step, the DSMC method is applied in a much smaller domain, with the subsonic boundary conditions taken from the first step. The use of such a new approach is based on the fact that DSMC modeling of a radiometric flow on a 10 cm vane in a 3 m chamber, where the accuracy of the radiometric force modeling needs to be on the order of 1%, is prohibitively expensive even for modern parallel computers. On the other hand, the ES-BGK method was found to be fairly accurate in predicting all gas macroparameters in the computational domain, but overpredicting the DSMC results on radiometric forces by ~10% in the range of pressures where the force is near its maximum. This is related to the approximations inherent in the ES-BGK equation, and difficulty of modeling the radiometric force, that is typically less than 1% of the force on either cold or hot side of the vane.

In this work, the computational tool SMILE (Ref. 28) was used to obtain the solutions with the DSMC method. In DSMC runs, the variable soft sphere model with parameters listed in Ref. 29 was used for the molecular collisions, and the Maxwell model was used to calculate gas-surface collisions. A finite volume solver SMOKE (Ref. 30) has been used to deterministically solve the ES model kinetic equation. SMOKE is a parallel code based on conservative numerical schemes developed by Mieussens.[31] A second order spatial discretization was used. The solutions were typically obtained in two successive steps. First, an implicit time integration scheme was run until the result is converged. Second, a conservative explicit time integration scheme was used with the initial conditions from the first step. This two-step approach allowed up to two orders of magnitude reduction in computational time compared to an explicit-only case.

The four macroparameters (density, temperature, and two velocities) from the ES-BGK solution were used at the external boundaries of the DSMC computational domain. That means that the velocities of molecules entering the DSMC computational domain are sampled from the Maxwellian distribution with parameters from the ES-BGK solution. It is important that the ES-BGK macroparameters used in the DSMC boundary conditions were computed from the incoming fluxes only. Good agreement between the full DSMC and the combined kinetic approach, obtained by the authors on a smaller, 0.2 m domain, allowed the application of the combined approach to analyze radiometric flows in a large vacuum chamber. A 3 m cylindrical chamber is simulated in this work, whose geometry with good accuracy reproduces the companion experimental setup. The radiometer size and location inside the chamber, as well as the temperature conditions, also correspond to those used in the experiment. Diffuse reflection with a complete energy and momentum accommodation was assumed on the chamber walls and the surface of the vane (with one exception explained below). Since the experimental setup closely approximates a flow with an axial symmetry, axisymmetric ES-BGK and DSMC codes were used in these computations. The subsonic boundaries of the DSMC computational domain were located 30 cm from the vane both in the axial and radial directions.

V. EVALUATION OF ACCOMMODATION COEFFICIENTS

Three gases were considered in this work, argon, xenon, and helium. The radiometric forces for these gases, obtained with the combined ES-BGK/DSMC approach as well as measured experimentally, are presented in Fig. 2. Generally, the radiometric force consists of two components, (i) the total radiometric force that includes the force resulting from the pressure difference between the hot and the cold sides of the vane, and (ii) the shear force on the lateral (circumferential) side of the vane. To show separate contribution of these forces, two sets of numerical results are shown, the total radiometric force that includes both component, and the radiometric force that is based on pressure alone. The results show that the shear force is a minor factor for pressures smaller than 0.6 Pa for argon, where the maximum force is observed. It becomes more significant for larger pressures, for which the contribution of the lateral side of the vane cannot be ignored. It may appear preferable to analyze the accommodation coefficients under conditions where the lateral side has a negligible effect, such as a much thinner vane, but it is difficult to realize in the experiment.

For all three gases, the experimental data lay lower than the numerical points, which is a clear indication of an incomplete surface accommodation. Beyond that, several other factors may play a role in this difference. First, there are numerical and experimental errors; they are not expected to cause a difference between the computation and the measurement larger than 5%. Then, there is a finite chamber size, with unknown accommodation on chamber walls. This has

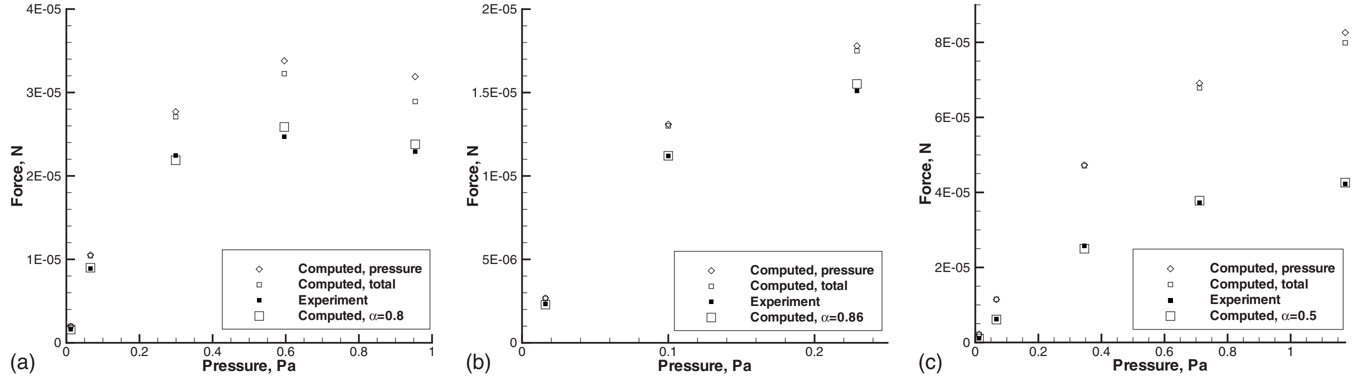

FIG. 2. Experimental and computed radiometric force for argon (left), xenon (center), and helium (right).

been found to be a minor issue in a series of ES-BGK calculations, where the chamber size larger than about 2 m was found to have a negligible effect on the radiometric force. Finally, there is some impact of intermolecular collision law, or, in other words, gas viscosity and heat conductivity. This factor is also believed to be minor, as the bulk gas properties correspond to well established experimental values for the temperature range under consideration. All these indicate that the gas accommodation on the vane surface is the main reason for the difference between the numerical and experimental values. For comparison, additional computations were conducted for the thee gases using the Maxwell model with an accommodation coefficients of 0.8 for argon, 0.86 for xenon, and 0.5 for helium. It is clearly seen that the use of a lower accommodation coefficient allows one to obtain good agreement with experimental data for all pressures and gases considered.

The value of 0.5 for accommodation coefficient used for helium to reproduce the experimental data is in fact close to the experimental-to-computed ratio of 0.53 obtained after averaging over pressures. Remember that the Maxwell model is characterized by a linear dependence between the force and the accommodation coefficient; obviously, the dependence is close to linear in the transitional regime as well. The value of 0.5 may in fact be obtained if the Knudsen model of accommodation is assumed, and the functional dependence of Eq. (11) is applied. In this case, the unknown α is calculated by equating the ratio of the right hand sides of Eq. (11) with $\alpha_K=\alpha$ and $\alpha_K=1$ to the experimental-to-computed force ratio. Note that the value 0.5 is obtained when the Knudsen model of accommodation is assumed, and the functional dependence of Eq. (11) and equating the ratio of the right hand sides of Eq. (11) with an unknown α_K and $\alpha_K=1$ to the experimental-to-computed force ratio.

Interestingly, the value of 0.5 also coincides with that of the Knudsen model of accommodation obtained assuming the functional dependence of Eq. (11) and equating the above ratio. As was mentioned earlier, the difference between the accommodation coefficients defined by the Maxwell model and the Knudsen expression is small for relatively small temperature differences examined in this work. It is therefore impossible to state which one is a better approximation for the transitional regime. For kinetic approaches, the authors believe that the use of Eq. (12) may be a better fit, with a simple ratio between the experimental and numerical radiometric forces being an estimate of the accommodation coefficient in the Maxwell model. Such a ratio for different gases is presented in Fig. 3. The accommodation coefficients for the Maxwell model, obtained in this work, are 0.81 for argon, 0.86 for xenon, and 0.53 for helium, all of them on a machined aluminum surface. Note that the value of the accommodation coefficient increases with molecular mass, which is consistent with the experimental observation of Ref. 32 but contradicts to a hypothesis of Ref. 33.

VI. COMPARISON WITH PREVIOUS MEASUREMENTS

Comparison of the above accommodation coefficients with those measured in the past is complicated by several factors in addition to their obvious dependence on particular gas and surface material. First, the coefficients obtained in this work are integral and not incident angle dependent. Therefore, it is difficult to compare them with molecular beam experiments. Second, the coefficients are generally sensitive to the wall and the surrounding gas temperature, and the results should be analyzed for the same temperature regime. Finally, the purity of the surface is very important, as the surface coverage and surface contamination change the accommodation coefficients. The last factor is related to the surface temperature and associated gas desorption, the sur-

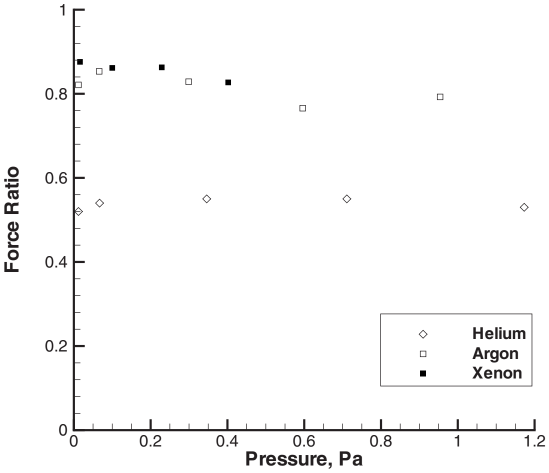

FIG. 3. Experimental-to-computed radiometric force ratio.

TABLE I. Comparison of the present accommodation coefficients to the previous measurements.

Gas	Present	Ref. 17	Ref. 32	Ref. 16	Ref. 18
Helium	0.53	0.38–0.47	0.65		
Argon	0.81	0.86		0.334–0.75	0.893
Xenon	0.86			0.4	0.95

face roughness and multiple gas-surface encounters, and the gas pressure. All these factors contribute to large differences often observed between accommodation coefficients measured by different authors. Some of the published results for the three gases considered in this work, along with the present data, are given in Table I.

For helium, the present accommodation coefficients, 0.53 for the Maxwell model and 0.5 for the Knudsen model, are close to that obtained in Ref. 17 for the thermal accommodation coefficient on machined aluminum kept at room temperature, for which the value of 0.47 was measured. The accommodation coefficient of helium on a plasma treated surface obtained in Ref. 17 is lower, 0.38. The normal momentum coefficients recommended[32] for helium on aluminum are somewhat higher, 0.65. It was also shown in Ref. 32 that the efficiency of the momentum transfer process increases with the mass of gas molecules, and relatively weakly depends on the surface material for temperatures ranging from 25 to 550 °C. The tangential momentum coefficients of helium on aluminum are not available, but for other materials were found to vary in a wide range depending on the experimental technique used, from 0.2 (Ref. 34) to about 0.9.[35]

The thermal accommodation coefficient of argon on aluminum, tabulated in Ref. 16, ranges from 0.334 to 0.75 for different experimental techniques and surface temperatures from 400 to 800 K. A larger value of 0.86 was measured[17] for argon atoms colliding with a machined aluminum surface. A tangential momentum accommodation coefficient of 0.893 was recommended in Ref. 18 based on the analysis of a large array of experimental data.

The accommodation of xenon on aluminum has not been extensively studied in the past. The thermal accommodation coefficient was reported for temperatures from 500 to 800 K as 0.4,[16] where a concentric-cylinder method was used. Among other materials, platinum was studied theoretically[36] and the energy and momentum accommodation coefficients were calculated for room temperature conditions to be 0.85 and 0.81, respectively. A mean value of 0.95 was recommended in Ref. 18 for the tangential momentum accommodation coefficient of xenon on commonly employed surface materials. In measurement,[33] this coefficient was estimated as 0.9 for xenon on bronze ribbon.

VII. CONCLUSIONS

A method for estimation of gas-surface accommodation coefficients, based on comparing measured and computed radiometric forces on heated vanes in rarefied flows, is presented. The method applies a new combined ES-BGK kinetic approach to match accurately measured force on a circular radiometer installed on a nNTS and mounted in a large vacuum chamber. Accommodation coefficients for the Maxwell model of gas-surface interaction may be deduced for a given pressure and gas-surface pair whether through the successive use of the combined approach with different values of the accommodation coefficient, or assuming a linear dependence of radiometric force on the accommodation coefficient.

Helium, argon, and xenon were considered in this work, for pressures ranging from approximately 0.01 to 1 Pa, and an aluminum vane with a diameter of 0.113 m was examined. The suggested values of the Maxwell model accommodation coefficients are 0.81 for argon, 0.86 for xenon, and 0.53 for helium, which reasonably agree with momentum and energy accommodation coefficients proposed in literature. The proposed experimental-computational method is general enough to be applied to a wide range of gases, surfaces, and temperature conditions.

ACKNOWLEDGMENTS

This work was supported in part by the Propulsion Directorate of the Air Force Research Laboratory at Edwards Air Force Base, California. The authors thank Ingrid Wysong and Dean Wadsworth for many fruitful discussions.

[1] H. Y. Wachman, "The thermal accommodation coefficient: A critical survey," Am. Rocket Soc. J. **32**, 2 (1962).
[2] A. Kundt and E. Warburg, "Ueber Reibung und Wärmeleitung verdünnter Gase," Ann. Phys. **232**, 177 (1875).
[3] J. C. Maxwell, "On stresses in rarified gases arising from inequalities of temperature," in *The Scientific Papers of James Clerk Maxwell*, edited by W. D. Niven (Dover, New York, 1965), Vol. 2, p. 707.
[4] M. N. Kogan, *Rarefied Gas Dynamics* (Plenum, New York, 1969).
[5] C. Cercignani and M. Lampis, "Kinetic models for gas-surface interactions," Transp. Theory Stat. Phys. **1**, 101 (1971).
[6] S. Nocilla, "The surface re-emission law in free molecule flow," *Proceedings of the Third International Symposium on Rarefied Gas Dynamics*, edited by J. A. Laurmann (Academic, New York, 1963), Vol. 1, pp. 327–346.
[7] G. Koppenwallner, D. Johannsmeier, H. Klinkrad, M. Ivanov, and A. Kashkovsky, "A rarefied aerodynamic modelling system for earth satellites (RAMSES)," *Proceedings of the 19th International Symposium on Rarefied Gas Dynamics*, edited by J. Harvey and G. Lord (Oxford University Press, Oxford, 1995), Vol. 2, pp. 1366–1372.
[8] S. Gimelshein, G. Markelov, and J. Muylaert, "Numerical modeling of low thrust solid propellant nozzles at high altitudes," in Proceedings of the 9th AIAA/ASME Joint Thermophysics and Heat Transfer Conference, 5–8 June 2006, San Francisco, CA, AIAA Paper No. 2006-3273, 2006.
[9] J. M. Haile, *Molecular Dynamics Simulation* (Wiley, New York, 1997).
[10] S. R. Cook and M. A. Hoffbauer, "Nocilla model parameters obtained from forces exerted on surfaces by molecular beams," J. Spacecr. Rockets **34**, 379 (1997).
[11] F. C. Hurlbut, "Gas surface interactions: Recent observations and interpretations," *Proceedings of the 20th International Symposium on Rarefied Gas Dynamics*, edited by C. Shen (Peking University Press, Beijing, 1997), pp. 355–367.

[12] F. C. Hurlbut, "Two contrasting models for the description of wall-gas interactions," *Progress in Astronautics and Aeronautics*, Proceedings of the 18th International Symposium on Rarefied Gas Dynamics, edited by B. D. Shizgal and D. P. Weaver (AIAA, Washington, DC, 1994), Vol. 158, pp. 494–506.

[13] L. B. Thomas and R. G. Lord, "Comparative measurement of tangential momentum and thermal accommodation on polished and roughened steel spheres," *Proceedings of the Eighth International Symposium on Rarefied Gas Dynamics*, edited by R. Karamcheti (Academic, New York, 1974), pp. 405–412.

[14] S. R. Cook, "Molecular beam measurements of absolute momentum accommodation on spacecraft surfaces using a specialized torsion balance," Ph.D. thesis, The University of Texas at Austin, 1995.

[15] A. P. Nikiforov, "Measuring the momentum flux of molecules reflected from a surface of given roughness in free molecule flow," Fluid Dyn. **20**, 630 (1985).

[16] S. C. Saxena and R. K. Joshi, "Thermal accommodation and adsorption coefficients of gases," *Thermal Accommodation and Adsorption Coefficients of Gases* (Hemisphere, New York, 1989).

[17] W. M. Trott, D. J. Rader, J. N. Castañeda, J. R. Torczynski, and M. A. Gallis, "Measurement of gas-surface accommodation," Proceedings of the 26th International Symposium on Rarefied Gas Dynamics, Kyoto, Japan, July 2008.

[18] A. Agrawal and S. V. Prabhu, "Survey on measurements of tangential momentum accommodation coefficient," J. Vac. Sci. Technol. A **26**, 634 (2008).

[19] W. B. Mann, "The exchange of energy between a platinum surface and gas molecules," Proc. R. Soc. London, Ser. A **146**, 776 (1934).

[20] P. Rolf, "The accommodation coefficient of helium on platinum," Phys. Rev. **65**, 185 (1944).

[21] L. B. Thomas and F. Olmer, "The accommodation coefficients of He, Ne, A, H2, D2, O2, CO2, and Hg on platinum as a function of temperature," J. Am. Chem. Soc. **65**, 1036 (1943).

[22] A. Passian, R. J. Warmack, T. L. Ferrell, and T. Thundat, "Thermal transpiration at the microscale: A Crookes cantilever," Phys. Rev. Lett. **90**, 124503 (2003).

[23] M. Knudsen, "Die molekulare Wärmeleitung der Gase und der Akkommodationskoeffizient," Ann. Phys. **339**, 593 (1911).

[24] N. P. Selden, S. F. Gimelshein, N. E. Gimelshein, and A. D. Ketsdever, "Effect of chamber wall proximity on radiometer force production," 26th International Symposium on Rarefied Gas Dynamics, Kyoto, Japan, 21–25 July 2008.

[25] H. E. Marsh, "Further experiments on the theory of the vane radiometer," J. Opt. Soc. Am. **12**, 135 (1926).

[26] A. J. Jamison, A. D. Ketsdever, and E. P. Muntz, "Gas dynamic calibration of a nano-Newton thrust stand," Rev. Sci. Instrum. **73**, 3629 (2002).

[27] N. P. Selden and A. D. Ketsdever, "Comparison of force balance calibration techniques for the nano-Newton range," Rev. Sci. Instrum. **74**, 5249 (2003).

[28] M. S. Ivanov, G. N. Markelov, and S. F. Gimelshein, "Statistical simulation of reactive rarefied flows: Numerical approach and applications," in Proceedings of the 31st AIAA Thermophysics Conference, Albuquerque, NM, June 1998, AIAA Paper No. 98-2669.

[29] G. A. Bird, *Molecular Gas Dynamics and the Direct Simulation of Gas Flows* (Clarendon, Oxford, 1994).

[30] D. C. Wadsworth, N. E. Gimelshein, S. F. Gimelshein, and I. J. Wysong, "Assessment of translational anisotropy in rarefied flows using kinetic approaches," Proceedings of the 26th International Symposium on Rarefied Gas Dynamics, Kyoto, Japan, July 2008.

[31] L. Mieussens, "Discrete-velocity models and numerical schemes for the Boltzmann-BGK equation in plane and axisymmetric geometries," J. Comput. Phys. **162**, 429 (2000).

[32] R. Stickney, "Momentum transfer between gas molecules and metallic surfaces in free molecule flow," Phys. Fluids **5**, 1617 (1962).

[33] T. Gronych, R. Ulman, L. Peksa, and P. Repa, "Measurements of the relative momentum accommodation coefficient for different gases with a viscosity vacuum gauge," Vacuum **73**, 275 (2004).

[34] R. G. Lord, "Tangential momentum coefficients of rare gases on polycrystalline surfaces," *Proceedings of the Tenth International Symposium on Rarefied Gas Dynamics* (American Institute of Astronautics and Aeronautics, New York, 1977), pp. 531–538.

[35] B. T. Porodnov, P. E. Suetin, S. F. Borisov, and V. D. Akinshin, "Experimental investigation of rarefied gas flow in different channels," J. Fluid Mech. **64**, 417 (1974).

[36] K. Yamamoto, "Slip flow over a smooth platinum surface," JSME Int J., Ser. B **45**, 788 (2002).

JOURNAL OF PROPULSION AND POWER
Vol. 25, No. 3, May–June 2009

Technical Notes

TECHNICAL NOTES are short manuscripts describing new developments or important results of a preliminary nature. These Notes should not exceed 2500 words (where a figure or table counts as 200 words). Following informal review by the Editors, they may be published within a few months of the date of receipt. Style requirements are the same as for regular contributions (see inside back cover).

Development of a Specific Impulse Balance for Capillary Discharge Pulsed Plasma Thrusters

T. C. Lilly* and A. D. Ketsdever†
University of Colorado, Colorado Springs, Colorado 80933
A. P. Pancotti‡
ERC Incorporated, Edwards Air Force Base, California 93524
and
M. Young§
Air Force Research Laboratory, Edwards Air Force Base, California 93524

DOI: 10.2514/1.40261

I. Introduction

CAPILLARY-DISCHARGE-BASED (CD), coaxial, electrothermal pulsed plasma thrusters (PPT) are currently under development as a high-efficiency alternative to more traditional ablative PPTs. The major drawback of the traditional ablative PPT is the propulsive efficiency. Even though specific impulses (I_{sp}) on the order of 1000 s have been achieved with ablative PPTs using electromagnetic acceleration, the propulsive efficiencies of flight-qualified thrusters typically remains below 10% [1]. Capillary discharges are relatively efficient sources of high-density, high-temperature plasmas, which are being developed for a number of applications [2–4]. The CD operates on a solid propellant ablated from a relatively long tube during a pulsed discharge. Previous performance calculations have suggested that a capillary-discharge-based electrothermal PPT can achieve propulsive efficiencies of 30–40% even without nozzle expansion [5]. Additional studies indicate that nozzle expansion of the high-pressure, high-temperature plasma generated by the capillary discharge will increase the efficiency above 50% [6]. With the potential for vast improvement in efficiency, the capillary-discharge, electrothermal PPT may be a strong candidate for satellite attitude control and station-keeping maneuvers.

In the present study, a diagnostic tool has been developed to investigate the applicability of a capillary discharge as an electrothermal PPT. A torsion thrust stand similar to that described in [7] has been designed and built to simultaneously measure the impulse and mass loss of the capillary discharge. The simultaneous nature of the developed technique will allow a per-pulse measurement of the discharge's specific impulse through the relation

$$I_{sp} = \frac{I_{tot}}{m_{prop} g_0} \tag{1}$$

where I_{tot} is the total impulse, m_{prop} is the total propellant mass loss, and g_0 is the gravitational constant. The thruster will be configured on the thrust stand such that the impulse generated by the discharge and the steady-state force generated by the propellant mass loss act in the same direction. The combined signal from these effects can then be decoupled to assess the ratio of the impulse to the weight of propellant expended, yielding the specific impulse.

The thrust stand system developed in [7] has several advantages over more traditional methods of measuring specific impulse in solid propellant thrusters. First, the amount of mass loss is relatively low when compared with the associated impulse provided by a high-I_{sp} thruster. Traditional mass loss measurements would require the averaging of multiple thruster firings to obtain meaningful data. By developing a system capable of measuring signals over several orders of magnitude, impulse and mass loss measurements can be made simultaneously on a shot-to-shot basis. Second, the system mass is traditionally measured before the performance measurements, and again after, to assess the propellant mass used [8]. These measurements may take place days apart and may require the system to be placed into a vacuum chamber and subsequently removed in between thruster firings at the cost of valuable time and resources. Finally, issues of handling, contamination, oxidation, and adsorption may complicate mass measurements that are not done in situ.

The simultaneous measurement of the total impulse and propellant mass loss is discussed in detail in [7]. In short, the thrust stand acts as an over-damped second-order oscillator whose motion in response to a known forcing moment can be predicted by its moment of inertia (I), damping coefficient (C), and torsion spring constant (K). For impulses with pulse widths much shorter than the period of the thrust stand, the magnitude of the total impulse imparted to the stand has a linear relation with the maximum deflection range of its motion. The mass loss has an equally well-defined relation to the difference between the initial zero position of the thrust stand and the final position once oscillatory motion has sufficiently damped. Examples of these relations can be seen in Figs. 1 and 2. Note that a thrust stand for a given application can be designed such that the range (governed by I, C, and K) is much larger than the steady-state deflection (governed only by K), thereby minimizing the error in the impulse measurement due to the steady-state mass loss. Using the model derived and validated in [9], the configuration of an operational thrust stand will be discussed in following sections.

II. Thrust Stand Design

The major components of the thrust stand are the rotational arm, damping magnets, flexure pivots (torsion springs), displacement sensor, and calibration system. The rotational arm contributes to the moment of inertia I of the stand and provides a structure to attach the thruster and other components. The damping magnets are used as eddy current generators to damp the stand's motion and define the

---

Presented as Paper 4740 at the 44th AIAA/ASME/SAE/ASEE Joint Propulsion Conference & Exhibit, Hartford, CT, 21–23 July 2008; received 5 August 2008; revision received 11 November 2008; accepted for publication 22 December 2008. Copyright © 2008 by the American Institute of Aeronautics and Astronautics, Inc. All rights reserved. Copies of this paper may be made for personal or internal use, on condition that the copier pay the $10.00 per-copy fee to the Copyright Clearance Center, Inc., 222 Rosewood Drive, Danvers, MA 01923; include the code 0748-4658/09 $10.00 in correspondence with the CCC.

*Senior Professional Research Assistant, 1420 Austin Bluffs Parkway, University Hall Room 231. Student Member AIAA.

†Assistant Professor of Mechanical and Aerospace Engineering, 1420 Austin Bluffs Parkway UH231. Associate Fellow AIAA.

‡Research Engineer, 10 East Saturn Boulevard. Student Member AIAA.

§Deputy Program Manager of Advanced Concepts, Propulsion Directorate, 10 East Saturn Boulevard. Member AIAA.

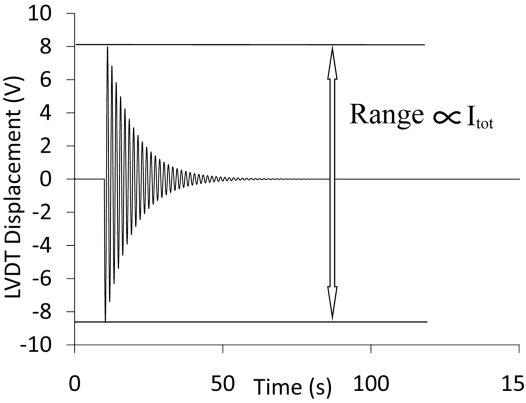

Fig. 1 Simulated LVDT reading for expected impulse from an operational capillary discharge.

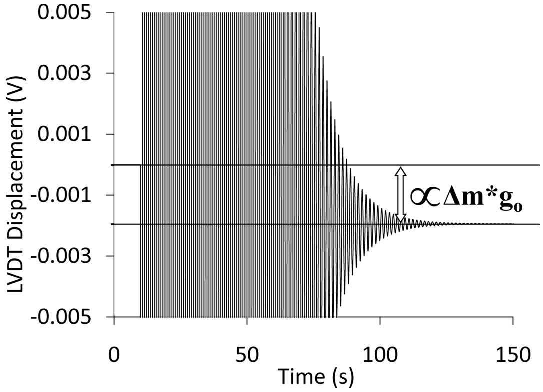

Fig. 2 Simulated LVDT reading for expected mass loss from an operational capillary discharge.

damping coefficient C of the stand. The torsion springs (flexures) contribute to the spring constant K by providing the restoring force for the stand. The displacement sensor measures the linear motion of the stand and defines the limits of the stand's motion as well as the precision of the measurements. The calibration system provides a known steady-state force or transient impulse to the stand and defines the useful range of the stand's accuracy. The major components of a thrust stand can be seen in Fig. 3.

Special consideration must be given to a choice in displacement sensors because the CD involves strong electromagnetic fields during the discharge. Such fields will interfere with any locally mounted electronic force sensors, such as piezo-based load cells. This interference is only present during the thruster firing, for which the thrust stand has an advantage. The pertinent measurement of the thrust stand's motion required for an impulse determination is made relatively long after the thruster firing. Thus, for sensors that recover from the electromagnetic interference sufficiently quick, the effect from the interference is negligible. Linear variable differential transformers (LVDTs) have been successfully implemented on a previous thrust stand [7]. These sensors have an advertised repeatability less than or equal to 0.01%. The useful range and accuracy of the detector, for a given thrust stand configuration, directly sets the maximum impulse and minimum mass loss able to be resolved by the thrust stand.

To correlate position measurements with known forces and impulses, the stand must be calibrated in the same configuration that the thruster testing is conducted. The most straightforward system of calibration is to place calibrated weights on the stand to create a known force. Unfortunately, this method is not easily replicated for in situ vacuum calibration or short-duration impulses. Previous iterations of thrust stands have used electrostatic combs to generate repeatable and known attractive forces [10]. To cover the lower region of impulse calibration and allow for steady-state force calibration, a larger-scale electrostatic calibration system has been designed and built to impart up to a 5×10^{-2} N force to the thrust stand. To cover the higher region of impulse calibration, a piezoelectric impact hammer will be implemented to calibrate in the $10^{-4} - 10^{1}$ $\mathrm{N \cdot s}$ range. Figure 4 shows the linear relationship obtained between the impact hammer impulse and the deflection range of the thrust stand.

When choosing a set of flexures for the stand, the primary concern for the specific impulse measurement is that the change in beginning and ending positions due to CD mass loss is large enough to be resolved by the displacement sensor and ancillary acquisition hardware, yet small enough not to cause a large error in the impulse measurement. For the steady-state condition before and after the CD discharge, the displacement of the thrust stand is only dependant on the magnitude and position of the mass loss and the spring constant K of the stand. Figure 5 shows the expected LVDT reading for a 12 mg mass loss, the amount predicted by the CD model in [6], as measured

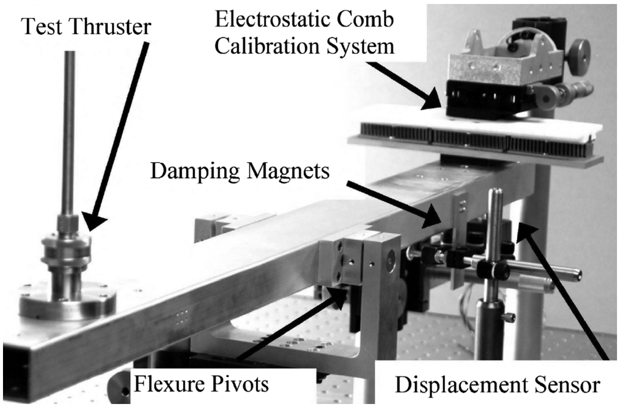

Fig. 3 Major thrust stand components.

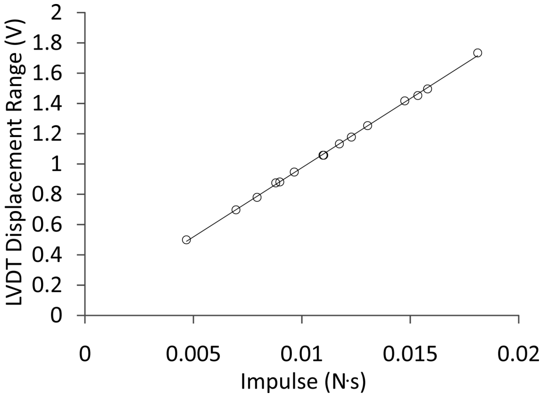

Fig. 4 Thrust stand deflection range vs imparted impulse from an impact hammer ($R^2 = 0.9993$).

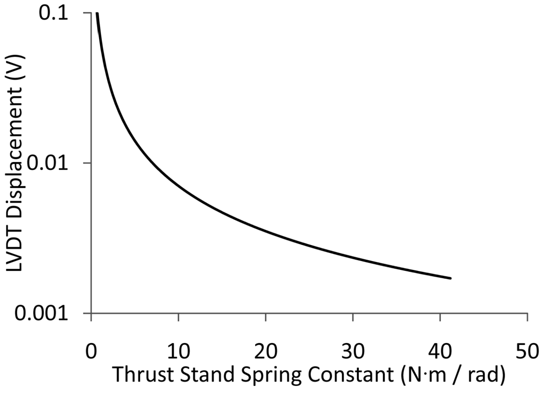

Fig. 5 Thrust stand deflection vs spring constant K.

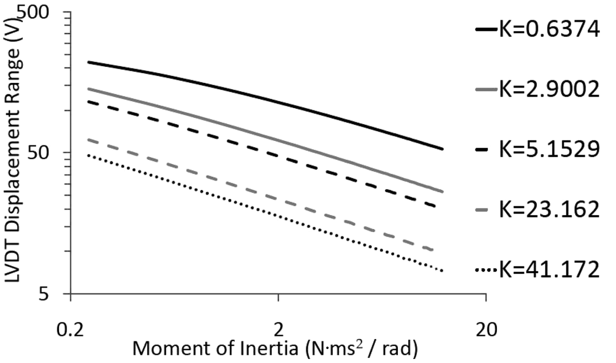

Fig. 6 Thrust stand deflection range vs I for multiple K (note logarithmic axes).

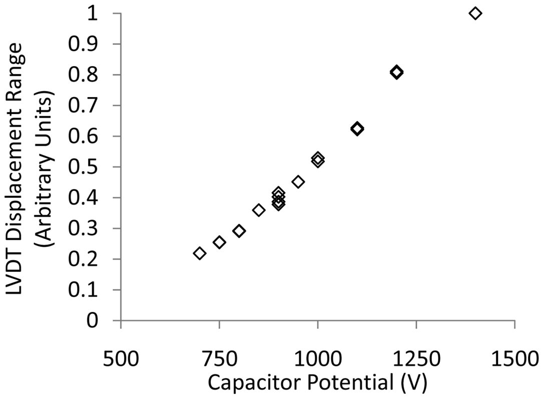

Fig. 7 Thrust stand displacement range vs CD capacitor potential.

by the designed thrust stand as a function of the spring constant. Given a data acquisition hardware resolution of better than 1 mV, a thrust stand using any of the spring constants in the plotted range would be able to resolve a single-shot mass loss measurement. For high resolution, the preference for larger displacements can be obtained for smaller values of the spring constant. The spring constant, as well as the moment of inertia, affects the maximum range of the thrust stand for a given impulse. The range decreases with increasing spring constant and moment of inertia, as seen in Fig. 6. There is a diminishing return for limiting the range by increasing the moment of inertia of the thrust stand; therefore, the inherent limit of the displacement sensor indicates that higher spring constants are needed to limit the range produced by a given applied impulse. This leads to a trade that yields an optimum value for the spring constant when balancing between the sensitivity needed for the mass loss measurements and the restoring force needed for the total impulse measurements.

III. Results and Discussion

As an iterative first step to CD-specific impulse measurements, a thrust stand comprising only the major elements was built. This iteration was used to validate the thrust stand model in [9] and its use for this application. It was also used as a test bed for integrating the thruster, calibration, and sensing equipment. The model coefficients for the first-iteration thrust stand can be seen in Table 1. The measured K value matches the advertised unloaded spring constant from the manufacturer (published as $\pm 10\%$) within 1.5%. The measured motion of the thrust stand matched the model predicted motion. To test the CD attachment, data acquisition and control, power transfer connections, and feasibility of using an LVDT in the vicinity of the discharge, the CD was attached to the first-iteration thrust stand. Because the first-iteration thrust stand was not designed for the CD at operational power levels, the CD was operated at relatively low power. The displacement range measured by the LVDT on this stand vs the voltage potential on the discharge capacitor bank can be seen in Fig. 7. From [6], the total impulse should increase with an increase in capacitor potential, a trend that is reflected by the increase in measured deflection range.

With an experimentally validated model, the design space for the modification of the thrust stand for measuring the expected CD performance values from [6] was investigated. This trade study consisted of running the model for a variety of flexures and moments of inertia shown in Fig. 6. The first-iteration thrust stand could not measure the operational capillary discharge impulse as it would result in a range larger than the linear section of the LVDT. From Fig. 6, it is possible to limit this range of motion by increasing the spring constant of the stand; however, too large a K value would not allow the stand to be useful for accurate mass loss measurements. Altering the moment of inertia offers near continuous values of the range simply by adding mass to the rotational arm without degrading resolution in the mass loss measurements.

Based on estimates from the preformed trade study, the first-iteration stand's moment of inertia was modified by adding 5 kg to the end of each side of the rotational arm. In addition, the original aluminum damping plate was replaced with a copper plate, which generated a larger damping force to reduce stand motion. These changes can be seen in Fig. 8 and the characteristics of the stand in Table 1. After modifications, the model and modified stand were tested. The change in I and observed change in K are properly reflected in a change in measured period and maximum deflection

Table 1 Thrust stand characteristics

Thrust stand	First iteration	Operational
K, N m/rad	41.75	36.22
C, N m s/rad	0.191	0.428
I, N m s^2/rad	0.245	1.988

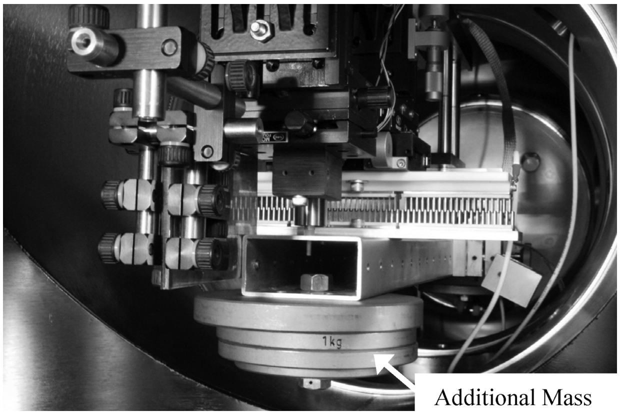

Fig. 8 Experimental thrust stand, calibration system, LVDT, and magnetic damping.

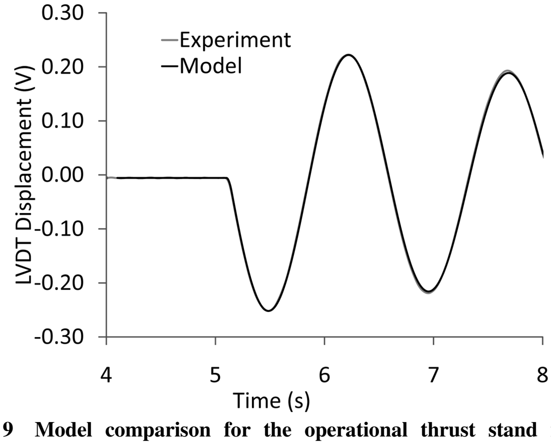

Fig. 9 Model comparison for the operational thrust stand for a $3.63\ \text{mN}\cdot\text{s}$ impulse.

range between the two iterations. The comparison between the operational (modified) thrust stand and the model used for the trade study can be seen in Fig. 9. (Note that the experimental line and the model line nearly overlap.)

While operating at its full discharge potential, the CD is expected to produce approximately 10^{-1} $\mathrm{N} \cdot \mathrm{s}$ impulse with a propellant mass loss of 12 mg [6]. The expected output of the LVDT for such a firing on the operational thrust stand can be seen in Figs. 1 and 2. This represents the operational levels for which the thrust stand was designed and modified. If experimental values are found to be significantly different than those predicted by the CD model, the thrust stand maintains the flexibility to be easily reconfigured for a large range of total impulse and propellant mass loss values by variations in the mass moment of inertia, spring constant and/or damping coefficient.

Acknowledgments

This work was supported by the Advanced Concepts Group at the Propulsion Directorate of the U.S. Air Force Research Laboratory at Edwards Air Force Base.

References

[1] Kamhawi, H., Arrington, L., Pencil, E., and Haag, T., "Performance Evaluation of a High Energy Density Pulsed Plasma Thruster," AIAA Paper 2005-3695, 2005.

[2] Zigler, A., Ehrlich, Y., Cohen, C., Krall, J., and Sprangle, P., "Optical Guiding of High-Intensity Laser Pulsed in a Long Plasma Channel Formed by a Slow Capillary Discharge," *Journal of the Optical Society of America B (Optical Physics)*, Vol. 13, 1996, pp. 68–71. doi:10.1364/JOSAB.13.000068

[3] Lee, R., and Zigler, A., "Multiple Pulse Laser Excitation of a Capillary Discharge," *Applied Physics Letters*, Vol. 53, No. 21, 1988, pp. 2028–2029. doi:10.1063/1.100311

[4] Powell, J., and Zielinski, A., "Theory and Experiment for an Ablating Capillary Discharge and Application to Electrothermal-Chemical Guns," U.S. Army Ballistic Research Lab., Rept. BRL-TR-3355, Aberdeen Proving Ground, MD, June 1992.

[5] Cambier, J., Young, M., Pekker, L., and Pancotti, A., "Capillary Discharge Based Pulsed Plasma Thrusters," *International Electric Propulsion Conference*, Electric Rocket Propulsion Society, Fairview Park, OH, Paper 2007-238, 2007.

[6] Pekker, L., and Cambier, J., "A Model of Ablative Capillary Discharge," Assembly for International Heat Transfer, IHTC-13, Aug. 2006.

[7] Ketsdever, A., Lee, R., and D'Souza, B., "Thrust Stand Micro-Mass Balance for the Direct Measurement of Specific Impulse," *Journal of Propulsion and Power*, Vol. 24, No. 6, 2008, pp. 1376–1381.doi: 10.2514/1.36921

[8] Fredrick, R. A., and Greiner, B. E., "Laboratory-Scale Hybrid Rocket Motor Uncertainty," *Journal of Propulsion and Power*, Vol. 12, No. 3, 1996, pp. 605–611. doi:10.2514/3.24076

[9] D'Souza, B., and Ketsdever, A., "Investigation of Time-Dependent Forces on a Nano-Newton-Second Impulse Balance," *Review of Scientific Instruments*, Vol. 76, No. 1, 2005, pp. 015105–015105-10.doi:10.1063/1.1834707

[10] Selden, N. P., and Ketsdever, A. D., "Comparison of Force Balance Calibration Techniques for the Nano-Newton Range," *Review of Scientific Instruments*, Vol. 74, No. 12, 2003, pp. 5249–54.doi: 10.1063/1.1623628

C. Segal
Associate Editor

AIP | Conference Proceedings

Experimental and Computational Investigation of a RF Plasma Micro Thruster

J. D. Olliges, A. D. Ketsdever, W. B. Stein, A. A. Alexeenko, and I. Hrbud

Citation: AIP Conf. Proc. **1084**, 863 (2008); doi: 10.1063/1.3076596

View online: http://dx.doi.org/10.1063/1.3076596

View Table of Contents: http://proceedings.aip.org/dbt/dbt.jsp?KEY=APCPCS&Volume=1084&Issue=1

Published by the American Institute of Physics.

Related Articles

Efficient laser-overdense plasma coupling via surface plasma waves and steady magnetic field generation
Phys. Plasmas 18, 102701 (2011)

Discontinuous Galerkin particle-in-cell simulation of longitudinal plasma wave damping and comparison to the Landau approximation and the exact solution of the dispersion relation
Phys. Plasmas 18, 062111 (2011)

Electron flow stability in magnetically insulated vacuum transmission lines
Phys. Plasmas 18, 033108 (2011)

Generalized matching criterion for electrostatic ion solitary propagations in quasineutral magnetized plasmas
Phys. Plasmas 18, 032103 (2011)

Development of nonlinearity in a growing self-excited dust-density wave
Phys. Plasmas 18, 013705 (2011)

Additional information on AIP Conf. Proc.

Journal Homepage: http://proceedings.aip.org/

Journal Information: http://proceedings.aip.org/about/about_the_proceedings

Top downloads: http://proceedings.aip.org/dbt/most_downloaded.jsp?KEY=APCPCS

Information for Authors: http://proceedings.aip.org/authors/information_for_authors

ADVERTISEMENT

AIPAdvances

Submit Now

Explore AIP's new open-access journal

- Article-level metrics now available
- Join the conversation! Rate & comment on articles

Downloaded 11 Apr 2012 to 129.198.241.47. Redistribution subject to AIP license or copyright; see http://proceedings.aip.org/about/rights_permissions

Experimental and Computational Investigation of a RF Plasma Micro-Thruster

J.D.Olliges[†], A.D. Ketsdever[‡],

[†] University of Southern California, Aerospace and Mechanical Engineering, Los Angeles, CA 90089
[‡] Air Force Research Laboratory, Edwards AFB, CA 93524

W.B. Stein, A.A. Alexeenko, and I. Hrbud

Purdue University, School of Aeronautical and Astronautical Engineering, West Lafayette, IN 47907

Abstract. A prototype RF plasma micro-thruster has been investigated numerically and experimentally. The experimental results were obtained on a thrust stand capable of micro-Newton resolution. Thrust and mass flow (hence specific impulse) were measured for an argon propellant at mass flows ranging from 0.4 to 5.5 mg/s. An increase over the cold gas thrust of up to 20% was observed for a discharge frequency of 100 MHz and an input power of 77 W. Propulsive efficiency was seen to increase both experimentally and numerically for increasing mass flow and decreasing discharge frequency.

Keywords: Micropropulsion, RF plasma thruster, plasma modeling, DSMC.
PACS: 51.50.+v, 52.25.Kn, 52.65.Pp, 52.65.Rr

NOMENCLATURE

A_e = Area of the nozzle exit [m^2]
A_o = Area of the orifice [m^2]
C = Effective exhaust velocity [m/s]
C_D = Discharge Coefficient [$\dot{m}_{actual} / \dot{m}_{ideal}$]
F = Thrust [N]
F_{CG} = Cold Gas thrust [N]
F_m = Momentum thrust [N]
F_P = Powered thrust [N]
F_{Pe} = Pressure thrust [N]
g_0 = Earth's gravitational constant [m/s^2]
I_{sp} = Specific impulse [s]
k = Boltzmann constant [J/K]
m = Molecular mass [kg]
M = Mach number at the nozzle exit
$\dot{m}$ = Mass flow rate [mg/s]
n_e = Electron number density [m^{-3}]
P_a = Ambient pressure [Pa]
P_e = Nozzle exit pressure [Pa]
P_{Jet} = Jet power [W]
P_{in} = Supplied electrical power [W]
P_o = Stagnation pressure [Pa]
r = Radius [m]
r_0 = Inner radius of discharge annulus [m]
r_1 = Outer radius of discharge annulus [m]
T = Temperature [K]
T_{gas} = Neutral gas temperature [K]
U_e = Nozzle exit velocity [m/s]
V = Applied electrode potential [V]
γ = Ratio of specific heats
η = Thruster efficiency

INTRODUCTION

An increasing need for inexpensive, highly flexible spacecraft for scientific and industrial applications has fostered research into designing practical microsatellites (satellites having less than 100 kg of mass). Microsatellites

CP1084, *Rarefied Gas Dynamics: 26th International Symposium*, edited by T. Abe
© 2009 American Institute of Physics 978-0-7354-0615-5/09/$25.00

Downloaded 11 Apr 2012 to 129.198.241.47. Redistribution subject to AIP license or copyright; see http://proceedings.aip.org/about/rights_permissions

have the prospect of replacing larger, more expensive spacecraft, either as solitary units or through multiple component formations, by utilizing a more adaptable, survivable platform.[1,2] The severe mass and power limitations imposed on small satellite design implies that individual subsystems, including propulsion systems, need to be highly optimized.[1] Providing efficient means for station-keeping, attitude control, and mission-specific maneuvering on small-scale satellites is extremely challenging, and optimizing these propulsion systems to minimize mass and meet power constraints, while maintaining strict performance requirements, becomes essential to the success of microsatellite systems.

One proposed concept for small spacecraft propulsion is the RF plasma thruster. Classified as an electrothermal propulsion system, this device uses a radio-frequency capacitively coupled discharge (RFCCD) to heat a propellant by creating a glow discharge plasma between two coaxial electrodes.[3] An electrothermal thruster is defined as one that uses electric power to heat a gas. Traditionally, this has involved a resistive heating element (resistojet)[4] or an arc (arcjet)[5] to heat the propellant. The RFCCD is composed of a central quasi-neutral region analogous to the positive column in a direct current glow discharge. The energy of the applied electric field in the RF discharge is transferred to the bulk gas from collisions between the generated plasma and the neutral propellant gas. Therefore in the RF plasma thruster, the generated plasma is merely being used as a heating element. Propulsive performance relies on several macroscopic parameters including RF frequency (1 MHz to 1GHz) and power, propellant gas species, mass flow rate, and thruster geometry. These parameters will determine plasma formation and plasma characteristics, which will ultimately affect propellant heating and thruster lifetime.[6]

The RFCCD thruster, shown schematically in Fig. 1(A), is a prototype device similar to that described in Ref. 3. The potential was applied to concentric electrodes via a coaxial (50-Ω impedance) feed from the RF power supply. The diameter ratio between the inner and outer electrodes produced a 50-Ω impedance to match that of the coaxial cables resulting in minimal power loss due to reflection. According to coaxial transmission line theory, the inner and outer diameters were 6.4mm and 12.7mm, respectively. An argon propellant was fed to the thruster plenum through a showerhead arrangement of twelve orifices of 1.59mm diameter. The discharge was struck between the inner and outer electrodes in the plenum. For the proof-of-principle experiments described here, the gas was expanded through a 2.69mm diameter orifice. The RFCCD used in the experimental study is shown in Fig. 1(B).

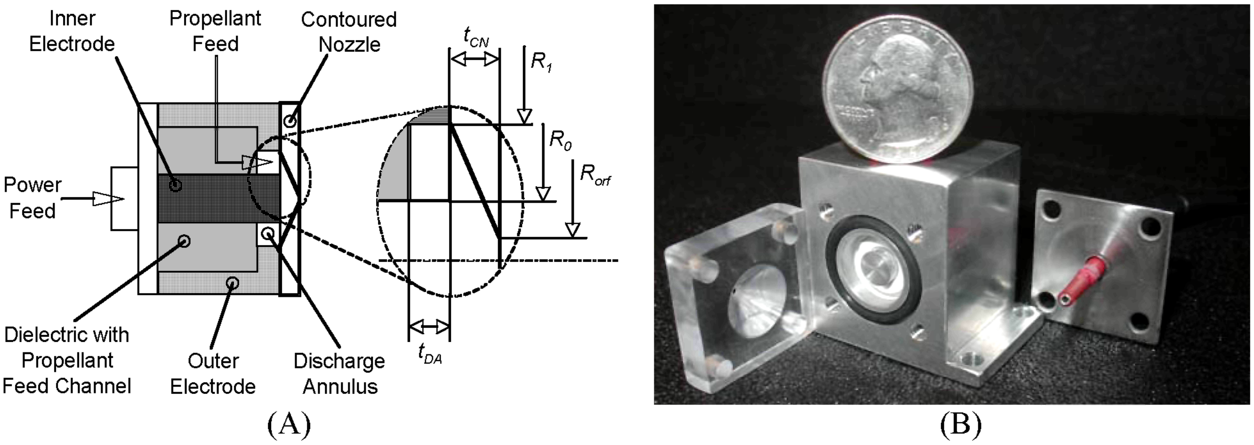

(A) (B)

FIGURE 1. Schematic (A) and hardware (B) of the experimental RF plasma thruster.

To assess the thruster's propulsive capabilities the RF plasma thruster can be modeled numerically utilizing Particle-In-Cell/Monte Carlo Collision (PIC/MCC) and direct simulation Monte Carlo (DSMC) algorithms.[6,7] The PIC/MCC method is used to determine plasma characteristics within the coaxial discharge annulus. The argon collision model employed in the computations includes electron-neutral ionization, charge exchange, lumped excitation, and elastic electron-neutral and ion-neutral scattering.[8] These collision mechanisms are considered in both plasma bulk and sheath regions. Neutral temperature variation within the discharge affects the plasma-neutral collision frequency and thus the power transmitted into the propellant. To account for heat transfer between the plasma and neutral propellant, a 1-D conduction model was incorporated into the PIC simulation which utilizes power transmitted to the fluid via charge exchange and elastic collisions. This allows the plasma collision frequency and heating to vary with changes in neutral temperature. Thruster performance can be obtained using the DSMC method in conjunction with the neutral temperature predicted by the PIC/MCC simulation.

Downloaded 11 Apr 2012 to 129.198.241.47. Redistribution subject to AIP license or copyright; see http://proceedings.aip.org/about/rights_permissions

Because of the strict weight and power requirements that microsatellites demand, successful micropropulsion systems require a rigorous optimization effort. Parametric optimization in the laboratory is expensive and time consuming, wherein a more cost-effective, practical option relies on numerical modeling to find optimal thruster operating conditions. Though numerical modeling provides a proficient method for thruster optimization, a macroscopic parameter verification is needed to verify the computational results. This paper experimentally addresses the RF plasma thruster's propulsive capabilities in order to substantiate the results obtained through PIC/MCC and DSMC modeling.

THEORY

Like most propulsive systems, the RF plasma thruster is designed to utilize propellant to create thrust. The thrust of a propulsion device is a measure of the force imparted by the expulsion of propellant (momentum thrust) and the force from the pressure differential across the nozzle exit plane (pressure thrust). Therefore, thrust is defined as

$$F = \dot{m}U_e + A_e\left(P_e - P_a\right) = F_m + F_{Pe} = \dot{m}C \tag{1}$$

where the momentum and pressure thrusts can be consolidated into a single term related to an effective exhaust velocity. For an isentropic expansion into vacuum, ($P_a = 0$), the ratio of momentum thrust to pressure thrust is given by

$$\frac{F_m}{F_{Pe}} = \gamma M^2 \tag{2}$$

which for the experimental configuration utilizing a sonic orifice expansion simplifies to γ. Thus for argon, the pressure thrust term is not negligible. The mass flow for a sonic orifice is given by

$$\dot{m} = C_D P_o A_o \sqrt{\frac{\gamma m}{kT}} \tag{3}$$

Propulsion systems are often characterized by their specific impulse, defined as

$$I_{sp} = \frac{F}{\dot{m}g_0} \tag{4}$$

The specific impulse is a measure of the amount of momentum transferred per unit mass of propellant. Generally, large I_{sp} indicates a propellant-efficient thruster. For electric thrusters, the propulsive efficiency is determined by the ratio of jet power (the power contained in the thruster plume) to the electrical power input into the system. P_{Jet} is defined by

$$P_{Jet} = \frac{1}{2}\dot{m}C^2 = \frac{1}{2}g_0 I_{sp} F \tag{5}$$

The thruster efficiency is then given by

$$\eta = \frac{P_{Jet}}{P_{in}} \tag{6}$$

NUMERICAL MODELING

The numerical method used to model the RF plasma thruster employed a combination of PIC/MCC[9] and DSMC algorithms. PIC/MCC was applied for kinetic plasma modeling in the inter-electrode spacing and was used to establish plasma characteristics within the thruster's discharge annulus. The charged test particles in the PIC/MCC calculations move in the electric field produced between the electrodes. Collisions between charged and neutral particles are calculated using the Monte Carlo method. The PIC code used was *XPDC1*, a bounded, one dimensional simulation developed at the University of California at Berkeley by the Plasma Theory and Simulation Group. *XPDC1* utilizes elastic scattering, lumped excitation, and electron-neutral ionization to model the power transfer to the propellant. The RF discharge in the annular gap between the coaxial electrodes was approximated by a one-dimensional PIC model thus neglecting the effects of neutral pressure drop along the electrodes which is expected to be insignificant. The PIC code was supplemented with a gas heat transfer (GHT) model to determine conductive heat-transfer due to plasma heating. Once the ion-neutral temperature was determined from PIC/MCC,

Downloaded 11 Apr 2012 to 129.198.241.47. Redistribution subject to AIP license or copyright; see http://proceedings.aip.org/about/rights_permissions

2-D axisymmetrical DSMC simulations modeled the converging section as well as the propellant expansion through the orifice and into the vacuum chamber. The PIC/MCC model inputs were pressure, voltage and frequency.

NUMERICAL RESULTS

Electron number density distributions for 0.5 and 2 Torr (corresponding to mass flows of 0.65 mg/s and 3.14 mg/s) at 100 V for applied frequencies of 100, 130, and 160 MHz are compared in Fig. 2 as a function of location (discharge annulus radius ratio). These density distributions illustrate the transition from a diffusion dominated discharge at low pressures to a collisional, asymmetric discharge at higher pressures. At lower pressures, electrons are able to traverse larger distances and diffuse through the gap between electrodes more easily. As a result the sheath width increases. A similar effect occurs when the applied frequency is decreased. Decreasing the frequency allows the electrons to travel in one direction longer per RF cycle and thus increases the sheath width. The average and peak number densities in Fig. 2 increase with both discharge pressure and applied frequency and show trends previously shown by Lee et al.[10]

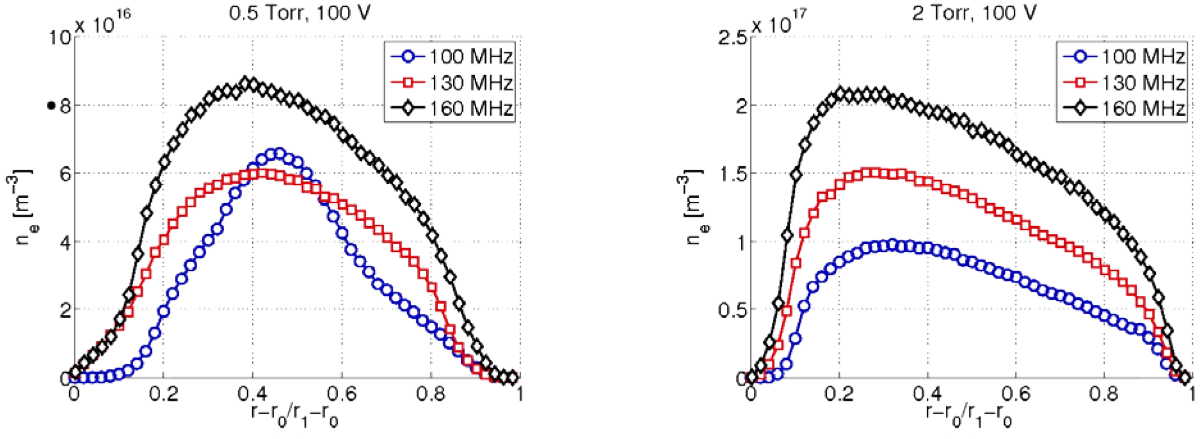

(A) (B)

FIGURE 2: Calculated electron number density for V=100 Volts. (A) P_o=0.5 Torr, (B) P_o=2.0 Torr.

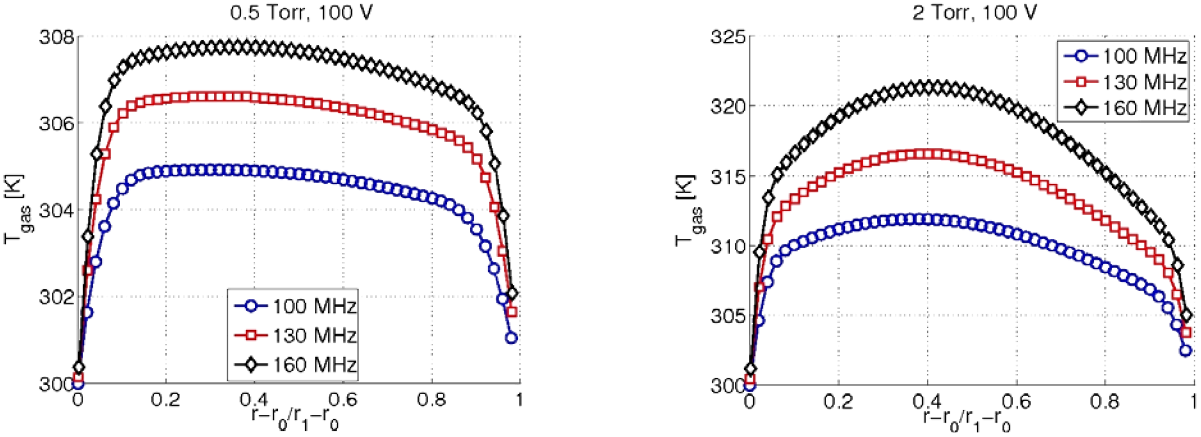

(A) (B)

FIGURE 3: Calculated neutral gas temperature for V=100 Volts. (A) P_o=0.5 Torr, (B) P_o=2.0 Torr.

Figure 3 shows the comparison of calculated neutral gas temperature distributions for discharge pressures of 0.5 and 2 Torr and applied frequencies of 100, 130, and 160 MHz at 100 V. At a constant applied voltage, the neutral temperatures increase with increasing pressure and frequency. Higher pressure discharges have a higher ion-neutral charge exchange collision frequency which provides higher heating. This not only increases the neutral temperature of the discharge, but it also causes the discharge to have a more curved shape due to the increased heating in the sheaths. Increasing the applied frequency also increases the neutral temperature through increased power

Downloaded 11 Apr 2012 to 129.198.241.47. Redistribution subject to AIP license or copyright; see http://proceedings.aip.org/about/rights_permissions

transmission into the fluid. Note that, increasing the applied frequency not only increases the neutral temperature but also decreases the discharge pressure if the mass flow rate through the thruster is held constant.

For electric thrusters, the measure of performance is the propulsive efficiency determined by Eq. (6). The results of the PIC simulations can be used to assess the effects of frequency on the propulsive efficiency. Figure 4 shows the total power transmitted to the propellant as a function of pressure and frequency for a constant applied voltage. An increase in frequency must be offset by a decrease in either pressure or voltage to keep a constant applied power. As the applied voltage increases, the power transmitted into the propellant increases which causes a rise in the neutral gas temperature. Since the mass flow rate is held constant, the rise in gas temperature must come with an increase in pressure, causing the power transmission to increase until the discharge stabilizes. An increase in the applied frequency will act to decrease the applied potential since the pressure and temperature are constrained by the mass flow and cannot change for a constant power. Thus, for constant power and mass flow, discharges which operate at a higher frequency will operate at a reduced voltage compared to their lower frequency counterparts. This increase in applied frequency, and corresponding decrease in applied potential, reduces the transmission efficiency and the microthruster performance.

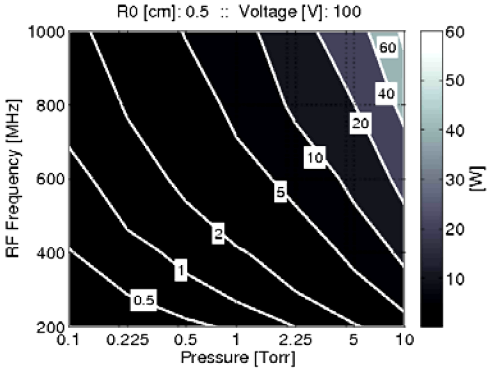

FIGURE 4. Power transmitted to propellant as a function of discharge pressure and applied frequency.

EXPERIMENTAL SETUP

The RF plasma thruster was tested inside the CHAFF-IV high vacuum chamber, a 6-m long, 3-m diameter stainless steel test chamber at the University of Southern California. CHAFF-IV is primarily pumped by a Zyrianka 900 diffusion pump capable of a 30,000 L/s pumping speed on nitrogen. The Zyrianka 900 provided background pressures of 10^{-5} to 10^{-4} Torr over the range of experimental thruster flow rates.

The thruster was attached to the arm of the nano-Newton thrust stand (nNTS) as shown in Fig. 5. The nNTS used in this study was a torsion thrust stand similar to that described by Jamison, et al.[11] Gas coupling was accomplished through a compression fitting-sealed, flexible rubber tube mounted along the rotational axis of the stand. RF power was attached through a 2.4-mm diameter, Kapton insulated coaxial cable secured above the stand and draped across the arm to minimize physical influence on the stand's movement. Thrust stand deflection was measured using a linear variable differential transformer (LVDT) attached to a 24-bit data acquisition card. An electrostatic comb calibration system, modified from the technique described by Selden and Ketsdever[12], was used for precise steady-state force calibration between 270 μN and 2.4 mN. The force curve provided by the electrostatic combs adequately spanned the range produced by the RF plasma thruster over the range of tested flow rates.

Gas flow to the thruster was measured with an Omega™ mass flowmeter. The flowmeter operates by creating a pressure differential in a laminar flow field. The flowmeter forces the gas into streamlined flow and measures the pressure drop across a known length of laminar flow. Measures of absolute temperature and pressure inside the meter correlate the volumetric flow rate to a standardized mass flow rate. Measurements correlating mass flow and line pressure were taken using a 1-Torr differential Baratron. Pressure measurements were obtained independently of thrust traces due to the complication of attaching the Baratron to the oscillating nNTS.

The RF power system consisted of a RF power amplifier and frequency generator. The RF power amplifier provided RF frequencies between 70 and 160 MHz at adjustable power levels between 0 and 100 W. The transmission line connecting the RF power system and thruster maintained 50-Ω impedance, minimizing power loss.

The total duration of a test sequence on the nNTS was 180 seconds and encompassed four 30-s segments and one 60-s segment. The first 30 seconds represents a zero baseline where neither gas nor power was supplied to the

Downloaded 11 Apr 2012 to 129.198.241.47. Redistribution subject to AIP license or copyright; see http://proceedings.aip.org/about/rights_permissions

thruster. The second 30 seconds established a cold gas baseline where only gas was delivered to the thruster. After 60 seconds, power was supplied to the thruster, igniting the plasma that remained lit until the 90th second when the power supply was turned off. Gas was turned off after 120 seconds allowing the thrust stand to damp towards its zero baseline for the remainder of the test sequence. A typical 160 Mhz powered trace with input power, $P_{in} = 83 \pm 1$ W, and mass flow, $\dot{m} = 4.52 \pm 0.02$ mg/s, is shown in Fig. 6. Figure 6 also shows the displacements corresponding to the cold gas and powered thrust segments.

Powered thrust trials were taken for 100 Mhz, 130 Mhz, and 160 Mhz at 100 W forward power while mass flow to the thruster was varied between 0.4 and 5.5 mg/s of argon. Input power, P_{in}, was considered the difference between forward power and reflected power. Reflected power varied with mass flow and frequency. Additional tests with $\dot{m} = 1.225 \pm 0.002$ mg/s and 160 Mhz frequency were taken with forward power levels of 30 W, 65 W, and 100 W to see the effects of various power levels on thruster performance.

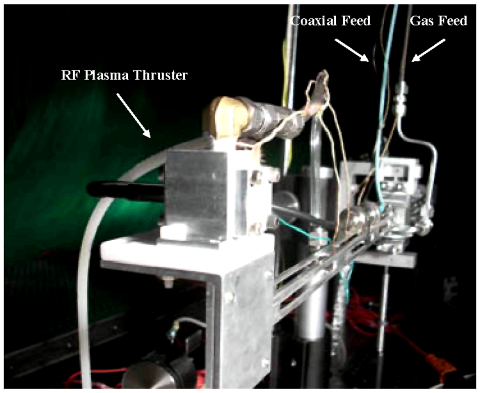

FIGURE 5. The RF Plasma thruster attached to the arm of the nNTS. The electrostatic comb calibration system was attached to the opposite arm of the thrust stand.

EXPERIMENTAL RESULTS

Several thruster performance characteristics were obtained experimentally in an effort to compare to numerical trends in order to verify the computational model. The ratio of RF powered thrust to unpowered (cold gas) thrust, F_P/F_{CG}, was measured to quantify the increase in thrust produced by igniting a plasma in the RF plasma thruster. A typical thrust trace sequence used to determine F_P/F_{CG} is shown in Fig. 6. For the nNTS trace shown in Fig. 6, the initial rise from zero is due to the unpowered gas flow to the thruster. Power was turned on at 60 seconds and allowed to remain on for the following 30 seconds. The slight increase in unpowered thrust when the power is turned off at 90 seconds is due to the heating of the thruster (and propellant) by the preceding powered operation. Figure 7 shows the thrust ratio, F_P/F_{CG}, for $\dot{m} = 1.225 \pm 0.002$ mg/s and 160 MHz frequency as a function of input power levels. The magnitude of F_P/F_{CG} is directly related to the power input of the system, where operating the thruster at higher power levels increased thrust.

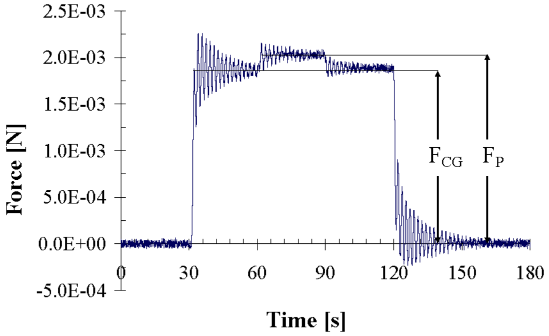

FIGURE 6. A typical powered trace from the nNTS.

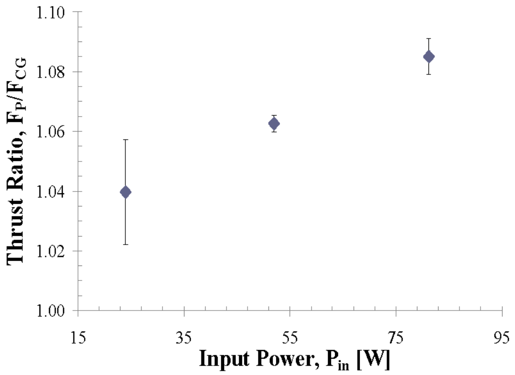

FIGURE 7. Thrust ratio as a function of input power.

Downloaded 11 Apr 2012 to 129.198.241.47. Redistribution subject to AIP license or copyright; see http://proceedings.aip.org/about/rights_permissions

The thrust ratio was also examined as a function of frequency and mass flow as shown in Fig. 8. There are two potential mechanisms contributing to the shape of the thrust ratio plot. Below a 1 mg/s mass flow rate, there is a diminishing return of ion-neutral energy transfer as pressure in the chamber increases. The neutral gas temperature increases primarily due to charge exchange collisions between relatively fast argon ions and slow neutrals. At low pressures, there are few ions created in the discharge annulus, however the ions gain relatively high speed in-between collisions. These fast ions transfer energy to the neutral gas, increasing the temperature. At high pressures, the ions do not get to the same energy as the low pressure case in-between collisions, which reduces the thrust ratio.

Above a mass flow of 1 mg/s the determining factor in Fig. 8 is a relatively high plasma density. At low pressures, the power-coupling to the gas is efficient; however, it only results in a weak or diffuse plasma discharge. There are few free electrons available to collide with argon atoms yielding an overall low number of ionizing collisions and correspondingly low plasma density. As pressure increases, the total power transferred to the gas also increases, increasing plasma density. More ions are produced, increasing collisions with atoms in the accelerating sheath. At the inflection point in Fig. 8, (~1 mg/s), the increase in plasma density begins to compensate for the diminishing energy transfer per ion-neutral collision. Though each charge exchange collision is transferring smaller amounts of energy, the increased number of impacts begins to give the atoms more total energy resulting in an increase in F_P/F_{CG}.

The thruster's specific impulse for various discharge frequencies is shown as a function of mass flow rate in Fig. 9. The theoretical maximum cold gas specific impulse, shown as a straight line in Fig. 9, was computed using 1-D ideal isentropic flow relationships. The experimental I_{sp} was several seconds less than the theoretical maximum due to viscous and other losses. Powered thrust measurements followed a trend similar to the thrust ratio in Fig. 8 and produced increases over cold gas specific impulse for all frequencies. For mass flow rates above 1.25 mg/s, powered I_{sp} increases with increasing mass flow. The increasing specific impulse signifies the thruster becomes more propellant efficient at larger mass flow rates and lower frequencies. The numerical results presented in Fig. 4 indicate that higher stagnation temperatures are produced at higher discharge frequencies. Although this should lead to higher specific impulse in an ideal case, the higher stagnation temperature leads to lower Reynolds number in the expansion orifice which increases the viscous losses. The higher viscous losses subsequently result in lower specific impulse.

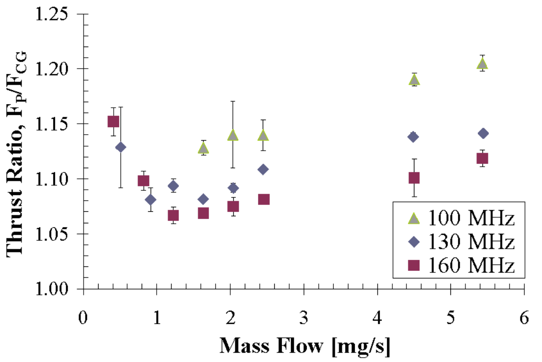

FIGURE 8. Thrust ratio as a function of $\dot{m}$ and frequency.

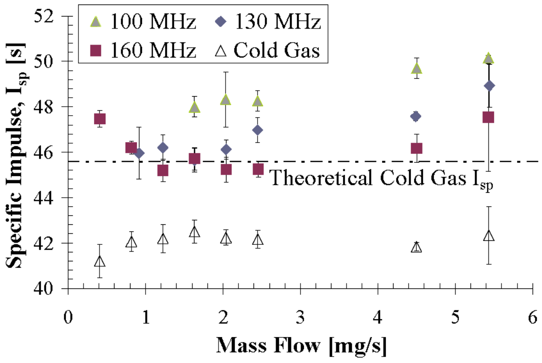

FIGURE 9. Specific impulse as a function of $\dot{m}$ and frequency.

Figure 10 shows how the RFCCD's propulsive efficiency varies with mass flow rate and frequency. As can be seen, the propulsive efficiency increases for increased mass flow. The efficiency also increases at a given mass flow rate for decreased discharge frequency. The input power used to calculate the propulsive efficiency in Fig. 10 was found by finding the difference in forward and reflected power. The jet power used was determined by taking the thrust and I_{sp} difference between the powered and unpowered (cold gas) values. The values in Fig. 10 are low for a micropropulsion system; however, the thruster was not optimized in this study nor was it operated in the most efficient regime.

DISCUSSION

Cold gas experimental data of thrust versus mass flow validated the DSMC model used to evaluate the gas expansion through the exit orifice. Figure 11 shows experimental and numerical results for cold gas thrust using an argon propellant. Computational modeling produced cold gas thrust values within 8% of those obtained

Downloaded 11 Apr 2012 to 129.198.241.47. Redistribution subject to AIP license or copyright; see http://proceedings.aip.org/about/rights_permissions

experimentally, further validating the use of DSMC for orifice flows. Previous studies[13] have shown that DSMC accurately predicts cold gas thrust and specific impulse for rarefied and near-continuum flows. Errors in this study most likely stem from machining and measurement tolerances associated with the experimental orifice diameter, surface roughness, and the axi-symmetric nature of the DSMC simulations.

For powered thrust operation, the experiments were performed to give an adequate representation of the trends in thruster performance as a function of mass flow rate and frequency. These trends have been duplicated in the numerical modeling in several ways. First, the thrust produced by the RFCCD increased as a function of input power. Second, the propulsive efficiency increased with increasing mass flow. From Fig. 4, an increased mass flow for a constant power and frequency must lead to an increase in voltage. A voltage increase generally led to a higher transmission efficiency which gave a higher overall propulsive efficiency for the thruster. Figure 10 shows this same trend in the experimental results. Finally, the propulsive efficiency was higher for lower values of the discharge frequency. Again, Fig. 4 shows this trend for the numerical results, and Fig. 10 shows a similar trend observed experimentally. Geometry and operating parameters of the RFCCD will be optimized using future numerical results in an effort to increase thrust, specific impulse, and propulsive efficiency.

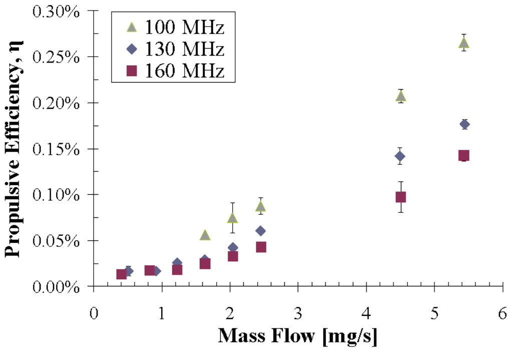

FIGURE 10. Propulsive efficiency as a function of $\dot{m}$ and frequency.

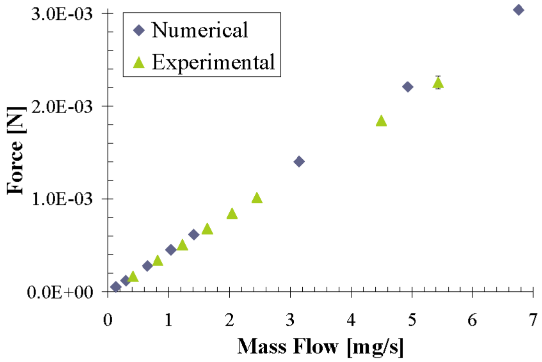

FIGURE 11. Cold gas thrust as a function of $\dot{m}$.

ACKNOWLEDGMENTS

The authors would like to thank the Air Force Research Laboratory, Propulsion Directorate, Advanced Concepts Group for their support of the experimental results. One of the authors (JDO) was partially supported by an undergraduate research fellowship from the University of Southern California (USC). The authors also thank Prof. E.P. Muntz of USC for the use of Chamber IV of the Collaborative High Altitude Flow Facility.

REFERENCES

1. A. D. Ketsdever, "Systems Considerations and Design Options for Microspacecraft Propulsion Systems," in *Micropropulsion for Small Spacecraft*, edited by M. M. Micci and A. D. Ketsdever, Reston, VA: AIAA, 2001, pp. 139-166.
2. C. Sultan, S. Seereram, and R. K. Mehra, *The International Journal of Robotics Research* **26** 405-430 (2007).
3. I. Hrbud, G. E. Kemp, A. H. Yan, and J. G. Gedrimas, "Review of RF Plasma Thruster Development" in *Proc. of the 30th International Electric Propulsion Conference*, IEPC-2007-309, Florence, Italy, 2007.
4. A. D. Ketsdever, R. H. Lee and T. C. Lilly, *J. Micromech. Microeng.* **15** 2254-2263 (2005).
5. H. Horisawa, and I. Kimura, *Vacuum.* **59** 106-117 (2000).
6. W. B. Stein, A. A. Alexeenko and I. Hrbud, "Performance Modeling of an RF Coaxial Plasma Thruster" in *Proc.of the 43rd Joint Propulsion Conference*, AIAA Paper-2007-5292, Cincinnati, OH, 2007.
7. W. B. Stein, A. A. Alexennko and I. Hrbud, "RFCCD Microthruster Performance via Numerical Simulation" in *Proc. of the 46th Aerospace Sciences Meeting*, AIAA Paper-2008-962, Reno, NV, 2007.
8. J. E. Lawler and U. Kortshagen, *J. Phy. D: Appl. Phys.* **32** 3188-3198 (1999).
9. C. K. Birdsall. *IEEE Transactions on Plasma Science.* **19** 65-85 (1991).
10. J. K. Lee, N. Babaeva, H. C. Kim, O. Manuilenko, and J. W. Shon, *Plasma Science* **32** 47-53 (2004).
11. A. J. Jamison, A. D. Ketsdever and E. P. Muntz, *Rev. Sci. Instrum.* **73** 3629-3637 (2002).
12. N. P. Selden and A. D. Ketsdever, *Rev. Sci. Instrum.* **74** 5249-5254 (2003).
13. A. D. Ketsdever, M. T. Clabough, S. F. Gimelshein, and A. A. Alexeenko, *AIAA J.* **43** 633-641 (2005).

Downloaded 11 Apr 2012 to 129.198.241.47. Redistribution subject to AIP license or copyright; see http://proceedings.aip.org/about/rights_permissions

AIP | Review of Scientific Instruments

Invited Article: Time accurate mass flow measurements of solid-fueled systems

Jordan D. Olliges, Taylor C. Lilly, Thomas B. Joslyn, and Andrew D. Ketsdever

Citation: Rev. Sci. Instrum. **79**, 101301 (2008); doi: 10.1063/1.2982492

View online: http://dx.doi.org/10.1063/1.2982492

View Table of Contents: http://rsi.aip.org/resource/1/RSINAK/v79/i10

Published by the American Institute of Physics.

Related Articles

Highly precise and compact ultrahigh vacuum rotary feedthrough
Rev. Sci. Instrum. 83, 035106 (2012)

Invited Article: A materials investigation of a phase-change micro-valve for greenhouse gas collection and other potential applications
Rev. Sci. Instrum. 83, 031301 (2012)

Observation of anomalous Hall effect in Cu-Py-crossed structure with in-plane magnetization
J. Appl. Phys. 111, 07D307 (2012)

Constructal design for pedestrian movement in living spaces: Evacuation configurations
J. Appl. Phys. 111, 054903 (2012)

Chemical, biological, radiological, and nuclear threats-Decontamination technologies and recent patents: A review
J. Renewable Sustainable Energy 4, 012704 (2012)

Additional information on Rev. Sci. Instrum.

Journal Homepage: http://rsi.aip.org

Journal Information: http://rsi.aip.org/about/about_the_journal

Top downloads: http://rsi.aip.org/features/most_downloaded

Information for Authors: http://rsi.aip.org/authors

ADVERTISEMENT

HAVE YOU HEARD?
Employers hiring scientists
and engineers trust
physicstoday JOBS
http://careers.physicstoday.org/post.cfm

REVIEW OF SCIENTIFIC INSTRUMENTS **79**, 101301 (2008)

Invited Article: Time accurate mass flow measurements of solid-fueled systems

Jordan D. Olliges,[1] Taylor C. Lilly,[1] Thomas B. Joslyn,[2] and Andrew D. Ketsdever[2]
[1]*Department of Aerospace and Mechanical Engineering, University of Southern California, Los Angeles, California 90089, USA*
[2]*Department of Mechanical and Aerospace Engineering, University of Colorado, Colorado Springs, Colorado 80918, USA*

(Received 31 January 2008; accepted 17 August 2008; published online 7 October 2008)

A novel diagnostic method is described that utilizes a thrust stand mass balance (TSMB) to directly measure time-accurate mass flow from a solid-fuel thruster. The accuracy of the TSMB mass flow measurement technique was demonstrated in three ways including the use of an idealized numerical simulation, verifying a fluid mass calibration with high-speed digital photography, and by measuring mass loss in more than 30 hybrid rocket motor firings. Dynamic response of the mass balance was assessed through weight calibration and used to derive spring, damping, and mass moment of inertia coefficients for the TSMB. These dynamic coefficients were used to determine the mass flow rate and total mass loss within an acrylic and gaseous oxygen hybrid rocket motor firing. Intentional variations in the oxygen flow rate resulted in corresponding variations in the total propellant mass flow as expected. The TSMB was optimized to determine mass losses of up to 2.5 g and measured total mass loss to within 2.5% of that calculated by a NIST-calibrated digital scale. Using this method, a mass flow resolution of 0.0011 g/s or 2% of the average mass flow in this study has been achieved. © *2008 American Institute of Physics.* [DOI: 10.1063/1.2982492]

I. INTRODUCTION

Measuring the time-accurate mass flow of ablating, subliming, or combusting solids has posed problems in several areas of application including microelectromechanical systems etching,[1] laser machining,[2] and solid-fuel thruster research.[3] For example, time-accurate mass flow of ablating material from laser interactions could be used to investigate efficient machining parameters of the laser system in real time. Current techniques to investigate the efficiency of laser machining processes involve removing the sample from the original setup and investigating the results using scanning electron microscopy.[2] The thrust stand mass balance (TSMB) technique described in this study allows for *in situ* measurements of mass loss in a time-accurate manner. Although the aforementioned applications involve systems where mass is being lost, there are also issues with measuring systems gaining solid mass as a function of time, most notably processes involving thin-film deposition.[4] Although this study will focus on mass flow measurements from a hybrid propulsion system which utilizes a solid-fuel propellant, the TSMB can be viewed as a general instrument for measuring the time-accurate mass flow of generic processes.

Widespread use of hybrid rockets as safe, low cost, and flexible alternatives to liquid and solid thrusters[3,5] has prompted the study of a novel diagnostics tool for their investigation. This study used a scaled hybrid motor as a proof of concept for the time-resolved, direct measurement of solid propellant mass flow. Several technologies exist to accurately measure the thrust[6–8] of small-scale propulsion devices; however, accurately measuring a solid propellant mass flow as a function of time is much more difficult due to the required instrument time response. In the case of most gaseous and liquid fuel thrusters, the mass flow of the propellant and oxidizer during a burn can be measured by a variety of well-characterized, time-resolved mass flow techniques. The problem is more difficult when applied to solid and hybrid propellant motors where standardized tools do not exist. To determine the propellant mass flow from a solid system, current techniques rely on known oxidizer flow rates or chamber pressures to extrapolate the propellant mass flow over time, or an averaged mass flow rate is measured based on the total mass loss and time of the burn.[9]

Two novel methods are currently under development to measure chamber volume during a burn which is then used to derive fuel regression and mass flow. Evans *et al.*[10] used x-rays to image a transparent hybrid motor and were able to track the regression rate in the chamber. Their method shows reasonable promise; however, scaling effects are significant because the chamber diameter to length ratio must be larger than optimum for thruster performance in order for the x rays to image the chamber effectively. Also, the x-ray technique only provides an image of one position along the axial length of the port. The difference between x-ray image-estimated port diameter and published data shows that the chamber radius at the end of the burn can be off by at least 10% corresponding to a 19% error in volume and mass.[10] De Zilwa *et al.*[11] used acoustic and photometric techniques to quantify chamber volume. These methods rely on accurately measuring Helmholtz oscillations that can occur whenever a large volume terminates in a narrow throat. The Helmholtz oscillation frequency is proportional to the inverse of the square root of the chamber volume and can be measured by observing flame flicker with a photomultiplier tube or with pressure transducers. Their tests showed that approximately a 3% accuracy is achievable with a time resolution of 45 Hz. However, like x-ray techniques, Helmholtz techniques have required motor conditions that can differ from those in an optimal thruster.[11]

To eliminate some error[12] and allow for direct measurement of the propellant mass flow as a function of time, the TSMB was developed for systems where the experimental uncertainty is of the same order as the measurement being made. In this study, a hybrid thruster core was aligned so that the thrust generated was perpendicular to the motion of the TSMB, and the thrust vector did not contribute to the deflection of the balance. As the solid propellant burned, the displacement of the TSMB varied directly with the change in mass of the hybrid thruster system. By analyzing the displacement of the test stand as that of a damped, spring-mass system, the forcing function was derived. By analyzing the rate of change in the forcing function, the mass flow rate was determined. To the authors' knowledge, it appears that the method presented in this report is the first means of determining the instantaneous mass flow of any size or type of solid propellant motor configuration.

II. THEORETICAL FRAMEWORK

The TSMB behaves like an underdamped, oscillating, mass-spring system. System motion is described by the following second order differential equation:

$$I\ddot{\theta}(t) + C\dot{\theta}(t) + K\theta(t) = M(t) = F(t)r. \tag{1}$$

For small angles of deflection, θ, the motion of the stand can be linearly approximated through the small angle identity as $\sin(\theta) = \theta = X/r$. The left side of Eq. (1) is related to the measurement of the stand's motion and the right side is related to its forcing. The stand's motion can then be written as

$$I\frac{\ddot{X}(t)}{R_L} + C\frac{\dot{X}(t)}{R_L} + K\frac{X(t)}{R_L} = F(t)R_R. \tag{2}$$

Equation (2) allows the linear, kinematic motion of the TSMB to be used to derive a time-resolved forcing function regardless of the natural frequency of the stand. The forcing function is found by the addition of the position, velocity, and acceleration components, scaled by the spring constant, K, damping coefficient, C, and moment of inertia, I, as shown in Eq. (2). Therefore, the position of the stand as a function of time can be used to derive the velocity and acceleration functions, and the time-resolved forcing function can be determined with a resolution independent of the period of the TSMB.[13]

In order to derive the forcing function from a measured deflection, the coefficients in Eq. (2) must be experimentally measured from the TSMB. By applying a steady state calibration force to the stand, as times goes to infinity, the resulting deflection becomes

$$K\frac{X}{R_L} = F_C R_C. \tag{3}$$

The remaining two coefficients can be found by analyzing the measured period and the decay of the deflection amplitude as a function of time. First, a logarithmic decrement is defined as

$$\delta_n = \ln(X_i/X_{i+n}), \tag{4}$$

where i is a positive integer, and X_i and X_{i+n} are peak amplitudes, separated by n periods. The damping ratio is then given by

$$\zeta = \delta_n/\sqrt{(n2\pi)^2 + \delta_n^2}. \tag{5}$$

The measured frequency of the stand can be found from the measured period and related to the natural frequency by

$$\frac{2\pi}{T} = \omega_d = \omega_o\sqrt{1-\zeta^2} \tag{6}$$

and the mass moment of inertia and damping coefficients are

$$I = \frac{K}{\omega_o^2}, \tag{7}$$

$$C = 2\zeta\sqrt{KI}. \tag{8}$$

Therefore, coefficients I, C, and K may be determined from any single test trace resulting from a known, static, steady state calibration load. It follows that if the deflection, $X(t)$, resulting from a dynamic load, is measured on a stand with no significant change in I, C, or K, the time dependent function $F(t)$, which describes that dynamic load, may be determined through Eq. (2). By assuming that the stand is only forced by the change in mass of the thruster system, the rate of change in Δm_p is simply the time derivative of the forcing function divided by the gravitation constant

$$\dot{m}(t) = \frac{\dot{F}(t)}{g_o}. \tag{9}$$

Before proceeding with the experiments in the laboratory, the diagnostic technique was verified using an idealized numerical model free of experimental noise and uncertainty. Equation (1) can be solved for the components of the stand's motion yielding

$$\theta(t) = \frac{M_o}{K} + e^{\alpha t}\left[\left(\theta_o - \frac{M_o}{K}\right)\cos(\beta t) + \left(\frac{\dot{\theta}_o K - \alpha K\theta_o + \alpha M_o}{K\beta}\right)\sin(\beta t)\right], \tag{10}$$

$$\dot{\theta}(t) = e^{\alpha t}\left[\dot{\theta}_o\cos(\beta t) + \left(\frac{I\alpha\dot{\theta}_o - K\theta_o + M_o}{I\beta}\right)\sin(\beta t)\right], \tag{11}$$

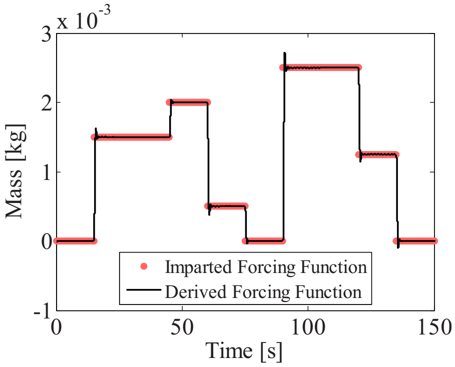

FIG. 1. (Color online) Derived forcing function from the simulated stand motion compared to the actual (imparted) forcing function.

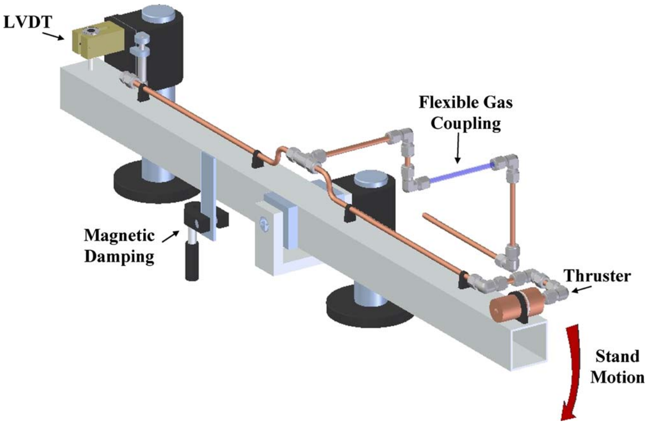

FIG. 2. (Color online) Schematic of the experimental TSMB.

$$\ddot{\theta}(t) = e^{\alpha t}\left[\left(\frac{M_o - C\dot{\theta}_o - K\theta_o}{I}\right)\cos(\beta t) + \left(\frac{\alpha(M_o - C\dot{\theta}_o - K\theta_o) - K\dot{\theta}_o}{I\beta}\right)\sin(\beta t)\right], \qquad (12)$$

where $\alpha = -C/2I$ and $\beta = \sqrt{K/I - \alpha^2}$.[13] This system of equations can be solved numerically to simulate a steady state forcing function.

Equations (10)–(12) were used to create an idealized, simulated TSMB response signal to arbitrary static (short duration) mass changes from 0 to 1.5, 2.0, 0.5, 0, 2.5, 1.25, and finally back to 0 g at the end of the trace. The signal was artificially sampled to see if the differential analysis could accurately derive the forcing function of the system when given an ideal case. The diagnostic technique correctly derived the constants K, C, and I to within less than 1% of the simulated values. Numerical differentiation techniques were used to calculate the derivative functions of the discretized waveform representing the stand's simulated motion. Scaling the displacement, velocity, and acceleration components by the calculated coefficients, the TSMB analysis technique was able to correctly derive the forcing function from Eq. (2) as shown in Fig. 1. The slight overshoots at each change in mass were due to the numerical differentiation of a discontinuous step function.

III. EXPERIMENTAL SETUP AND METHODS

The TSMB design was based on the nanonewton thrust stand[8] (nNTS) and the nanoimpulse balance stand[13] (NIBS) developed by the Air Force Research Laboratory. These stands measure thrust or impulse using a torsion pendulum that pivots around a vertical axis of rotation. A force imparted to the nNTS or NIBS results in a horizontal displacement of the stand, which is precisely measured using a linear variable differential transformer (LVDT). Using these systems, robust techniques exist to perform thrust and impulse measurements for forces as low as 80 nN (steady state) or 7 nN/s (impulse). The TSMB used in this study differed from the nNTS and NIBS systems because the arms of the stand were set on a horizontal axis of rotation as shown in Fig. 2. A horizontal axis of rotation allowed the stand to rotate in the vertical plane and thereby detect changes in mass resulting from changes in force due to gravity instead of measuring the thrust produced from the hybrid motor. The TSMB also differed from its predecessors in that the arms of the stand were bigger in order to support relatively large hybrid thrusters. In sizing the arms of the stand, trade-offs were made between the rigidity of the torsional flexures and the maximum deflection of the stand. The goal for the system was to measure a total mass loss of approximately 2.5 g (i.e., a force of 25.5 mN) at a radial distance of approximately 45 cm from the center of the stand's rotation.

As with previous versions of the stand, adjustable magnetic eddy currents were used to damp the TSMB motion.[13] Gaseous oxidizer for the hybrid thruster was delivered to the stand through a small flexible tube aligned with the axis of rotation to minimize influence on the TSMB's motion as shown in Fig. 2. Because of the small rotation angles produced during motor firings, the effect of the gas supply tube was minimal. However, any resistance to rotation caused by the feed line added to the torsional spring constant and was accounted for in the calibration process. The oxidizer flow rate was measured using an Omega® 5.0 SLM (SLM denotes standard liters per minute) flowmeter.

TSMB calibration was accomplished using calibration masses of approximately 0.5, 1.0, 1.5, and 2.1 g. Each mass was measured by a NIST-calibrated digital scale with a resolution of 10 μg. The calibration masses were lowered onto the stand by an electric winch to provide consistent drop velocity and placement location. A rigid bracket ensured that the winch system did not touch any part of the weight or stand once the mass had been lowered. Calibration traces were run for 210 s and consisted of 45 s of unloaded trace, 90 s with the calibration mass on the TSMB, and 75 s with the calibration mass removed (again unloaded). The calibration time was adequate to establish a zero reference point and determine the steady state deflection. The unloaded traces at the beginning and end of the calibration were compared to ensure that thermal and electronic drifts of the LVDT were negligible. Approximately six calibration traces were completed for each test firing and were performed both before and after the motor fired. The resulting displacement caused by the calibration or thruster firing was measured as a voltage difference by the LVDT and sampled by a data acquisition unit at either 60 or 1000 Hz. Analysis of the calibrations

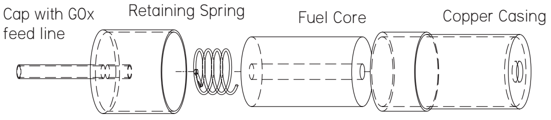

FIG. 3. Schematic of the hybrid motor test casing and PMMA core.

yielded K, C, and I used in Eq. (2). The coefficients determined from each calibration set were averaged and were specific to the particular test motor setup. Both 60 and 1000 Hz sampling rates yielded adequate time resolution for the time scales presented in this study.

To validate the TSMB's dynamic response, a dynamic calibration was conducted using a known volumetric flow rate of ethanol from a graduated syringe. The stream from the syringe was directed onto the inside wall of a receiving cup on the TSMB arm. The syringe was depressed by hand, expelling the ethanol in approximately 15 s. The mass of the syringe was measured before and after the trace (full and empty) by the NIST-calibrated scale. During the ethanol stream traces, a high-speed camera recorded the position of the plunger in the barrel of the syringe at a rate of 120 frames/s. The volumetric flow rate of ethanol was determined by the number of frames it took the plunger to traverse between gradations on the syringe and was multiplied by the density to obtain the mass flow. The photographically determined mass flow rate was compared to that determined by the TSMB analysis.

The hybrid rocket motors tested in this study consisted of polymethyl methacrylate (acrylic, PMMA, or PMM) cylindrical fuel cores with gaseous oxygen (GOx) used as an oxidizer. The PMMA fuel core cylinders were 4.5 ± 0.3 cm long with a diameter of 3.810 ± 0.003 cm. The center bore (combustion chamber) was drilled down the length of the cylinders with a diameter of 0.686 cm. A test casing was manufactured from copper with a 1.27 cm orifice plate welded to one end and the oxidizer inlet line connected to the other as shown schematically in Fig. 3. The copper feed line fit within the port of the fuel core sealing tightly and preventing any combustion on the feed-end face of the fuel core. A Ni-chrome wire was used to ignite the test core.

The hybrid firing traces were 260 s long to allow for a thruster burn duration of up to 1 min as well as adequate time to identify the reference TSMB zero deflections. The first 45 s recorded the unloaded deflection of the stand. Because of possible variables that could contribute to off-axis thrust (machining errors during thruster construction or misalignment in motor positioning) the unloaded state was followed by 10 s with only the oxidizer flowing to verify that there was no off-axis thrust being generated. The core was then ignited and allowed to burn for 10–60 s, after which the oxidizer was turned off and combustion was terminated. The oxidizer flow rate varied from 1.0 to 3.0 SLM. The mass of the core and igniter was measured on the NIST-calibrated digital scale before and after each burn as a means to investigate the accuracy of the total mass loss measured by the TSMB. Variable flow rate tests were performed to verify detection of increased mass loss associated with increased oxidizer and fuel combustion.

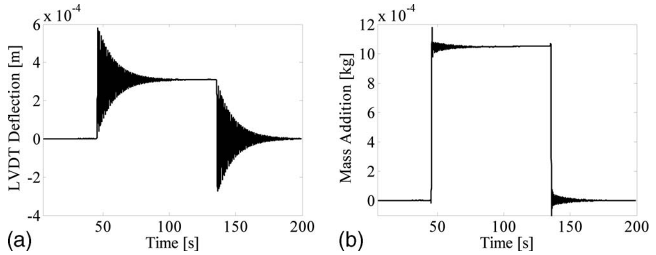

FIG. 4. (a) A typical calibration weight drop test (1.05 g) and (b) corresponding derived mass function.

The LVDT output voltage as a function of time was translated into time varying linear displacement, $X(t)$. A Savitzky–Golay algorithm and Butterworth low-pass filter[14,15] were used to smooth and filter the LVDT signal while the first and second derivatives of the function were taken using standard five-point, finite-difference, numerical differentiation methods. The error in the five-point method is on the order of the time step to the fourth power. Less accurate numerical differentiation techniques can cause phase shifting during differential analysis. At slower sampling rates, the differential phase shifting can become problematic when deriving the forcing function. The five-point method effectively eliminates any problems that arise from larger time steps between samples due to slower sampling rates. Once the signal was differentiated, the time-dependent derivatives were combined with the displacement function and the values for I, C, K, R_L, and R_R, as developed in Eq. (2). This approach yielded the forcing function, $F(t)$, and allowed for a derivation of $\dot{m}(t)$. Values of Δm_p were determined by two methods: (i) computing a numerical time integral of $\dot{m}(t)$ over the course of an entire burn (or fluid mass flow test) and (ii) measuring the change in stand deflection between the unloaded and loaded states. These Δm_p values were then compared to the pre- and postfuel weights measured by the NIST digital scale.

IV. RESULTS AND DISCUSSION

The coefficients of mass moment of inertia, I, damping, C, and the spring constant, K, varied slightly from test to test, and thus, test specific constants were used in the analysis of each firing. One complication of the TSMB as used in this study was that the mass moment of inertia changed as the stand added or removed mass. However, the change in mass moment was small (<0.002 N m s^2/rad) compared to the overall moment of inertia of the TSMB which was measured to have an average value of 0.187 ± 0.002 N m s^2/rad. The value for the TSMB spring constant was found to be 4.81 ± 0.01 N m/rad. This was consistent with the published value from the torsional spring manufacturer of 5.2 ± 0.5 N m/rad. The average damping coefficient was measured to be 0.034 ± 0.002 N m s/rad. A typical calibration trace used to determine K, C, and I is shown in Fig. 4(a). Figure 4(b) shows the analysis of Fig. 4(a) using the TSMB method. The average derived mass addition function agrees with the $1.048\,92 \pm 0.000\,01$ g mass applied to the stand to within 0.29%. The small oscillations in the mass function were due to data filtering and were propagated through the

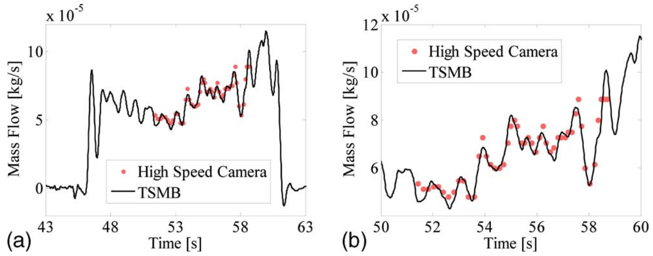

FIG. 5. (Color online) (a) The TSMB-derived mass flow rate and high-speed camera measurements from an ethanol stream with (b) a close up view.

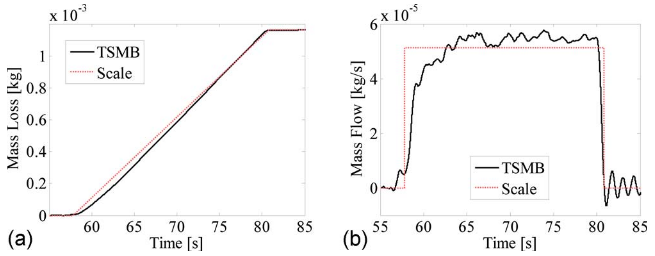

FIG. 6. (Color online) TSMB-derived and scale-averaged (a) mass loss and (b) mass flow rate for hybrid rocket motor No. 23.

analysis by the numerical differentiation. The numerically induced ringing was seen whenever there were abrupt changes in the force applied to the stand including calibration mass drops and hybrid thruster shutdown.

The mass flow from the dynamic fluid flow calibration is shown in Fig. 5. The data points represent the mass flow rate found by high-speed video camera footage. This is considered the standard mass flow and is found by measuring the number of frames required for the syringe plunger to move from one gradation on the barrel to the next multiplied by the density of the ethanol used. The derived flow rate measured on the TSMB shows good agreement with the mass flow rate recorded on the high-speed camera. Because the plunger of the syringe was depressed by hand (i.e., not uniformly), the good agreement between the two values suggests that the oscillations are physical variations in the mass flow rate.

The total mass loss measured by a NIST-calibrated digital scale was used to check the accuracy of the experimental TSMB values. The total propellant mass loss for various motor cores can be seen in Table I. There is good agreement between the digital scale values and those from the two methods of TSMB data analysis with an average difference for both methods of less than 1.5%. The values found by comparing the loaded versus the unloaded state of the TSMB were typically within 0.2% of the values found by integrating the mass flow over the entire burn duration. Thus, the TSMB provided a consistently accurate method of evaluating the total mass lost during the burn. It is noteworthy that the TSMB calculated mass loss was consistently below the mass loss measured by the NIST scale. This is most likely caused during transport of the thruster from the TSMB to the scale. The extra mass loss measured by the scale is on the order of milligrams and can be explained by small amounts of loose fuel, igniter wire, or exhaust deposits falling from the thruster during handling. Possible errors caused during transportation to and from the scale, which cannot be accounted for by traditional means of mass loss measurement, are eliminated by the TSMB method.

Figure 6 shows the (a) propellant mass loss and (b) propellant mass flow rate of an experimental hybrid fuel core as a function of time. The GOx flow rate was held constant at 1.5 SLM. Figure 6(b) shows that following the igniter firing at 57 s, the fuel mass flow rate took about a second to establish. This was consistent with the flame spreading across the interior of the hybrid motor combustion port. From 58 to 67 s, the mass flow had an upward trend, consistent with an increase in sublimating fuel surface area that occurred as the fuel port burned radially. From 67 to 80 s, the mass flow rate stopped increasing, perhaps because more oxidizer passed through the motor without mixing with fuel in the boundary

TABLE I. Comparison of measured and derived mass loss.

Motor No.	NIST scale Δm (10^{-3} kg)	TSMB Δm (load vs unload) (10^{-3} kg)	Difference from NIST scale (%)	TSMB Δm ($\int \dot{m} dt$) (10^{-3} kg)	Difference from NIST scale (%)
5	1.046	1.036	1.00	1.031	1.42
7	1.400	1.388	0.87	1.387	0.90
8	1.098	1.094	0.40	1.095	0.27
9	1.259	1.248	0.89	1.246	0.99
10	1.323	1.291	2.43	1.291	2.42
11	1.564	1.537	1.75	1.535	1.85
12	1.497	1.471	1.71	1.471	1.75
13	1.637	1.615	1.36	1.616	1.28
19	3.171	3.108	2.00	3.108	1.98
20	1.977	1.931	2.35	1.930	2.36
21	1.722	1.702	1.19	1.704	1.03
22	2.110	2.071	1.86	2.072	1.81
23	1.183	1.163	1.67	1.165	1.54
24	1.221	1.200	1.65	1.202	1.50
25	1.142	1.133	0.82	1.134	0.68
		Average error:	1.46%	Average error:	1.45%

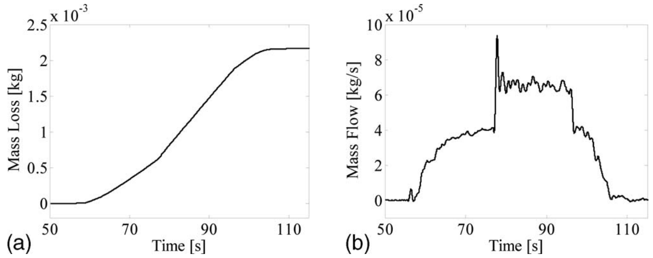

FIG. 7. TSMB-derived (a) mass loss and (b) mass flow rate for a hybrid rocket motor firing with a varying GOx flow rate.

layer flame zone. The mass loss and mass flow rate measured by the TSMB are also compared to the average mass loss and mass flow rate calculated from the NIST scale, assuming a constant rate of change during the thruster burn time. The average mass loss and mass flow were found by the traditional method of measuring the total system mass before and after the burn and dividing by the burn time. The discrepancy between the TSMB-derived and scale-averaged analyses highlights the difference between a theoretical rocket with constant mass loss, and an experimental motor with realistic operating conditions. In Fig. 6, the plots stray from a theoretical average burn rate primarily at ignition and shutdown as expected.

A motor firing with two levels of GOx flow rate (1.0 and 2.0 SLM) is shown in Fig. 7. The good temporal sampling allows speculation as to the nature of the fluctuations in mass flow seen in Fig. 7(b) to be developed. There was a spike at about 56 s where the igniter fired in the presence of 1.0 SLM oxidizer flow causing igniter mass loss for about a second. Mass flow from the igniter spike nearly returns to zero before combustion of the fuel begins. Such information could help engineers in the design of more efficient igniter systems.

Following the igniter spike there was mass loss due to combustion of the PMMA fuel at the exit end of the motor and increasing fuel mass loss as the flame propagated across the length of the combustion port. Between 60 and 77 s, the mass flow rate continued to rise as the port burned radially, increasing the port diameter and exposing more fuel surface area. At 77 s, a second valve was opened doubling the GOx flow rate, which resulted in an increase in mass loss. The spike at 77 s could be caused by a momentary pulse of off-axis thrust though no such effect was seen when the initial 1.0 SLM flow was established in the motor prior to ignition.

The mass flow at 2.0 SLM remained relatively flat with time. The lack of an upward trend at 2.0 SLM may be caused by a trade-off between increasing exposed fuel surface and a decreasing percentage of oxidizer reaching the flame zone. Also, the fuel mass flow rate at a GOx flow of 2.0 SLM was not twice that of the 1.0 SLM oxidizer flow. The total propellant mass flow resulting from a doubled oxidizer flow was only about 1.5 times greater (about 0.063 versus 0.040 g/s at GOx=1.0 SLM). At 96 s one GOx valve was closed and mass flow returned to the previous level before the remaining flow was throttled back to zero. Throttling the GOx to zero eliminated the numerical ringing in Fig. 7 that was induced when the oxidizer flow was abruptly shut off. Following oxidizer flow shutoff, there was still a small amount of combustion as residual or atmospheric oxygen allowed the grain to smolder for a few seconds.

By monitoring chamber pressure it may be possible to refine pressure based regression rate models that are more specific to a particular phase of a burn profile using the TSMB. It may also be possible to develop active controllers for hybrid motors that optimize specific impulse or maximize thrust while maintaining safe chamber pressures. The TSMB method could lead to a better understanding of combustion chamber dynamics, resulting in more efficient hybrid and solid rockets.

V. CONCLUSION

A novel diagnostic technique was developed, utilizing the TSMB, to directly measure the propellant mass flow of a hybrid rocket core as a function of time. By analyzing the TSMB as a damped spring-mass system, the position of the stand as a function of time was used to derive the forcing function that induced the TSMB motion. From the forcing function, accurate mass flow rates were derived for the hybrid thruster fuel cores. The technique was verified using two calibration methods. The first used known weights added and removed from the stand. The second used a dynamic system with a known mass flow rate of ethanol added to the mass balance. Measurement of time-accurate, propellant mass flow rates from a hybrid thruster in the range of $10^{-6}-10^{-3}$ kg/s was demonstrated. Total mass loss measured by the stand differed from mass loss measured by a NIST-calibrated digital scale by less than 2.5%. Using this method, a mass flow resolution of 0.0011 g/s or 2% of the average mass flow in this study was achieved. Further research is now underway to demonstrate the utility of such accuracy when analyzing combustion dynamics within solid-fueled combustion chambers.

Future research should aim to investigate ways mass flow and motor efficiency can be improved using TSMB analysis, perhaps incorporating chamber pressure data. TSMB mass flow data should be compared with x-ray and Helmholtz oscillation test data from ongoing programs.[10,11] This will require scaling up of the TSMB setup since these other techniques require larger combustion chambers to achieve mass flow resolution approaching that of the TSMB. The principles governing TSMB operation are, in theory, unaffected by scaling of the device and should lead to better mass flow accuracy than the 2% error presented here. Despite the small scale of current testing, and the promise of improved accuracy with larger scale testing, TSMB time-accurate measurements already appear to be more accurate than any other method in the literature.

ACKNOWLEDGMENTS

This work was supported by the Air Force Research Laboratory, Propulsion Directorate at Edwards AFB, CA. The authors wish to thank Mr. Miles Killingsworth for his invaluable assistance with the TSMB model.

NOMENCLATURE

δ_n = logarithmic decrement
ζ = damping ratio
ω_o = natural frequency (rad/s)
ω_d = damped frequency (rad/s)
C = torsional damping coefficient (N m s/rad)
F_C = static calibration force (N)
g_o = acceleration due to gravity on earth (m/s^2)
I = mass moment of inertia (N m s^2/rad) or (kg m^2/rad)
$I_{\rm sp}$ = specific impulse (s)
$I_{\rm tot}$ = total impulse (N s)
K = torsional spring constant (N m/rad)
M_o = steady state forcing moment (N m)
$\dot{m}_p$ = mass flow of propellant (kg/s)
Δm_p = total propellant mass loss (kg)
m_C = mass of steady state calibration weight (kg)
R_C = radial distance from pivot to center of calibration load (m)
R_L = radial distance from pivot to LVDT (m)
R_R = radial distance from pivot to center of test load (m)
X = measured LVDT deflection (m)

[1] J. Bustillo, R. Howe, and R. Muller, Proc. IEEE **86**, 1552 (1998).
[2] K. Abedin, D. Coutts, and C. Webb, Appl. Phys. A: Mater. Sci. Process. **78**, 737 (2004).
[3] G. Sutton and O. Biblarz, *Rocket Propulsion Elements*, 7th ed. (Wiley, New York, 2001), pp. 579–580.
[4] L. Freund and S. Suresh, *Thin Film Materials: Stress, Defect Formation, and Surface Evolution* (Cambridge University Press, Cambridge, London, 2003), pp. 52–53.
[5] R. Shanks and M. Hudson, J. Pyrotechnics **11**, 1 (2000).
[6] E. Cubbin, J. Ziemer, E. Choueiri, and R. Jahn, Rev. Sci. Instrum. **68**, 2339 (1997).
[7] M. Gamero-Castano, Rev. Sci. Instrum. **74**, 4509 (2003).
[8] A. Jamison, A. Ketsdever, and E. P. Muntz, Rev. Sci. Instrum. **73**, 3629 (2002).
[9] K. Lohner, J. Dyer, E. Doran, Z. Dunn, and G. Zilliac, Proceedings of the 42nd Joint Propulsion Conference, Sacramento, California, 2006 (unpublished), AIAA Paper No. 2006-4671.
[10] B. Evans, G. Risha, N. Favorito, E. Boyer, R. Wehman, N. Libis, and K. K. Kuo, Proceedings of the 39th Joint Propulsion Conference, Huntsville, Alabama, 2003 (unpublished), AIAA Paper No. 2003-4592.
[11] S. De Zilwa, G. Zilliac, M. Reinath, and A. Karabeyoglu, J. Propul. Power **20**, 684 (2004).
[12] R. Frederick, Jr., and B. Greinerf, J. Propul. Power **12**, 605 (1996).
[13] B. D'Souza and A. Ketsdever, Rev. Sci. Instrum. **76**, 015105 (2005).
[14] A. Savitzky and M. Golay, Anal. Chem. **36**, 1627 (1964).
[15] I. Selesnick and C. Burrus, IEEE Trans. Signal Process. **46**, 1688 (1998).

JOURNAL OF PROPULSION AND POWER
Vol. 24, No. 6, November–December 2008

Thrust Stand Micromass Balance for the Direct Measurement of Specific Impulse

Andrew D. Ketsdever*
University of Colorado at Colorado Springs, Colorado Springs, Colorado 80933
and
Brian C. D'Souza† and Riki H. Lee†
University of Southern California, Los Angeles, California 90089-1191

DOI: 10.2514/1.36921

A technique has been developed to directly measure the specific impulse from pulsed thruster systems. The technique is especially useful for propulsion devices that use solid propellants, for which a direct measurement of the propellant mass flow is extremely difficult. A torsion balance is used with a horizontal axis of rotation. A thruster is placed on the balance such that the impulse of the thruster firing and the change in mass due to the expelled propellant act in the same direction. A combined impulse and steady-state force measurement (due to propellant mass loss) can then be decoupled to assess the ratio of the impulse to the weight of propellant expended, or the specific impulse. A model has been developed to show the utility of the technique for pulsed systems with a firing time less than the natural period of the balance. An experimental proof of principle study was also undertaken using the laser ablation of engineering-grade Buna, Viton, and Teflon propellants. Specific-impulse measurements on the order of 200 s have been demonstrated with this laser ablation thruster.

Nomenclature

C = torsional damping coefficient, $\mathrm{N \cdot m\, s/rad}$
C_m = laser-material momentum coupling coefficient, dyne/W
E = laser energy, W
F_C = static calibration force, N
g_o = acceleration due to gravity on Earth, $\mathrm{m/s^2}$
I = mass moment of inertia, $\mathrm{N \cdot m\, s^2/rad}$, $\mathrm{kg \cdot m^2/rad}$
I_{sp} = specific impulse, s
I_{tot} = total impulse, $\mathrm{N \cdot s}$
K = torsional spring constant, $\mathrm{N \cdot m/rad}$
M = forcing moment, $\mathrm{N \cdot m}$
M_o = steady-state forcing moment, $\mathrm{N \cdot m}$
P = laser power, J
Q^* = laser energy consumed per unit mass ablated, J/kg
R_C = radial distance from pivot to center of calibration load, m
R_L = radial distance from pivot to linear variable differential transformer, m
R_R = radial distance from pivot to center of test load, m
T = natural period of the stand, s
t = time, s
X = measured linear variable differential transformer deflection, m
Δm = change in mass due to laser ablation, kg
δ_n = logarithmic decrement
ζ = damping ratio
θ = angular deflection, rad
τ = pulse duration, s
ω_o = natural frequency, rad/s
ω_d = damped frequency, rad/s

Introduction

THE impulse produced by a thruster can be found by integrating the thrust produced with time. The specific impulse I_{sp} is defined as the impulse delivered by a propulsion system divided by the weight of the propellant used to produce that impulse [1]. Traditional specific-impulse measurements for propulsion systems that use solid propellants are complicated by several issues. First, the amount of mass loss and the associated impulse provided by pulsed systems may be relatively low, requiring the averaging of multiple thruster firings to obtain meaningful data. The performance of individual pulses can be lost through the averaging of multiple tests. Understanding of individual pulse performance can lead to more efficient thrusters if parameters between subsequent tests can be quantified.

Second, the system mass is traditionally measured before the performance measurements, and again after, to assess the propellant mass used [2]. These measurements may take place days apart and may require the system to be placed into a vacuum chamber and subsequently removed between thruster firings at the cost of valuable resources. Finally, issues of handling, contamination, oxidation, and adsorption may complicate mass measurements that are not done in situ.

To combat these issues for pulsed thruster systems, a thrust stand mass balance (TSMB) and associated experimental techniques have been developed in which both the total mass loss and impulse are measured simultaneously. The concurrent measurement of the impulse and mass loss leads to a direct measure of specific impulse. The benefits of the developed technique include the ability to measure specific impulse directly and in situ without the complications and potential inaccuracies of multiple measurements. The resolution of the TSMB is such that it could measure the impulse and mass loss of individual pulses from most micropropulsion systems currently under development. The developed technique allows both mass and impulse measurements simultaneously while the thruster is in vacuum, reducing the influence of oxidation, adsorption, and contamination. The major limitation of the technique is that it is only currently valid for pulsed systems in which the pulse width is less than the natural period of the thrust stand.

The technique has been applied in this work to investigate a laser ablation system, although the technique is also valid for a variety of pulsed propulsion systems such as solid microthrusters [3] and pulsed plasma thrusters [4]. Laser ablation affords some benefits

---

Presented as Paper 5300 at the 43rd AIAA/ASME/SAE/ASEE Joint Propulsion Conference and Exhibit, Cincinnati, OH, 8–11 July 2007; received 30 January 2008; accepted for publication 13 May 2008. This material is declared a work of the U.S. Government and is not subject to copyright protection in the United States. Copies of this paper may be made for personal or internal use, on condition that the copier pay the $10.00 per-copy fee to the Copyright Clearance Center, Inc., 222 Rosewood Drive, Danvers, MA 01923; include the code 0748-4658/08 $10.00 in correspondence with the CCC.

*Group Leader, Aerophysics Branch, Department of Mechanical and Aerospace Engineering. Senior Member AIAA.

†Graduate Research Assistant, Department of Aerospace and Mechanical Engineering. Student Member AIAA.

when developing the TSMB. First, the laser pulse energy can be tuned to allow more or less ablative mass loss in a particular laser pulse. Second, a variety of propellants (target materials) can be used to assess the ability of the technique to distinguish the specific impulse over a relatively wide range. One of the disadvantages to using laser propulsion is the inherent scatter in the data between pulses. Drift in the laser energy output and physical differences between ablation sites on engineering targets account for much of the scatter. However, this scatter can also be viewed as a benefit in the development of the TSMB because the ability to measure the performance of individual impulses can be demonstrated.

Numerous experimental techniques have been employed in the past to measure mass loss and other fundamental properties of laser ablation events. The techniques include time-of-flight mass spectroscopy, plasma spectroscopy, nanosecond-shadowgraphy [5], and other plasma imaging techniques [6]. Each technique may be useful in understanding certain aspects as they monitor specific components of the ejected material. However, each has limitations and weaknesses in their application for investigating a broad range of mechanisms for laser ablation. Because the ejected material is expected to contain particles of different sizes, charged and neutrals particles, and particles of varying velocity, it is difficult to simultaneously capture all components to accurately determine the amount of mass lost. By only monitoring some portions of the ablated material, it is often possible to underestimate the mass loss, which generally results in overestimating the specific impulse.

Thrust Stand Mass Balance

The TSMB is based on the nano-Newton-second impulse balance system (NIBS) described by D'Souza and Ketsdever [7]. By inverting the NIBS to allow for a horizontal axis of rotation, both the impulse and the change in mass from the propulsive event provide forces acting in the same direction, as illustrated in Fig. 1. In this system, the weight of the propulsion system acts as a steady-state force on the TSMB. As a thruster fires, mass is released and the propulsion system gets lighter, with the change in mass resulting in a measurable deflection of the TSMB. The resulting steady deflection is calibrated to indicate the net change in mass due to the loss of propellant. With both the impulse and mass loss force acting in the same direction, the two forces couple to produce a single deflection trace on the TSMB. For the performance of the thruster to be quantified, each component must be resolved individually from the single deflection trace.

To assess the feasibility of such an analysis, a model was created to simulate the behavior of the TSMB. The TSMB model is based directly on the NIBS model [7]. The model takes the force profile for each component (impulse and weight change) and plots their individual and combined dynamic effects on the TSMB. The TSMB behaves like an underdamped, oscillating, mass-spring system. System motion is described by the following second-order differential equation for a rigid bar:

$$I\ddot{\theta}(t) + C\dot{\theta}(t) + K\theta(t) = M(t) = F(t)r \tag{1}$$

For small angles of deflection θ, the motion of the stand can be linearly approximated through the small-angle approximation, such that Eq. (1) can be written as

$$I\frac{\ddot{X}(t)}{R_L} + C\frac{\dot{X}(t)}{R_L} + K\frac{X(t)}{R_L} = F(t)R_R \tag{2}$$

To derive the forcing function from a measured deflection, the coefficients in Eq. (2) must be experimentally measured from the TSMB. By applying a steady-state calibration force to the stand, the resulting deflection, as time goes to infinity, becomes

$$K\frac{X}{R_L} = F_C R_C \tag{3}$$

The remaining two coefficients can be found by analyzing the measured period and the decay of the deflection amplitude as a function of time. First, a logarithmic decrement is defined as

$$\delta_n = \ln(X_i/X_{i+n}) \tag{4}$$

where i is a positive integer, and X_i and X_{i+n} are peak amplitudes, separated by n periods. The damping ratio is then given by

$$\zeta = \delta_n/\sqrt{(n\cdot 2\pi)^2 + \delta_n^2} \tag{5}$$

The measured frequency of the stand can be found from the measured period and related to the natural frequency by

$$\frac{2\pi}{T} = \omega_d = \omega_o\sqrt{1-\zeta^2} \tag{6}$$

and the mass moment of inertia and damping coefficients are

$$I = \frac{K}{\omega_o^2} \tag{7}$$

$$C = 2\zeta\sqrt{KI} \tag{8}$$

Therefore, the coefficients I, C, and K may be determined from any single test trace resulting from a known, static, steady-state, calibration load. It follows that if the deflection $X(t)$, resulting from a dynamic load, is measured on a stand with no significant change in I, C, or K, the time dependent function $F(t)$, which describes that dynamic load, may be determined through Eq. (2). Therefore, the system in Eq. (1) can be solved numerically for a steady-state forcing function as

$$\theta(t) = \frac{M_o}{K} + e^{\alpha t}\left[\left(\theta_o - \frac{M_o}{K}\right)\cos(\beta t) + \left(\frac{\dot{\theta}_o K - \alpha K\theta_o + \alpha M_o}{K\beta}\right)\sin(\beta t)\right] \tag{9}$$

$$\dot{\theta}(t) = e^{\alpha t}\left[\dot{\theta}_o\cos(\beta t) + \left(\frac{I\alpha\dot{\theta}_o - K\theta_o + M_o}{I\beta}\right)\sin(\beta t)\right] \tag{10}$$

$$\ddot{\theta}(t) = e^{\alpha t}\left[\left(\frac{M_o - C\dot{\theta}_o - K\theta_o}{I}\right)\cos(\beta t) + \left(\frac{\alpha(M_o - C\dot{\theta}_o - K\theta_o) - K\dot{\theta}_o}{I\beta}\right)\sin(\beta t)\right] \tag{11}$$

where $\alpha = -C/2I$ and $\beta = \sqrt{K/I - \alpha^2}$.

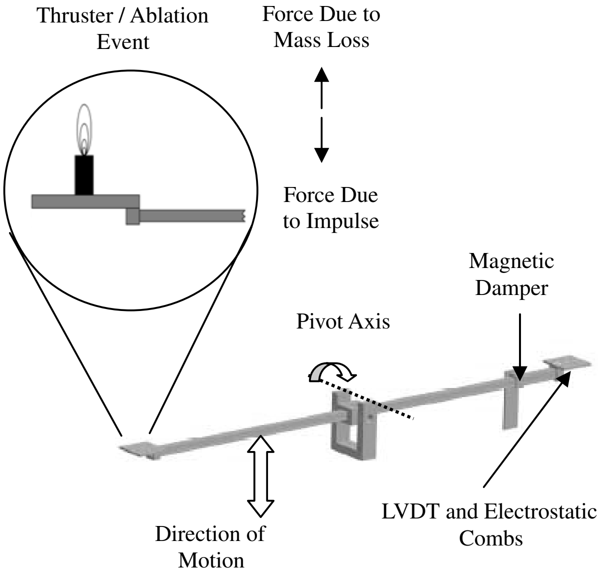

Fig. 1 Schematic of the TSMB setup and configuration.

It has already been shown that any arbitrary or irregular force can be approximated using a series of constant-force segments of small time widths $\mathrm{d}\tau$ [7]. As such, the combined effect of two overlapping forces does not pose a particular problem for the TSMB. For simplicity, a constant force **F** is applied for a duration of τ, resulting in the modeling of an impulse bit. The force profile corresponding to the mass change can be determined for a given specific impulse such that the weight loss is given by the total impulse ($\mathbf{F}^*\tau$) divided by the specific impulse. Assuming that the mass loss occurs steadily over the duration of the impulse, the force profile for the mass loss ramps up to a plateau, as seen in Fig. 2. Figure 2 shows the manifested force applied to the TSMB by the propellant mass loss and by the thruster impulse.

Figure 3 shows results from the TSMB model for a simulated pulsed thruster delivering a typical impulse of 1 mN · s. Shown are traces for the dynamic response of the TSMB for each effect individually and their combined result on the TSMB. The individual traces (for mass loss and impulse) assume that the TSMB has experienced only that force in the absence of the other. It is evident in Fig. 3 that between the individual impulse trace and mass loss trace, a phase shift exists in the timing, which results from the accommodation of the stand to the effective natural period of oscillation. In the case of the impulse, the pulse width is short relative to the natural period of the TSMB, allowing the stand to accommodate almost instantaneously. However, the force associated with the mass loss is continuously applied. This manifests as a slight phase shift in the two individual effect curves that, when combined, results in a curve that is close in magnitude to the curve for the impulse acting by itself but is temporally shifted. Because of the fact that the impulse is measured by taking the range of deflection from the first peak to the first valley, the magnitude of the curve for the impulse acting alone tends to be preserved in the combined trace. The mass loss is then simply measured by examining the total deflection of the tail of the trace compared with the initial zero point.

To verify that the magnitude of the impulse is preserved and can be decoupled from the mass loss, the input parameters of pulse width, specific impulse, and total impulse were varied in the model. The total impulses were varied from 3 nN · s up to 1 mN · s to fully cover the dynamic range of the stand, which was limited by the sensitivity of the current version of the TSMB. This entire impulse range was generated using a wide range of simulated pulse widths that were all less than the natural period of the stand, T. Additionally, for each set of impulse and pulse-width parameters, the specific impulse was varied from 1 to over 25,000 s. The results are summarized in Fig. 4 for an impulse of 1 mN · s. The spread in the data points (represented by error bars) shows the effects of the variation in specific impulse from 1 to 25,000 s. The magnitude of the mass loss varies with the specific impulse and has varying effects on the resulting TSMB deflection. It is interesting to note that the mass loss effect for a given impulse consistently manifests itself as a percentage of the impulse magnitude, such that smaller impulses result in proportionately smaller errors. For pulse widths below a tenth of the natural period, the deflection for a given specific impulse appears to be constant. For pulse widths above a tenth of a period, an expected decrease in the overall TSMB deflection is evident. Figure 4 also shows that as the pulse width approaches the natural period of the TSMB, the range of error from the mass loss increases, which results from the accommodation to the natural period. As the pulse width increases, the impulse component of the trace begins to shift in phase. Similar to the superposition of waves out of phase, constructive and destructive interference can be expected. As the phases between the components begin to synchronize, constructive interference results in larger error in the magnitude of the deflection range.

Figure 5 depicts the trend of the error caused by simultaneously measuring the impulse and the corresponding mass loss. Note that Fig. 5 only includes points for pulse widths less than 0.25 T, to

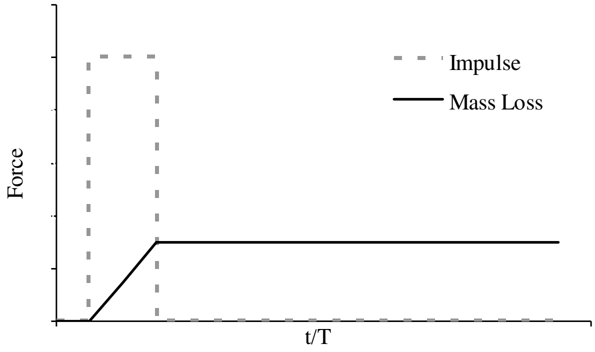

Fig. 2 Force profiles for an impulse and its corresponding mass loss.

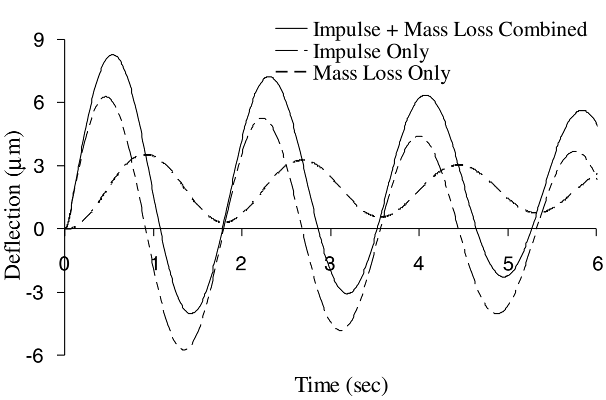

Fig. 3 Individual impulse and mass loss traces generated by model simulation.

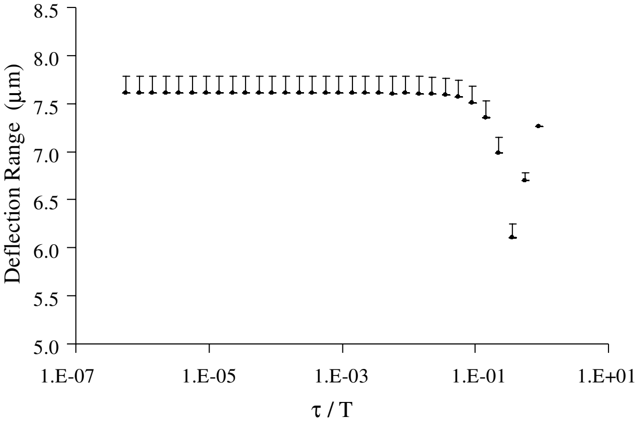

Fig. 4 TSMB maximum deflection as a function of normalized impulse pulse width compared with the analytical model results.

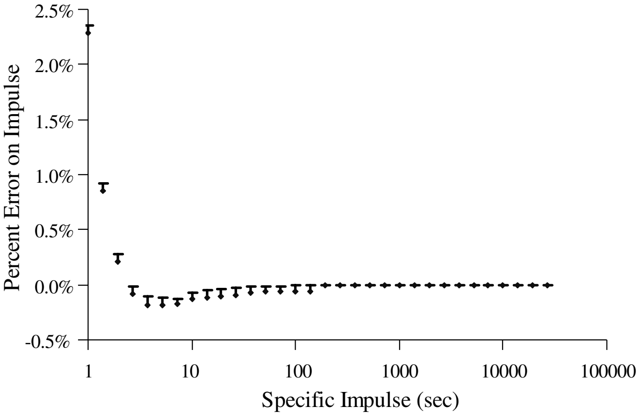

Fig. 5 Error profile for impulse measurements with simultaneous mass loss measurements. This curve can be used to correct calculated impulses once the I_{sp} of the thruster has been determined.

minimize the scatter that is caused by pulse-width effects. Above a specific impulse of approximately 2 s, the percentage error in the calculated deflection range is less than 0.5%. For specific-impulse ranges in which thrusters would typically be tested, the error is almost negligible. Therefore, the standard and simple deflection technique for measuring impulse is sufficient for most micropropulsion systems currently being developed.

Experimental Setup

The TSMB, shown in Fig. 1, is a torsion balance that consists of two flexure pivots that are used to support the balance and to provide a restoring force and is similar to the thrust stand described by Jamison et al. [8] The flexures have a spring constant of approximately 0.0016 Nm/deg. The TSMB is completely symmetric about the center of rotation, with two armatures extending from each side of the stand. The TSMB is inertially balanced to reduce the effects of outside vibrations on the measurements. The force measurements involve the sensing of an angular displacement resulting from the torque applied to the damped rotary system. The method for detecting angular deflection is to measure the linear displacement at a known radial distance using a linear variable differential transformer (LVDT). For the forces measured in this study, the linear movement at the end of the TSMB arm is on the order of a micrometer. Therefore, the error associated with the angular movement of the thrust stand arm is negligible. The motion of the TSMB is damped by a permanent magnet arrangement that uses eddy currents to provide a viscous force. The TSMB is calibrated using an electrostatic comb system described by Selden and Ketsdever [9].

For pulsed thruster systems, the TSMB is inverted with a horizontal axis of rotation. In this configuration, the TSMB can measure impulse and propellant mass loss simultaneously. To demonstrate the effectiveness of the TSMB, laser ablation events were investigated. Tests were configured using an 800-mJ-per-pulse Infinity Nd:YAG laser to ablate several material targets. Target materials were placed on the TSMB, located in a vacuum chamber capable of maintaining background pressures of 10^{-6} torr. The Infinity laser was configured to emit a wavelength of 532 nm at a repetition rate of 100 Hz. A shutter was situated in the path of the laser, and a pulse generator was used to trigger the shutter, resulting in an average of 35 shots arriving at the target. On the path to the target, the laser passed through a beam splitter, allowing the power of the laser to be monitored and the number of pulses per test to be counted. Testing was performed on several engineering surfaces, including machine-grade Teflon, Buna, and Viton. For these tests, the average number of shots on each site was held constant, whereas the energy of the laser was varied between 50 and 400 mJ IR. A calibration procedure using electrostatic combs [9] was conducted before the start of testing on each new target.

Upon completion of the tests, the data were analyzed to determine the impulse and mass loss of the material. This procedure required the data trace from the TSMB to undergo two different analyses. The first step was the determination of the mass lost during the ablation event. The analysis takes the average of the data points both before and after the ablation event. These averages are then used to determine the total stand deflection due to the steady-state mass lost from the target. The averages are also used to remove any electronic (thermal) drift in the LVDT. Because the total sampling time of an individual impulse event is relatively short (on the order of minutes), thermal drift is not significant, as shown in previous work [7,8]. The corresponding LVDT voltage change due to the propellant mass loss is shown in Fig. 6a. Using the steady-state calibration data from the electrostatic combs, the change in voltage can be directly correlated with a force associated with the change in target weight. The second step of the data analysis is to determine the impulse from the laser ablation event. This step analyzes the maximum deflection of the LVDT, which occurred between the first peak and first valley of the trace, as shown in Fig. 6b. Using pulsed-mode calibration data from the electrostatic combs, the maximum deflection can be directly correlated with an impulse.

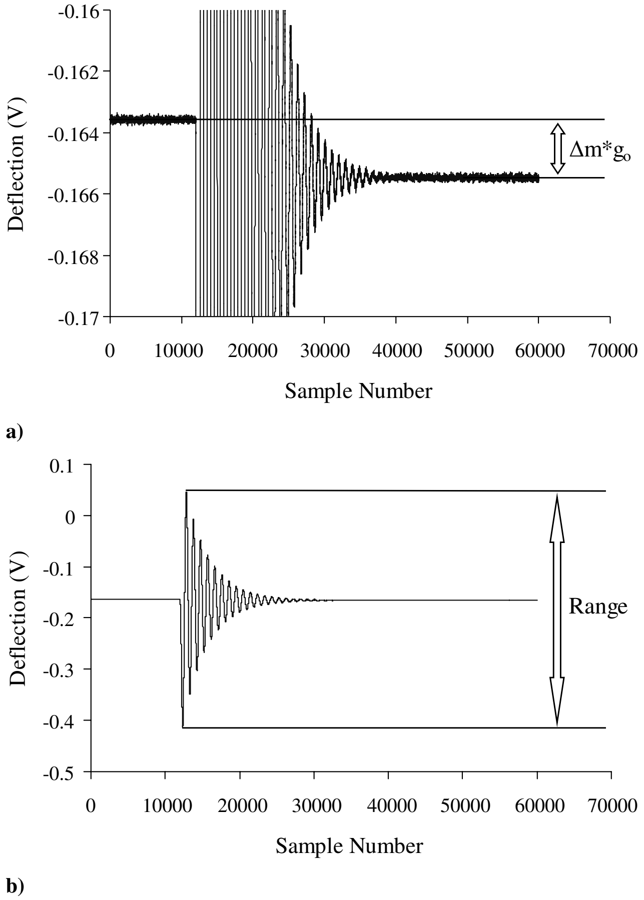

a)

b)

Fig. 6 Sample trace from TSMB showing a) LVDT voltage change due to mass loss and b) the range.

Results and Discussion

The common measure of propulsive efficiency is the specific impulse. The specific impulse is a measure of the impulse per unit of expended propellant weight. From a propulsion-efficiency perspective, it is desirable to get the largest impulse for the lowest mass loss (i.e., high specific impulse). In its simplest form only the total impulse measurement and mass loss measurement are required to calculate the specific impulse. Figure 7 shows the impulse and corresponding ablative mass loss for a Buna target as a function of the total laser energy delivered to the target material. There is an increase in both impulse and mass loss as the laser energy increases, which leads to a general increase in the specific impulse shown in Fig. 8. The scatter in the data evident in Fig. 8 may come from a variety of sources. In the calibration process, the TSMB has repeatability of less than 1% (one sigma error). The scatter in Fig. 8 is much greater than 1%, indicating that the physical ablation process is most likely the

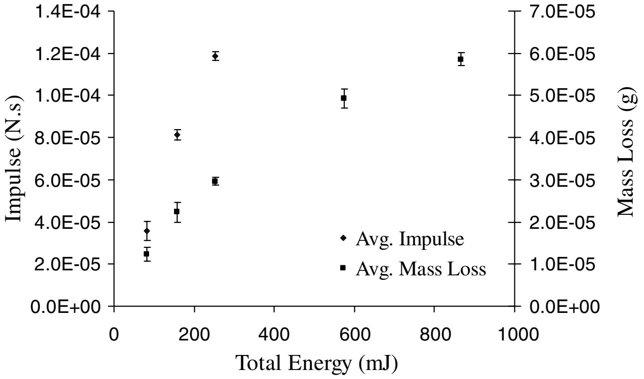

Fig. 7 Impulse and mass loss for Buna target.

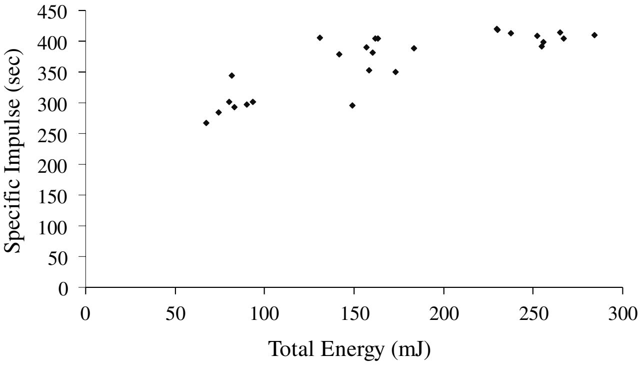

Fig. 8 Specific impulse of Buna.

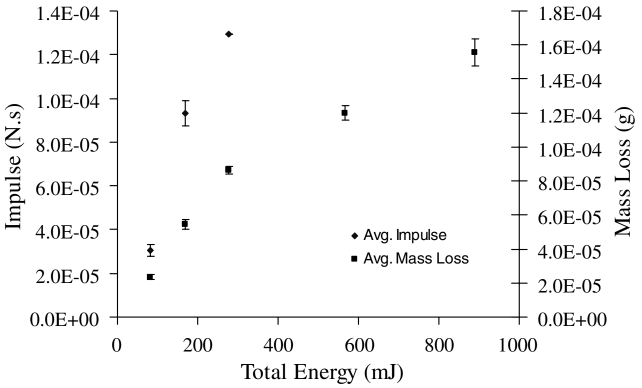

Fig. 9 Impulse and mass loss for Viton.

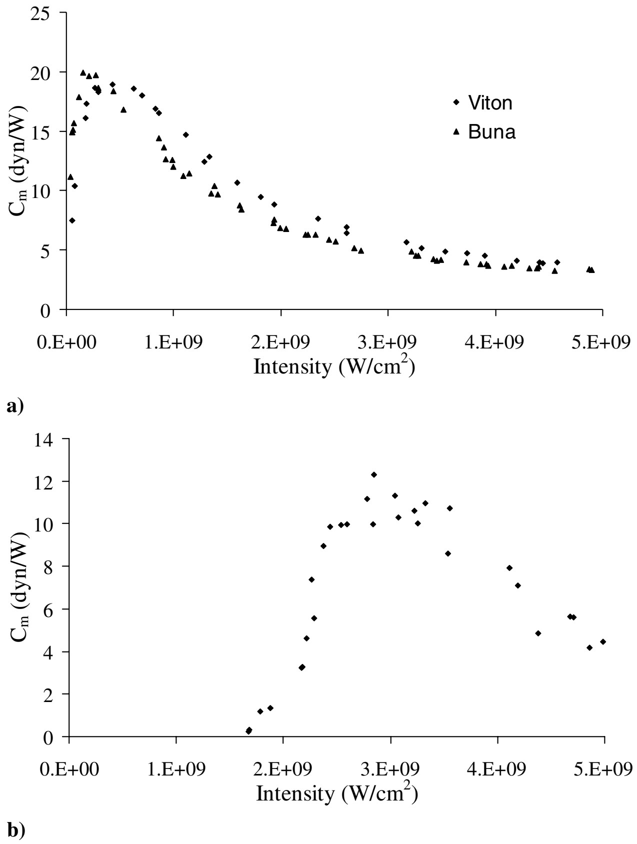

Fig. 11 Coupling coefficients for a) mechanical grade Teflon and b) Viton and Buna.

reason. Each data point represents a different test at a different target material location. Variations in laser output, surface roughness, and material impurities are the most likely causes of the scatter.

Figure 9 shows similar impulse and mass loss results for Viton. The specific impulse for these measurements is shown in Fig. 10. It is evident that the specific impulse increases with total laser energy up to about 175 mJ. At energies above 175 mJ the specific impulse tends to decrease. This trend can be explained by investigating the momentum coupling coefficient between the material and the incident laser beam. Phipps et al. [10] predict that the impulse efficiency, as measured by the momentum coupling coefficient, rapidly reaches a maximum once the ablation threshold is surpassed and then decreases with increasing laser intensity. The reduction in the efficiency can stem from several factors, including the shielding of the laser beam by ablating material. The coupling coefficients as a function of laser intensity are shown in Fig. 11a for Viton and Buna [11]. It should be noted that both materials have relatively low ablation thresholds and correspondingly high maximum coupling coefficients. Figure 11b shows the coupling coefficient for machine-grade Teflon. Note that the ablation threshold for Teflon is noticeably higher than for either Buna or Viton and the maximum coupling coefficient is lower.

Figure 12 shows impulse and mass loss for machine-grade Teflon with the corresponding specific impulse shown in Fig. 13. The specific impulse tends to decrease for total laser energies above about 300 mJ. The specific impulse for Teflon is generally lower than it is for either Buna or Viton, which correlates to its lower maximum coupling coefficient. The momentum coupling coefficient can be found from

$$C_m = \frac{I_{\text{tot}}}{E} = \frac{F}{P} \tag{12}$$

and the specific impulse can then be written as

$$I_{\text{sp}} = \frac{C_m Q^*}{g_o} \tag{13}$$

where $Q^* = E/\Delta m$. Therefore, both C_m and Q^* are dependent on the laser energy incident upon a particular material target. Figure 7 or

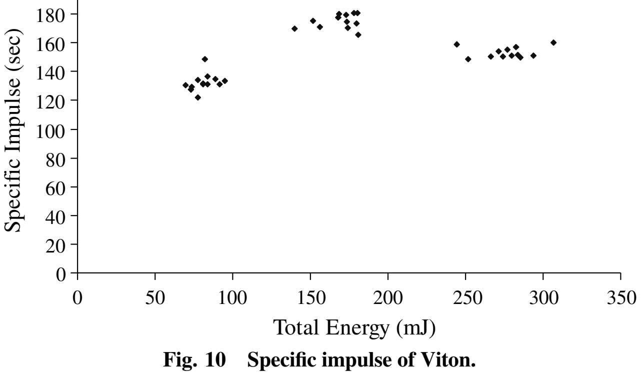

Fig. 10 Specific impulse of Viton.

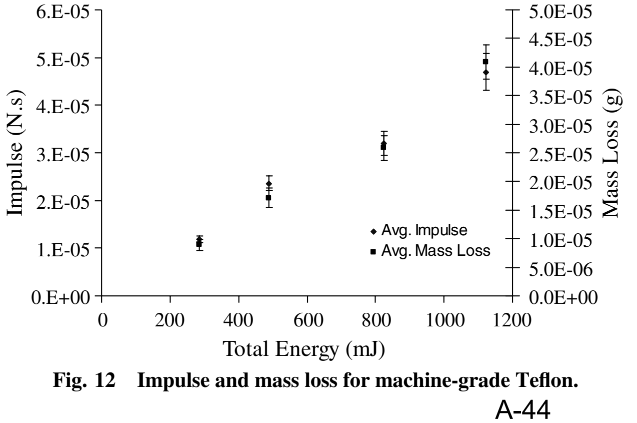

Fig. 12 Impulse and mass loss for machine-grade Teflon.

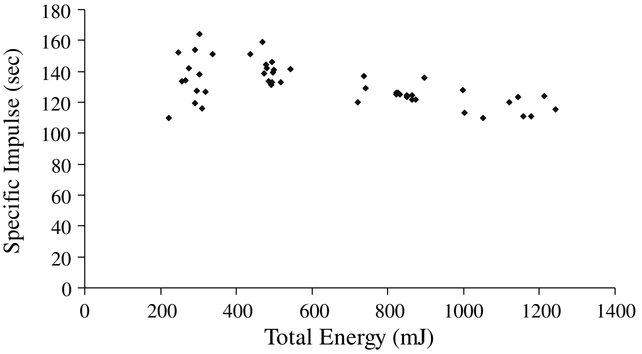

Fig. 13 Specific impulse of machine-grade Teflon.

Fig. 9 could be reformatted to show C_m and Q^* as a function of laser energy or total power. As can be seen, both the impulse C_m and mass loss Q^* are functions of the laser operating conditions, and thus Q^* is not a constant. This implies that there is not a straightforward relationship between I_{sp} and C_m. However, general trends in I_{sp} can be inferred from Eq. (13). For a given Q^*, a larger C_m implies a larger I_{sp}. Also, the I_{sp} will be zero for laser energies below the ablation threshold at which $C_m = 0$. In general, these trends are verified by the data shown for the specific impulse. The data in Figs. 8, 10, and 13 show the ability of the TSMB to consistently measure the specific impulse from laser ablation events. In these cases, both mass loss and impulse were successfully extracted from a single TSMB trace.

Conclusions

The TSMB has been used to consistently measure mass loss and impulse for laser ablation events. The ability to concurrently resolve impulse and mass loss from a single TSMB trace allows for the direct measurement of specific impulse. Although some scatter is visible in the data, there are multiple factors that could contribute to this scatter. For instance, the surface roughness of the spot being ablated could vary between test sites. The trends measured in the laser ablation specific impulse were consistent with the coupling coefficients for the various target materials. Buna exhibited the largest specific impulse for the incident laser energies investigated in this study. The TSMB showed its usefulness as a diagnostic tool for the direct measurement of specific impulse from laser ablation thrusters by demonstrating that specific impulses in the range of hundreds of seconds were achievable for laser ablation thrusters on engineering surfaces. However, the model results also indicate that the TSMB will be useful for other pulsed thruster systems. The major requirement of the thruster system is that the thruster firing time be no more than approximately one-quarter of the TSMB natural period for the inherent measurement error to remain below 0.5%. The natural period of the balance can be modified by changing either the associated spring constant or moment of inertia, allowing flexibility for a particular thruster system. The TSMB has shown its utility as a diagnostic tool for propulsion systems in which the measurement of mass flow is not straightforward. Mostly, these are solid propellant systems such as laser ablation thrusters, pulsed plasma thrusters, and hybrid thrusters.

Acknowledgments

This work was supported by the U.S. Air Force Office of Scientific Research and the U.S. Air Force Research Laboratory (AFRL), Propulsion Directorate, Edwards Air Force Base, California. The authors wish to thank Jean-Luc Cambier (AFRL) for his support of the laser ablation measurements.

References

[1] Sutton, G. P., and Biblarz, O., *Rocket Propulsion Elements*, 7th ed., Wiley-Interscience, New York, 2001.

[2] Fredrick, R. A., and Greiner, B. E., "Laboratory-Scale Hybrid Rocket Motor Uncertainty," *Journal of Propulsion and Power*, Vol. 12, No. 3, 1996, pp. 605–611.
doi:10.2514/3.24076

[3] Lewis, D., Janson, S., Cohen, R., and Antonsson, E., "Digital Micro-Propulsion," *Sensors and Actuators A (Physical)*, Vol. 80, No. 2, 2000, pp. 143–154.
doi:10.1016/S0924-4247(99)00260-5

[4] Burton, R. L., and Turchi, P. J., "Pulsed Plasma Thruster," *Journal of Propulsion and Power*, Vol. 14, No. 5, 1998, pp. 716–735.

[5] Hauer, M. R., "Laser Ablation of Polymers Studied by Time Resolved Methods," Ph.D. Dissertation, Swiss Federal Inst. of Technology, Zurich, 2004.

[6] Lin, J., Thompson, M. S., and Pakhomov, A. V.,"Ablative Laser Propulsion: Determination of Specific Impulse from Plasma Imaging," *High-Power Laser Ablation V*, Proceedings of SPIE, Vol. 5448, SPIE—The International Society for Optical Engineering, Bellingham, WA, 2004, pp. 465–476.

[7] D'Souza, B. C., and Ketsdever, A. D., "Investigation of Time-Dependent Forces on a Nano-Newton-Second Impulse Balance," *Review of Scientific Instruments*, Vol. 76, No. 1, 2005, Paper 015105.
doi:10.1063/1.1834707

[8] Jamison, A., Ketsdever, A. D., and Muntz, E. P., "Gas Dynamic Calibration of a Nano-Newton Thrust Stand," *Review of Scientific Instruments*, Vol. 73, No. 10, 2002, pp. 3629–3637.
doi:10.1063/1.1505096

[9] Selden, N., and Ketsdever, A. D., "Comparison of Force Balance Calibration Techniques for the Nano-Newton Range," *Review of Scientific Instruments*, Vol. 74, No. 12, 2003, pp. 5249–5254.
doi:10.1063/1.1623628

[10] Phipps, C. R., Turner, T. P., Harrison, R. F., York, G. W., and Osbourne, W. Z., "Impulse Coupling to Targets in Vacuum by KrF, HF, and CO_2 Single-Pulse Lasers," *Journal of Applied Physics*, Vol. 64, No. 3, 1988, pp. 1083–1096.
doi:10.1063/1.341867

[11] D'Souza, B. C., "Development of Impulse Measurement Techniques for the Investigation of Transient Forces Due to Laser-Induced Ablation," Ph.D. Dissertation, Univ. of Southern California, Dept. of Mechanical and Aerospace Engineering, Los Angeles, 2006.

C. Segal
Associate Editor

JOURNAL OF SPACECRAFT AND ROCKETS
Vol. 45, No. 2, March–April 2008

Free-Molecule-Microresistojet Performance Using Water Propellant for Nanosatellite Applications

R. H. Lee,[*] A. M. Bauer,[†] M. D. Killingsworth,[‡] T. C. Lilly,[§] and J. A. Duncan[†]
University of Southern California, Los Angeles, Los Angeles California 90089-1191
and
A. D Ketsdever[¶]
U.S. Air Force Research Laboratory, Edwards Air Force Base, California 93524

DOI: 10.2514/1.32341

Advances in microtechnology manufacturing and capability have led to an increased interest in micro- and nanosatellites. A propulsion system was designed to meet the on-orbit attitude control requirements for nanospacecraft. The free-molecule microresistojet, a low-cost, low-power, high propellant-storage density, and green propulsion system, was analyzed in this study to determine its ability to provide a slew maneuver for a typical 10-kg nanosatellite. Additionally, a free-molecule-microresistojet technology demonstrator was fabricated using traditional and microelectromechanical systems techniques. The technology demonstrator was analyzed and tested in this study to determine its performance characteristics when operating with water propellant. Experimental data show that the free-molecule microresistojet, with a heated wall temperature of 580 K, can attain a specific impulse of 79.2 s with a thrust level of 129 μN. For a given mass flow, higher thrust levels can be achieved by increasing the temperature of the free-molecule-microresistojet heater chip. The experimental results agree favorably with predicted values from kinetic theory. Applying the measured performance of the technology demonstrator to an optimized setup, the free-molecule-microresistojet system could provide a 45-deg slew of a typical nanosatellite in 60 s, which is acceptable for many nanosatellite applications.

Nomenclature

A_s = area of the expansion slots, m^2
C = mass flow rate constant, $m \cdot s$
D_{pore} = diameter of the pore, m
F_{dyn} = fluid dynamic force, N
F_{st} = surface tension force, N
g_o = gravitational constant ($9.81\ m/s^2$)
h_e = height of the empty cavity, m
h_p = height of the propellant, m
I_{sp} = specific impulse, s
I_{tot} = total impulse, s
k = Boltzmann's constant (1.38E-23 J/K)
m = molecular mass, kg
M = total mass of the satellite, kg
m_w = mass of the sloshing wave, kg
m_{prop} = mass of the propellant, kg
P_o = stagnation pressure, bar
P_{vap} = vapor pressure, bar
r_t = radius of the propellant tank, m
T_o = stagnation temperature, K
T_w = expansion-slot wall temperature, K
V_e = volume of the empty cavity, m^3
α = transmission probability
γ = surface tension of water, dyne/m
θ = contact angle, deg

I. Introduction

NANOSATELLITE missions are currently being conceived as a result of the development of micro- and nanotechnologies. The general agreement in the spacecraft community is that a nanosatellite represents a total system mass between 1 and 10 kg [1]. Nanosatellites impose significant limitations on the mass, power, and volume available for all subsystems, including propulsion [2]. The presence of such a propulsion system will allow orbit maintenance, pointing-angle adjustments, or formation repositioning. Figure 1 shows the thrust versus the maneuver time required for various pointing-angle adjustments. These slew maneuvers assume a 10-kg cylindrical nanosatellite of consistent density. The satellite was defined as consisting of 30% aluminum covering the structures, whereas the remainder of the satellite was silicon, based on the requirement for microelectromechanical system (MEMS) fabrication. The nanosatellite was assumed to be 14.50 cm in diameter and 24.92 cm in height, giving a moment of inertia about the spin axis of $0.0263\ kg \cdot m^2$. As seen in Fig. 1, thrusters can provide a 45-deg slew in 60 s at a thrust level of 0.3 mN. According to Janson et al. [3], a slew on the order of tens of seconds would be considered to be a relatively quick maneuver. Although propulsion systems can prove to be enabling for nanosatellite missions, many current systems are too massive and draw too much power for consideration on nanosatellites [2].

The free-molecule microresistojet (FMMR) was designed to meet the strict requirements of nanosatellites [4]. The FMMR exhibits many system features that are beneficial to nanosatellite operations, including low-pressure operation, low power consumption, low mass, and low propellant-storage volume. The FMMR's ability to operate on lower pressures permits the use of a propellant stored as either a liquid or solid at nominal storage temperatures. The storage density of the propellant is important to minimize the volume required for the propellant tanks. In this study, the performance of the FMMR with a liquid water propellant is of interest. Several factors were identified that make the use of water propellant beneficial to the

---

Presented as Paper 5185 at the AIAA 43rd Joint Propulsion Conference, Cincinnati, OH; received 24 May 2007; revision received 17 September 2007; accepted for publication 22 September 2007. This material is declared a work of the U.S. Government and is not subject to copyright protection in the United States. Copies of this paper may be made for personal or internal use, on condition that the copier pay the $10.00 per-copy fee to the Copyright Clearance Center, Inc., 222 Rosewood Drive, Danvers, MA 01923; include the code 0022-4650/08 $10.00 in correspondence with the CCC.

[*] Graduate Research Assistant, Astronautics and Space Technology Division. Student Member AIAA.

[†] Undergraduate Research Assistant, Department of Aerospace and Mechanical Engineering. Student Member AIAA.

[‡] Undergraduate Research Assistant, Astronautics and Space Technology Division. Student Member AIAA.

[§] Graduate Research Assistant, Department of Aerospace and Mechanical Engineering. Student Member AIAA.

[¶] Group Leader, Aerophysics Branch, Propulsion Directorate. Senior Member AIAA.

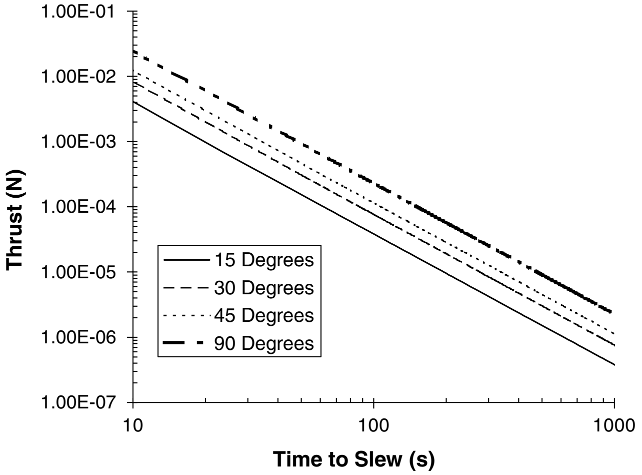

Fig. 1 Thrust versus maneuver time for a typical nanosatellite slew; the moment of inertia is 0.0236 $kg \cdot m^2$ and the radius is 0.0725 m.

FMMR system. First, water is stored as a liquid onboard the nanosatellite, with a relatively high storage density compared with gaseous propellants. Second, water has a relatively low molecular mass, which enhances the specific impulse for electrothermal thrusters. Third, water has a relatively high vapor pressure at typical nanosatellite on-orbit temperatures. The vapor pressure is sufficient to provide FMMR operating pressures without the need to prevaporize the liquid propellant. Finally, water's surface tension allows for phase separation with a hydrophobic microporous membrane, to insure that only gaseous propellant makes it to the FMMR plenum.

The FMMR consists of three main parts: the heater chip, the flow control, and the propellant storage. These parts are shown in Fig. 2 for an optimized nanosatellite propulsion system. The propellant gas arrives in the plenum after passing through a set of phase-separating filters and an actuating valve. The FMMR generates thrust by expelling the propellant gas in the plenum through a series of the expansion slots in the MEMS-fabricated heater chip.

Although the FMMR system illustrated in Fig. 2 is optimized for a nanosatellite, a technology demonstrator (TD) was fabricated using traditional and MEMS techniques. The TD is shown in Fig. 3. This system was designed to perform a spin maneuver on a university microsatellite [3]. Because the thrust requirement for the microsatellite was significantly larger than for a typical nanosatellite, the TD design was driven by factors not necessarily consistent with the FMMR concept. However, the FMMR was scalable and offered a reasonable propulsion system for the 25-kg-class satellite. The TD also offered a reduced cost of fabrication, easier performance testing of the system, and met all of the flight safety requirements for a payload flying on modern launch vehicles.

The FMMR heater chips for the optimized and TD systems are shown in Fig. 4. The TD heater chip is significantly larger, for the purpose of producing a larger thrust level. This shows the flexibility of the FMMR system for satellite design. By adding expansion slots and thus increasing the propellant mass flow, the FMMR system can be tuned to the thrust level required by a particular mission. The expansion-slot design also leads to a reduction in possible single-point failures over the expansion of the propellant through a traditional single-nozzle configuration. A high-pressure nozzle expansion, producing thrust comparable with FMMR, would be limited by a relatively small throat diameter. Plugging of the throat by a contaminant could lead to a failure; however, the plugging of a portion of a slot would still leave the remaining slot area available for thrust generation. A potential drawback of the expansion-slot design is the loss of propulsive efficiency over a contoured-nozzle design. However, a previous study showed that for low-Reynolds-number operation (consistent with the FMMR design), a nozzle does not offer a distinct enhancement in performance over a simple orifice or slot [5].

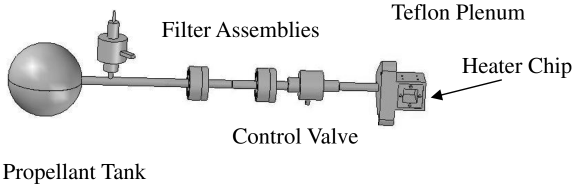

Fig. 2 Optimized nanosatellite FMMR propulsion system.

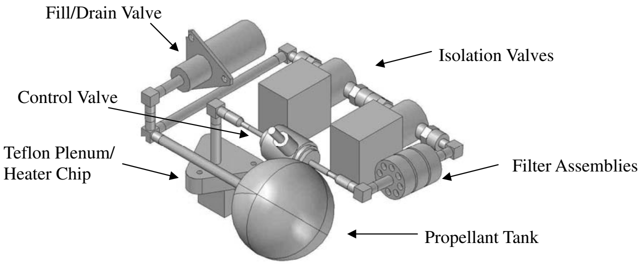

Fig. 3 Technology-demonstration FMMR (flight version).

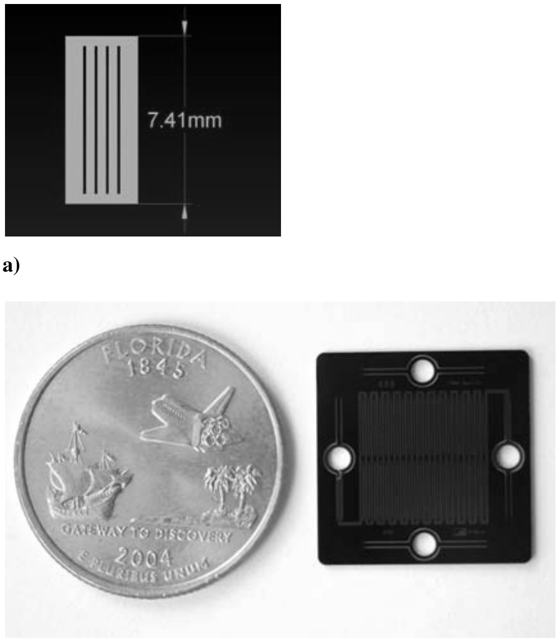

a)

b)

Fig. 4 Top view of the FMMR heater chip: a) optimized for a typical nanosatellite and b) technology-demonstration version.

II. System Configuration

Figure 3 shows the flight version of the technology-demonstration FMMR that was described in detail in [4]. The TD system consists of a stainless steel propellant tank, a service (fill/drain) valve, two one-time latching valves, a phase-separation housing, an actuating valve, and a Teflon plenum onto which the heater chip is mounted. The propellant tank is 63.11 mm in diameter, which is capable of holding 130 g of water propellant. The propellant tank has a burst pressure of 5.17 MPa, making it far heavier than a low-pressure FMMR system would actually require. The two latching valves are required for mechanical inhibits by the launch vehicle. The latching valves on the TD were selected for their low cost and relatively low power. For the optimized nanosatellite version, these valves could be replaced by one-time MEMS isolation valves described by Mueller et al. [6], which would significantly reduce the mass and volume used to inhibit the flow during the launch phase.

The TD phase-separation housing consists of two membranes, to insure only water vapor reaches the plenum and heater chip. Water propellant is restricted from flowing past the membranes by surface tension forces. Teflon microporous membranes are used due to their hydrophobic nature, with the pore size determined by the worst-case propellant tank operating pressure. Because of the high mass flow required for the TD, the phase-separation housing shown in Fig. 3 is relatively large. The distance between the actuating valve and the plenum in the TD led to the use of two microporous membranes. The second membrane reduces the possibility of water propellant condensing in the propellant feed system between the actuating valve and the plenum. In the optimized nanosatellite design, the housing size could be minimized with the use of a single membrane, due to the short distance expected between the housing and the plenum with a typical microvalve. The phase separator also serves as a filter system to remove particulates.

The TD actuating valve was selected because of its flight heritage and relatively low power consumption. As the only moving part during the flight demonstration phase, it was critical to have a component with flight heritage to increase the reliability of the overall propulsion system. For the optimized nanosatellite design, a microscale valve would be used, such as the piezoelectric valve described by Yang et al. [7] or the thermopneumatic valve described by Henning et al. [8]. Although the development of microvalves has been ongoing, suitable valves for micropropulsion systems remain elusive. For power-limited nanosatellites, low-power microvalves are required. In the particular case of low-pressure FMMR operation, microvalves with relatively large orifice diameters are required, complicating design. Although a notional optimized FMMR design can be conceived, a suitable microvalve has not been identified.

Teflon is the material of choice for the FMMR plenum, due to its inherently low thermal conductivity. In optimized designs, Pyrex plenums may be ideal, because the silicon heater chips can be directly bonded (anodically) to the plenum. For smaller heater chips resulting in lower-power operation than the TD, the heat transfer from the chip to the plenum could be reasonably reduced, making Pyrex more attractive. Initial results indicate that anodic bonding between a silicon heater chip and a Pyrex plenum for chip temperatures up to 700 K did not result in failure due to stresses formed by differential thermal expansion. Figure 4 shows the optimized FMMR heater chip. Note that the attachment holes for mechanical mating to the plenum on the TD version are removed as a result of the anodic bonding.

The operating characteristics of the TD and the optimized nanosatellite FMMR are given in Table 1. The power required for the heater chip in the optimized design was derived from area scaling of the measured TD values. Therefore, the estimates for the power to the optimized design are considered to be reasonably conservative. The system-preparation power shown in Table 1 indicates the necessity to actuate the one-time inhibit valves before general operation of the thruster can commence. For the TD, the two inhibit valves are actuated and latched in series, resulting in two separate system-preparation periods. These periods can be temporally spaced to meet driving satellite power requirements. The transient power required for the FMMR represents the initial power draw of the actuating valve and heater chip, which eventually reach (~20 ms for the valve and ~1 min for the heater chip) a steady-state power draw. Component masses for the TD and an optimized design are given in Table 2.

Table 1 FMMR operating characteristics

	System-preparation power, W	Transient power, W	Steady-state power, W
Technology demonstrator			
Inhibit valves	9	n/a	n/a
Actuating valve	n/a	4.36	1
Heater chip	n/a	5	3.2
Optimized nanosatellite design			
Inhibit valves	1	n/a	n/a
Actuating valve	n/a	<1	<1
Heater chip	n/a	1	0.22

Table 2 FMMR system mass

	TD mass, g	Optimized mass, g
Actuating control valve	130	<10
Fill/drain valve	150	<10
Inhibit valves (x2)	353	<20
Plenum, heater chip, mounting	87	35
Phase-separation system	110	35
Feed lines	92	5
Propellant tank	50	10
Propellant	90	90
Total	1062	175

III. Theory

A. FMMR Performance

The performance of the FMMR has been theoretically analyzed elsewhere as a free-molecule flow of the propellant through the expansion slots [4]. This previous study has shown that the measured specific impulse for the FMMR is generally 10–15% higher than the analytical predictions for gaseous propellants. The major reason for the difference is that the FMMR operating range is in the transitional flow regime and not in the free-molecule flow regime. Higher-pressure operation would lead to more efficient thruster operation, but this trend is counteracted by the propellant tank mass and the leak rate of available microvalves [9].

B. Propellant Slosh

The effect of slosh in a liquid propellant can be detrimental to a stabilized satellite. If the mass of the sloshing waves is too large, the satellite could begin to nutate. The mass of the sloshing waves is a function of the height of the propellant and the radius of the propellant tank. The volume of the empty portion of a spherical propellant tank is given by

$$V_e = \tfrac{1}{3}\pi h_e^2(3r_t + h_e) \tag{1}$$

where the resulting height of the propellant is

$$h_p = 2r_t - h_e \tag{2}$$

A correlation between h_p/r_t and m_w/M is found in [10]. For the parameters of the TD, the resulting mass of the sloshing waves before the burn maneuver and after half of the propellant has been used is 22.5 g for both cases. Even in the worst-case scenario in which the entire propellant is sloshing ($m_w = m_{\text{prop}}$), the mass of the sloshing wave is well below 1% of the total satellite mass for the TD mission. According to Bauer [11], the effect of the propellant slosh on satellite attitude should be minimal.

C. Propellant Phase Separation

Microporous membranes are used in the FMMR system to remove particulate contaminants and to achieve propellant phase separation. Water propellant is stored as a liquid in the propellant tank. The thruster operates by expanding water vapor through the expansion slots. Because nanosatellites are extremely power-limited, the power required to actively vaporize the liquid water propellant would be prohibitive. For the FMMR, phase separation is accomplished through surface tension forces between the liquid water propellant and a hydrophobic (nonwetting) porous material. The surface tension force is given by

$$F_{\text{st}} = \pi D_{\text{pore}}\gamma(T)\cos\theta \tag{3}$$

For a hydrophobic Teflon material, the contact angle is 110 deg [12].

The competing fluid dynamic force trying to force liquid water through the Teflon membrane is given by

$$F_{\text{dyn}} = P_{\text{vap}}(T)\left(\frac{\pi D_{\text{pore}}^2}{4}\right) \tag{4}$$

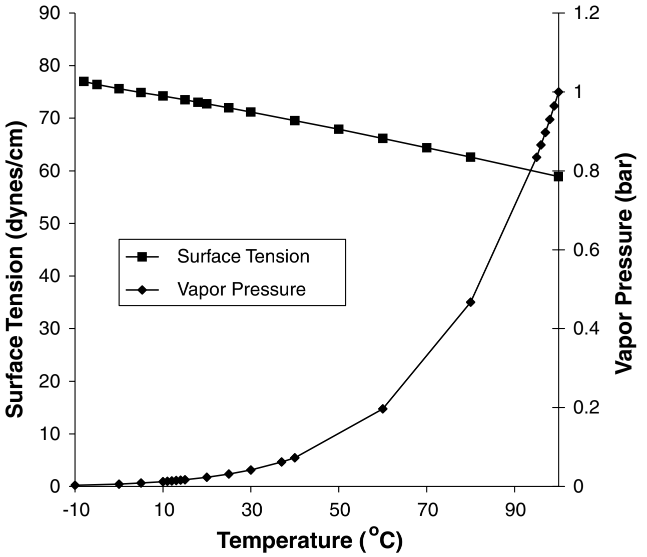

Fig. 5 Surface tension and vapor pressure of water as a function of temperature.

The pore size in the phase-separating Teflon membrane was determined from the worst-case pressure in the propellant tank. In this case, the design requirement is for the microporous membrane to restrict the liquid water from passing through the membrane, or $F_{\mathrm{st}} \geq F_{\mathrm{dyn}}$. Therefore,

$$D_{\mathrm{pore}} \leq \left| \frac{4\gamma(T)\cos\theta}{P_{\mathrm{vap}}(T)} \right| \tag{5}$$

The surface tension and vapor pressure of water as a function of temperature is shown in Fig. 5 [13]. From the worst-case scenario from the TD mission ($T = 30°\mathrm{C}$), D_{pore} from Eq. (5) should be less than or equal to 23.3 μm. For the design of the actual TD, the pore size was selected to be 1 μm, due to its ready availability.

Evaporative cooling could lead to the propellant menisci freezing in the micropores. The current TD does not have active heating of the propellant tank, feed lines, or phase-separation system. Instead, integration control has placed the phase-separating membranes in an area in which waste heat exists from nearby electronic components. Although the availability of waste heat is not a strict requirement for the TD or any future versions of the FMMR system, advantage is taken of its availability for critical components such as the phase-separation system.

IV. Experimental Setup

The propulsive characteristics of the FMMR were measured using the nano-Newton thrust stand (nNTS) with an electrostatic comb calibration system, described in detail elsewhere [14,15]. The operation of the nNTS was performed in chamber-IV of the Collaborative High-Altitude Flow Facility (CHAFF-IV) at the University of Southern California. CHAFF-IV was capable of maintaining background pressures below 10^{-5} torr throughout the range of experiments performed in this study. Maintaining low background pressure was critical in obtaining accurate thrust measurements [16].

For the thrust measurements involving water, propellant was fed from a chilled vacuum-insulated container that brought the propellant to a stable temperature of approximately 0°C, corresponding to a stable vapor pressure of approximately 4.6 torr. Standard Venturi mass flow meters did not produce accurate results for the relatively low water vapor flow rates investigated here. The mass flow of the propellant was instead determined from recorded stagnation pressures in the plenum over the flow period and extrapolating a mass flow. From the theoretical model [4], we can take the mass flow to be the time rate of change of the mass of the propellant, which yields

$$\frac{\mathrm{d}m_p}{\mathrm{d}t} = \alpha P_0 \sqrt{\frac{M}{2\pi k T_0}} A_s \tag{6}$$

For a given temperature, the right-hand side of the equation is directly proportional to the pressure. The integration of both sides of Eq. (6) over the time of the trace gives a relation for the total mass loss and the plenum pressure:

$$\Delta m_p|_o^t = C \int_0^t P_0 \,\mathrm{d}t \tag{7}$$

where C is the constant defined as

$$C = \alpha \sqrt{\frac{M}{2\pi k T_0}} A_s \tag{8}$$

Because the transmission probability a is not known a priori, the value of C must be found experimentally. The constant C can be experimentally determined though Eq. (7) by measuring the total mass loss of the propellant over a specified time and dividing by the integral of the pressure in the plenum over that time. The experimental setup for determining C consisted of connecting a sealable 2-cm-diam bulb of liquid water to the FMMR plenum. A valve between the bulb and the plenum was opened for a time period of several hours. As the water vapor flowed to the plenum, it caused both an aggregate loss of fluid in the bulb and a measurable pressure in the plenum. The mass change in the bulb was measured with a precision of ± 0.1 mg. The pressure in the plenum was also recorded to measure its variation as a function of time. The time-integral of the plenum pressure was approximated using a standard trapezoidal Riemann sum over all of the data, and this integral was compared against the associated mass loss for each trace to determine the constant C. Once C is determined, the specific impulse is found through

$$I_{\mathrm{sp}} = \frac{I_{\mathrm{tot}}}{g_0 C \int_0^t P_0 \,\mathrm{d}t} \tag{9}$$

The experimental setup for thrust testing was such that P_o could not be directly recorded simultaneously with thrust, due to the movement of the nNTS. However, rigorous testing proved that for a given T_o, a proportional relationship exists between P_o and the pressure recorded upstream from the plenum, P_1. This relationship was experimentally established using a static plenum at a nominal chip temperature $T_o = 300$ K. It was experimentally determined that at a constant position upstream of the plenum, P_1 was only dependent on the mass flow through the system and not on T_o.

The burst-pressure characteristics of the Teflon phase-separating membranes were tested by placing the filter in a housing with liquid water on one side and atmosphere on the other. The liquid water column was pressurized as each membrane was tested to failure, a condition that was defined and observed when a single drop of liquid water was forced through the membrane. If liquid water were to bypass the membrane, it would likely freeze in the feed system or in the heater-chip expansion slots, causing unpredictable and uncontrollable thrust as it sublimated.

V. Results and Discussion

As mentioned earlier, the current version of the FMMR was designed for technology demonstration on a university micro-satellite. As such, it was critical to fully characterize its performance using water propellant, which will be used on the mission. These results were also applied to the optimized nanosatellite FMMR design to lend some basis for the estimation of thermal and propulsive characteristics. To establish that the FMMR design meets both the transient and steady-state power requirements for the proposed technology-demonstration mission, experiments were performed to measure thermal characteristics of the heater chip and plenum assembly. The heater-chip temperature is shown in Fig. 6 as a function of the input power. The data were taken for a propellant flow

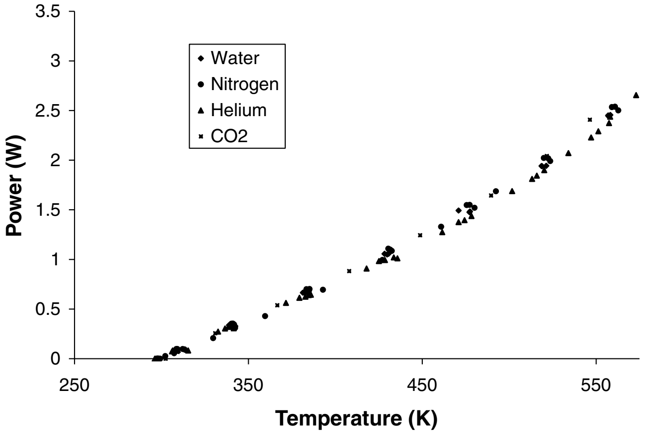

Fig. 6 Input power versus heater-chip temperature.

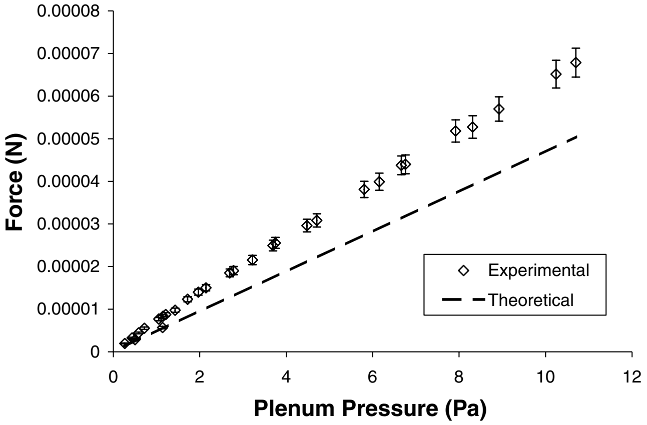

Fig. 7 Experimental and theoretical thrust as a function of H_2O pressure.

rate of 10 sccm (the mass flow expected in orbit) using various propellants. As shown in Fig. 6, the power requirement for the FMMR heater chip is fairly independent of the propellant being used.

Figure 7 shows the experimental and theoretical thrust versus the plenum pressure. As Fig. 7 indicates, the experimental thrust trends toward the theory line at low pressure. As stated in [4], the theory developed assumes free-molecule flow with $Kn \gg 1$. For the pressure and temperature range in Fig. 7, the water Knudsen number ranges from 1 to 0.3, based on the stagnation number density and expansion-slot width. This is classified as the transitional flow regime [17] for which there is no analytical solution. The low Knudsen numbers imply that the FMMR flows for these conditions are not free-molecular and that there are a significant number of collisions between propellant molecules. As the FMMR plenum pressure increases, a continuum flow regime is approached ($Kn \ll 1$) and the transport of momentum through the expansion slots is expected to become more efficient [5]. The optimum performance of the FMMR is a trade between higher efficiency at higher operating pressure and the systems complications that high pressure entails. High pressures in the propulsion system could lead to the complications of massive propellant tanks, high power vaporization of the propellant, or MEMS valve leakage [9].

Figure 8 shows the thrust of the FMMR using water as a function of the heater-chip temperature T_w for a constant mass flow rate of 1.72×10^{-7} kg/s (14-sccm flow rate). From the theoretical model, the relationship between thrust and the heater-chip temperature is expected to vary as $\sqrt{T_w}$, which is consistent for the water propellant data. Figure 9 shows the total water propellant mass used as a function of the integral of the plenum pressure with time. The slope of the line in Fig. 9 gives the constant $C = 1.062 \times 10^{-8}$ [Eq. (7)]. Figure 10 shows the specific impulse as a function of heater-chip temperature T_w for various propellants. As with higher-pressure

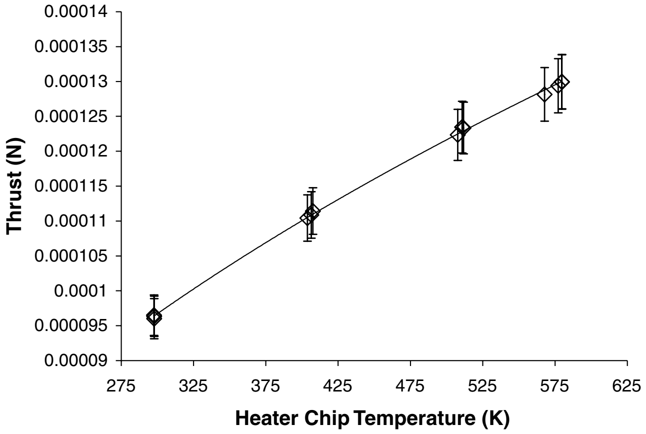

Fig. 8 Thrust versus heater-chip temperature for H_2O propellant.

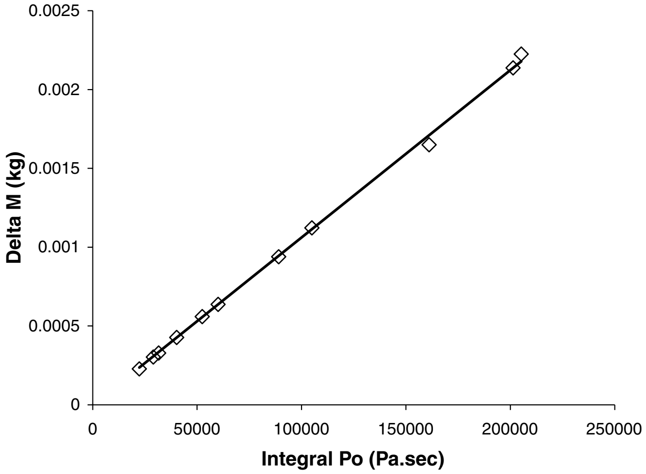

Fig. 9 Mass used as a function of the integral of plenum pressure with time.

propulsion systems, the free-molecule theoretical model also predicts the specific impulse to vary as $\sqrt{T_w/m}$.

As shown in Fig. 10, the specific impulse for water lies between the data for helium and nitrogen, as expected for the entire range of heater-chip temperatures. At the operating heater-chip temperature expected for the TD ($T_w = 580$ K), the specific impulse was measured to be 79.2 s. The results in Fig. 8 indicate that some level of thrust control can be obtained by varying the heater-chip temperature. However, the heater-chip temperature is obviously tied to the propulsion system power, as shown in Fig. 6, and

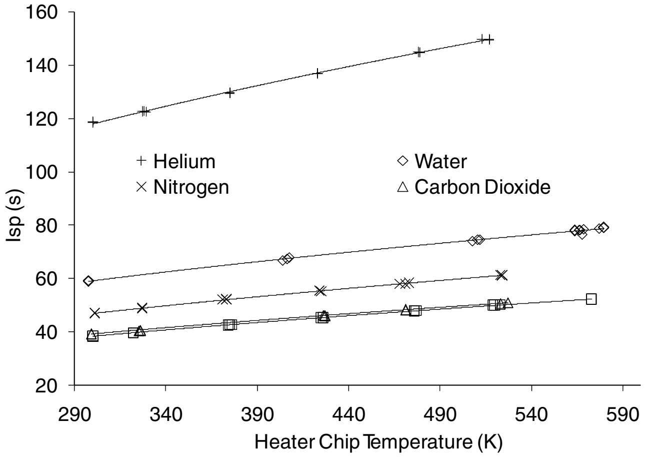

Fig. 10 Specific impulse versus heater-chip temperature.

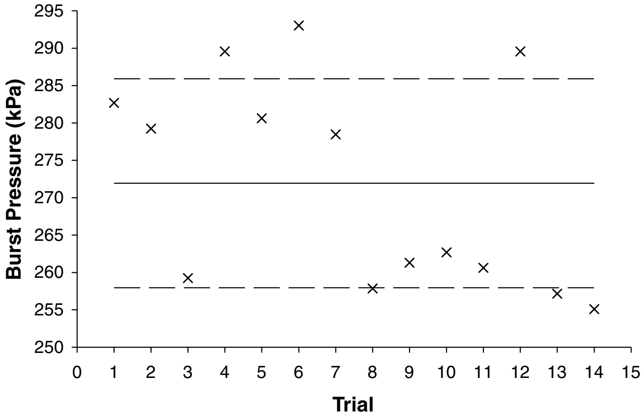

Fig. 11 Burst-pressure test results for phase-separating membranes.

temperature variations can impact the propulsion system power by several watts. In addition, the heater-chip temperature is also tied to the overall specific impulse, as shown in Fig. 10. Reduced-temperature operation to reduce the thrust produced can lead to a lower specific impulse and potentially lower thruster efficiencies.

The results of several burst tests on the phase-separating membranes are shown in Fig. 11. The average pressure that induced a membrane failure was 272 kPa. Considering the internal temperature of a typical nanosatellite, the vapor pressure of a water propellant could reach as high as 13.5 kPa, giving a factor of safety of almost 20. Phase-separating membranes with a larger pore diameter could lead to an increase in the membrane open area, increasing the maximum flow rate through the membrane.

The TD FMMR was designed to meet the requirements of a relatively high-mass nanosatellite. To show utility in the technology demonstration, a relatively large thrust was required to spin up the nanosatellite within a time period acceptable to the overall mission architecture. The large thrust level and required secondary payload safety requirements drove the design and efficiency of the propulsion system. The technology demonstration has several success criteria, including the successful operation of the MEMS-fabricated heater-chip, demonstration of the phase-separating membranes, and demonstration of a thrust level capable of spinning up the nanosatellite. The success criteria drove the use of commercial-off-the-shelf (COTS) valves due to reliability issues and a lack of flight heritage associated with microvalves. The use of COTS valves dramatically increased the propulsion system's mass and power requirements. Future designs capable of propulsive efficiencies on the order of 30% have been envisioned and are shown as the optimum design in Table 1 and Figs. 2 and 4. These future designs include MEMS-fabricated valves and system integration consistent with MEMS fabrication techniques.

VI. Conclusions

For propulsion, the limited resources of a typical nanosatellite result in a trade between the desired performance (thrust and specific impulse) and the required power. This trade space was experimentally investigated for the FMMR using a typical nanosatellite design, and the system can provide a 45-deg slew in 60 s, a time considered to be reasonably fast for nanosatellite maneuvers. Additionally, the technology-demonstration FMMR was fully characterized in this study using water as a propellant. The data obtained from the experiments adhere reasonably well to theory. At the current operating temperature and pressure, the TD produces 129 μN with a specific impulse of 79.2 s. The mass of sloshing waves in the propellant is well below the value considered to be detrimental to the stability of a stabilized satellite. For the TD FMMR, a phase-separating membrane was needed to ensure that the water propellant reaches the plenum in the gaseous phase. The burst pressure of the phase-separating membranes is well above the normal operating pressure of the thruster, resulting in a factor of safety of approximately 20.

Acknowledgments

This work was supported by the Propulsion Directorate of the U.S. Air Force Research Laboratory at Edwards Air Force Base. The authors wish to thank Mike Huggins and Ingrid Wysong for their continued support. The authors are also indebted to Stephen Vargo for his efforts in assisting with the design and fabrication of the free-molecule-microresistojet heater chip.

References

[1] Ketsdever, A., "System Considerations and Design Options for Microspacecraft Propulsion Systems," *Micropropulsion for Small Spacecraft*, edited by M. Micci and A. Ketsdever, Progress in Astronautics and Aeronautics, Vol. 187, AIAA, Reston, VA, 2000, pp. 139–163.

[2] Mueller, J., "Thruster Options for Microspacecraft: A Review and Evaluation of State-of-the-Art and Emerging Technologies," *Micropropulsion for Small Spacecraft*, edited by M. Micci and A. Ketsdever, Progress in Astronautics and Aeronautics, Vol. 187, AIAA, Reston, VA, 2000, pp. 45–137.

[3] Janson, S., Helvajian, H., Hansen, W., and Lodmell, J., "Microthrusters for Nanosatellites," *The Second International Conference on Integrated Micro Nanotechnology for Space Applications (MNT99)*, The Aerospace Corp., El Segundo, CA, Apr. 1999.

[4] Ketsdever, A., Lee, R., and Lilly, T., "Performance Testing of a Microfabricated Propulsion System for Nanosatellite Applications," *Journal of Micromechanics and Microengineering*, Vol. 15, No. 12, 2005, pp. 2254–2263.
doi:10.1088/0960-1317/15/12/007

[5] Ketsdever, A., Clabough, M., Gimelshein, S., and Alexeenko, A., "Experimental and Numerical Determination of Micropropulsion Device Efficiencies at Low Reynolds Number," *AIAA Journal*, Vol. 43, No. 3, 2005, pp. 633–641.

[6] Mueller, J., Vargo, S., Green, A., Bame, D., Orens, R., and Roe, L., "Development of a Micro-Isolation Valve: Minimum Energy Requirements, Repeatability of Actuation, and Preliminary Studies of Debris Generation," 36th Joint Propulsion Conference, Huntsville, AL, AIAA Paper 2000-3675, 2000.

[7] Yang, E., Rohatgi, N., and Wild, L., "A Piezoelectric Microvalve for Micropropulsion," NanoTech 2002 Conference, Houston, TX, AIAA Paper 2002-5713, Sept. 2002.

[8] Henning, A. K., Fitch, J., Hopkins, D., Lilly, L., Faeth, R., Falsken, E., and Zdeblick, M., "A Thermopneumatically Actuated Microvalve for Liquid Expansion and Proportional Control," *Solid State Sensors and Actuators*, Vol. 2, Inst. of Electrical and Electronics Engineers, Piscataway, NJ, June 1997, pp. 825–828.

[9] Ketsdever, A., Wadsworth, D., and Muntz, E. P., "Predicted Performance and Systems Analysis of the Free Molecule Micro-Resistojet," *Micropropulsion for Small Spacecraft*, edited by M. Micci and A. Ketsdever, AIAA Progress in Astronautics and Aeronautics, Vol. 187, AIAA, Reston, VA, 2000, pp. 167–183.

[10] Barter, N. J. (ed.), *TRW Space Data*, 5th ed., TRW Space and Electronics Group, Redondo Beach, CA, 1999.

[11] Bauer, H. F., "Fluid Oscillations in the Containers of a Space Vehicle and Their Influence Upon Stability," NASA TR-R-187, Feb. 1964.

[12] O'Brien, W. J., "Capillary Penetration of Liquids Between Dissimilar Solids," Ph.D. Dissertation, Univ. of Michigan, Ann Arbor, MI, Univ. Microfilm No. 6715666, 1967.

[13] Lide, D. R. (ed.), *Handbook of Chemistry and Physics*, 78th ed., CRC Press, Boca Raton, FL, 1997, pp. 6–3.

[14] Jamison, A., Ketsdever, A., and Muntz, E. P., "Gas Dynamic Calibration of a Nano-Newton Thrust Stand," *Review of Scientific Instruments*, Vol. 73, No. 10, 2002, pp. 3629–3637.
doi:10.1063/1.1505096

[15] Selden, N., and Ketsdever, A., "Comparison of Force Balance Calibration Techniques for the Nano-Newton Range," *Review of Scientific Instruments*, Vol. 74, No. 12, 2003, pp. 5249–5254.
doi:10.1063/1.1623628

[16] Ketsdever, A., "Facility Effects on Performance Measurements of Micropropulsion Systems that Utilize Gas Expansion," *Journal of Propulsion and Power*, Vol. 18, No. 4, 2002, pp. 797–804.

[17] Bird, G. A., *Molecular Gas Dynamics and the Direct Simulation of Gas Flows*, Oxford Univ. Press, Oxford, 1994.

D. Spencer
Associate Editor

AIP | Physics of Fluids

Numerical and experimental investigation of microchannel flows with rough surfaces

T. C. Lilly, J. A. Duncan, S. L. Nothnagel, S. F. Gimelshein, N. E. Gimelshein et al.

Citation: Phys. Fluids **19**, 106101 (2007); doi: 10.1063/1.2775977

View online: http://dx.doi.org/10.1063/1.2775977

View Table of Contents: http://pof.aip.org/resource/1/PHFLE6/v19/i10

Published by the American Institute of Physics.

Related Articles

Localized non-contact manipulation using artificial bacterial flagella
Appl. Phys. Lett. 99, 174101 (2011)

Irreversibility and pinching in deterministic particle separation
Appl. Phys. Lett. 99, 064102 (2011)

Influence of nanoparticles on the dynamics of miscible Hele-Shaw flows
J. Appl. Phys. 109, 104907 (2011)

Controlling droplet incubation using close-packed plug flow
Biomicrofluidics 5, 024101 (2011)

Syringe-vacuum microfluidics: A portable technique to create monodisperse emulsions
Biomicrofluidics 5, 014107 (2011)

Additional information on Phys. Fluids

Journal Homepage: http://pof.aip.org/

Journal Information: http://pof.aip.org/about/about_the_journal

Top downloads: http://pof.aip.org/features/most_downloaded

Information for Authors: http://pof.aip.org/authors

ADVERTISEMENT

Running in Circles Looking
for the Best Science Job?
Search hundreds of exciting
new jobs each month!
http://careers.physicstoday.org/jobs
physicstoday JOBS

PHYSICS OF FLUIDS **19**, 106101 (2007)

Numerical and experimental investigation of microchannel flows with rough surfaces

T. C. Lilly,[a] J. A. Duncan, and S. L. Nothnagel
Department of Aerospace and Mechanical Engineering, University of Southern California, Los Angeles, California 90089, USA

S. F. Gimelshein and N. E. Gimelshein
ERC Inc., Edwards Air Force Base, California 93524, USA

A. D. Ketsdever and I. J. Wysong
Air Force Research Laboratory, Propulsion Directorate, Edwards Air Force Base, California 93524, USA

(Received 26 March 2007; accepted 31 July 2007; published online 4 October 2007)

A conical surface roughness model applicable to particle simulations has been developed. The model has been experimentally validated for channel flows using helium and nitrogen gases at Reynolds numbers from 0.01 to 10 based on inlet conditions. To efficiently simulate gas-surface interaction, molecular collisions with the actual rough surface are simulated by collisions with a randomly positioned conical hole having a fixed opening angle. This model requires only one surface parameter, average surface roughness angle. This model has also been linked to the Cercignani-Lampis scattering kernel as a required reference for use in deterministic kinetic solvers. Experiments were conducted on transitional flows through a 150 μm tall, 1 cm wide, 1.5 cm long microchannel where the mean free path is on the order of the roughness size. The channel walls were made of silicon with: (i) polished smooth surfaces, (ii) regular triangular roughness, and (iii) regular square roughness with characteristic roughness scales of <1 μm, 11 μm, and 29 μm, respectively. For the triangular roughness, mass flow reductions ranged from 6% at the higher stagnation pressures tested to 25% at the lower stagnation pressures tested when compared to the smooth channel. © *2007 American Institute of Physics*. [DOI: 10.1063/1.2775977]

I. INTRODUCTION

Surface structure and roughness plays a role, to some extent, in all flow-surface interactions regardless of speed or scale. Traditionally, surface roughness is considered important in low speed microflows, where the surface to volume ratio is large and boundary conditions dominate the flow.[1] Since the first report was published, almost a century ago,[2] a substantial amount of research on the impact of surface roughness on gas flows in ducts has been accomplished. For instance, the mass flow degradation due to surface roughness was shown numerically and experimentally by Davis *et al.*[3] More recently, significant effect of surface roughness on pressure and heat transfer in circular tubes and channels was demonstrated experimentally in Mala and Li[4] and Kandikar *et al.*[5] In the experiments by Turner *et al.*[6] however, the surface roughness was found to have a small effect on gas pressures inside a channel for several pressure ratios. In addition to low speed flows, surface roughness has been seen to cause a noticeable impact on some high-speed flows, such as micronozzle expansions.[7]

The applicability of continuum numerical approaches, such as those based on the solution of Navier-Stokes equations,[8] is limited for flows where the roughness size is smaller than the gas mean free path. There has been work recently on slip conditions which overcome this limitation.[9] In most of the aforementioned applications, the characteristic roughness size is smaller than 1 μm, and is usually on the order of or smaller than the gas mean free path. Being essentially a kinetic effect, the interaction of gas molecules with such small surface roughness requires a kinetic numerical approach in order to properly address the gas-surface interaction at the level of molecular velocity distribution functions. Kinetic modeling of surface roughness effects[10] is hindered by a number of problems, from the accurate representation of complex shapes and roughness patterns to difficulties of experimental validation.

The former has been approached by a number of models, different in their numerical complexity and physical accuracy. Among the simplified models are the Cercignani-Lampis (CL) kernel[11,12] and cone model.[13,14] In the CL model, rough surfaces may be simulated by specifying the tangential accommodation coefficient α_t larger than unity.[15] A similar idea was applied by Ketsdever *et al.*[16] where an antispecular reflection was introduced. In that model, a fixed fraction of molecules, α, is reflected so that the reflected normal and tangential momentum is the same magnitude as the incoming, but with opposite directions. The models[11,16] are easy to implement and may be used with particle as well as deterministic kinetic solvers, but they do not have a clear correlation between the parameters of the models and the physical properties of the rough surface. This drawback was overcome for particle simulations in the cone models[13,14]

---

[a] Author to whom correspondence should be addressed: 854 West 36th Pl. RRB 101, Los Angeles, California 90089. Telephone: 213-740-1635. Fax: 213-740-7774. Electronic mail: tlilly@usc.edu

1070-6631/2007/19(10)/106101/9/$23.00

© 2007 American Institute of Physics

where the surface is either represented by a number of virtual cones or precomputed distribution functions are used at the processing stage. These models refer to the actual average angle of the rough surface, although it is hard to use a prescribed angular distribution, and a special cut-off has to be used limiting the number of cones. Another approach is to explicitly specify the rough surface as a set of randomized or regular structures.[17] While this is a reasonable approach for simple geometries, it may be difficult to use for complex, especially three-dimensional, surfaces and roughness structure. Among the more sophisticated, although difficult to implement, roughness models is the fractal model[18,19] and an analytic model.[20]

The experimental validation of rough surface models is hampered by requirements of high precision and small scale, both of which increase the difficulty of experimental measurements, as well as the superposition of different physical effects.[21] Examples of related work on surface roughness are[15] where flow rates through short channels were measured and calculated with a Monte Carlo method, and,[22] where triangular roughness in channel flows was studied numerically and experimentally for large Knudsen numbers. Adding to the difficulty of numerical validation is the complexity of relating the measured macroparameters to the microphenomenon of interest to the investigation. Although changes in macroparameters, such as pressure distribution and mass flow, can be affected by changes in microparameters, such as accommodation coefficient, these macroparameters do not necessarily indicate specific reasons for the change in accommodation. Changes in angle of incidence,[23] gas temperature, surface temperature, surface material, and surface cleanliness can all lead to changes in accommodation. To complicate matters, these parameters can be difficult to quantify experimentally. In addition to the change in accommodation due to the surface, a long microchannel flow may be affected by variation of accommodation with local gas pressure. In most cases, the probability of surface sticking/accommodation decreases as the availability of surface sites decrease. Lundstrom[24] observed the surprising result that Knudsen flow diffusion increased with backing pressure. This was hypothesized to be due to the variation in sticking with local gas density and the tendency of molecules to scatter more specularly off an absorbed wall gas than off the surface.

This study consists of a numerical investigation and experimental validation of the effects of surface roughness. Specifically, the scope will be limited to two-dimensional helium and nitrogen microchannel flows with well-characterized surface roughness. These flows will be in the low Reynolds number regime, based on entrance conditions, with surface rarefaction from near free molecular to near continuum, based on surface roughness. A simple model of the surface roughness that maintains the detailed balance and is applicable to the direct simulation Monte Carlo (DSMC) method has been developed, and its connection to the Cercignani-Lampis scattering kernel is established. This new model is more efficient in both setup cost and simulation time than the direct representation of the physical geometry. It does not exhibit the shortcomings seen in previous simple surface roughness models while being versatile enough to incorporate either an average surface angle or a distribution of surface angles, as well as arbitrary roughness coverage.

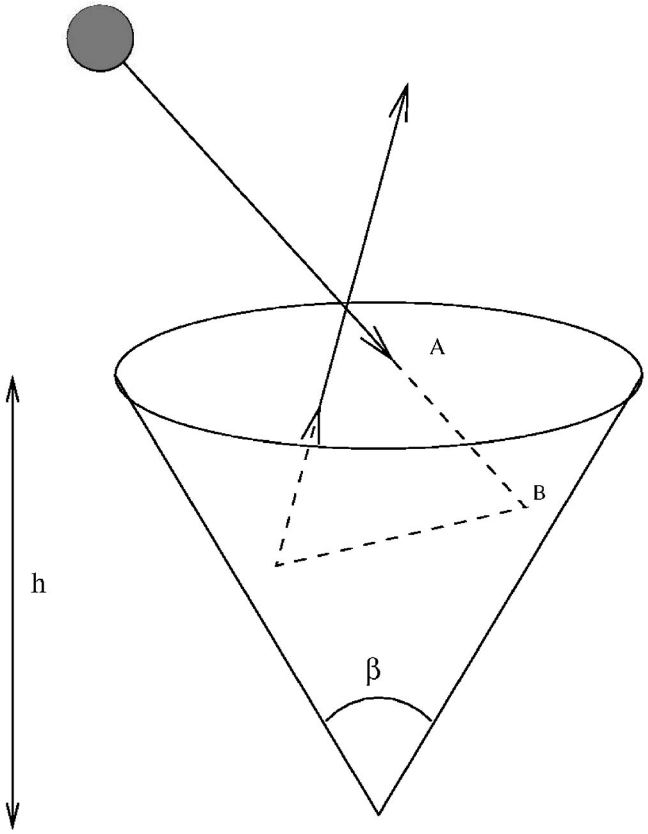

FIG. 1. Schematic of new conical model reflection algorithm.

II. NUMERICAL APPROACH

A. Conical model

Molecular collisions with a rough surface can be separated into two stages: (1) a molecule strikes the wall at a particular point and (2) the molecule experiences one or more collisions with the surface roughness feature before leaving the surface. When the characteristic roughness size is significantly less than the mean free path of the gas, no intermolecular collisions occur during the second stage. The time taken for this stage is much smaller than the mean collision time, and the distance traveled is on the order of the roughness size. Therefore, for numerical simulation, the time and distance can be ignored and it is sufficient to specify only the reflected velocity of the molecule after the collision.

To represent this two-stage process in an efficient, yet representative way, a conical model is used to select the reflected velocity of the collided molecule. At the point of collision, the rough surface is represented as a randomly positioned virtual conical hole with fixed opening angle β and height h. The molecule is assumed to enter the cone through the base at point A, as seen in Fig. 1. The collision point for the molecule and the cone wall is then calculated at point B. Here the molecule's reflected velocity is selected assuming a diffuse reflection, although a different reflection model can be used. The process of calculating subsequent collision

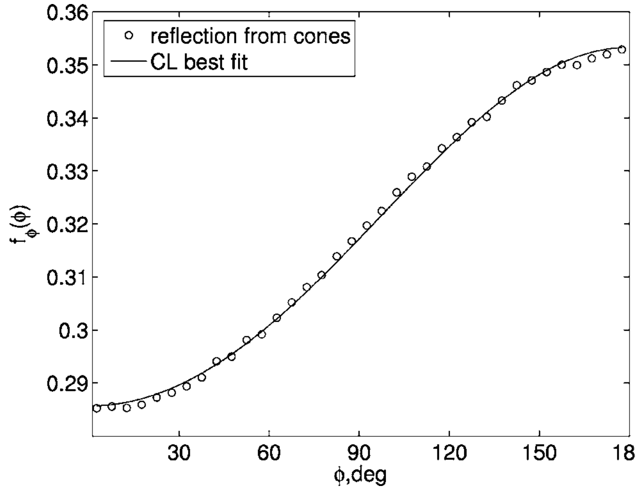

FIG. 2. Distribution function of the angle between the reflected tangential velocity and the flow direction, $M=0.3$, $\beta=66°$.

points and determining postcollision velocities is continued until the molecule leaves the cone. The point of origin for the reflected molecule is assumed to be the same as the incoming point of collision; all movement in the virtual cone is only a means for determining the reflected velocity of the colliding molecule. Therefore, the actual value of h is not important (e.g., $h=1$ m can be used). In this algorithm, there are no uncertainties associated with cutoff for very long traveling distances such as those in Ref. 13. Due to surface shape simplification, this algorithm requires only one parameter, the average surface slope (represented as the cone angle β), making it easy to implement in DSMC.

To study the influence of a rough wall, represented by the conical model, on flow properties, examine how the velocity distribution of incident molecules is transformed by collisions with the wall. Consider a distribution of incoming molecules from an equilibrium flow characterized by a Mach number M and directed along the x-axis, assuming the rough surface to be in the xy plane. This scenario has been simulated using the algorithm described above and the distribution of the angle, φ, between the reflected tangential molecular velocity and the flow direction is plotted in Fig. 2. Note that the maximum of the distribution corresponds to the direction opposite to the flow, which is generally expected to increase flow resistance.

Verification for the conical surface model has been performed for a two-dimensional thermal bath to assure adherence to detailed balance. The thermal bath constituted helium gas initially heated to 1000 K within a 2D box with a surface temperature of 300 K. Gas-surface collisions were simulated by the conical roughness model with a cone angle of $\beta=45°$. The temperature relaxation time inside the test box is illustrated in Fig. 3 for a cross section along the centerline. As particles collide with the surface, the temperature decreases from its initial value to the equilibrium value of 300 K. By coming to a stable equilibrium, the simulation proves adherence to the detailed principle.

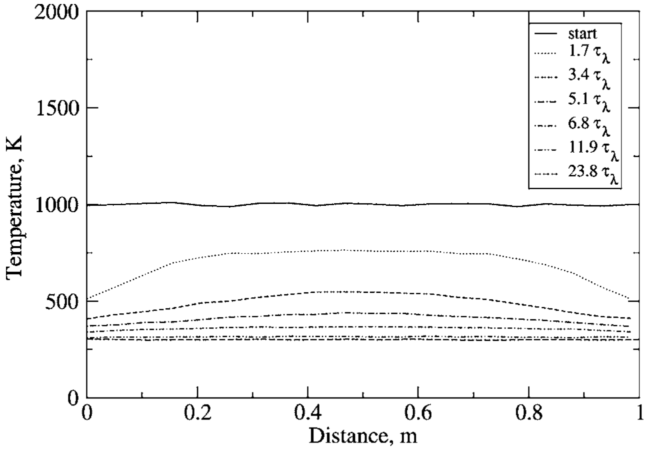

FIG. 3. Thermal relaxation of helium in a 300 K box. Time is in mean collision times, τ_λ, at 1000 K.

B. Cercignani-Lampis scattering kernel

The above stated cone model technique is valuable for particle simulations, but does not have a direct applicability in deterministic kinetic solvers since it is based on individual particle velocities and not on distribution functions. It is reasonable to establish a connection between the conical model and a kernel that is directly applicable to a kinetic solver. One such kernel, the Cercignani-Lampis (CL) (Refs. 11 and 25) scattering kernel, can be used in kinetic solvers but lacks correlation between the physical surface and the main input parameter for the kernel. The conical surface model can be used to relate this parameter, the tangential momentum accommodation coefficient α_t, to an average surface roughness angle.

To facilitate this relation it is necessary to create an analytic expression for the distribution of φ as a function of α_t. Assuming the temperature of the gas and the wall are equal and velocities are normalized by $\sqrt{m/kT}$, the distribution functions of x and y velocity components of incident molecules are

$$f_x^{\mathrm{inc}}(v)=\frac{1}{\sqrt{2\pi}}\exp(-(v-M\sqrt{\gamma})^2/2), \tag{1}$$

$$f_y^{\mathrm{inc}}(v)=\frac{1}{\sqrt{2\pi}}\exp(-v^2/2), \tag{2}$$

respectively. After the CL transformation, the x component of the reflected velocity is equal to

$$v_x^{\mathrm{refl}}=\frac{1-\alpha_t}{\sqrt{1-\alpha_t}}v_x^{\mathrm{inc}}+v_x^{\mathrm{CL}}, \tag{3}$$

where the distribution function of v_x^{CL} is given by

$$f_x^{\mathrm{CL}}(v)=\frac{1}{\sqrt{2\pi(1-|1-\alpha_t|)}}\exp\left(-\frac{v^2}{2\pi(1-|1-\alpha_t|)}\right). \tag{4}$$

Here, α_t is the CL parameter that corresponds to the tangential accommodation coefficient, $0\leq\alpha_t\leq 2$. $\alpha_t=1$ corresponds to zero average tangential momentum relative to the surface; the larger the deviation between α_t and unity, the larger the

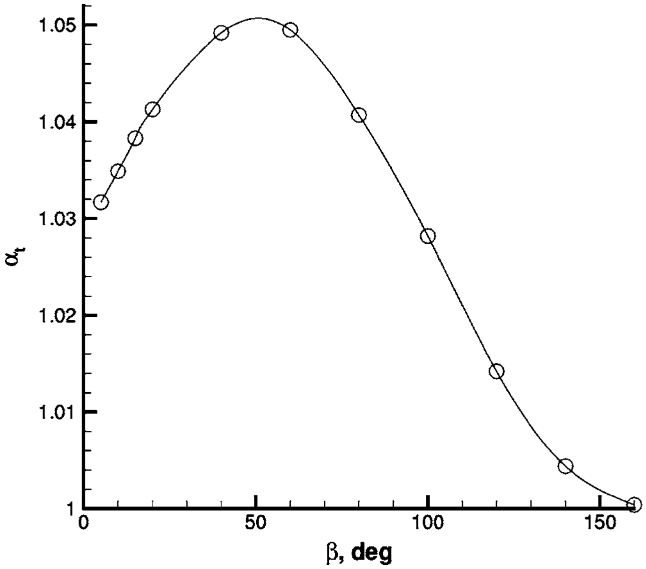

FIG. 4. Tangential momentum accommodation coefficient, α_t, as a function of cone opening angle β, for $M=0.3$.

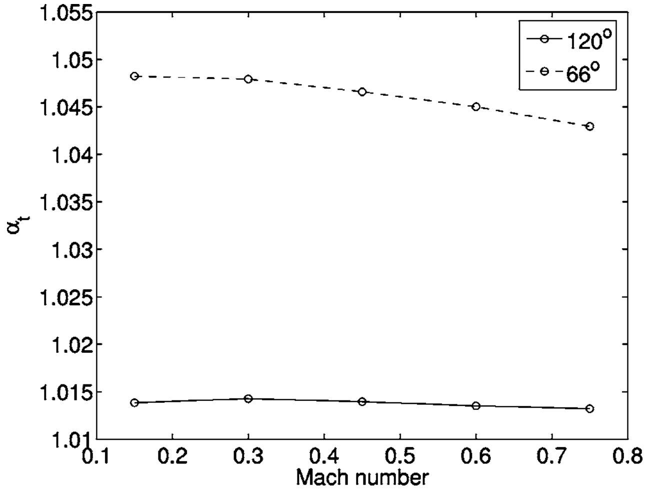

FIG. 5. Tangential momentum accommodation coefficient, α_t as a function of Mach number for two cone opening angles.

average momentum of the reflected molecules. Note that v_x^{refl} is the sum of the two independent normally distributed components, therefore, its distribution function can be written as

$$f(v_x^{\text{refl}}) = \frac{1}{2\pi}\exp\left(-\left(v_x^{\text{refl}} - M\sqrt{\gamma}\frac{1-\alpha_t}{\sqrt{|1-\alpha_t|}}\right)^2\right). \tag{5}$$

The distribution function of the y velocity component does not change during the CL transformation. Note that $\tan(\phi) = |v_y^{\text{refl}}|/v_x^{\text{refl}}$, so for $0<\phi<\pi/2$ the distribution function of ϕ can be obtained with

$$f(\tan\phi) = \int_0^{\infty} u_x f_x^{\text{refl}}(u_x) f_y^{\text{refl}}(u_x\tan\phi)\,du_x, \tag{6}$$

and for $\pi/2<\phi<\pi$

$$f(\tan\phi) = -\int_{-\infty}^{0} u_x f_x^{\text{refl}}(u_x) f_y^{\text{refl}}(u_x\tan\phi)\,du_x. \tag{7}$$

Finally, the reflected velocity distribution function can be written

$$f_\phi(\phi) = 2f(\tan\phi)(1+\tan^2\phi) \tag{8}$$

or

$$f_\phi(\phi) = \frac{e^{-t^2}}{\pi} + \frac{t\cos\phi}{\sqrt{\pi}}\exp(-t^2\sin^2\phi)(1+\operatorname{erf}(t\cos\phi)), \tag{9}$$

where $t=M\sqrt{\gamma}(1-\alpha_t)/\sqrt{|1-\alpha_t|}$.

Parameter α_t of the CL transformation can be found by least square fitting of ϕ distributions obtained using the cone reflection algorithm described in Sec. II A as seen in Fig. 2. Figure 4 shows the value of α_t, found by a least square fit, for $M=0.3$ and different cone angles β. As expected, α_t is maximum at some intermediate value of the cone angle. Since α_t is larger than 1, the average tangential momentum of the reflected molecules points in the opposite direction with respect to the average tangential momentum of the incoming molecules.

The value of α_t only weakly depends on Mach number, as seen in Fig. 5, where α_t is shown as a function of Mach number for two different opening angles, $\beta=120°$ and $\beta=66°$. This fact facilitates the use of the CL model in simulations, since the value of α_t can be selected universally depending on the degree of roughness of the surface, and not on the flow properties.

C. Simulation conditions

In order to validate the conical roughness model and its link to the CL scattering kernel, both were individually incorporated into a DSMC solver and simulations were run for comparison against experiment. To maximize the measurable effect of the different surface models on the flow, the simulations were conducted on a long, narrow microchannel with an $L/H=100$ and an assumed infinite width. The 2D capability of SMILE (Ref. 26) was used in all DSMC computations. This system utilizes the majorant frequency scheme to calculate intermolecular interactions,[27] while using the variable hard sphere model for intermolecular potentials. Four surfaces were used: (i) a fully diffuse smooth surface with complete energy and momentum accommodation, (ii) a smooth surface utilizing the conical surface roughness model with an opening angle of 66° which corresponded to an earlier experimental setup concept, (iii) CL model with a tangential momentum accommodation coefficient of 1.045 attained using the conical model with a 66° cone opening angle, and (iv) a diffuse surface consisting of about 900 triangles representative of an actual experimental shape.

The channel length and half height, from plane of symmetry to the tops of the surface features, were 1.5 cm and 75 μm, respectively. Helium was used as the test gas with stagnation pressure from 200 Pa to 8000 Pa for all four surfaces. The Knudsen number is defined as

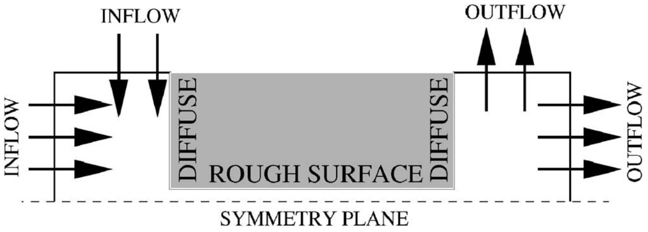

FIG. 6. Schematic of the computational domain.

$$\mathrm{Kn} = \frac{\lambda}{L} = \frac{1}{\sqrt{2} n \pi d^2 L} = \frac{kT}{\sqrt{2} P \pi d^2 L}, \tag{10}$$

where P is the stagnation pressure, k is Boltzmann's constant, T is the stagnation temperature (300 K), d is the molecular diameter, and L is the feature size (about 20 μm). The Knudsen number for these tests ranged from 0.1 to 5. Nitrogen was used as the test gas for only surfaces (i) and (ii), with stagnation pressures from 200 Pa to 6000 Pa. Again, based on the stagnation conditions and the surface roughness size, the Knudsen number ranged from 0.05 to 2. A convergence study was performed to assess the impact of the inflow boundary conditions on the results of the computations. These computations were performed using helium at 6000 Pa and two inflow boundary locations: the first extending 1700 μm from the channel entrance and 1700 μm from the symmetry plane, the other 850 and 850 μm, respectively. A Maxwellian distribution function with zero flow velocity was assumed at these boundaries. No impact from the boundary location was found. The larger domain was used in all subsequent computations, with the number of molecules ranging from about 1.6 million for the lower pressures to about 10 million for the larger ones. A schematic for the computational domain can be seen in Fig. 6, where the outflow boundary condition is modeled as a vacuum.

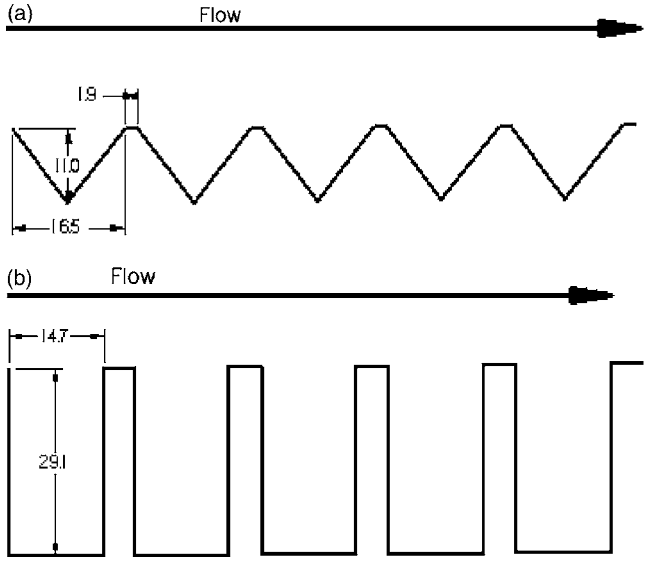

FIG. 7. Average experimental surface roughness feature dimensions for (a) the triangular surface and (b) the square surface.

III. EXPERIMENTAL APPROACH

The experiments were conducted using atomically smooth, triangular patterned, and square patterned silicon textures. Standard microelectromechanical systems (MEMS) processes were performed to create 1 cm by 1.5 cm textured areas centered on 2 cm by 1.5 cm chips. The feature width for both square and triangular textures is approximately 15 μm. The triangles are approximately 11 μm deep with an etched angle of 54.7° from surface parallel, which would give an opening angle of approximately 70°, very close to the numerical simulation. The squares are approximately 30 μm deep, and both geometries can be seen in Fig. 7. Teflon shims were placed between the chips to create a channel 1 cm wide, 150 μm high, and 1.5 cm long such that gas flow along the length of the channel was perpendicular to the textures etched in the silicon chip. Along this length there were approximately 900 features. This channel was secured in an aluminum holder and dimensions of the channel were measured with a scanning electron microscope before and after testing as seen in Fig. 8. The ratio of the measured open area of the channel to the open area of the numerical simulation was used to linearly correct the experimental mass flow data. Typical deviation for the channel height was 3%–5%. Deviation for the width was less than 1%.

The aluminum-Teflon-silicon assembly was placed in the wall of a 3550 cm^3 plenum, which acted as a stagnation

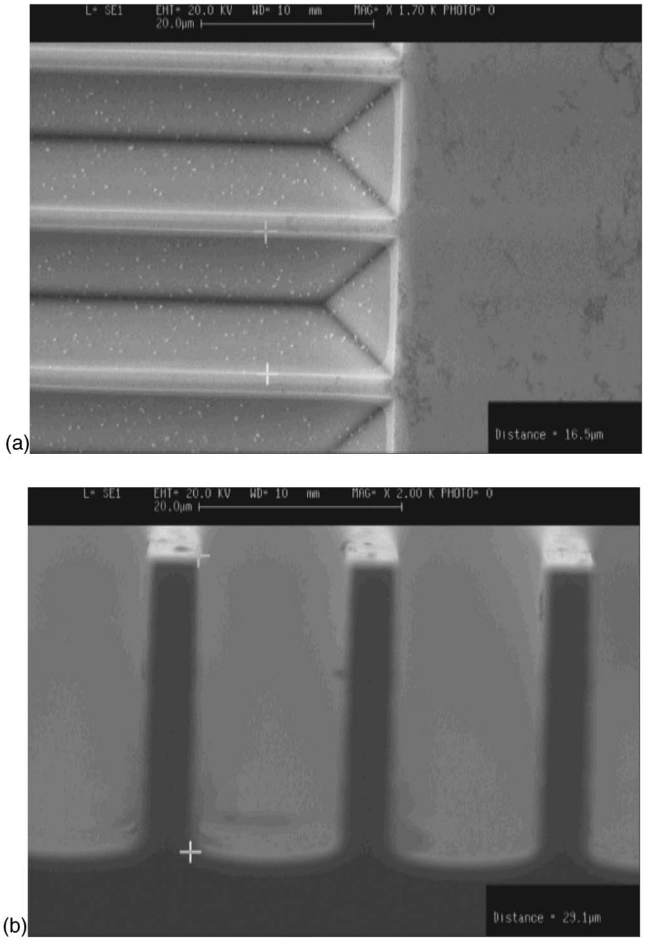
L= SE1 EHT= 20.0 KV WD= 10 mm MAG= X 1.70 K PHOTO= 0
20.0μm
Distance = 16.5μm
(a)
L= SE1 EHT= 20.0 KV WD= 10 mm MAG= X 2.00 K PHOTO= 0
20.0μm
Distance = 29.1μm
(b)

FIG. 8. SEM pictures of (a) the end of the triangular textures (from above), and (b) the view along cleaved square textures (from side).

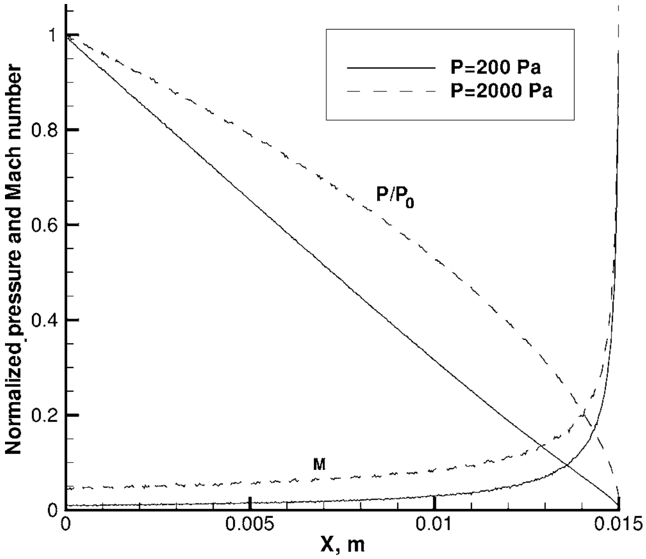

FIG. 9. Normalized pressure and Mach number as a function of distance downstream along the centerline for two stagnation conditions.

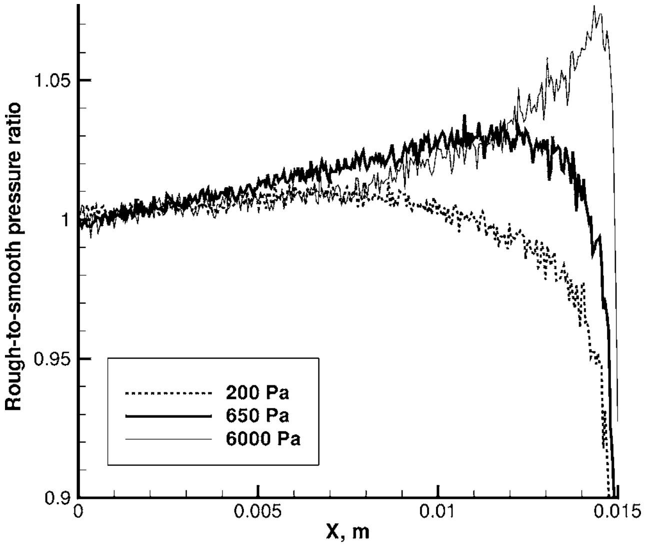

FIG. 10. Pressure ratio as a function of distance downstream along the centerline, conical rough surface to the smooth surface.

chamber. The plenum was machined with two gas inlet ports and three ports for pressure measurements. The setup was operated in the CHAFF IV vacuum chamber at the University of Southern California, which is capable of an ultimate pressure of 10^{-6} Torr with working pressures no higher than 10^{-4} Torr. This allowed plenum pressures from approximately 1 to 100 Torr with ratios of stagnation to ambient pressures greater than 10^5 maintained throughout. Helium or nitrogen test gases were used. Upstream gas flow was measured with a mass flow meter and regulated through a needle valve. The pressure in the plenum was monitored with several differential baratrons. This array of instrumentation allowed measurements of pressure and mass flow with instrumental precisions below 1%.

IV. RESULTS AND DISCUSSION

The first result to consider is that of the numerical simulation using the smooth, fully diffuse surface with a helium test gas. Figure 9 shows the local pressure, normalized by the stagnation value, and Mach number along the centerline of the channel for plenum pressures of 200 Pa and 2000 Pa. The Knudsen number, based on the channel height of 150 μm instead of the feature size, for the 200 Pa case increases from below 1 to about 100. As seen in Fig. 9, the pressure in the free molecular flow drops linearly from $P_0 = 200$ Pa to $0.01P_0$ through the channel. The Mach number stays below 0.05 for the majority of the channel, increasing to 1 at the exit; the Mach number for the $P_0=2000$ Pa case is higher, as expected. This allows for the use of a constant α_t value in the CL model along the length of the channel.

Figure 10 shows the ratio of local pressure for the conical surface simulation divided by the local pressure for the smooth surface as a function of longitudinal distance down the channel. As expected, the pressure along the channel increases for the rough surface compared to the smooth, since the rough surface impedes the flow. This effect decreases as the flow becomes free molecular, at which point the pressure ratio down the channel asymptotes to 1 far from the exit. The ratio drops below 1 at the point where the local mean free path exceeds the channel height allowing molecules to "see" the exit without intermolecular collisions. Downstream from this point, any molecules traveling downstream are more likely to leave the channel after colliding with the rough surface than they would be after colliding with a smooth surface. Upstream from this point, molecular collisions are likely to prevent this. Note that a relatively small difference between pressures for the rough and smooth surfaces is observed for much of the channel length, consistent with the measurements of Turner *et al.*[6]

Calculated helium mass flow as a function of stagnation pressure is listed in Table I for all four surfaces. A reduction in mass flow of 25% at the lower pressures and 6% at higher pressures is seen between the conical surface model and the smooth, fully diffuse case. The CL model with an $\alpha_t = 1.045$ matches the conical model to 7% at the lower pressures and less than 1% at the higher pressures. The conical surface matches the triangular geometry pattern within 3% at the lower pressures and less than 1% at the higher pressures. The impact of the surface roughness is larger for helium than for nitrogen at any given pressure; however, when plotted versus Knudsen number, the impact is similar. Assumptions made for the cone surface model require a noncontinuum

TABLE I. Numerical results for mass flow as a function of stagnation pressure for various surface models using a helium test gas.

Pressure Pa	Surface (i) kg/s	Surface (ii) kg/s	Surface (iii) kg/s	Surface (iv) kg/s
200	4.132E-09	3.188E-09	3.440E-09	3.093E-09
650	1.381E-08	1.125E-08	1.162E-08	1.105E-08
2000	5.680E-08	4.939E-08	4.997E-08	4.898E-08
4000	1.623E-07	1.484E-07	1.502E-07	1.483E-07
6000	3.094E-07	2.899E-07	2.893E-07	2.896E-07
8000	5.098E-07	4.810E-07	4.830E-07	4.810E-07

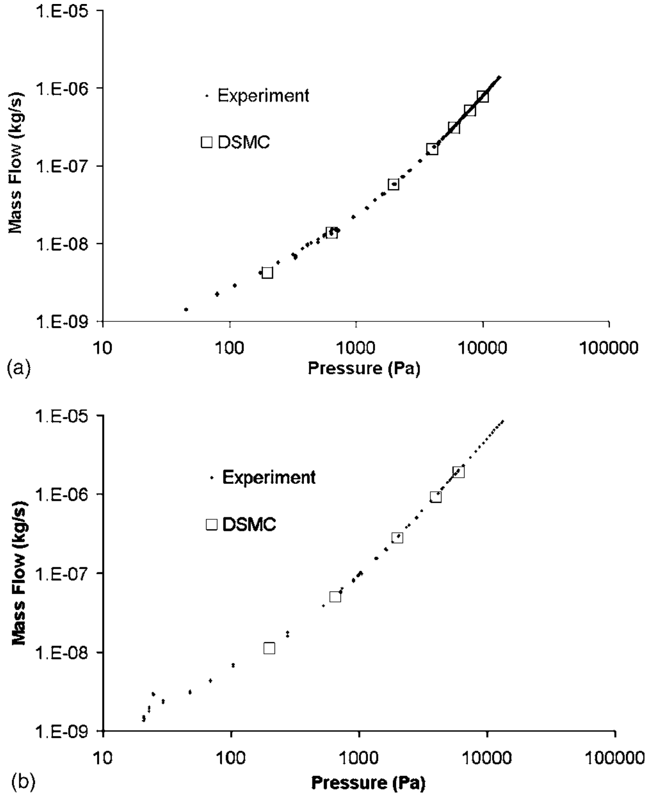

FIG. 11. Comparison of the experimental smooth texture geometry and numerical smooth diffuse roughness model for (a) helium gas, (b) nitrogen gas.

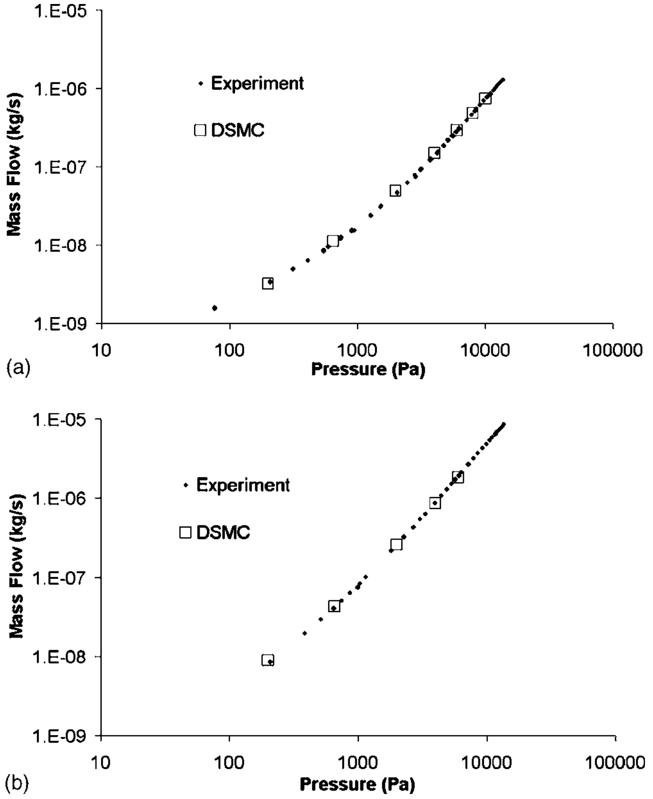

FIG. 12. Comparison of the experimental triangular texture geometry and numerical cone roughness model for (a) helium gas, (b) nitrogen gas.

Knudsen number based on the feature size of the roughness. Although the cone model agrees favorably with the direct representation over the full range tested, it is not a given conclusion that the cone model is applicable in low Knudsen number cases.

There is good agreement between the experimental smooth silicon surface and the smooth fully diffuse simulation as seen in Fig. 11. The experimental uncertainty, based on standard deviation, varies from about 10% at $P_0 < 200$ Pa to less than 1% at $P_0 > 10000$ Pa. There is a 2% underprediction by the DSMC simulations along the range of pressures tested. One of three effects can cause this deviation. The first is a finite specularity that may have existed in the experiment and was unaccounted for in the simulations. The second is an uncertainty of approximately 2% in the area of the channel based on the SEM pictures. The third is the previously mentioned influence of surface absorption and the decrease of surface sites at higher pressures, also creating a higher physical specularity then accounted for in the simulation. However, relative influence of these effects are unknown. It is important to note that the pressure dependence of the underprediction is hard to determine due to the larger experimental uncertainty at lower pressures.

There is also good agreement between the experimental triangular surface and the cone model simulations as seen in Fig. 12. As with the smooth surface, the experimental uncertainty, based on standard deviation, varies from about 10% at $P_0 < 200$ Pa to less than 1% at $P_0 > 10000$ Pa. At the higher pressures, there is less than 2% difference between the experiment and simulation; however, at the lower pressures, there is a 5% overprediction by the DSMC. Again both the uncertainty in the experimental channel area and the larger statistical scatter at lower pressures could contribute to this difference.

The experimental data for the square surface features can be seen in Fig. 13 compared with the other two experimental surfaces. Molecular interaction with the vertical walls of the square surfaces could be approximated as cones with opening angles $\beta = 0°$. As expected, the square data falls between the smooth $\beta = 180°$ and triangular $\beta = 70°$ experimental points. Although the square surface data trends towards the triangular data at lower pressures, it moves towards the smooth data at higher pressures. This could be attributed to the influence of the exit plane on the flow and the reduction in Knudsen number as the pressure ratio increases. At higher pressures and densities, the square texture acts more like a fully diffuse surface than a series of roughness features, until a few mean free paths before the exit plane, ultimately asymptoting at the smooth surface value.

V. CONCLUSION

A conical surface roughness model has been developed, numerically verified, and experimentally validated. For a particle simulation, the conical model reduces both setup and simulation time over direct geometric representation without sacrificing accuracy. For deterministic solvers, this conical model gives a crucial link between the Cercignani-Lampis (CL) scattering kernel, which requires a defined tangential

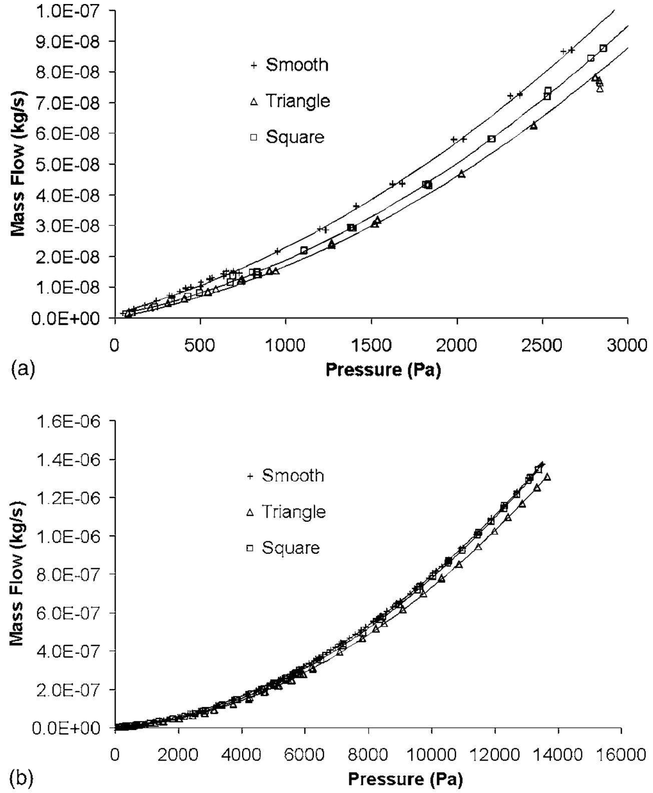

FIG. 13. Experimental results for the textured geometries for helium gas. (a) is a zoom of the lower portion of (b).

momentum accommodation coefficient, α_t, and a physical surface characteristic, the average surface roughness angle. The conical model is general enough to be used for surfaces with both prescribed roughness features and nonuniform roughness features. In the latter case, a mix of conical opening angles and traditional diffuse interactions can be used based on the surface distribution.

Numerical simulations using the conical model, the CL scattering kernel, and a direct geometric representation of a regular triangular surface were compared against a smooth, fully diffuse model. All four cases were simulated with the DSMC method as two-dimensional flows of helium or nitrogen through a 150 μm tall, 1.5 cm long microchannel with Reynolds numbers from 0.01 to 10 based on inlet conditions. The direct geometric representation, the most costly but most accurate compared to experiment, showed a decrease in mass flow between 25% for the lower stagnation pressures simulated and 6% for the higher stagnation pressures simulated. The conical model matched this result to within 3% at the lower stagnation pressures and less than 1% for the higher stagnation pressures while the CL model matched this result within 7% and less than 1%, respectively.

Experiments were conducted on transitional flows, where the mean free path is on the order of or larger than the roughness size, through a 1 cm wide channel with similar height and length to the simulations to approximate 2D conditions. The channel walls were made of silicon with: (i) polished smooth surfaces; (ii) regular triangular roughness; and (iii) regular square roughness with characteristic roughness scales of <1 μm, 11 μm, and 29 μm, respectively. Experimental results validate the numerical simulations, which match to within 2% throughout the range tested for the smooth geometry and between 2% and 5% for the high and low stagnation pressures, respectively, for the triangular roughness geometry. The experimental mass flow for the square roughness geometry falls between the smooth and triangular cases over the entire test range as expected based on β.

ACKNOWLEDGMENTS

This work was supported by the U.S. Air Force Office of Scientific Research, administered by Dr. Mitat Birkan. Special thanks to Mr. Nathaniel Selden for his design of the textured silicon inserts which constitute the top and bottom of the experimental channel and Dr. Amish Desai at Tanner Research for his assistance in their manufacture. Also, thanks to Mr. Bruce Wilton at Mechanical Concepts for his assistance in the precision manufacture of the aluminum and Teflon components for the test assembly.

[1] T. Veijola, "Model for flow resistance of a rare gas accounting for surface roughness," *Modeling and Simulation of Microsystems*, NANOTECH 2003, San Francisco, February 2003, Vol. 2, pp. 492–495.
[2] W. Gaede, "Die innere Reibung der Gase," Ann. Phys. **41**, 289 (1913).
[3] D. H. Davis, L. L. Levenson, and N. Milleron, "Effects of 'rougher-than-rough' surfaces on molecular flow through short ducts," J. Appl. Phys. **35**, 529 (1964).
[4] G. M. Mala and D. Li, "Flow characteristics of water in microtubes," Int. J. Heat Mass Transfer **20**, 142 (1999).
[5] S. G. Kandlikar, S. Joshi, and S. Tian, "Effect of channel roughness on heat transfer and fluid flow characteristics at low Reynolds numbers in small diameter tubes," in Proceedings of the NHTC'01 35th National Heat Transfer Conference, Anaheim, CA, June 2001, pp. 1–10.
[6] S. E. Turner, C. C. Lam, M. Faghri, and O. J. Gregory, "Experimental investigation of gas flow in microchannels," J. Heat Transfer **126**, 753 (2004).
[7] C. Ngalande, T. Lilly, M. Killingsworth, S. Gimelshein, and A. Ketsdever, "Nozzle plume impingement on spacecraft surfaces: Effects of surface roughness," J. Spacecr. Rockets **43**, 1013 (2006).
[8] Y. Ji, K. Yuan, and J. N. Chung, "Numerical simulation of wall roughness on gaseous flow and heat transfer in a microchannel," Int. J. Heat Mass Transfer **49**, 1329 (2006).
[9] S. Ansumali, I. V. Karlin, S. Arcidiacono, A. Abbas, and N. I. Prasianakis, "Hydrodynamics beyond Navier-Stokes: Exact solution to the lattice Boltzmann hierarchy," Phys. Rev. Lett. **98**, 124502 (2007).
[10] S. Ansumali and I. Karlin, "Kinetic boundary conditions in the lattice Boltzmann method," Phys. Rev. E **66**, 026311 (2002).
[11] C. Cercignani and M. Lampis, "Kinetic models for gas-surface interactions," Transp. Theory Stat. Phys. **1**, 101 (1971).
[12] R. Benzi, L. Biferale, M. Sbragaglia, S. Succi, and F. Tuschi, "Mesoscopic modelling of heterogeneous boundary conditions for microchannel flows," J. Fluid Mech. **548**, 257 (2006).
[13] T. Sawada, B. Y. Horie, and W. Sugiyama, "Diffuse scattering of gas molecules from conical surface roughness," Vacuum **47**, 795 (1996).
[14] W. Sugiyama, T. Sawada, M. Yabuki, and Y. Chiba, "Effects of surface roughness on gas flow conductance in channels estimated by a conical roughness model," Appl. Surf. Sci. **169–170**, 787 (2001).
[15] F. Sharipov, "Application of the Cercignani–Lampis scattering kernel to calculations of rarefied gas flows. II. Slip and jump coefficients," Eur. J. Mech. B/Fluids **22**, 133 (2003).
[16] A. D. Ketsdever, M. T. Clabough, S. F. Gimelshein, and A. A. Alexeenko, "Experimental and numerical determination of micropropulsion device efficiencies at low Reynolds numbers," AIAA J. **43**, 633 (2005).
[17] H. Sun and M. Faghri, "Effect of surface roughness on nitrogen flow in a Microchannel using the direct simulation Monte Carlo method," Numer. Heat Transfer, Part A **43**, 1 (2003).

[18] O. A. Aksenova and I. A. Khalidov, "Fractal and statistical models of rough surface interaction with rarefied gas flow," in *Proceedings of the 24th International Symposium on Rarefied Gas Dynamics*, edited by M. Capitelli (AIP, New York, 2005), pp. 993–998.

[19] O. A. Aksenova, "The comparison of fractal and statistical models of surface roughness in the problem of scattering rarefied gas atoms," St. Petersbg. Math. J. **1**, 61 (2004).

[20] M. V. Anolik and I. Kiulvari, "Direct modeling of gas atom reflection from a rough surface," Aerodinamika Razrezhennykh Gazov **7**, 26 (1974).

[21] G. Croce and P. D'Agara, "Numerical analysis of roughness effect on microtube heat transfer," Superlattices Microstruct. **35**, 601 (2004).

[22] W. Sugiyama, T. Sawadaa, and K. Nakamori, "Rarefied gas flow between two flat plates with two dimensional surface roughness," Vacuum **47**, 791 (1996).

[23] S. F. Borisov, "Progress in gas-surface interaction study," in *Proceedings of the 24th International Symposium on Rarefied Gas Dynamics*, edited by M. Capitelli (AIP, New York, 2005), pp. 933–940.

[24] I. Lundstrom, P. Norberg, and L. G. Petersson, "Wall-induced effects in gas transport through micromachined channels in silicon," J. Appl. Phys. **76**, 142 (2005).

[25] R. G. Lord, "Some extensions to the Cercignani-Lampis gas-surface scattering kernel," Phys. Fluids A **3**, 706 (1991).

[26] M. S. Ivanov, G. N. Markelov, and S. F. Gimelshein, "Statistical simulation of reactive rarefied flows: Numerical approach applications," AIAA Pap. 98-2669, 31st AIAA Thermophysics Conference, Albuquerque, NM, June 1998.

[27] M. S. Ivanov and S. V. Rogasinsky, "Analysis of numerical techniques of the direct simulation Monte Carlo method in the rarefied gas dynamics," SIAM (Soc. Ind. Appl. Math.) J. Numer. Anal. **3**, 453 (1988).

Surface Roughness Effects in Low Reynolds Number Channel Flows

N. Gimelshein*, J. Duncan†, T. Lilly†, S. Gimelshein†, A. Ketsdever** and I. Wysong**

*ERC, Inc., CA 93524
†University of Southern California, Los Angeles, CA 90089
** Air Force Research Laboratory, Edwards AFB, CA 93524

Abstract. Rarefied helium and nitrogen flow expanding into vacuum through 150μm high and 1.5 cm long channels is studied experimentally and numerically with the DSMC method. Different types of channel walls are examined, both polished and rough with well characterized roughness shaped as triangles and rectangles. The pressure varies from 200 to 13,000 Pa, with the gas mean free path being both much larger and much smaller than the roughness size of about 20μm. A conical surface roughness model applicable for the DSMC method is proposed. An expression relating this model to the Cercignani-Lampis scattering model is derived. Good agreement between the numerical and experimental results is observed for the rough walled channel.

Keywords: Surface roughness, rarefied gas flows, DSMC, mass flow measurements
PACS: 51.10.+y, 51.90.+r

INTRODUCTION

Surface roughness plays a significant role for a number of gas dynamic problems. Traditionally, the surface structure and roughness are important in low-speed microflows, where the surface-to-volume ratio is high and surface effects dominate the gas flow. One example is the contribution of surface roughness to the resistance of gas channel flows currently drawing significant interest from researchers [1]. In addition to low-speed gas flows, the surface roughness effect may be significant in a number of high-speed flows [2]. This is true not only for micro-scale high-speed flows, where the roughness characteristic size becomes comparable to the flow dimensions, but also for large scale flows, where the local rarefaction may be observed even in flows that are generally in continuum regime.

Numerical modeling of the surface roughness effects in rarefied gas flows encounters a number of problems, from the difficulty of accurate description of complex surface shapes and roughness patterns, to the uncertainties of numerical validation. The description of rough surfaces has been approached before, both using simplified models such as cone models [3, 4] as well as more sophisticated models such as fractals models [5, 6]. The conical roughness model [4] where the surface is represented by a number of virtual cones has been applied to model the flow conductance in channels with the direct simulation Monte Carlo method, and the results were compared with available experimental data. It is not clear however whether the model satisfies detailed balance principle at equilibrium. The fractal model [6] is much more general, although still needs to be validated for rarefied gas flows.

The problems of validation of numerical models of surface roughness are related not only to the challenges of reliable and accurate measurement of low speed rarefied flows, but also to the physical complexities associated with gas-surface collisions. The related experimental studies of surface roughness are the work by Sugiyama et al [7] where triangular roughness in channel flows was studied numerically and experimentally for large Knudsen numbers and by Turner et al [8] where the surface roughness was found to have small effect on gas pressures inside a channel for several pressure ratios.

The accommodation of gas molecules is different for different angles of incidence [9], gas temperatures, surface temperatures, surface material and cleanliness. An additional process that may affect the flow in long microchannels is the variation of accommodation with local gas pressure via coverage dependence. In most cases, the probability of surface sticking/adsorption (and resulting near-complete thermal accommodation) decreases as the availability of surface sites decreases. Lundstrom [10] observed the surprising result that Knudsen flow diffusion increased with backing pressure. This was hypothesized to be due to the variation in sticking with local gas density and a tendency of molecules to scatter more specularly off adsorbed molecules than off the bare wall.

Additional complexity of the surface roughness modeling is associated with the fact that in gaseous microflows, where the pressures are typically on the order of one atmosphere, and the mean free path is several tens of nanometers, the Knudsen number based on the characteristic roughness size varies significantly. The main objective of this paper is the numerical and experimental study of the surface roughness effects in the two-dimensional channel flow with well characterized surface roughness in the regimes from near free molecular to near continuum based on the roughness size. A simple model of the surface roughness that maintains the detailed balance and is applicable to the direct simulation Monte Carlo method is developed and its connection to the Cercignani-Lampis scattering kernel is established. The model is used in the DSMC computations of a helium flow through a long channel expanding into vacuum. The companion experimental study includes both nitrogen and helium mass flow measurements in the pressure range from about 1 Torr to 100 Torr for a channel thickness of 150μm.

CONICAL MODEL OF SURFACE ROUGHNESS FOR PARTICLE APPROACHES

The process of collisions of molecules with a rough surface can be split into the following stages: a molecule hits the wall at a certain point, experiences one or several collisions with the surface, and then leaves the wall. When the characteristic size of the roughness is significantly less that the gas mean free path, no intermolecular collisions take place during the second stage. The time for this stage is in this case much smaller than the mean collision time, and the distance traveled along the wall is on the order of the roughness size. Therefore, this time and distance can be ignored, and it is sufficient to specify only the reflected velocity of the molecule. The following approach is proposed to calculate the velocity of the reflected molecule. The surface is presented as a number of virtual conical holes with a fixed opening angle β and a height h randomly scattered over the actual surface. The after-collision velocity is calculated through the following steps. First, the molecule is assumed to cross the base of the cone at a random point A, as shown in Fig. 1s. Then, its subsequent collision point B with the side of the cone is calculated, and reflected velocity according to the diffuse reflection law is selected. The process of finding collision points and selecting new velocities is repeated until the molecule leaves the surface, that is, exits the conical hole through the base. Note again, the reflection point is assumed to be the same as the initial approach point, therefore, the actual value of h is not important (for example, $h = 1$m can be used). In this algorithm, there are no uncertainties associated with the cut-off for very long traveling distances such as those in [3]. It can also be easily implemented in DSMC. With such a surface shape simplification, there is only one parameter, namely average surface slope, that is used.

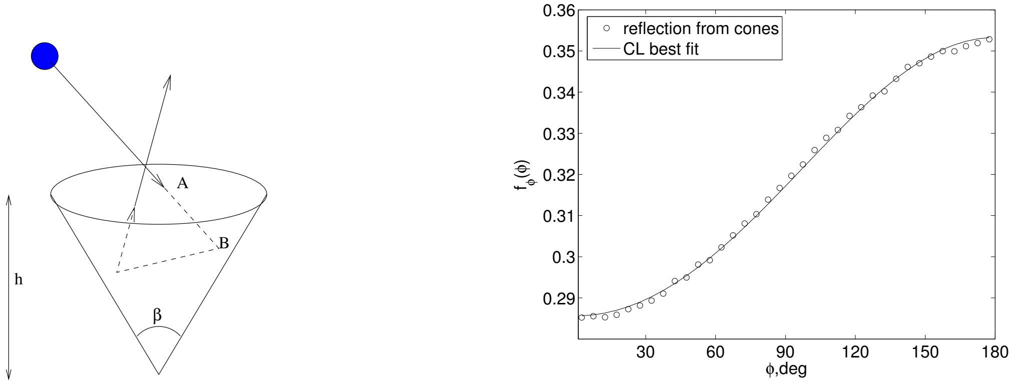

FIGURE 1. (a) Schematic of molecule reflection from the wall. (b) Distribution function of the angle between the reflected molecular velocity and flow direction, M=0.3, $\beta = 66^o$.

To study the influence of the rough wall on the flow properties, let us now examine how the velocity distribution function of the incident molecules is transformed by collisions with the wall. In what follows, the velocity distribution function of the incoming molecules is assumed to be equilibrium at a flow velocity characterized by the Mach number M and directed along x axis, where the wall is assumed to lie in xy plane. The distribution function of the angle ϕ $(0 < \phi < \pi)$ between the reflected tangential molecular velocity and flow direction obtained using the reflection algorithm described above is plotted in Fig. 1b (circles) for $\beta = 66^\circ$ and M=0.3. Note that the maximum of the distribution function corresponds to the direction opposite to the flow direction, which is reasonable for a rough surface that is generally expected to increase flow resistance.

MODELING SURFACE ROUGHNESS USING CL SCATTERING KERNEL

Let us show that this distribution can be fitted by the distribution obtained with the Cercignani-Lampis (CL) [11],[12] transformation of incident velocities. The analytical form of the distribution function obtained by using CL transformation is derived as follows. In what follows, it is assumed that the temperatures of the gas and the wall are equal, and the velocities are normalized by $\sqrt{m/kT}$. Then, the distribution functions of x and y velocity components of incident molecules are

$$f_x^{\text{inc}}(v) = \frac{1}{\sqrt{2\pi}} \exp(-(v - M\sqrt{\gamma})^2/2) \text{ and } f_y^{\text{inc}}(v) = \frac{1}{\sqrt{2\pi}} \exp(-v^2/2), \tag{1}$$

respectively. After the CL transformation, the x component of the reflected velocity is equal to

$$v_x^{\text{refl}} = \frac{1-\alpha_t}{\sqrt{|1-\alpha_t|}} v_x^{\text{inc}} + v_x^{CL}, \tag{2}$$

where the distribution function of v_x^{CL} is given by

$$f_x^{CL}(v) = \frac{1}{\sqrt{2\pi(1-|1-\alpha_t|)}} \exp\left(-\frac{v^2}{2(1-|1-\alpha_t|)}\right). \tag{3}$$

Here, α_t is the CL parameter that corresponds to the tangential accommodation coefficient, $0 \leq \alpha_t \leq 2$. Note that v_x^{refl} is the sum of the two independent normally distributed variables, therefore, its distribution function can be written as

$$f(v_x^{\text{refl}}) = \frac{1}{2\pi} \exp\left(-\left(v_x^{\text{refl}} - M\sqrt{\gamma}\frac{1-\alpha_t}{\sqrt{|1-\alpha_t|}}\right)^2\right). \tag{4}$$

Similarly, it can be concluded that the distribution function of y velocity component does not change during CL transformation. Note that $\tan(\phi) = \frac{|v_y^{\text{refl}}|}{v_x^{\text{refl}}}$, so for $0 < \phi < \pi/2$ the distribution function of ϕ can be obtained with

$$f(\tan\phi) = \int_0^{\infty} u_x f_x^{\text{refl}}(u_x) f_y^{\text{refl}}(u_x \tan\phi) du_x \tag{5}$$

and for $\pi/2 < \phi < \pi$

$$f(\tan\phi) = -\int_{-\infty}^{0} u_x f_x^{\text{refl}}(u_x) f_y^{\text{refl}}(u_x \tan\phi) du_x. \tag{6}$$

Finally, the reflected velocity distribution function

$$f_\phi(\phi) = 2f(\tan\phi)(1+\tan^2\phi) = \frac{\exp(-t^2)}{\pi} + \frac{t\cos\phi}{\sqrt{\pi}} \exp\left(-t^2\sin^2\phi\right)(1+\text{erf}(t\cos\phi)), \tag{7}$$

where $t = \frac{1-\alpha_t}{\sqrt{|1-\alpha_t|}} M\sqrt{\gamma}$.

Parameter α_t of the CL transformation can be found by least square fitting of ϕ distributions obtained using the reflection algorithm described in section to Eq.(7). Figure 1b shows such a fit. α_t is larger than 1, which means that the average tangential momentum of the reflected molecules points in the opposite direction with respect to the average tangential momentum of the incident molecules. $\alpha_t = 1$ corresponds to zero average momentum of reflected molecules, and the bigger the difference between α_t and 1, the bigger the average momentum of reflected molecules.

Figure 2a shows the values of α_t found by a least square fit for M=0.3 and different cone opening angles. As expected, α_t is maximum for some intermediate value of cone opening angle. A large opening angle essentially means that the surface is flat, so α_t tends to 1 in this case. Also, α_t decreases for small opening angles.

The value of α_t only weakly depends on Mach number, which is illustrated in Fig. 2b, where α_t is shown as a function of the Mach number for two different opening angles, $\beta = 120^o$ and $\beta = 66^o$ (the latter one is used in the

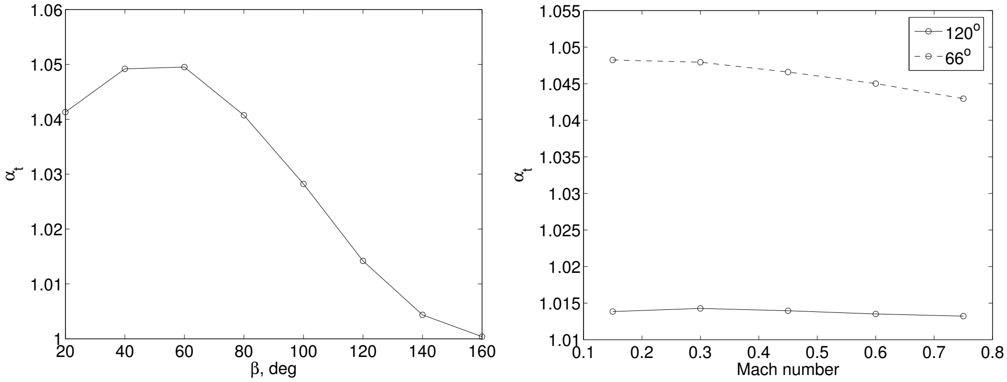

FIGURE 2. (a) α_t as a function of cone opening angle β, M=0.3 (b) α_t as a function of Mach number for two cone opening angles.

experiments). This fact facilitates the use of the CL model in DSMC simulations, since the value of α_t can be selected depending on the degree of roughness of the surface, and not on flow properties.

The verification of the rough surface model has been performed for a two-dimensional thermal bath test case, with the test gas being helium initially heated to 1000 K. The surface temperature was assumed constant at 300 K, and the conical roughness model was used with a cone angle of 45 deg. The temporal temperature relaxation inside the test box is illustrated in Fig. 3 for a cross section along the centerline. As particles collide with the surface, the temperature decreases from its initial value to the equilibrium value of 300 K. This test case shows that the detailed balance is maintained in the conical roughness model, and in may be used in DSMC modeling of gas flows. The present numerical and experimental study concentrates on rarefied gas flows though a long channel into vacuum, and the flow conditions and setup are given in the next sections.

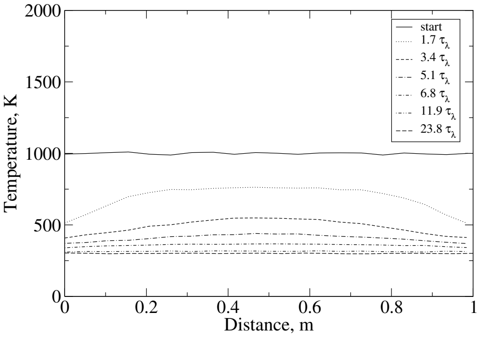

FIGURE 3. Temporal relaxation of gas temperature in a 300 K box. Time is in mean collision times τ_λ at 1000 K.

EXPERIMENTAL SETUP AND CONDITIONS

A flat polished surface, a regular triangular groove, and a regular square groove texture was tested during this experiment. The details of tested geometries are summarized in Fig. 4. The 2 cm by 1.5 cm silicon texture inserts were fabricated through standard MEMS processes. At the entrance and exit of the channel is a shelf between 1 and 5 features long; with approximately 800 features down the length of the channel, the influence of this shelf is negligible. The inserts were placed in an aluminum holder and Teflon sheet assembly. The spacing between the two center Teflon sheets determines the width of the channel while the thickness of these sheets determines the height. The design dimensions for the channel are 1 cm wide, 150 microns high, and 1.5 cm long (the later being the flow direction). This assembly was then placed in one wall of a 3550 cm^3 plenum, which acted as a stagnation chamber. Two inlet ports and three pressure ports also penetrate the wall of the plenum.

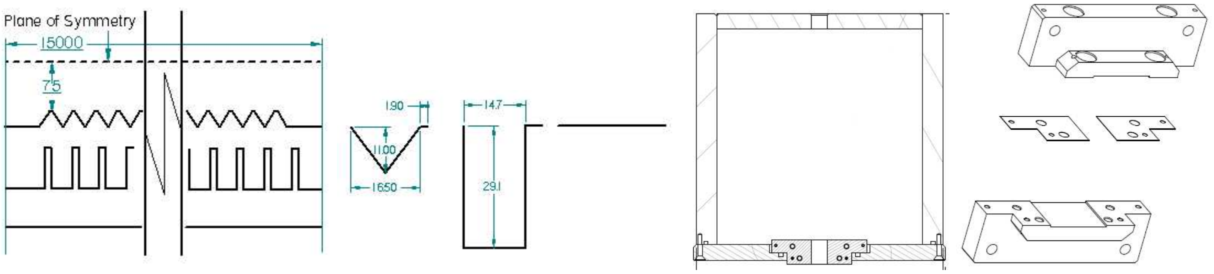

FIGURE 4. Experimental specifications and setup.

The entire setup was then placed in the Collaborative High Altitude Flow Facility (CHAFF) at the University of Southern California (USC) Chamber IV. The chamber is a 3 m diameter by 6 m long high vacuum chamber pumped by a 1 m diameter diffusion pump capable of 25,000 L/s for nitrogen and 42,000 L/s for helium. The ultimate background pressure of the chamber is 10^{-6} Torr with working pressures as high as 10^{-4} Torr. The stagnation pressure in the plenum was tested between 1 and 100 Torr for both helium and nitrogen. Before and immediately after testing, the assembly was analyzed in a Cambridge 360 Scanning Electron Microscope (SEM). The SEM images of three surfaces under consideration are presented in Fig. 5. The assembly was measured to find the exact channel height with an accuracy of 2 microns. A jeweler's microscope with an accuracy of 25.4 microns was used to find the channel width. The accuracy of the groove dimension measurements were 0.2 microns.

The mass flow of the test gas was monitored until the pressure in the plenum became constant. The data was recorded and the mass flow adjusted to the next data point. This was conducted for both helium and nitrogen using Omega 1000, 100, 10, and 5 SCCM mass flow meters and MKS 100, 10, 1, and .2 Torr Baratrons.

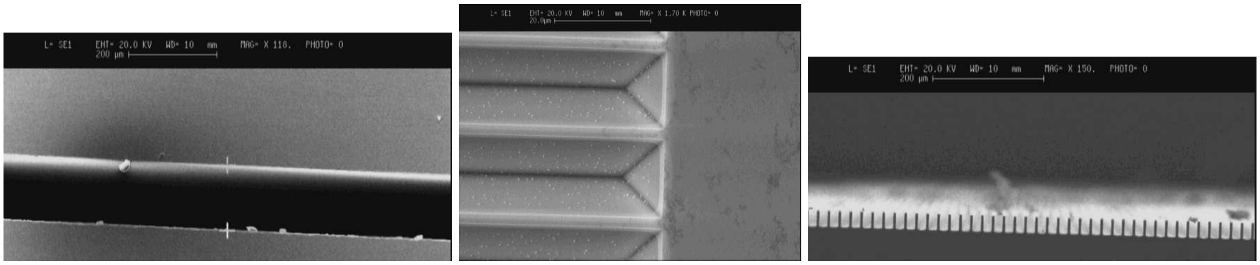
L= SE1 EHT= 20.0 KV WD= 10 mm MAG= X 118. PHOTO= 0
200 µm
L= SE1 EHT= 20.0 KV WD= 10 mm MAG= X 1.70 K PHOTO= 0
20.0µm
L= SE1 EHT= 20.0 KV WD= 10 mm MAG= X 150. PHOTO= 0
200 µm

FIGURE 5. SEM images of a polished channel (left), triangular grooves (center), and rectangular grooves (right).

NUMERICAL APPROACH

The DSMC-based software system SMILE [13] was used in all computations. A 2D capability of SMILE was used in this work. The majorant frequency scheme was used to calculate intermolecular interactions. The intermolecular potential was assumed to be a variable hard sphere. The conical roughness model has been implemented in SMILE for the gas-surface interactions, and the following four surfaces were used in the computations: (i) fully diffuse flat surface with complete energy and momentum accommodation; (ii) flat surface with the conical roughness and diffuse accommodation on cone sides and an opening angle of 66° that corresponds to the experimental conditions; (iii) CL model with a tangential momentum accommodation coefficient of 1.045 to approximate (ii); (iv) a diffuse surface that consists of about 800 triangles and approximate the actual experimental shape.

The channel height and length were 150 μm and 1.5 cm, respectively. Helium was used as the test gas, and the chamber pressure varied from 200 Pa to 13,000 Pa. The Knudsen number based on the stagnation conditions and the feature size of about 20μm ranged from about 5 down to 0.1. The convergence study computations were performed for 6000 Pa and two inflow boundaries, the first extending 1700μm from the channel entrance and 1700μm from the symmetry plane, the other 850 by 850μm, respectively. The Maxwellian distribution function with zero flow velocity was assumed at these boundaries; no impact of the boundary location on the results was found. The larger domain was used in all subsequent computations, with the number of molecules ranging from about 1.6 million for the smaller pressures to about 10 million for the larger ones.

RESULTS AND DISCUSSION

Consider first the results of the DSMC modeling of a helium flow inside a two-dimensional channel. The distribution of pressure and Mach number along the channel is shown in Fig. 6a for the smallest and the largest pressures under consideration and a fully diffuse flat surface. For the stagnation pressure of 200 Pa, the local Knudsen number based on the channel height increases from about 1 to 100, and for this essentially free molecular flow the gas pressure decreases linearly from the stagnation value, P_0, to about $0.01P_0$ at the channel exit. The Mach number is below 0.05 for most of the channel, except for the vicinity of the exit where it increases to 1. As expected, the Mach number is higher for the larger pressure, but still mostly less than 0.1.

The calculated mass flow as a function of stagnation pressure is given in Fig. 6b for four surface models under consideration. Several conclusions can be drawn from these results. First, the surface roughness results in decreasing the mass flow by about 30% for 200 Pa, and then the difference decreases to about 6% for 10,000 Pa. Second, the CL model with $\alpha_t = 1.045$ agrees with the conical roughness model within two percent for lower pressures and less than one percent for higher pressures. Finally, the results for the two surface roughness models are in good agreement with the results for the triangulated surface, thus providing additional verification for the roughness models.

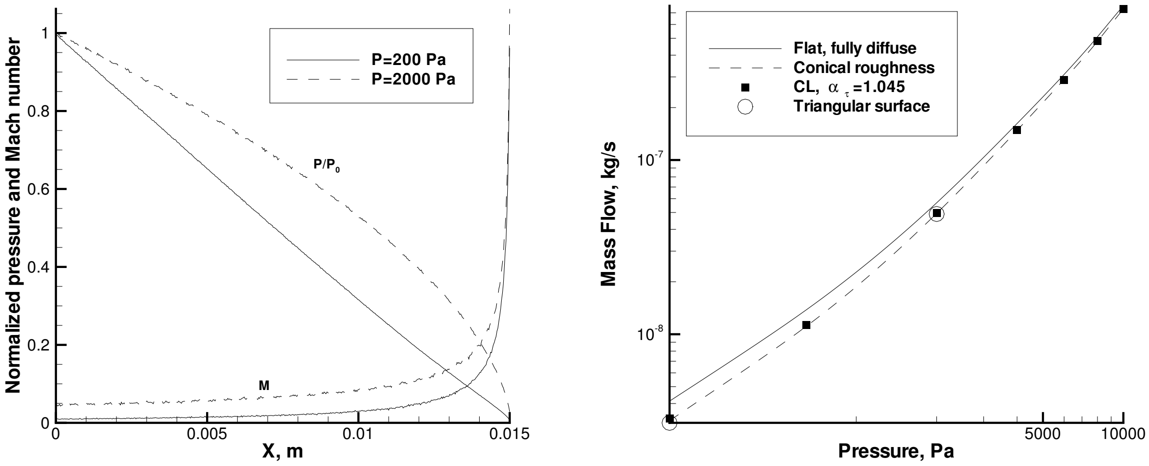

FIGURE 6. (a) Pressure normalized by the stagnation value and Mach number profiles along the channel centerline for two stagnation pressures. (b) Computed mass flow for different surface models.

The experimental results for three surfaces under consideration are presented in Fig. 7 for two gases. The results provide evidence for significant reduction in mass flow for rough surface channels both for helium and nitrogen. This result may appear contradicting to the conclusions of [8], but it may be explained by much larger (flatter) roughness angles used in [8] than that examined in this work. Although the impact of surface roughness at each given pressure is larger for helium than for nitrogen, it is similar if mass flow is plotted as a function of Knudsen number. The rectangular grooves result in mass flows higher than those for triangles, especially for the nitrogen flow, where they are relatively close to the flat surface case.

Let us now compare the experimental and numerical results on helium mass flow for smooth and rough surfaces. There is a good agreement between the results, with the numerical values being within the experimental error bar, estimated at about 10% for 200 Pa and less than 2% for 10,000 Pa, based on standard deviation. The only exception is at high pressures for the flat surface, where the DSMC results are over 4% lower than the measured points. There are three effects that may cause the difference between the numerical and experimental results: the side walls (three-dimensionality), surface specularity, and surface absorption.

The absence of the side walls in DSMC may result in overprediction of the mass flow, especially for lower pressures [14]. This effect may also be responsible for a slight difference between the experiment and DSMC for the rough

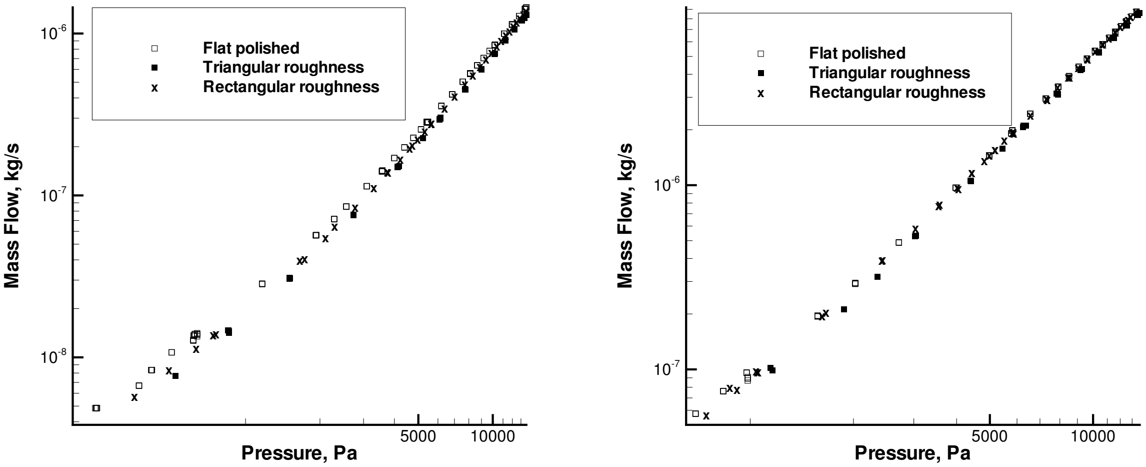

FIGURE 7. Measured mass flow through channel for helium (left) and nitrogen (right).

surface. On the other hand, a polished surface considered in the experiments may have some finite specularity not included in the numerical modeling, that would generally increase numerical values. The effect of surface absorption may increase with gas pressure. Although the magnitude of the effect of increasing adsorption leading to lower overall accommodation at higher pressure is difficult to estimate, it will lead to some increase in flow at higher pressure and could be another explanation of the data trend for the flat surface.

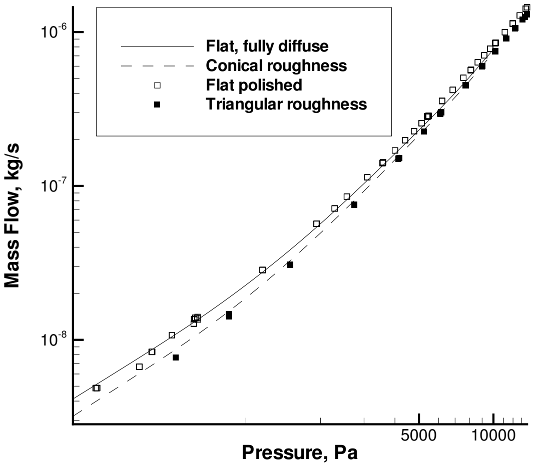

FIGURE 8. Comparison of computed (lines) and measured (symbols) mass flows for smooth and rough surfaces. Helium flow.

CONCLUSIONS

Rarefied gas flow expanding into vacuum through long channels with smooth or rough walls was examined experimentally and numerically with the DSMC method. Two gases, helium and nitrogen, were considered, with stagnation pressures varied from 200 Pa to 13,000 Pa for a 150μm high and 1.5 cm long channel. A conical surface roughness model applicable for the DSMC method was suggested and used in this work. An expression relating this model to the Cercignani-Lampis scattering model is found, and reflected particle velocity distribution for the two models was shown to be close when the tangential accommodation coefficient is chosen appropriately. A significant impact of the surface roughness on mass flow through a channel was observed both experimentally and numerically. The mass flow in a rough channel is lower than that of a polished surface channel, with the difference amounting to 6% for larger pressures and 30% for smaller pressures. A good agreement between the numerical and experimental results is obtained for a rough surface channel, thus validating the conical roughness model. Experimental slope of the mass flow as a function of pressure for a flat plate is somewhat higher than that in DSMC, with the difference attributed to the effects of the flow three-dimensionality, specularity, and surface coverage.

ACKNOWLEDGMENT

This work was supported in part by the Propulsion Directorate of the Air Force Research Laboratory at Edwards Air Force Base, California.

REFERENCES

1. Veijola, T. "Model for Flow Resistance of a Rare Gas Accounting for Surface Roughness," Modeling and Simulation of Microsystems, NANOTECH 2003, San Fransisco, February 2003, Vol. 2, pp. 492-495.
2. Ketsdever, A.D., Lilly, T.C., Gimelshein, S.F., and Alexeenko, A.A. “Experimental and Numerical Study of Nozzle Plume Impingement on Spacecraft Surfaces,” 24th International Symposium on Rarefied Gas Dynamics, AIP Conference Proceedings, Mellville NY, 2005, Vol. 762, pp. 367-372.
3. Sawada, T., Horie, B. Y., Sugiyama, W. “Diffuse scattering of gas molecules from conical surface roughness,” *Vacuum*, Vol. 47, No. 6-8, pp. 795-797. 1996.
4. Sugiyama, W., Sawada, T., Yabuki, M., Chiba, Y. “Effects of surface roughness on gas ¯ow conductance in channels estimated by conical roughness model,” Applied Surface Science 169-170 (2001) 787-791
5. Aksenova, O.A., Khalidov, I.A. “Fractal And Statistical Models Of Rough Surface Interacting With Rarefied Gas Flow,” 24th International Symposium on Rarefied Gas Dynamics, AIP Conference Proceedings, Mellville NY, 2005, Vol. 762, pp. 993-998.
6. Aksenova, O. A. “The comparison of fractal and statistical models of surface roughness in the problem of scattering rare-fied gas atoms,” Vestnik St. Petersburg University: Mathematics, Issue 1, 2004, pp. 61-66.
7. Sugiyama,W., Sawadaa, T., and Nakamori, K. “Rarefied gas flow between two flat plates with two dimensional surface roughness,” *Vacuum*, 1996, Vol. 47, No. 6-8, pp. 791-794.
8. Turner, S.E., Lam, L.C, Faghri, M., Gregory, O.J., “Experimental Investigation of Gas Flow in Microchannels,” *Journal of Heat Transfer,* 2004, Vol. 126, pp.753-764.
9. Borisov, S.F. “Progress in Gas-Surface Interaction Study,” 24th International Symposium on Rarefied Gas Dynamics, AIP Conference Proceedings, Mellville NY, 2005, Vol. 762, pp. 933-940.
10. Lundstrom, I., Norberg, P. and Petersson, L.-G. “Wall-induced effects in gas transport through micromachined channels in silicon,” *J. Appl. Phys.,* Vol. 76. pp. 142-147.
11. Cercignani, C; Lampis, M, "Kinetic models for gas-surface interactions", *Transp. Theory and Stat. Phys.*,1971, Vol.1,N.2,p.101-114
12. Lord, R.G. “Some extensions to the Cercignani-Lampis gas-surface scattering kernel”, *Phys.Fluids A*, Vol.3, April 1991, p.706-710
13. Ivanov, M.S., Markelov, G.N., Gimelshein, S.F. "Statistical Simulation of Reactive Rarefied Flows: Numerical Approach and Applications," AIAA Paper 98-2669, 31st AIAA Thermophysics Conference, Albuquerque, NM, June 1998.
14. Sharipov, F. “Rarefied gas flow through a long rectangular channel,” J. Vac. Sci. Technol. A, 1999, 17(5), pp. 3062-3066.

JOURNAL OF SPACECRAFT AND ROCKETS
Vol. 43, No. 5, September–October 2006

Nozzle Plume Impingement on Spacecraft Surfaces: Effects of Surface Roughness

C. Ngalande,* T. Lilly,* M. Killingsworth,* and S. Gimelshein†
University of Southern California, Los Angeles, California 90089
and
A. Ketsdever‡
U.S. Air Force Research Laboratory, Edwards Air Force Base, California 93524

An experimental and numerical effort was undertaken to assess the effects of a cold-gas ($T_0 = 300$ K) nozzle plume impinging on simulated spacecraft surfaces. The nozzle flow impingement is investigated experimentally using a nanonewton resolution force balance and numerically using the direct simulation Monte Carlo numerical technique. The Reynolds number range investigated in this study is from approximately 2 to 350 using nitrogen propellant. The thrust produced by the nozzle was first assessed on a force balance to provide a baseline case. Subsequently, aluminum plates were attached to the same force balance parallel to the plume flow to simulate spacecraft surfaces in proximity to the thruster. Three plates were used, an electropolished plate with smooth surface and two rough surface plates with equally spaced rectangular and triangular grooves. A 15% degradation in thrust was observed both experimentally and numerically for the plate relative to the free plume expansion case. The effect of surface roughness on thrust was found to be small due to molecules backscattered from the plate to the nozzle plenum wall. Additionally, the influence of surface roughness in the diverging part of the nozzle on thrust was examined numerically and found to be significant at Reynolds numbers less than 10.

I. Introduction

WHEN in orbit, spacecraft require onboard or secondary propulsion systems to perform orbit transfer, orbit maintenance, and attitude control maneuvers. An important issue in the use of any spacecraft propulsion system involves the assessment and reduction of effects caused by the interaction between the thruster plume and spacecraft surfaces.[1] Direct impingement of a thruster plume on surfaces can generate unwanted torques, localized surface heating, and surface contamination. Self-impingement, that is, the impingement of a thruster plume on a host satellite surface, generally occurs for small surface angles with respect to the propulsion system's thrust vector or occurs in the thruster backflow. Cross impingement, that is, the impingement of one spacecraft's thruster plume onto another spacecraft, can occur at essentially any angle and is becoming increasingly important with the advent of microsatellite constellations. Many studies, both numerical[2–4] and experimental,[5,6] have been performed by various investigators to assess the impingement of plumes onto surfaces.

In recent years, micropropulsion systems have been developed to address the need for highly mobile microspacecraft. A wide array of concepts will require the expansion of propellant gases through microscale nozzles. Because many micropropulsion systems will also operate at relatively low pressures, the investigation of low-Reynolds-number flow has become increasingly important.[7] In the present study, an experimental and numerical effort has been developed to assess the effects of a nozzle plume impinging on a simulated spacecraft surface. Special attention is paid to the impact of roughness on surface forces and flowfield structure.

The nozzle flow impingement is investigated experimentally using a nanonewton resolution force balance and numerically using the direct simulation Monte Carlo (DSMC) method. The purpose of this work is to extend previous nozzle plume impingement results,[5,8] to the low-Reynolds-number-flow range for application to micropropulsion systems. The Reynolds number range investigated in this study is from 2 to approximately 350, based on the nozzle throat diameter using a molecular nitrogen propellant.

II. Experimental Setup

All thrust measurements were performed on the nanonewton thrust stand (nNTS), which has been described in detail by Jamison et al.[9] The nNTS was installed in chamber 4 of the Collaborative High Altitude Flow Facilities (CHAFF-4), which is a 3-m-diam, 6-m-long cylindrical, high vacuum chamber. The facility was pumped with a 1-m-diam diffusion pump with an alternate pumping speed of 25,000 l/s for molecular nitrogen. The ultimate facility pressure was approximately 10^{-4} Pa with all operational pressures below 10^{-2} Pa. A previous study[10] has shown that at these background pressures and corresponding thrust levels there is a negligible effect of background pressure on the thrust measurements in CHAFF-4.

The conical De Laval nozzle used in this study is shown schematically in Fig. 1. The conical nozzle was scaled from the geometry used by Rothe.[11] The scaled Rothe geometry has a 30-deg subsonic section, a relatively sharp 1-mm-diam throat with radius of curvature $r_c = d_t/4$, a 20-deg diverging section, and an expansion ratio of 62.4. This geometry was selected because there is extensive experimental data for it, which were previously used to verify the DSMC model's accuracy.[12,13] The nozzle machined from aluminum was attached to a cylindrical aluminum plenum and mounted on the nNTS. Figure 2 shows a scanning electron microscope image of the nozzle side wall, where the surface features caused by the machining process are clearly evident. The effect of the rough diverging section walls on the nozzle's performance parameters will be investigated numerically in subsequent sections.

After the free expansion thrust was measured, aluminum engineering surfaces with different surface roughness were attached to the thrust stand in the configuration shown in Fig. 1. The following three surfaces were used: 1) a electropolished flat surface (called smooth hereafter), 2) a surface with triangular (prismlike) grooves perpendicular to the plume axis, and 3) a surface with rectangular

---

Received 3 August 2005; revision received 18 November 2005; accepted for publication 29 November 2005. Copyright © 2006 by the authors. Published by the American Institute of Aeronautics and Astronautics, Inc., with permission. Copies of this paper may be made for personal or internal use, on condition that the copier pay the $10.00 per-copy fee to the Copyright Clearance Center, Inc., 222 Rosewood Drive, Danvers, MA 01923; include the code 0022-4650/06 $10.00 in correspondence with the CCC.

*Graduate Student, Department of Aerospace and Mechanical Engineering.

†Research Assistant Professor, Department of Aerospace and Mechanical Engineering.

‡Group Leader, Nonequilibrium Flows Group, Propulsion Directorate.

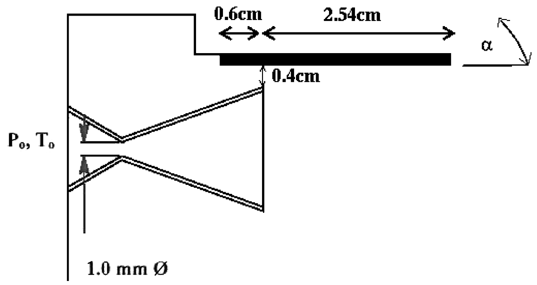

Fig. 1 Geometric setup in experiment.

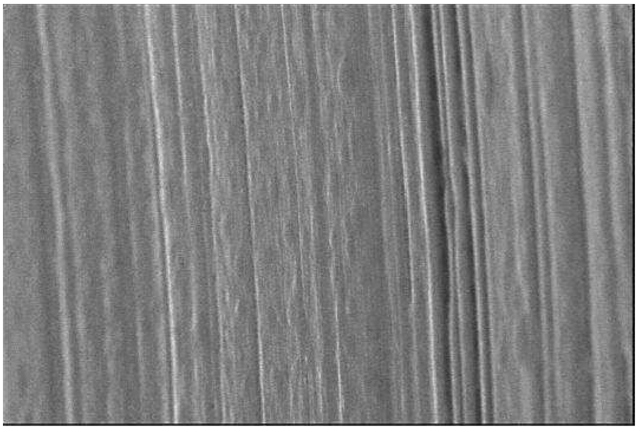

Fig. 2 Scanning electron microscope image, surface roughness of expanding section of conical nozzle.

grooves perpendicular to the plume axis. The grooves are equally spaced with a spacing of 0.05 cm. The angle of triangular grooves is 90 deg, and the depth of rectangular grooves is the same as their thickness of 0.05 cm. The length of the plate in the plume direction is 3 cm, and its width is 3.81 cm. The grooves are made only in the 2.45-cm-long region downstream from the nozzle exit plane.

The total force measured on the nNTS for this configuration is given by

$$F_{\text{tot}} = F_{\text{th}} - F_s + F_b \tag{1}$$

where F_{th} is the thrust produced by the nozzle in the absence of the plate, F_s is the incident shear force on the plate (acting in the opposite direction as the thrust force), and F_b is the force exerted on the plenum wall due to gas pressure in the backflow. The angle of the plate was varied from 0 to 10 deg. The surface temperature was 300 K.

The propellant was introduced to the plenum through an adjustable needle valve located downstream of a mass flow meter. In the experimental configuration, the mass flow meters were operated in the continuum regime throughout the pressure range investigated. The propellant used was molecular nitrogen. In this study, the stagnation pressures ranged from about 13 to approximately 2300 Pa, and the stagnation temperature was measured to be 300 K. The combination of stagnation pressure and temperature gave maximum Reynolds numbers of 350.

III. Numerical Method

Two geometric configurations have been considered in the computations. First, the free nozzle expansion into a vacuum has been modeled. The experimental nozzle geometry has been used with stagnation pressures ranging from 18 to 1800 Pa. Second, a three-dimensional interaction of the nozzle plume with a plate, smooth or rough, is simulated. The computational geometry includes the nozzle with the external side of the plenum and the plate, which size and location correspond to the experimental setup.

The DSMC-based software system SMILE[14] was used in all computations. The important features of SMILE that are relevant to this work are parallel capability, different collision and macroparameter grids with manual and automatic adaptations, and spatial weighting for axisymmetric flows. The majorant frequency scheme was used to calculate intermolecular interactions. The intermolecular potential was assumed to be variable hard sphere. Energy redistribution between the rotational and translational modes was performed in accordance with the Larsen–Borgnakke model. A temperature-dependent rotational relaxation number was used. The reflection of molecules on the surface was assumed to be diffuse with complete energy and accommodation.

All walls were assumed to be at a temperature of 300 K, except where specified otherwise, and the propellant gas was nitrogen at a stagnation temperature of 300 K. A background pressure of zero was set in all calculations. In the first series of computations (nozzle plume expansion into a vacuum), the computational domain included a part of the plenum large enough to avoid the impact of the domain size on the results, and the total number of collision cells and molecules was about 400,000 and 4,000,000, respectively. The three-dimensional plume–surface interaction was modeled using a starting surface at the nozzle exit, generated using an axisymmetric solution of a nozzle plume expansion. An elliptic distribution function was used for inflow molecules. The number of simulated molecules and cells was about 20,000,000 and 3,000,000, respectively.

IV. Nozzle Surface Roughness

A close examination of the surface structure inside the actual nozzle manifested a very rough, groovelike structure, as shown in Fig. 2, with micrometer-size grooves set out perpendicular to the main flow direction. The evident surface roughness prompted the authors to study numerically the effect of roughness inside the nozzle on thrust. To this end, axisymmetric DSMC computations were performed for a rough surface of the diverging part of the nozzle, assumed to have a regular triangular, saw-toothed structure with the triangle angle of 90 deg and the triangle base of 10 μm. The diffuse model of reflection with full energy and momentum accommodation was used on triangle surfaces. A total of more than 1000 was used, and the results are compared with those obtained for a flat diffusely reflecting surface (called smooth hereafter).

The comparison of number density fields inside a rough and a smooth nozzle is presented in Fig. 3 for the smallest chamber pressure considered, $P_0 = 18$ Pa. Note that the mean free path of the gas is over 500 times larger than the surface roughness size, and the flow may, therefore, be considered as free molecular based on this roughness size. Figure 3 also illustrates the geometry of the nozzle and the computational domain. The results show that the influence of the surface roughness in the diverging part propagates into the plenum and the density for the rough surface is about 10% higher than the corresponding values inside the smooth nozzle. This is explained by the fact that the flow is mostly subsonic in the nozzle and only becomes supersonic near the exit. The difference between rough and smooth is larger near the surface than at the centerline and amounts to almost 20% at the nozzle lip. The larger density for the rough case is explained by a significant amount of molecules,

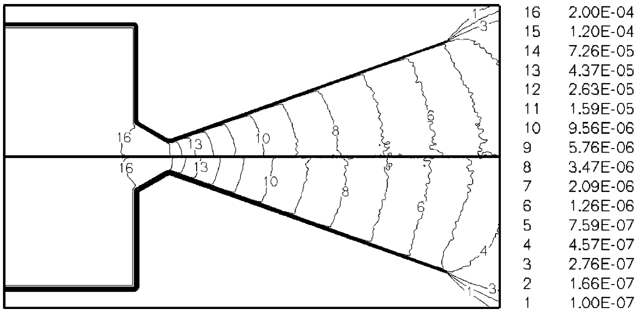

Fig. 3 Mass density fields for smooth (top) and rough (bottom) nozzles.

Table 1 Impact of surface roughness on nozzle properties

P_o, N/m^2	Surface type	Mass flow, kg/s	Thrust, N	I_{sp}, s
1.821×10^3	Smooth	0.2804×10^{-5}	0.1780×10^{-2}	0.6475×10^2
1.821×10^3	Rough	0.2800×10^{-5}	0.1770×10^{-2}	0.6449×10^2
1.821×10^2	Smooth	0.2301×10^{-6}	0.1176×10^{-3}	0.5213×10^2
1.821×10^2	Rough	0.2226×10^{-6}	0.1122×10^{-3}	0.5143×10^2
1.821×10^1	Smooth	0.1548×10^{-7}	0.7424×10^{-5}	0.4892×10^2
1.821×10^1	Rough	0.1375×10^{-7}	0.6614×10^{-5}	0.4908×10^2

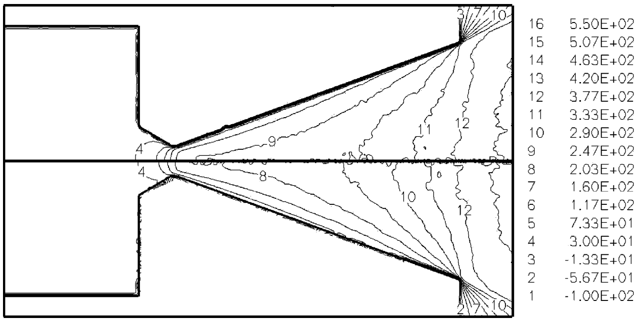

Fig. 4 Axial velocity fields for smooth (top) and rough (bottom) nozzles.

traveling toward the throat, that are reflected on the windside of the triangles.

The molecules reflected on the windside of triangles increase density and decrease axial velocity in the diverging part of the nozzle. This decrease in axial velocity, however, is compensated by the contribution from molecules reflected on the triangle lee sides that on average are reflected in the axial direction. The combined effect of these two trends results in a small influence of the surface roughness on the axial flow velocity fields, as shown in Fig. 4. Although there is a visible difference near the nozzle surface, with the rough case values at the surface being lower by over 50 m/s, the profiles at the nozzle exit are close.

The quantitative impact of the surface roughness inside the nozzle on the flow properties is given in Table 1, where the nozzle performance properties are shown for three plenum pressures. As expected, the effect of roughness is maximum at the lowest pressure, with the rough case mass flow being over 12% lower than the corresponding smooth case. Because the axial velocity at the nozzle exit is weakly affected by the surface roughness, the thrust force is also about 12% lower, and the specific impulse does not change with roughness. For a 10 times larger pressure, $P_0 = 180$ Pa, the surface roughness causes only a 3% decrease in the mass flow and practically no change in the specific impulse. At an even higher pressure of 1800 Pa, no visible influence of the nozzle roughness was found.

The conclusion from these computations is that the surface roughness in the nozzle impacts mostly the density fields; its effect on the axial velocity is much smaller. The mass flow is significantly reduced by the surface roughness only for throat-based Reynolds numbers of about unity or lower, when the subsonic region occupies large part of the diverging part of the nozzle. The surface roughness was found to have little effect on the specific impulse. This also shows that the experimental data on plume and surface forces shown in subsequent sections as a function of the mass flow rate are not affected by the nozzle surface roughness.

V. Interaction of Plume with a Plate: Numerical Modeling

Consider now the three-dimensional interaction of a rarefied plume with a plate. The pressure flowfield in the plane perpendicular to the plate surface and coming through the nozzle axis is given in Fig. 5 for a smooth plate and the stagnation pressure of 405 Pa. The interaction region between the plume and the plate is clearly seen, with the local pressure maximum located near the plate surface about 6 mm downstream from the nozzle exit plane. The pressure values in that region are over an order of magnitude larger than those at the corresponding location in the bottom half of the plume, (i.e., part of the plume where no surface interaction exists). There is significant backflow observed as the result of the plume–surface interaction. A strong backflow will result in a contribution of backflow molecules interacting with the plenum surface to the total force. This contribution increases the total force in X direction.

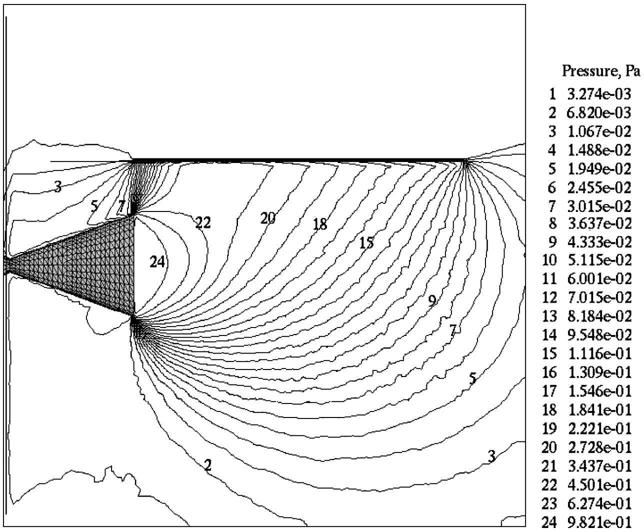

Fig. 5 Pressure field (pascals) over smooth plate at 0 deg.

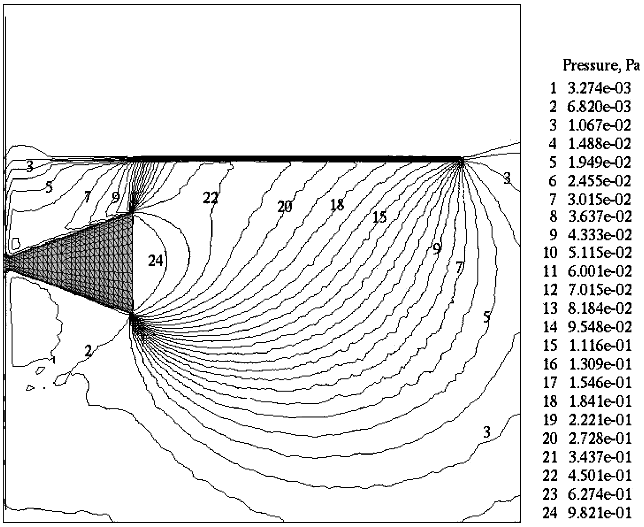

Fig. 6 Pressure field (pascals) over rough plate with triangular grooves.

The flow does not change qualitatively when a plate with a triangular surface roughness is used (Fig. 6). Quantitatively, however, the pressure maximum at the plate shifts about 1 mm downstream compared to the smooth surface case and the maximum value increases by about 10%. The pressure is generally higher for the rough plate because most of the plume molecules that collide with the surface are reflected backward in that case. This is especially noticeable in the backflow region where the pressure for the rough surface case is about two times higher. Note that the mean free path of the gas near the plate is on the order of 1 cm and is an order of magnitude larger that the roughness size. In addition to the triangular groove roughness, a rectangular groove shape has also been examined. The pressure for the latter case is somewhat lower than for the triangular one, but is still higher than for the smooth surface, as shown in Fig. 7.

The increase in the angle α of the plate measured from the plume direction from 0 to 10 deg significantly weakens the plume–surface

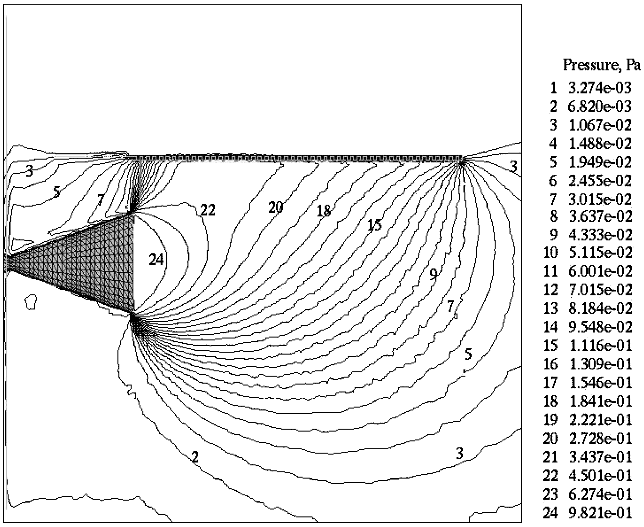

Fig. 7 Pressure field (pascals) over rough plate with rectangular grooves.

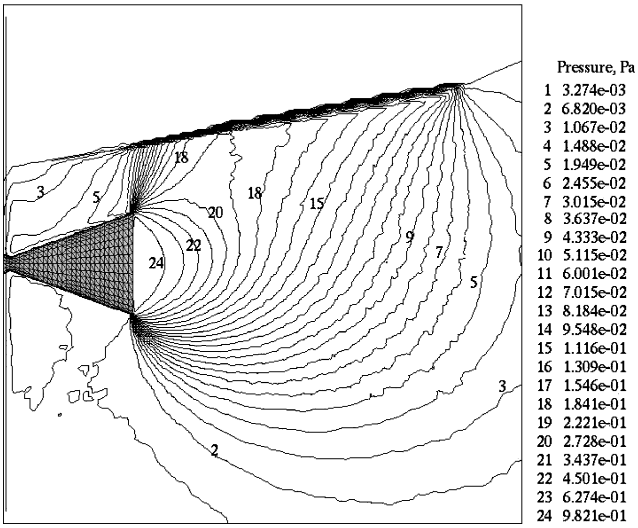

Fig. 8 Pressure field (pascals) over rough plate with triangular grooves; 10-deg plate angle.

interaction, as shown in Fig. 8. The pressure maximum is more than two times smaller for $\alpha = 10$ deg than it was for $\alpha = 0$, and the plate no longer has a noticeable effect on the flowfield in the immediate vicinity of the nozzle exit. The backflow pressure is also reduced and is only slightly higher than the corresponding pressure at the bottom-half of the plume backflow. The effect of the plate surface roughness on the pressure field for $\alpha = 10$ deg is similar to that for $\alpha = 0$ deg and is not shown here.

Consider now the effect of the surface roughness on surface forces. The distribution of the forces in the X direction (shear force) and Y direction (pressure force) over a smooth plate is shown in Figs. 9 and 10. Here, the X direction coincides with the direction of the plume, and the Y direction is perpendicular to the plate surface. The maximum of the force in the X direction, F_x, is about 0.26 N and is located close to the plate center, in the region where both molecular density and axial velocities are sufficiently large. The maximum of the force in the Y direction, F_y, is shifted a few millimeters to the nozzle exit plane, where the local gas pressure maximum is observed. The maximum F_y is about two times larger than the corresponding maximum F_x, primarily because the force from reflected molecules is finite for F_y and zero for F_x. Also, the axial velocity component of plume molecules in that region is somewhat larger than the radial one, with the incidence angle typically larger than $\alpha = 45$ deg.

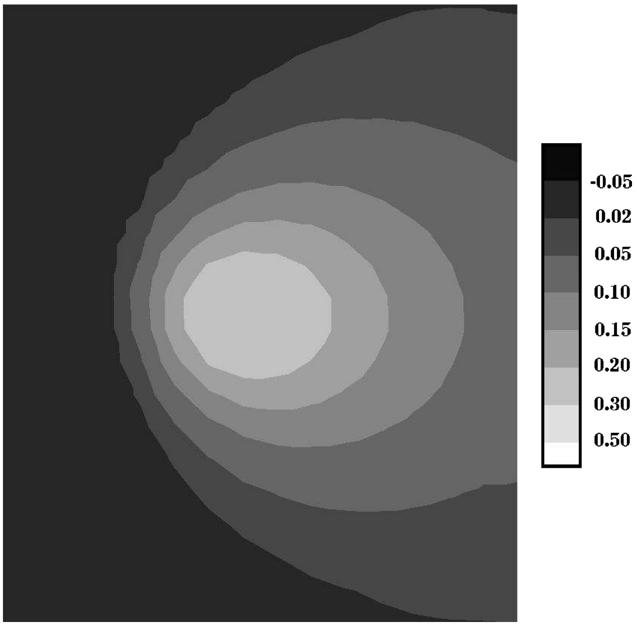

Fig. 9 Force in X direction per unit area (newtons per square meter) on a smooth plate for the 0-deg plate angle and $P_0 = 405$ Pa.

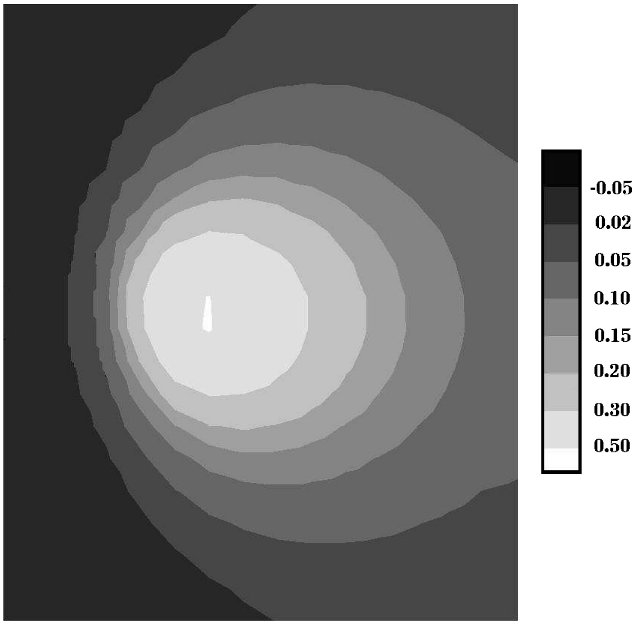

Fig. 10 Force in Y direction per unit area (newtons per square meter) on smooth plate for 0-deg plate angle and $P_0 = 405$ Pa.

Figures 11 and 12 present the corresponding force distributions for a rough surface of plate (triangular roughness). They clearly show the discontinuous structure of the force distributions. The F_x values are large on the sides of the grooves directed toward the nozzle (wind side), with the maximum value almost three times larger than the corresponding maximum on a smooth plate. The lee sides of the grooves, however, are characterized by forces that act in the direction opposite to the plume direction, therefore, reducing the large force from the wind sides. The maximum value of F_x on a rough plate is close to that of F_y. The wind–lee side structure of the surface is also clearly seen in F_y, although the direction of the forces is the same for this case.

The forces on the plate F_x and F_y and on the plenum surface F_b are presented in Table 2 for two roughness types and two angles of the plate. For the plate angle of $\alpha = 0$, the magnitude of the forces on the plate is comparable to the plume thrust force F_{th},

Table 2 Surface forces for $P_0 = 405$ Pa

Surface	Angle	F_{th}, N	$F_{x,s}$, N	$F_{y,s}$, N	F_b, N	F_{tot}, N
Smooth	0	0.309×10^{-3}	-0.6762×10^{-4}	0.1093×10^{-3}	0.1204×10^{-4}	2.5342×10^{-4}
Rectangular	0	0.309×10^{-3}	-0.7340×10^{-4}	0.1083×10^{-3}	0.1519×10^{-4}	2.5079×10^{-4}
Triangular	0	0.309×10^{-3}	-0.8256×10^{-4}	0.1124×10^{-3}	0.1808×10^{-4}	2.4452×10^{-4}
Smooth	10	0.309×10^{-3}	-0.3076×10^{-4}	0.7252×10^{-4}	0.5641×10^{-5}	2.8388×10^{-4}
Triangular	10	0.309×10^{-3}	-0.4059×10^{-4}	0.7481×10^{-4}	0.9040×10^{-5}	2.7745×10^{-4}

Table 3 Surface forces for $P_0 = 155$ Pa

Surface	Angle	F_{th}, N	$F_{x,s}$, N	$F_{y,s}$, N	F_b, N	F_{tot}, N
Smooth	0	0.949×10^{-4}	-0.2368×10^{-4}	0.3799×10^{-4}	0.4618×10^{-5}	0.7584×10^{-4}
Rectangular	0	0.949×10^{-4}	-0.2595×10^{-4}	0.3770×10^{-4}	0.6036×10^{-5}	0.7499×10^{-4}
Triangular	0	0.949×10^{-4}	-0.2960×10^{-4}	0.3822×10^{-4}	0.7315×10^{-5}	0.7262×10^{-4}

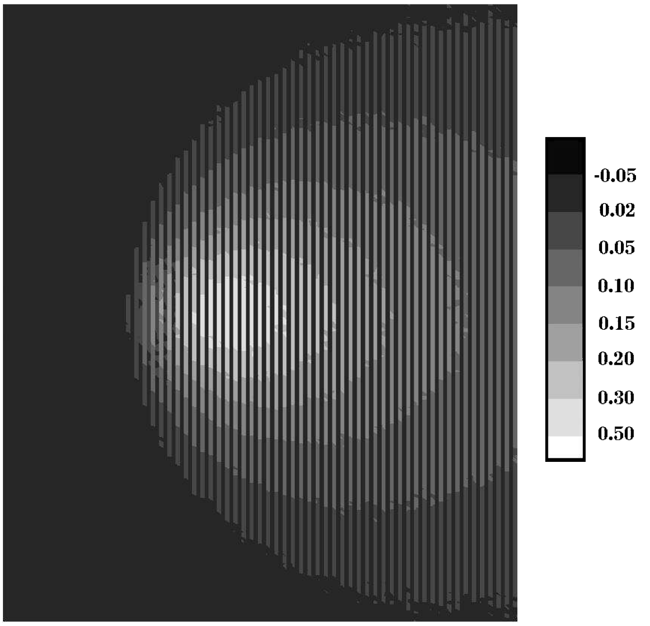

Fig. 11 Force in *X* direction per unit area (newtons per square meter) on rough plate for 0-deg plate angle and $P_0 = 405$ Pa.

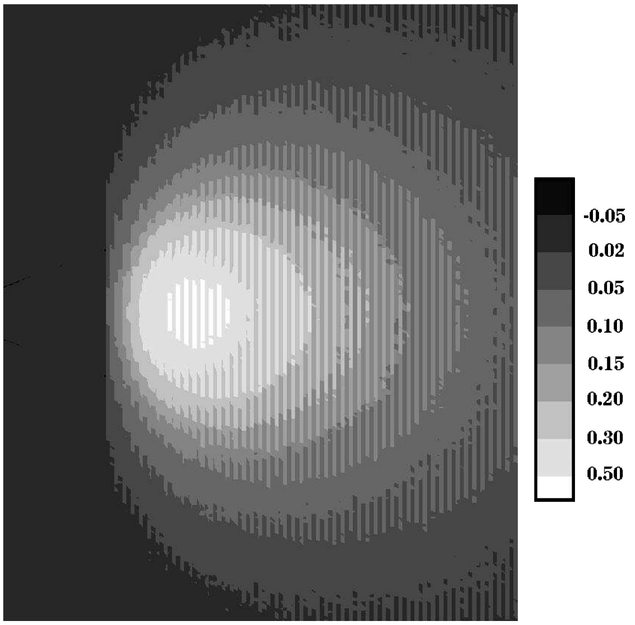

Fig. 12 Force in *Y* direction per unit area (newtons per square meter) on rough plate for 0-deg plate angle and $P_0 = 405$ Pa.

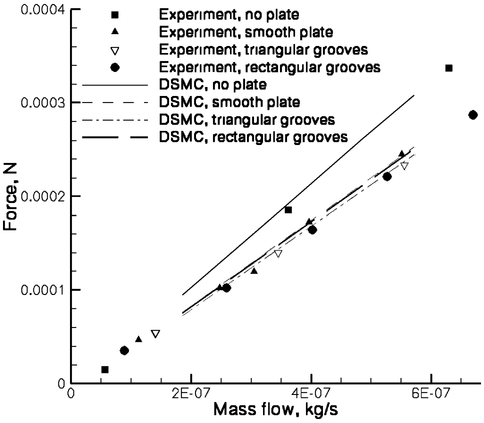

Fig. 13 Total force vs mass flow for free expansion and smooth and rough surfaces: numerical and experimental modeling.

with F_x and F_y being about 25 and 30% of the thrust, respectively. Comparison of rough and smooth surfaces shows that the magnitude of F_x is smallest for the smooth plate and largest for a plate with the triangular roughness shape. The difference is about 20% for these cases. The force in Y direction is weakly dependent on surface roughness.

Another important contributor to the total force in X direction, F_{tot}, is the force on the nozzle plenum, primarily caused by molecules reflected on the plate. This force is significantly larger for rough plates, with the value for the triangular roughness type about 50% higher than that for the smooth plate. Because the force on the plenum is in the direction opposite to that on the plate, this 50% difference considerably reduces the effect of surface roughness on F_{tot}. The difference between F_{tot} for a smooth and a rough plate with triangular grooves amounts to only about 3% of the total force. For the angle of 10 deg, this difference is only about 2.5%.

The comparison of contributions to the total force for a plume flow at $P_0 = 155$ Pa, interacting with smooth and rough surfaces, is given in Table 3. As compared to $P_0 = 405$ Pa, all forces scale approximately with the stagnation pressure, and the conclusions made for the higher pressure case are applicable for $P_0 = 155$ Pa.

VI. Interaction of Plume with a Plate: Experimental Study

Comparison of computed and measured total forces vs mass flow is presented in Fig. 13. Here, the lines that show numerical solutions were created using the values of F_{tot} listed in Tables 2 and 3, which correspond to the chamber pressures of 155 and 405 Pa. The agreement between the experimental and computed force values is good, and the difference in all cases does not go beyond a few percent. The experimental and numerical forces are within 1% for a smooth polished plate and a rough plate with triangular roughness. The values for a plate with rectangular grooves are closer to those for a smooth plate in DSMC and to a triangular grooved plate in the experiment,

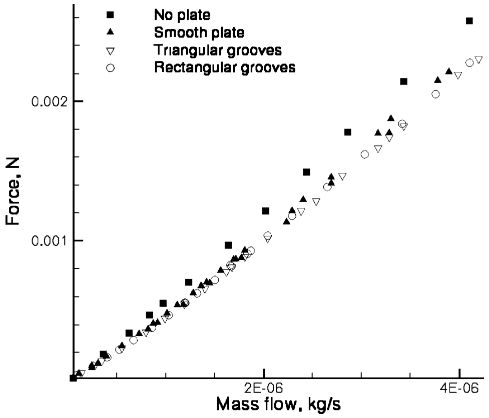

Fig. 14 Measurements of total force vs mass flow for free expansion and smooth and rough surfaces.

although the difference is rather small and may be attributed to one or several causes of experimental and numerical inaccuracies.

There are several possible sources of experimental uncertainties in this work. First, there is always a finite background gas pressure in the chamber that increases with mass flow. The background gas may impact the mass flow measurements only for plenum pressures larger than 1333 Pa, although the force (momentum flux) measurements are affected to some extent at all plenum pressures. A previous study[10] indicated that the force can be affected by less than 0.5% at the experimental conditions of this work. A thrust stand calibration of deflection angle vs applied force has been approximated to be within 3%. For a given applied force to the stand, the standard deviation of the stand's deflection was less than 1%; however, the accuracy of the calibration system must also be taken into account. Finally, there was some error associated with the manufacturing of the nozzle. The nozzle throat diameter is known only with an accuracy of 1%, and the nozzle surfaces are significantly rough. In addition to the experimental uncertainties, there are a number of numerical uncertainties. Grid resolution, maximum number of simulated molecules, effects of the subsonic boundary conditions, and gas–gas collision models all account for a numerical uncertainty estimated to be on the order of 1–2%.

The experimental results for a wider range of mass flows that correspond to plenum pressures up to about 2266 Pa are shown in Fig. 14. The addition of an engineering surface parallel to plume flow significantly reduces total force, up to 15%. The surface roughness effect is much smaller, and the effect of the roughness type is negligible. The small difference between rough and smooth surfaces is explained by the effect of the plume molecules colliding with the nozzle plenum, as discussed in the preceding section.

VII. Conclusions

Experimental and numerical modeling of a cold-gas nozzle plume interacting with engineering surfaces is performed for nitrogen propellant in the range of nozzle-throat-based Reynolds numbers from about 2 to 350. A nanonewton resolution force balance was used in the experimental study to measure thrust force of a plume expanding from a conical nozzle, and then the total force resulted from the interaction of the plume with aluminum plates attached to the same force balance. Smooth and rough plates were examined, with surface roughness introduced through a set of equally spaced 0.5-mm-wide grooves perpendicular to the flow direction.

The DSMC method was used in the numerical study, with the setup corresponding to that in the experiment. The calculated force vs mass flow was found to be in a good agreement with the corresponding experimental data. The experiments and computations showed that there is significant thrust degradation due to the plume surface interaction, with the total decrease being up to 15%. The force on the plate increases in magnitude by about 20% for the rough surface as compared to the smooth one. However, the impact of the surface roughness on total force is small, which is attributed primarily to the effect of nozzle plume molecules reflected from the plate backward to the plenum surface. The number of such molecules is significantly larger for rough surfaces.

The impact of the surface roughness inside the nozzle has been studied numerically. It was shown that the surface roughness decreases both mass flow and thrust by over 10% for Reynolds numbers on the order of one. The effect decreases with the increase of the Reynolds number and is negligible at $Re > 100$. The specific impulse is not affected by the surface roughness even at small Reynolds numbers.

Acknowledgments

This work was supported in part by the U.S. Air Force Office of Scientific Research and the Propulsion Directorate of the Air Force Research Laboratory at Edwards Air Force Base, California.

References

[1] Boyd, I., and Ketsdever, A., "Interactions Between Spacecraft and Thruster Plumes," *Journal of Spacecraft and Rockets*, Vol. 38, No. 2, 2001, p. 380.

[2] Lengrand, J.-C., Allegre, J., Bisch, D., and Skovorodko, P., "Impingement of a Simulated Rocket Exhaust Plume onto a Surface," *Rarefied Gas Dynamics, Proceedings of the 20th International Symposium*, edited by C. Shen, Bejing Univ. Press, Beijing, 1997, pp. 537–542.

[3] Ivanov, M., Markelov, G., Kaskhovsky, A., and Giordano, D., "Numerical Analysis of Thurster Plume Interaction Problems," *Proceedings of Second European Spacecraft Propulsion Conference*, ESA SP-38, 1997, pp. 603–610.

[4] Hyakutake, T., and Nishida, M., "Numerical Simulation of Rarefied Nozzle Plume Impingements," *Rarefied Gas Dynamics, Proceedings of the 22nd International Symposium*, edited by T. Bartel and M. Gallis, AIP CP 585, American Inst. of Physics, New York, 2001, pp. 806–811.

[5] Legge, H., "Plume Impingement Forces on Inclined Flat Plates," *Rarefied Gas Dynamics, Proceedings of the 17th International Symposium*, edited by A. Beylich, VCH, Aachen, Germany, 1991, pp. 955–962.

[6] Deependran, B., Sujith, R., and Kurian, J., "Impingement of Low Density Freejets on a Flat Plate," *Rarefied Gas Dynamics, Proceedings of the 20th International Symposium*, edited by C. Shen, Bejing Univ. Press, Beijing, 1997, pp. 465–466.

[7] Ketsdever, A., *Micropropulsion for Small Spacecraft*, Vol. 187, Progress Series in Astronautics and Aeronautics, edited by M. Micci and A. Ketsdever, AIAA, Reston, VA, 2000, pp. 139–166.

[8] Ketsdever, A. D., Lilly, T. C., Gimelshein, S. F., and Alexeenko, A. A., "Experimental and Numerical Study of Nozzle Plume Impingement on Spacecraft Surfaces," *24th International Symposium on Rarefied Gas Dynamics*, edited by M. Capitelli, Vol. 762, AIP Conf. Proceedings, American Inst. of Physics, Melville, NY, 2005, pp. 367–372.

[9] Jamison, A., Ketsdever, A., and Muntz, E. P., "Gas Dynamic Calibration of a Nano-Newton Thrust Stand," *Review of Scientific Instruments*, Vol. 73, No. 10, 2002, pp. 3629–3637.

[10] Ketsdever, A., "Facility Effects on Performance Measurements of Micropropulsion Systems Which Utilize Gas Expansion," *Journal of Propulsion and Power*, Vol. 18, No. 4, 2002, pp. 797–804.

[11] Rothe, D., "Electron-Beam Studies of Viscous Flow in Supersonic Nozzles," AIAA Journal, Vol. 9, No. 5, 1971, pp. 804–810.

[12] Ivanov, M., Markelov, G., Ketsdever, A., and Wadsworth, D., "Numerical Study of Cold Gas Micronozzle Flows," AIAA Paper 99-0166, Jan. 1999.

[13] Ketsdever, A. D., Clabough, M. T., Gimelshein, S. F., and Alexeenko, A. A., "Experimental and Numerical Determination of Micropropulsion Device Efficiencies at Low Reynolds Numbers," *AIAA Journal*, Vol. 43, No. 3, 2005, pp. 633–641.

[14] Ivanov, M. S., Markelov, G. N., and Gimelshein, S. F., "Statistical Simulation of Reactive Rarefied Flows: Numerical Approach and Applications," AIAA Paper 98-2669, June 1998.

I. Boyd
Associate Editor

AIP | Physics of Fluids

Measurements and computations of mass flow and momentum flux through short tubes in rarefied gases

T. C. Lilly, S. F. Gimelshein, A. D. Ketsdever, and G. N. Markelov

Citation: Phys. Fluids **18**, 093601 (2006); doi: 10.1063/1.2345681

View online: http://dx.doi.org/10.1063/1.2345681

View Table of Contents: http://pof.aip.org/resource/1/PHFLE6/v18/i9

Published by the American Institute of Physics.

Related Articles

Effect of plate thickness on particle deposition velocity onto a face-up flat plate situated parallel to an airflow
J. Appl. Phys. 110, 063518 (2011)

Traveling wave-induced aerodynamic propulsive forces using piezoelectrically deformed substrates
Appl. Phys. Lett. 99, 114102 (2011)

Effects of continuum breakdown on hypersonic aerothermodynamics for reacting flow
Phys. Fluids 23, 027101 (2011)

Evaluation of active flow control applied to wind turbine blade section
J. Renewable Sustainable Energy 2, 063101 (2010)

Effect of wing inertia on hovering performance of flexible flapping wings
Phys. Fluids 22, 111902 (2010)

Additional information on Phys. Fluids

Journal Homepage: http://pof.aip.org/

Journal Information: http://pof.aip.org/about/about_the_journal

Top downloads: http://pof.aip.org/features/most_downloaded

Information for Authors: http://pof.aip.org/authors

ADVERTISEMENT

Running in Circles Looking for the Best Science Job?
Search hundreds of exciting new jobs each month!
http://careers.physicstoday.org/jobs
physicstoday JOBS

PHYSICS OF FLUIDS **18**, 093601 (2006)

Measurements and computations of mass flow and momentum flux through short tubes in rarefied gases

T. C. Lilly and S. F. Gimelshein
University of Southern California, Los Angeles, California 90089

A. D. Ketsdever
Air Force Research Laboratory, Propulsion Directorate, Edwards Air Force Base, California 93524

G. N. Markelov
Advanced Operations and Engineering Services, 2332 KG Leiden, The Netherlands

(Received 6 February 2006; accepted 31 July 2006; published online 8 September 2006)

Gas flows through orifices and short tubes have been extensively studied from the 1960s through the 1980s for both fundamental and practical reasons. These flows are a basic and often important element of various modern gas driven instruments. Recent advances in micro- and nanoscale technologies have paved the way for a generation of miniaturized devices in various application areas, from clinical analyses to biochemical detection to aerospace propulsion. The latter is the main area of interest of this study, where rarefied gas flow into a vacuum through short tubes with thickness-to-diameter ratios varying from 0.015 to 1.2 is investigated both experimentally and numerically with kinetic and continuum approaches. Helium and nitrogen gases are used in the range of Reynolds numbers from 0.02 to 770 (based on the tube diameter), corresponding to Knudsen numbers from 40 down to about 0.001. Propulsion properties of relatively thin and thick tubes are examined. Good agreement between experimental and numerical results is observed for mass flow rate and momentum flux, the latter being corrected for the experimental facility background pressure. For thick-to-thin tube ratios of mass flow and momentum flux versus pressure, a minimum is observed at a Knudsen number of about 0.5. A short tube propulsion efficiency is shown to be much higher than that of a thin orifice. The effect of surface specularity on a thicker tube specific impulse was found to be relatively small. © *2006 American Institute of Physics*. [DOI: 10.1063/1.2345681]

I. INTRODUCTION

Low thrust propulsion systems have attracted significant attention over the last few years due to their potential application in future micro- and nanosatellites. Various orbital maneuvers, such as fine pointing and orbital maintenance, will require micropropulsion systems with thrust levels in the range from 1 N to as low as 1 mN to counter the effects of orbital perturbations. The low thrust levels imply either low pressure operation or a decrease in the throat dimensions, both leading to low Reynolds number flows. The further development of efficient microchemical and electrothermal thrusters is associated with higher combustion chamber temperatures and will therefore also continue the trend toward a decreasing Reynolds number for nozzle flows. Therefore, the investigation of low Reynolds number nozzle flows, both experimental and numerical, has become increasingly important for designing efficient low thrust nozzles.

It is well known that the Reynolds number is a measure of the nozzle efficiency in terms of the viscous losses inherent in the subsonic layer near the nozzle surfaces. For a given stagnation pressure and temperature, the thrust decreases with the square of the characteristic diameter of the nozzle throat, while the Reynolds number only decreases linearly. Therefore, the geometric scaling of nozzles, i.e., decrease in the throat dimensions, for low thrust appears favorable. The availability of microfabrication techniques allows for nozzle throats on the order of several micrometers creating the possibility of efficient low thrust systems primarily through the scaling of the throat diameter. In practice, however, systems limitations of microsatellites may force micronozzle propulsion systems to operate at low Reynolds numbers due to small nozzle dimensions as well as lower chamber pressures.[1] From an overall microsatellite systems point of view, storing propellant on-orbit as a liquid or solid has obvious benefits in terms of available storage volume and tankage mass. Because available power on microsatellites is also quite limited, low pressure operation will most likely result from liquid vaporization or solid sublimation propulsion concepts.

At sufficiently low Reynolds numbers, the viscous losses within a micronozzle become large enough for the specific impulse along the nozzle centerline to decrease from the nozzle throat to the exit plane making the concept of a nozzle expansion useless. In the transitional flow regime, therefore, a thin-walled sonic orifice or a short circular tube may perform as well as a typical micronozzle.[2]

Gas flows through circular orifices and short and long tubes have been rigorously studied in the past, and extensive summaries may be found in Refs. 3 and 4 and references therein. Therefore, here we mention only few of them. Free molecular and transitional flow in tubes and ducts was first studied experimentally and theoretically by Knudsen,[5] who

© 2006 American Institute of Physics

examined the dependence of the conductance at different pressure and geometrical parameters. He observed a conductance minimum at $\mathrm{Kn} \approx 1$ for long ducts and tubes. A qualitative explanation for conductance minimum was suggested in Ref. 6. The minimum was attributed to a small population of molecules that enter the tube or reflect on the tube surface with a very small radial velocity. These molecules give a disproportionately large contribution to the mass flow at high Knudsen numbers. As the Knudsen number decreases, molecular collisions disrupt the path of such molecules, therefore decreasing the mass flow. A further increase in the molecular collision frequency stimulates an overall drift velocity that in turn increases the mass flow through the tube.

The conductance and the transmission probabilities in long tubes and channels in the transitional flow has been extensively studied in the 1960s and 1970s, both experimentally[7] and analytically.[8] There were also several studies aimed at flows through short tubes and apertures.[9,10] An example of such studies is in Ref. 11, where the effect of round edges on mass flow was analyzed. This type of flow was also investigated in detail in the past decade, most noticeably with respect to emerging micro- and nanotechnologies (such as lubrication problems that deal with transitional flows in long channels and tubes) and porous media (represented by a single or multiple capillaries). Many researchers have made a significant contribution to the field, such as Ref. 12, where a method for solving low-velocity microflows by scaling the temperature of the fluid such that the molecular thermal velocity is on the same order of magnitude as the fluid velocity; Ref. 13, where the mass flow, heat flux, and diffusion flux of rarefied gas mixture through long tubes caused by gradients of pressure, temperature, and concentration were calculated; and Ref. 14, where rarefied gas flows in thin film slider bearings are studied in a wide range of Knudsen numbers.

Although an extensive knowledge has been accumulated on transitional flows in orifices and short tubes, there have been few investigations of these geometries from the point of view of micropropulsion, which requires a detailed study of the mass flow rate, momentum flux, and specific impulse.[15–17] The importance of such a study is related to the lack of information on a specific impulse for the above geometries, that was emphasized in Refs. 18 and 19, where gas flow in a Free Molecule Micro-Resistojet was examined experimentally.

The primary scope of this work is experimental and numerical study of this effect in short circular tubes as compared to a thin-walled orifice. In this study we also extend the low end of the Reynolds number range that previous studies have investigated by extending operating conditions down to the free molecule flow regime. To the best of the author's knowledge, this represents the first work, where momentum flux through short tubes in rarefied flow has been measured.

The experiments and computations were conducted at room temperature, using nitrogen and helium with stagnation pressures from 1 to 5000 Pa. The computations are performed using two different approaches: a kinetic approach (the direct simulation Monte Carlo method, DSMC) and a continuum approach (a solution of the Navier-Stokes equations, NS hereafter).

II. EXPERIMENTAL SETUP AND FLOW CONDITIONS

All measurements were performed on the nano-Newton Thrust Stand (nNTS), which has been described in detail in Ref. 1 and specially modified for this experiment's particular needs. The nNTS was installed in Chamber IV of the Collaborative High Altitude Flow Facilities (CHAFF-IV), which is a 3 m diameter by 6 m long cylindrical, high vacuum chamber. The facility was pumped with a 1 m diameter diffusion pump with a pumping speed of 42 000 L/s for helium and 25 000 L/s for molecular nitrogen in conjunction with a turbomolecular pump with a pumping speed of 3500 L/s for molecular nitrogen. The ultimate facility pressure was approximately 10^{-4} Pa with all operational pressures below 0.1 Pa. Measurements of the chamber background pressure were taken with an absolute pressure transducer in conjunction with an ionization gauge.

The thickness of the tube, t, was varied from 0.015 mm to 1.2 mm, while the diameter d was constant at 1 mm. All considered geometries were sharp edged. The tube was attached to a plenum with a cross-sectional area much larger than the tube area to help ensure uniform flow. The thinnest tube was machined in a 0.015 mm thick tantalum shim giving $t/d=0.015$. The medium and thickest tubes were machined into aluminum plates with t/d values of 0.508 and 1.2, respectively. The plenum size ($66 \times 35 \times 17.5$ mm) is the same for all three geometries.

The stagnation pressures were measured through taps on the side of the plenums using calibrated differential pressure transducers. The carrier gas was introduced to the plenum through an adjustable needle valve located downstream of a mass flow meter. In the experimental configuration, the mass flow meters were operated in the continuum regime throughout the pressure range investigated. The gases used were molecular nitrogen and helium. The stagnation pressures ranged from 1 Pa to 5000 Pa. The stagnation temperature was measured to be 295 K in equilibrium with ambient. The combination of stagnation pressure and temperature gave a maximum Reynolds number of 770 for nitrogen and about 290 for helium, based on the tube diameter.

The nNTS was calibrated using electrostatic calibration techniques described by Selden.[19] A unique feature of the nNTS is its ability to measure the force levels of a 1.0 mm tube from the free molecule through continuum range. The low force measuring capability of the nNTS allowed for the investigation of the transitional flow regime overlooked in previous low Reynolds number studies.

III. NUMERICAL APPROACHES

Two approaches, kinetic and continuum, are used in this study to model gas expansion into vacuum. The kinetic approach (DSMC method) is used for the entire range of pressures under consideration. The continuum method (solution of Navier-Stokes equations) is applied for pressures 35 Pa and higher, where the flow regime changes from transitional to near continuum.

A. Kinetic approach

The DSMC-based software system SMILE[20] was used in all DSMC computations. The majorant frequency scheme[21] was used to calculate intermolecular interactions. The intermolecular potential was assumed to be a variable hard sphere.[22] Energy redistribution between the rotational and translational modes was performed in accordance with the Larsen-Borgnakke model. A temperature-dependent rotational relaxation number was used. The reflection of molecules on the surface was assumed to be diffuse with complete energy accommodation.

The DSMC method is conventionally used to model supersonic and hypersonic flows, where the boundary conditions are either supersonic inflow or vacuum outflow. Their implementation for these cases is straightforward. For subsonic flows, such as the flow inside the stagnation chamber, the application of the DSMC method is more complicated. In the present study, a large computational domain was used so that the disturbances arising downstream do not significantly influence the flow near the subsonic boundaries. This allows one to use constant flow properties at these boundaries. Zero flow velocity was assumed at the inflow boundaries, with the pressure and temperature corresponding to given stagnation conditions.

The impact of the computational domain was found to have no visible effect on flow parameters, both distributed and integral, when the domains of 8×4 mm and 16×8 mm were examined. The smaller one was therefore used in all computations presented below. The DSMC modeling was performed for two different sets of numerical parameters, about 25 million molecules and 10 million cells for pressure larger than 2000 Pa, and about 3 million molecules and 1 million cells for pressures smaller than 2000 Pa. These numbers were used to satisfy the DSMC requirements for the linear cell size be less than the gas mean free path, λ (the cell size was about the mean free path for the most dense case of 5200 Pa in nitrogen), and the number of molecules in a λ^2 area be larger than one (at least two were taken). The time of 0.2 ms was found to be sufficient to reach steady state. The macroparameter sampling was performed over 100 000 time steps of 3 ns for the first set, and 100 000 time steps of 80 ns for the second set, with a typical statistical error in flow fields below 2%, and in mass flow and momentum flux below 0.4%.

B. Continuum approach

The Navier-Stokes computations were performed with commercial software, CFD-ACE, which is a pressure-based finite-volume flow solver (CFD-Ace: User Manual, Version 2003, CFD Research Corporation, 2003). CFD-ACE is a set of computer programs for multiphysics computational analysis. It is designed to simulate steady and unsteady flows, perfect gas and multispecies reacting flows.

The following features of CFD-ACE are used for present computations: structured grid solver, conjugate gradient squared method with preconditioning, algebraic multigrid solver, Sutherland law for the viscosity, and slip boundary conditions on plenum and tube walls. These conditions allowed us to obtain reliable, stable, and converged solutions for significantly lower stagnation pressures than in Ref. 17 (410 against 3570 Pa). Boundary conditions with a fixed value of stagnation pressure at the inflow boundaries and a fixed value of pressure at the outflow boundaries are applied. The prescribed value of the outflow pressure is four orders of magnitude lower than the stagnation pressure, and used primarily for the transient stage of computations. If the Mach number at the outflow boundary exceeds unity, the solver automatically switches the conditions to extrapolation from internal nodes. The computational domain is 7×4 mm, and a multiblock grid is used consisting of 71 000 to 88 000 nodes depending on the tube thickness. The nodes are clustered to the tube in order to properly resolve strong flow gradients in this region. Note that an increase of the computational domain or a decrease in the number of nodes did not have visible effect on the mass flow rate and momentum flux. For example, doubling the number of nodes in the vicinity and inside of the tube (the total number of nodes was changed from 51 000 to 71 000) for helium at a stagnation pressure of 5200 Pa changes mass flow rate and momentum flux only by 0.2% and 0.1%, respectively.

IV. EXPERIMENTAL AND NUMERICAL UNCERTAINTIES

There are several possible sources of experimental uncertainties in this work. First, there is always a finite background gas pressure in the chamber that increases with mass flow. The background gas may impact the mass flow measurements only for stagnation pressures larger than 1500 Pa, although the force (momentum flux) measurements are affected to some extent at all plenum pressures. A previous study[23] indicated that the force can be affected by less than 0.5% at the experimental conditions of this work. The previous study is supplemented here with the numerical modeling in order to quantify the facility effect on force measurements. Another source is the standard deviation of the stagnation pressure and mass flow measurements; those were found to be within approximately 1% over the range used. For the momentum flux measurements, a stand calibration of deflection angle versus applied force has been approximated to be within 3%. For a given applied force to the stand, the standard deviation of the stand's deflection was less than 1%; however, the accuracy of the calibration system must also be taken into account. Finally, there was some error associated with the manufacturing of the tubes. In general, the tube diameter of thicker tubes, manufactured of aluminum, is known to be within 0.2%. The thinnest configuration was machined from a thin tantalum shim, and the measurement of its diameter is therefore not quite as accurate and is estimated to be within approximately 2%.

In addition to the experimental uncertainties, there are a number of numerical uncertainties. Grid resolution, the maximum number of simulated molecules, effects of the subsonic boundary conditions, and the gas-gas collision models were all found to be within the statistical error of the DSMC computations mentioned above, and may account for a numerical uncertainty estimated to be on the order of 1% to

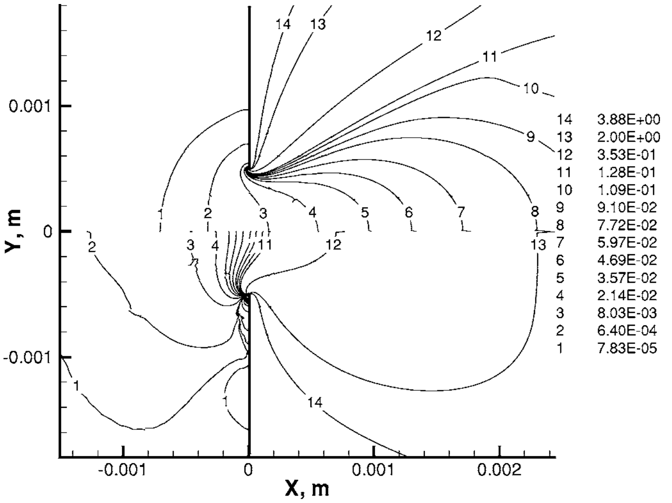

FIG. 1. Local Knudsen number for $t/d=0.015$. Helium flow, $P_0=5200$ Pa (top) and $P_0=410$ Pa (bottom).

2%. The effects of the tube surface roughness present in the experimental device are not known, and a simple diffuse scattering model was used.

V. FLOW SOLUTIONS BY KINETIC AND CONTINUUM APPROACHES

The two approaches, kinetic and continuum, are used to model gas flows through short tubes for the higher pressures under consideration, which allows us to address the accuracy issues of the numerical solutions. It is well known that the Boltzmann equation, and therefore the DSMC method, is applicable to simulate gas flows in the binary collision regime. This regime is observed at pressures up to several atmospheres, which is well above the range of pressures examined in this work. The use of the DSMC method for modeling very low Knudsen number flows, on the order of 0.001 and lower, however, is still raising questions to the numerical accuracy of obtained solutions, primarily related to the number of simulated molecules and cells. This is further magnified by uncertainty in the subsonic boundary conditions, as well as the long time required to reach steady state. The solution of the NS equations, on the other hand, is limited by its area of applicability.

The NS equations may be derived from the Boltzmann equation with the assumption of a small deviation of the velocity distribution function from Maxwellian,

$$f=f_{\mathrm{M}}[1+O(\mathrm{Kn})].$$

Here, Kn is the local Knudsen number equal to the ratio of the local mean free path to a distance $\rho/(d\rho/dx)$, where ρ is the gas density. The local Knudsen number, Kn, is therefore used to analyze the difference between the continuum and kinetic methods, and therefore the applicability of the continuum results.

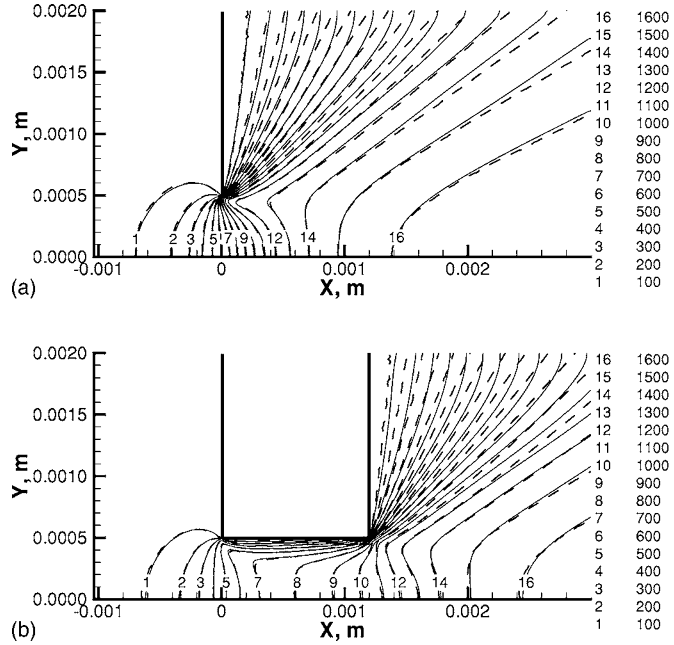

FIG. 2. Helium axial velocity (m/s) at $P_0=5200$ Pa obtained by kinetic (dashed lines) and continuum (solid lines) approaches, $t/d=0.015$ (top) and $t/d=1.2$ (bottom).

The local Knudsen number calculated by the continuum approach for $t/d=0.015$ in helium is plotted in Fig. 1. Gas expansion through a short tube into vacuum is characterized by strong rarefaction in the region near the outer lip, and one can expect large values of the local Knudsen number with the continuum approach failing in that region. For the highest plenum pressure under consideration of 5200 Pa, the value of the local Knudsen number at the exit plane reaches 0.1 near the surface. At as much as quarter of the exit area, it is larger than the value of 0.2 found to correlate with the breakdown of the continuum approach. The values of the local Knudsen number increase by over an order of magnitude as the pressure decreases to 410 Pa, which corresponds to the diameter-based Knudsen number of 0.0425. In this case, the 0.2 isoline lies in the subsonic region inside the plenum, and the values at the exit plane change from 0.08 to 0.5 closer to the surface.

A comparison of the macroparameters obtained with the kinetic and continuum approaches shows that the agreement is very good between the two for higher pressures. This is illustrated in Fig. 2, where the velocity in the axial direction is shown for a helium flow through tubes of different thickness. A comparison of the velocity and the local Knudsen number fields shows that the NS solution is close to the DSMC result in the region, where the local Knudsen number is less than 0.1. The axial velocities are different for the two approaches only in the expansion region where flow angle

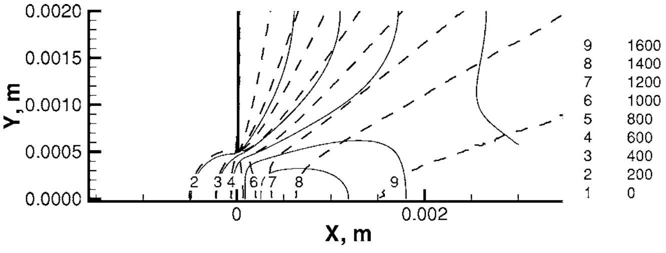

FIG. 3. Helium axial velocity (m/s) at $P_0=410$ Pa obtained by kinetic (dashed lines) and continuum (solid lines) approaches, $t/d=0.015$.

TABLE I. Helium mass flow (kg/s) and momentum flux (N) for different plenum pressures (Pa) and two thickness-to-diameter ratios.

		$t/d=0.015$				$t/d=1.2$			
P_0	Kn	ṁ, DSMC $\times 10^{-6}$	ṁ, NS $\times 10^{-6}$	F, DSMC $\times 10^{-3}$	F, NS $\times 10^{-3}$	ṁ, DSMC $\times 10^{-6}$	ṁ, NS $\times 10^{-6}$	F, DSMC $\times 10^{-3}$	F, NS $\times 10^{-3}$
410	0.0425	0.234	0.197	0.302	0.312	0.126		0.164	
1071	0.0163	0.638	0.602	0.877	0.885	0.411	0.376	0.565	0.547
1605	0.0109	0.950	0.927	1.336	1.351	0.662	0.634	0.927	0.912
2142	0.0081	1.252	1.254	1.792	1.819	0.930	0.927	1.305	1.351
3570	0.0049	2.145	2.119	3.040	3.065	1.674	1.670	2.368	2.387
5200	0.0033	3.140	3.105	4.440	4.485	2.576	2.581	3.658	3.686

relative to the plume axis is larger than 30. The difference is primarily attributed to the nonequilibrium between translational modes, with the actual ratio of temperature in the axial direction to the total translational temperature being as small as 0.4. Note also that the account for the velocity slip in the NS solver allows one to match the DSMC solution inside the tube for $t/d=1.2$, whereas the no-slip NS flow fields differ from the DSMC ones near the surface, as was pointed out by Ref. 17.

The decrease in stagnation pressure results in a significant deviation of continuum results from the DSMC, as illustrated in Fig. 3. The difference is relatively small in the regions where the local Knudsen number is less than 0.1, and becomes large downstream of the exit. Note that a similar trend was observed for other macroparameters, such as temperature and density, which generally points to the inapplicability of the continuum solver to predict flows through tubes into vacuum at this Knudsen number.

The lower flow velocities at the exit predicted with the continuum approach (see Fig. 3) result in smaller mass flow rates for low pressures. This is illustrated in Table I, where the helium mass flow and momentum flux are summarized for two thickness-to-diameter ratios and several plenum pressures. The results show that the continuum solution significantly deviates from the kinetic one at $\mathrm{Kn} > 0.01$. This conclusion holds both for $t/d=0.015$ and $t/d=1.2$. For $t/d=1.2$, the difference in the mass flow reaches 5% for $\mathrm{Kn}=0.0109$ and 10% for $\mathrm{Kn}=0.016$, with the continuum mass flow being lower, even though the velocity slip was included in the calculations. For plenum pressures larger than 2000 Pa, corresponding to $\mathrm{Kn} < 0.008$, the difference between the two approaches is less than 1%, within the computational error, even for conditions when the local Knudsen number at the exit is as big as 0.3. For the largest pressure under consideration, the NS computations were also performed with the no-slip boundary conditions. For those computations, the mass flow was about 1.5% and the momentum flux about 0.5% lower than the corresponding values with slip.

Numerical modeling of flows through short tubes has shown that for a diatomic gas the area of validity of the continuum solver in terms of Knudsen number is similar to the monatomic gas flow. This is illustrated in Table II for $t/d=0.015$, where the nitrogen properties are listed. For larger t/d, the agreement between the DSMC and NS solutions at $\mathrm{Kn} \approx 0.01$ is better for nitrogen than for helium. At $\mathrm{Kn} < 0.01$, the difference between the DSMC and NS is within the boundaries of numerical error both for the mass flow and momentum flux.

It is interesting to note that when the plenum pressure is large enough the momentum flux through a $t/d=0.015$ tube is close for helium and nitrogen (compare the continuum values of 4.485×10^{-3} N for helium and 4.486×10^{-3} N for nitrogen at $P_0=5200$ Pa). This is explained as follows. The main differences between nitrogen and helium in terms of modeling momentum flux are mass, gas-surface interaction, and internal energy modes. The latter does not impact the flow inside the plenum or in the vicinity of the exit since the surface temperature is equal to the stagnation temperature. The gas-surface interaction does not play an important role for $t/d=0.015$. The first factor, the mass, should not significantly affect the force measured at the exit (i.e., close to the sonic line), since the momentum flux at the sonic line is essentially a function of the pressure, the area, and the specific heat ratio.

This is shown in Fig. 4, where the DSMC normalized

TABLE II. Nitrogen mass flow (kg/s) and momentum flux (N) for different plenum pressures (Pa) and two thickness-to-diameter ratios.

		$t/d=0.015$				$t/d=1.2$			
P_0	Kn	ṁ, DSMC $\times 10^{-6}$	ṁ, NS $\times 10^{-6}$	F, DSMC $\times 10^{-3}$	F, NS $\times 10^{-3}$	ṁ, DSMC $\times 10^{-6}$	ṁ, NS $\times 10^{-6}$	F, DSMC $\times 10^{-3}$	F, NS $\times 10^{-3}$
410	0.0133	0.634	0.601	0.334	0.312	0.419	0.413	0.224	0.231
1071	0.0051	1.658	1.621	0.907	0.918	1.282	1.284	0.706	0.717
3570	0.0015	5.520	5.443	3.093	3.079	4.869	4.912	2.724	2.752
5200	0.0010	8.037	7.924	4.519	4.486	7.275	7.369	4.080	4.129

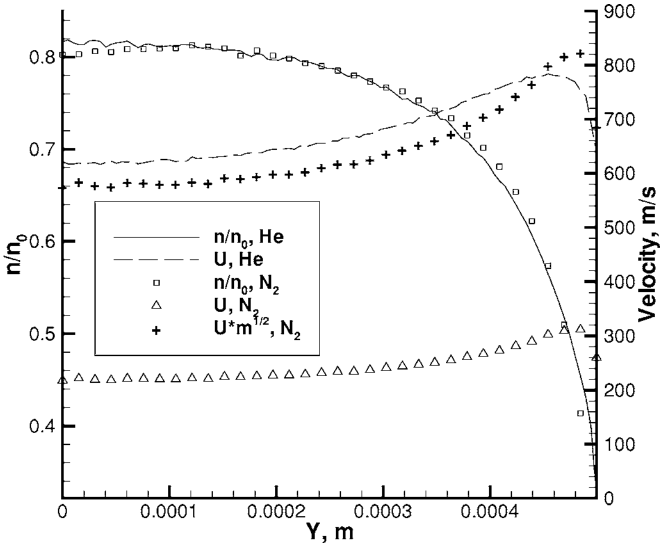

FIG. 4. Normalized density and velocity profiles along the exit for two gases. $t/d=0.15$, $P_0=3570$ Pa. Here, $m=m(N_2)/m(He)$.

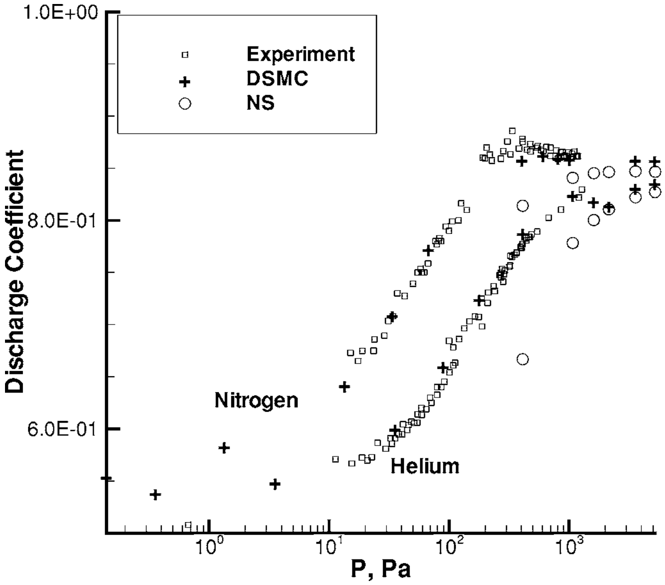

FIG. 5. Discharge coefficient versus plenum pressure for helium and nitrogen at $t/d=0.015$: numerical modeling and experiment.

density and velocity profiles are given along the exit for a stagnation pressure of 3570 Pa. The axis is located at Y=0. It is seen that there is a negligible difference between the number density profiles for the two gases. The axial velocity profiles are different by approximately a factor equal to the square root of the mass ratio. To illustrate this, a profile is shown of the variable $U_x(N_2)\sqrt{m(N_2)/m(He)}$ (compare it to the helium axial velocity profile). All this results in a very small difference between helium and nitrogen momentum flux values.

VI. NUMERICAL AND EXPERIMENTAL DATA

Mass flow through short tubes has been measured and calculated in a wide range of pressure both for helium and nitrogen. The comparison of the computed and measured mass flows is presented below in terms of a discharge coefficient to better illustrate the differences between the obtained results. The discharge coefficient is the ratio of the actual mass flow to the corresponding value for the one-dimensional (1-D) inviscid flow through a sonic orifice,

$$\dot{m} = \rho^* a^* A^*,$$

where ρ^* and a^* are the gas density and velocity at the throat, determined by the plenum conditions through the isentropic relations (see, for example, Ref. 24), and A^* is the throat area.

The computed and measured values of the discharge coefficient $t/d=0.015$ are presented in Fig. 5. The experimental results are given here for plenum pressures below 1000 Pa; the facility (background gas) effects are negligible in this case. The agreement between the kinetic solution and the experiment is very good for the two gases under consideration. The continuum solution consistently underpredicts the data, although the region where the two overlap is, in fact, outside the applicability region of the continuum solver. The discharge coefficient reaches its continuum values of about 0.86 for nitrogen and 0.83 for helium at pressures of about 500 Pa and 2000 Pa, respectively. This corresponds to the Knudsen number of about 0.01. The asymptotic values of 0.86 and 0.83 are in good agreement with previous experimental and numerical studies (see, for example, Refs. 11 and 13).

Note that there is a small maximum in discharge coefficient observed for the nitrogen flow at pressures about 300 Pa. However, the magnitude of this maximum (about or less than 1%) is within both experimental and numerical error, and more accurate data would be necessary to support the existence of the maximum. The kinetic results in the free molecular regime (Kn=50) are somewhat lower than the corresponding theoretical free molecular limits of 0.58 for nitrogen and 0.55 for helium. This is attributed to the finite thickness of the wall of $t/d=0.015$. The number of particles hitting the internal surface of a very short tube amounts to roughly $2t/d$. Since about half of those molecules are returning back to the chamber, the total mass flow is reduced approximately by a factor of $(1-t/d)$.

A comparison of computed and measured discharge coefficients for a larger t/d of 1.2 is presented in Fig. 6. As expected, the formation of the boundary layer inside the tube results in much lower experimental and numerical values of the discharge coefficient in the entire range of pressures under consideration, as compared to $t/d=0.015$. It is also clear that even at pressures above 5000 Pa (Knudsen numbers less than 0.001) the discharge coefficient has not reached continuum limits corresponding to this geometry. Similar to the $t/d=0.015$ case, the discharge coefficient values obtained by the DSMC method are in good agreement with the corresponding experimental values both for helium and nitrogen. For nitrogen, the experimental points are somewhat lower for the high end of pressures, which is attributed to a small but finite effect of the chamber background gas. The continuum solution has a steeper slope than the kinetic and experimental

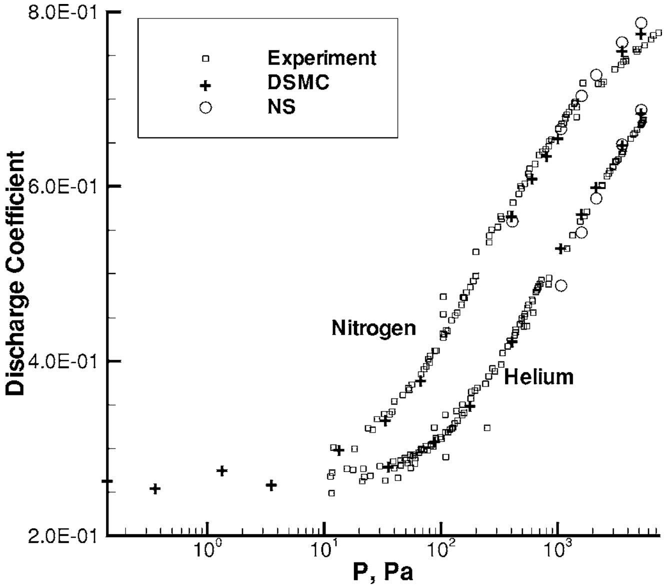

FIG. 6. Discharge coefficient versus plenum pressure for helium and nitrogen at $t/d=1.2$: numerical modeling and experiment.

ones, but is generally in better agreement with the experiment than for $t/d=0.015$.

In this study, the measurements of momentum flux were performed versus mass flow and not pressure. Therefore, it is reasonable to compare the experimental momentum flux with numerical results as a function of mass flow. This allows us to avoid unnecessary uncertainties associated with mass flow versus pressure measurements, and minimize the effect of the experimental tube diameter uncertainty. The comparison of computational and experimental results for $t/d=0.015$ is given in Fig. 7. It is seen that the agreement between the measured and calculated forces is very good, with the exception of the continuum values outside of the applicability limits of the NS approach. The momentum flux changes linearly with the mass flow both for helium and nitrogen. The momentum flux for helium is larger than that for nitrogen by a factor equal to the square root of the inverse ratio of their molecular masses, due to the corresponding difference in the thermal velocities.

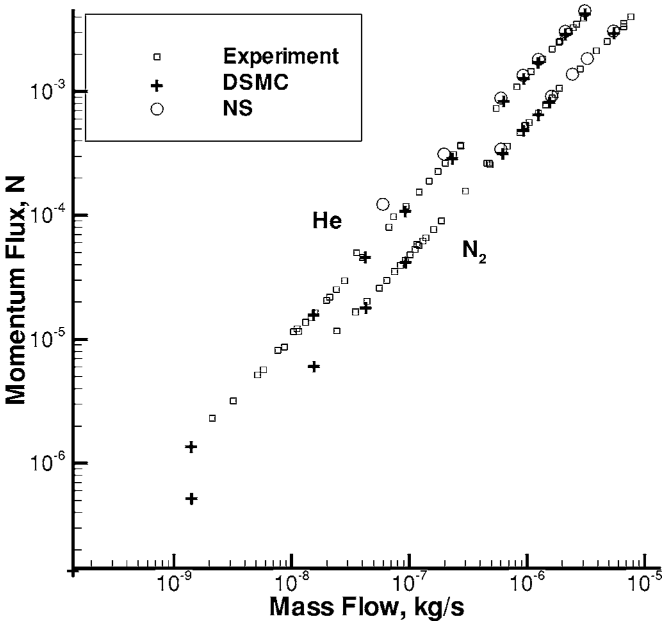

FIG. 7. Momentum flux versus mass flow for helium and nitrogen at $t/d=0.015$: numerical modeling and experiment.

One of the important issues in the comparison of measured and computed momentum fluxes is the presence of background molecules in the chamber, which was not accounted for in the above calculations. In the absence of the gas flow through a tube, the background gas in the plenum is uniform, and the momentum flux is the same over all sides of the plenum. When there is a flow through a tube, there are two types of side effects possible that may impact the momentum flux measurements. First, an average velocity of the background gas may be induced in the chamber, different in different locations throughout the chamber. This average velocity may generally either decrease or increase the total force on the plenum. Second, and more important, the plume molecules move background molecules away from the tube (front) side of the plenum,[23] which in turn reduces the background gas pressure on the front side compared to the back side, and acts toward decreasing the total measured momentum flux. This effect is, in fact, even more complex, since there may be also a significant flux of plume molecules coming on the front side. It is clear that this effect is minimum in the continuum flow, and not present in the free molecular flow. However, in the transitional regime the effect is not clear *a priori*, and has to be characterized.

The DSMC computations have therefore been performed to quantify the contribution of the plume-background gas interaction on the total force change. The computations were three dimensional, included the front side of the plenum with the actual dimensions of 0.035×0.066 m and $t=0.015$, and used an inflow starting surface at $M=2$, generated from corresponding the 2-D computations. Helium flow was considered with the stagnation pressures of 410 and 5200 Pa, and the background pressures of 0.01 and 0.11 Pa, respectively. Note that these values of the background pressures were taken from the pressure sensor measurements in the center of the wind side of the chamber. The computations showed that the pressure force on the front side of the plenum is lower than that on the back side, with the difference amounting to about 1% of the corresponding plume force for $P_0=410$ Pa and 0.75% of the plume force for $P_0=5200$ Pa. This difference is considered not significant, and therefore no special correction of the experimental data has been conducted. In order to analyze the impact of the induced background gas flow in the chamber, DSMC computations has also been carried out for $P_0=410$ Pa, that included a full internal geometry of the CHAFF-IV facility with one and two diffusion pumps working. The computations showed that there is no noticeable flow of the background gas in the chamber, and, with the exception of the plume region, it is essentially stagnant at constant temperature and pressure.

The conclusions on negligible facility effects shown numerically for $t=0.015$ are believed to be applicable to the same extent to larger thickness-to-diameter ratios. The increase of t/d generally results in a better flow directionality,

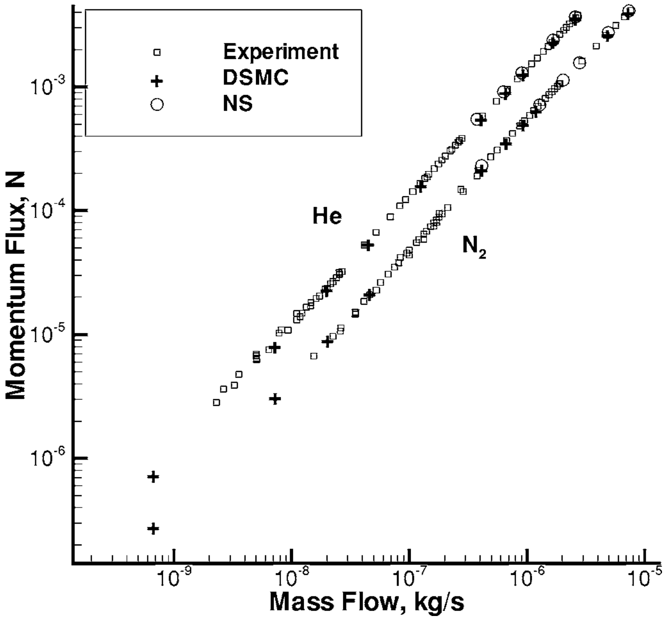

FIG. 8. Momentum flux versus mass flow for helium and nitrogen at $t/d=1.2$: numerical modeling and experiment.

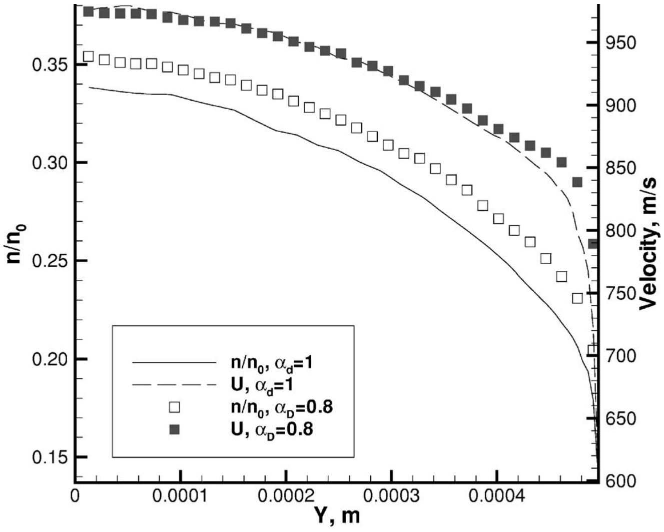

FIG. 9. Normalized density and axial velocity (m/s) profiles at the orifice exit for $\alpha_D=1$ and $\alpha_D=0.8$. Helium, $t/d=1.2$, $P_0=410$ Pa.

and therefore smaller influence of the plume-background gas interaction on the force on the front side of the plenum. The results of measurements of the momentum flux are given in Fig. 8 for $t/d=1.2$ and two gases. Similar to the $t/d=0.015$ case, the momentum flux is nearly linear versus the mass flow. The numerical predictions of the momentum flux through a tube with $t/d=1.2$, both kinetic and continuum, are in very good agreement with the experimental data in the entire range of considered pressures.

While the facility effects are the primary reason for experimental uncertainties, the most probable reason for numerical inaccuracy is thought to be the uncertainty in the gas-surface interaction model. Obviously, flows with larger t/d are especially sensitive to the choice of this model. Although the agreement between the numerical and experimental data for mass flow and momentum flux speaks for the diffuse model as a reasonable assumption in this case, the DSMC computations have also been performed for $t/d=1.2$ with a Maxwell (specular-diffuse) model with an accommodation coefficient $\alpha_D=0.8$ (20% molecules are reflected specularly, and 80% diffuse). Generally, surface specularity in a straight tube increases the mass flow, and for a fully specular reflection of molecules on the surface the mass flow is the same as for an infinitely thin orifice. For a diffuse-specular reflection, the mass flow is expected to fall between these two limits, with the surface impact being smaller for higher pressures due to a thinner boundary layer. An interesting fact is that surface specularity primarily affects the density field, and not the axial velocity. This is illustrated in Fig. 9, where the normalized density and axial velocity profiles are given along the exit. The results are shown for a plenum pressure of 410 Pa (Kn=0.0425) since the impact of the accommodation coefficient is maximum in this case. Axial velocity for the two α_D parameters almost coincide, except for a small region near the surface where the velocity of the more specular case is higher. The number density, however, is proportionally lower for $\alpha_D=0.8$ at any location inside the tube exit. The mass flow and the momentum flux for $\alpha_D=0.8$ are 0.136×10^{-6} kg/s and 0.178×10^{-3} N, respectively. This is an increase about 8% compared to the fully diffuse case. Since the numerical data agree with the measurements within 1 to 2%, the actual surface specularity is much smaller than the assumed 20% for $\alpha_D=0.8$.

VII. INFLUENCE OF WALL THICKNESS ON MASS FLOW AND MOMENTUM FLUX

The friction at the tube surface results in significantly lower mass flows for thicker tubes, even for relatively high pressures. This is illustrated in Fig. 10, where the experimental values of mass flow for different thickness-to-diameter ratios and two gases are presented. Note that the mass flow as a function of pressure is almost linear in the range of pressures from 100 to 2000 Pa, which means that the flow structure essentially does not change for Knudsen numbers Kn<0.1. The situation is different when the tube length becomes comparable to the tube diameter. In this case, the flow slowly transitions from free molecular, when molecules pass through a tube without collisions, to continuum, when the boundary layer thickness becomes negligibly small. This transition is responsible for the noticeable, especially at $t/d=1.2$, curvature of the mass flow versus pressure. This is true both for a monatomic and a diatomic gas. The boundary layer inside the tube significantly lowers that tube throughput, and in the transitional regime the mass flow for $t/d=0.5$ is closer to $t/d=1.2$ than $t/d=0.015$. The momentum flux versus mass flow weakly depends on the tube length (cf. Figs. 7 and 8). The momentum flux for the thickest tube, $t/d=1.2$, is only a few percent higher than that for $t/d=0.015$ for the entire range of considered mass flows.

In order to better understand the reasons for difference between the thinnest and the thickest tubes considered in this work, it is beneficial to examine the thick-to-thin ratios of momentum fluxes and mass flows. These ratios were ob-

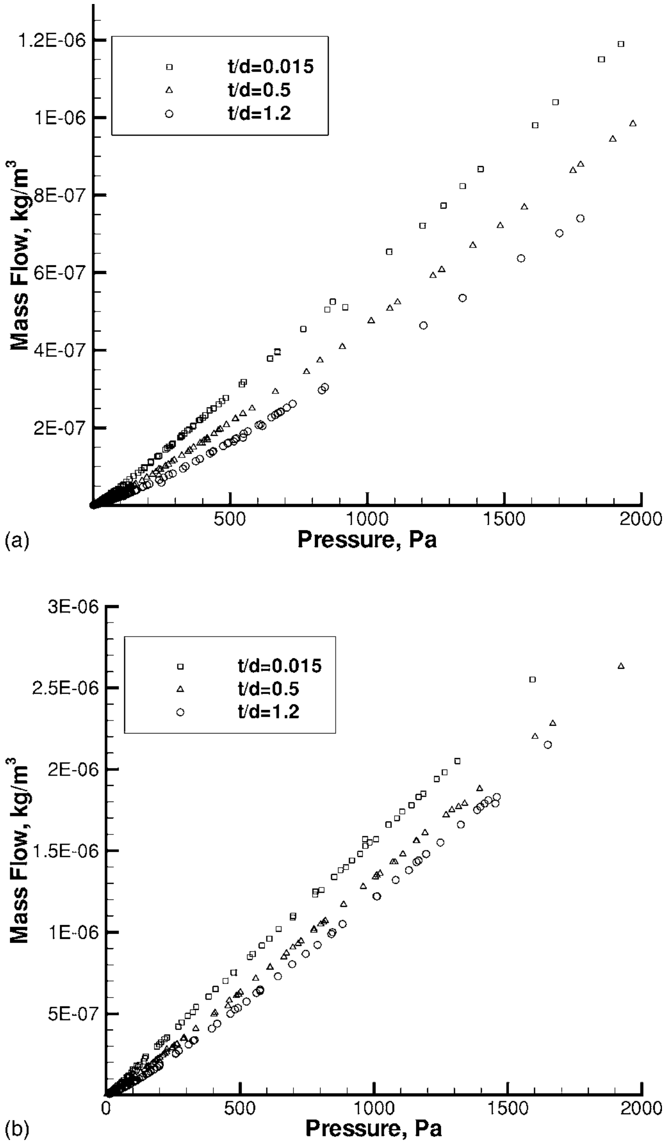

FIG. 10. Measured mass flow as a function of plenum pressure for three t/d ratios. Helium (top) and nitrogen (bottom).

tained at fixed pressures both using the DSMC method and experimentally, and the results are shown in Fig. 11. Both mass flow and momentum flux ratios generally decrease with pressure for pressures ranging from nearly continuum regime down to $P \approx 100$ Pa, which correspond to a Knudsen number of about 0.25. The most remarkable feature is a minimum observed both for mass flow and force ratios at pressures between 50 and 100 Pa ($0.25 < \mathrm{Kn} < 0.5$). After that, the ratios increase slightly toward the free molecular regime.

The minimum is very small, about 1%, for the mass flow ratio, and although it is visible in numerical modeling, it could not be confirmed experimentally due to larger scatter in experimental data. For the momentum flux, however, this minimum amounts to almost 10% of the free molecular value, and is clearly seen both numerically and experimentally, as shown in Fig. 11. The qualitative explanation for the minimum is somewhat similar to that for the Knudsen minimum effect, cited in Sec. I. Let us first compare the flow though tubes with $t/d=0.015$ and $t/d=1.2$ in the free molecular regime. Practically all molecules that intersect the tube entrance plane leave the plenum when $t/d=0.015$ (only about 1.5% of the total number of intersecting molecules will return back to the plenum). For a larger thickness, however, the transmission probability may be much lower than unity, depending on t/d ratio, which explains much lower mass flows in this regime.

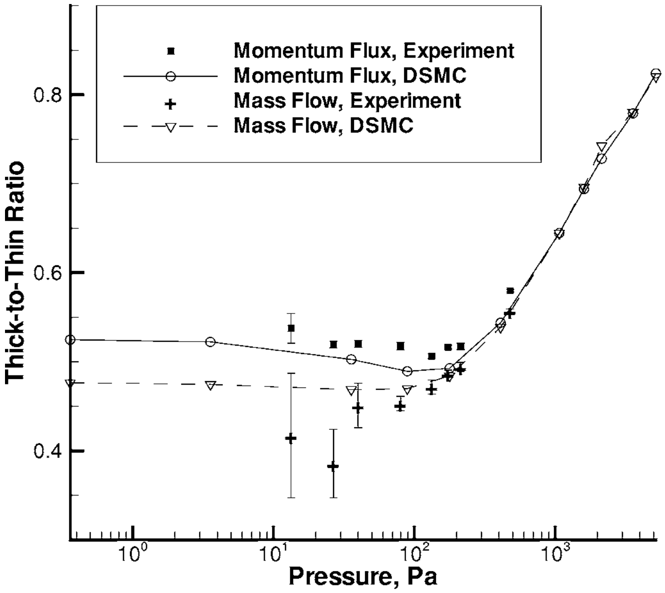

FIG. 11. Ratio of the mass flow and momentum flux for $t/d=1.2$ to the corresponding values at $t/d=0.015$. Helium flow.

As the Knudsen number decreases, the effect of collisions for $t/d=1.2$ becomes significant. This effect for relatively high Knudsen numbers results in a decrease in mass flow since molecules that have relatively high axial velocities and whose contribution to mass flow is highest now have a finite probability to collide with molecules that previously collided with the tube surface. The contribution of these high axial velocity molecules therefore goes down as their axial velocity decreases after such collisions. The further decrease in the Knudsen number results in a general drift of molecules downstream toward the exit due to intermolecular collisions. The overall drift velocity increases as the boundary layer inside the tube decreases, thus reducing the difference between mass flow and force obtained for $t/d=1.2$ and $t/d=0.015$.

To examine the observed minimum in more detail, the DSMC computation has been performed for a $t/d=1.2$ tube at $P_0=35.7$ Pa ($\mathrm{Kn}=0.5$), using four chemically identical species characterized as follows: Species 1 is assigned to molecules that come from the upstream boundaries inside the plenum. To see the effect of molecular collisions, species 2 is created from molecules of species 1 after they collide with any other species inside the tube. When molecules of species 1 collide with the tube surface, they are transformed to species 3. Finally, species 4 is created from molecules of species 2 that collide with the tube surface and molecules of species 3 that collide with other molecules inside the tube.

The distribution of mole fractions of these species along the tube axis is shown in Fig. 12. Here, the tube starts at

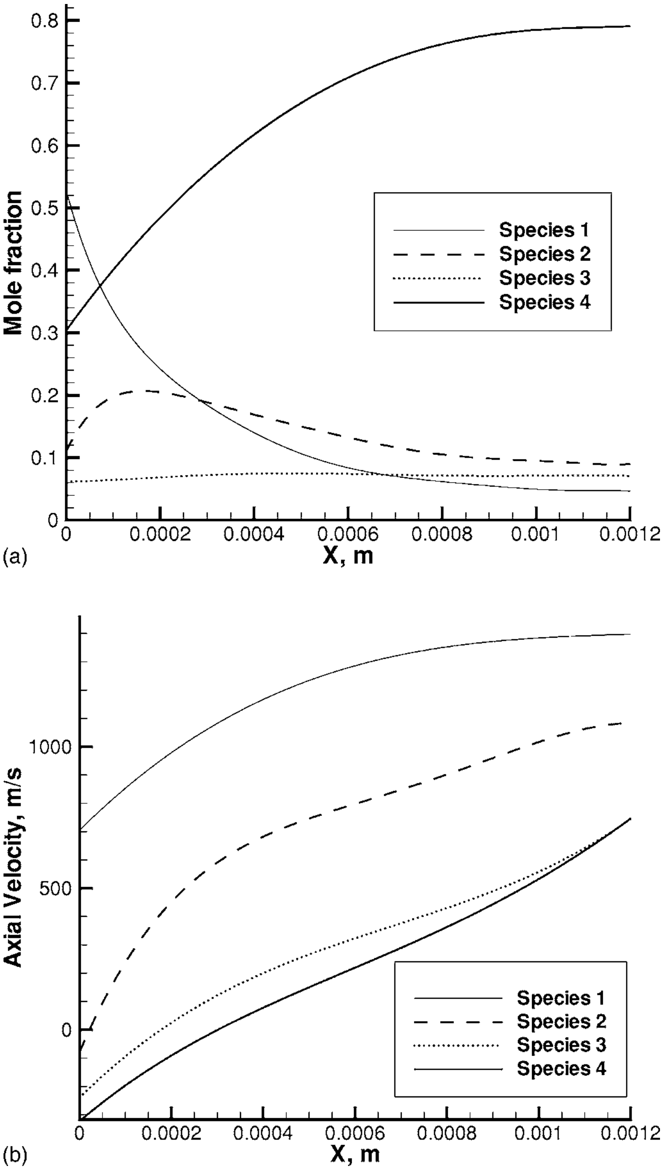

FIG. 12. Distribution of the mole fractions (top) and axial velocities (bottom) of different species along the tube axis. Helium flow, $t/d=1.2$, $P_0=35.7$.

$X=0$ and ends at $X=0.001\ 20$ m. Note that although the fraction of molecules with no surface or molecular collisions (species 1) decreases significantly through the tube, it still remains at about 5% at the exit plane. Species 1 is quickly replaced by species 2, 3, and 4. The computation also shows that most particles leaving the tube collide both with the surface and with other particles (species 4).

A small number of particles that do not experience any collisions inside the tube still make significant contribution to the mass flow and momentum flux due to their high axial velocity. As shown in Fig. 12, the average axial velocity of molecules of species 1 at the exit is about two time higher than those of species that collided with the tube surface. The velocity of molecules that have only intermolecular collisions inside the tube is between these two limits. It is obvious that the decrease in the number of intermolecular collisions in gas toward the free molecular regime results in a larger fraction of molecules of species 1 at the exit plane, and as the result an increase in the mass flow and especially momentum flux. For larger pressures, the average velocity of species 4 is expected to be higher due to the combined effect of molecular collisions on drift velocity.

VIII. CONCLUSIONS

Low density flows through short circular tubes have been studied experimentally and numerically for thickness-to-diameter ratios from 0.015 to 1.2. The nano-Newton Thrust Stand installed in CHAFF-IV was used in the experiments; the computations were performed with the kinetic (the direct simulation Monte Carlo) and continuum (solution of the Navier-Stokes equations) methods. The scope of the work was to examine the mass flow and momentum flux for two gases, helium and nitrogen, in the range of Knudsen numbers from 0.001 to 40. The primary motivation for the work was to study propulsion efficiency of short tubes at low Reynolds numbers, from 0.02 to 770. For the first time, momentum flux through short tubes has been measured, and propulsion efficiency of orifices versus short tubes has been analyzed.

The results obtained with the continuum approach for $\mathrm{Kn}<0.01$ are in very good agreement with the DSMC predictions in terms of the flow fields, and mass flow, and momentum flux. It was also shown that the numerical predictions of the mass flow/discharge coefficient and momentum flux are in good agreement with the experimental data for all plenum pressures under consideration. The impact of background gas pressure in the chamber was analyzed and found to be insignificant for pressures smaller than 1000 Pa. Although millimeter-scaled configurations have been used in this study, similarity parameters such as the Reynolds and Knudsen numbers allow one to generalize the conclusions of this work to microscale flows. Lately, the area of microscale flows has drawn considerable interest from researchers, which has stimulated the reconsideration of old numerical techniques (such as solutions to the Barnett equations) and the development of new approaches (such as the Information Preservation technique). Excellent agreement between both numerical solutions and the experimental data shows that these more conventional computational approaches are still capable of an accurate prediction of gas flows through short tubes in the entire flow regime from free molecular to continuum. This agreement also indicates that the data, both numerical and experimental, may serve as a reliable basis for comparison and method validation.

The effect of the tube thickness was studied, and a minimum was observed both numerically and experimentally for thick-to-thin orifice ratios of momentum flux versus pressure. The minimum occurs at a Knudsen number between 0.25 and 0.5 and is approximately 10% of the corresponding free molecular values. The minimum in the mass flow ratio on the order of 1% was also shown numerically. The qualitative explanation for the minimum is similar to that of the Knudsen minimum effect; namely, a disproportionately large contribution to mass flow and force from molecules with large axial and small radial velocities. This contribution decreases as these molecules collide with molecules reflected from the surface at the flow regime where intermolecular collisions are too rare for a collisional drift to be initiated.

The thick orifice propulsion efficiency is much higher than that of a thin orifice, but does not change significantly when thickness-to-diameter ratio changes from 0.5 to 1. The effect of surface specularity on a thick orifice specific impulse were found to be relatively small.

ACKNOWLEDGMENTS

This work was supported in part by the Propulsion Directorate of the Air Force Research Laboratory at Edwards Air Force Base, California. G.N.M. thanks Jean Muylaert (ESA-ESTEC/TEC-MPA, the Netherlands) for his support of this work, and Paul Pearson (AOES, the Netherlands) for his help with computer resources for the Navier-Stokes computations. S.F.G. and A.D.K. thank Cedrick Ngalande for his assistance with the CHAFF-IV flow analysis.

[1] A. Jamison, A. Ketsdever, and E. P. Muntz, "Gas dynamic calibration of a nano-Newton thrust stand," Rev. Sci. Instrum. **73**, 3629 (2002).
[2] A. D. Ketsdever, M. T. Clabough, S. F. Gimelshein, and A. A. Alexeenko, "Experimental and numerical determination of micropropulsion device efficiencies at low Reynolds numbers," AIAA J. **43**, 633 (2005).
[3] F. Sharipov and V. Seleznev, "Data on internal rarefied gas flows" J. Phys. Chem. Ref. Data **27**, 657 (1998).
[4] I. Papautsky, T. Ameel, and A. B. Frazier, "A review of laminar single-phase flow in microchannels," in *Proceedings of the 2001 ASME International Mechanical Engineering Congress*, 11–16 November 2001 (ASME, New York, 2001).
[5] M. Knudsen, Ann. Phys. **28**, 999 (1909).
[6] W. G. Pollard and R. D. Present, "On gaseous self-diffusion in long capillary tubes," Phys. Rev. **73**, 762 (1948).
[7] A. K. Sreekanth, "Slip flow through long circular tubes," in *6th International Symposium on Rarefied Gas Dynamics* (Academic, New York, 1969), Vol. 1, pp. 667–680.
[8] H. Henning, "The approximate calculation of transmission probability for the conductance of tubulation in the molecular flow regime," Vacuum **28**, 151 (1977).
[9] R. G. Lord, F. C. Hurlbut, and D. R. Willis, "Nearly free molecule flow through a circular orifice at high pressure ratios," in *6th International Symposium on Rarefied Gas Dynamics* (Academic, New York, 1969), Vol. 2, pp. 1235–1243.
[10] A. K. Sreekanth, "Transition flow through short circular tubes," Phys. Fluids **8**, 1951 (1965).
[11] F. O. Smetana, W. A. Sherrill, and D. A. Schort, "Measurements of the discharge characteristics of sharp-edged and round-edged orifices in the transition regime," in *6th International Symposium on Rarefied Gas Dynamics* (Academic, New York, 1969), Vol. 2, pp. 1243–1257.
[12] C. R. Kaplan and E. S. Oran, "Scaling issues for calculations of low-velocity gaseous microflows," in 1999 International Conference on Modeling and Simulation of Microsystems; Nano Science and Technology Institute, Cambridge, MA, Nano Science and Technology Institute, 1999, pp. 506–509.
[13] F. Sharipov and D. Kalempa, "Gaseous mixture flow through a long tube at arbitrary Knudsen numbers," J. Vac. Sci. Technol. A **20**, 814 (2002).
[14] P. Bahukudumbi and A. Beskok, "A phenomenological lubrication model for the entire Knudsen regime," J. Micromech. Microeng. **13**, 873 (2003).
[15] A. Ketsdever, "Thrust measurements of an underexpanded orifice in the transitional regime," in *Proceedings of the 23rd International Symposium on Rarefied Gas Dynamics*, edited by A. Ketsdever and E. P. Muntz (American Institute of Physics, Melville, NY, 2002), pp. 1057–1064.
[16] A. Alexeenko, S. Gimelshein, D. Levin, A. Ketsdever, and M. Ivanov, "Measurements and simulation of orifice flow for micropropulsion testing," J. Propul. Power **19**, 588 (2003).
[17] T. Lilly, N. P. Selden, S. F. Gimelshein, A. D. Ketsdever, and G. N. Markelov, "Numerical and experimental study of low Reynolds number flow through thin-walled orifice and short circular tube," AIAA Paper No. 2004-2385, June 2004.
[18] A. D. Ketsdever, R. H. Lee, and T. C. Lilly, "Performance testing of a microfabricated propulsion system for nanosatellite applications," J. Micromech. Microeng. **15**, 2254 (2005).
[19] N. Selden and A. Ketsdever, "Comparison of force balance calibration techniques for the nano-Newton range," Rev. Sci. Instrum. **74**, 5249 (2003).
[20] M. S. Ivanov, G. N. Markelov, and S. F. Gimelshein, "Statistical simulation of reactive rarefied flows: Numerical approach and applications," AIAA Paper 98-2669, June 1998.
[21] M. S. Ivanov and S. V. Rogasinsky, "Analysis of the numerical techniques of the direct simulation Monte Carlo method in the rarefied gas dynamics," Int. J. Math. Model. **3**, 453 (1988).
[22] G. A. Bird, *Molecular Gas Dynamics and the Direct Simulation of Gas Flows* (Clarendon, Oxford, 1994).
[23] A. D. Ketsdever, "Facility effects on performance measurements of micropropulsion systems that utilize gas expansion," J. Propul. Power **18**, 797 (2002).
[24] J. D. Anderson, *Fundamentals of Aerodynamics* (McGraw-Hill, New York, 1984).

JOURNAL OF PROPULSION AND POWER
Vol. 22, No. 4, July–August 2006

Numerical Analysis of Free-Molecule Microresistojet Performance

Zeeshan Ahmed* and Sergey F. Gimelshein†
University of Southern California, Los Angeles, California 90089
and
Andrew D. Ketsdever‡
U.S. Air Force Research Laboratory, Edwards Air Force Base, California 93524

The direct-simulation Monte Carlo method was used to study the flow in a free-molecule microresistojet (FMMR). The FMMR is a microelectromechanical-systems (MEMS) fabricated resistojet that operates by heating a propellant gas as it expands through a series of slots. The flow through a single heater slot of the FMMR was modeled in two dimensions for a range of chamber pressures from 50 to 200 Pa and heater chip temperatures from 300 to 573 K. Using this, the numerical performance of FMMR was computed. The resultant specific impulse was found to agree within 2% of experimental data for nitrogen propellant and within 4% for helium propellant. Then, a full three-dimensional model of the FMMR geometry was made for water vapor as propellant in two steps. First, the flow in the plenum was modeled. FMMR performance parameters were found to be 10% lower than those of the two-dimensional model. Second, the FMMR plume flow was calculated using a starting surface generated from the plenum simulation for two possible locations of the FMMR as a despin thruster on a nanosatellite. The thrust degradation caused by the resultant surface forces was examined, and the net moment of one configuration was found to be 60% higher than the other.

I. Introduction

ONE of the increasing trends in the design of modern space missions is the miniaturization of spacecraft and satellites. As a result, new space technologies, such as spacecraft formation flying, have been promoted by the U.S. Air Force, Defense Advanced Research Projects Agency, and NASA. The growing emphasis on small satellite systems necessitates the development of new propulsion systems able to deliver precise impulse bits while meeting strict mass, size, and power usage limitations.[1]

Various micropropulsion concepts, such as cold gas,[2] catalytic decomposition,[3] mono-propellant, and bipropellant[4] thrusters, are currently being considered for small satellite applications. For chemical and electrothermal micropropulsion devices, the fluid mechanics of reduced length scales (low Reynolds numbers) results in a significant degradation of the thrust efficiency as a result of increased viscous and heat-transfer losses. Both experimental and numerical investigation of fluid flow and performance of microthrusters is necessary for realistic evaluation of new concepts.

The free-molecule microresistojet (FMMR) is an electrothermal propulsion system designed for on-orbit maneuvers of nanospacecraft (mass < 10 kg) (Refs. 5 and 6). The current version of the FMMR[6] is being developed for a Texas A&M (TAM) nanosatellite flight. The flight will investigate the survivability and capability of the water-propelled microthruster for attitude control maneuvers. The FMMR will provide a spin-up capability for the nanosatellite. The thruster system will operate on the vapor pressure of water, stored in either a liquid or solid state (depending on the internal satellite temperature). The propellant gas, originating from a propellant tank and passing through hydrophobic microporous membrane filters and a valve, enters the base of a Teflon® plenum through an inlet. The hydrophobic microporous membrane uses the surface tension of the propellant to serve as a phase separator, allowing only the propellant vapor to pass through. The FMMR heater chip shown in Fig. 1 is attached to the top of the plenum. Propellant molecules gain kinetic energy as they collide with heated walls of the expansion slots. The increase in kinetic energy of the propellant molecules is critical to the performance and operation of the FMMR. Because of the inherently low operating pressures of the FMMR, the propellant molecules are heated primarily through the direct interaction with the expansion slots.[5]

The FMMR exhibits many systemic features that are beneficial to small satellite operations such as low cost, low power consumption, low mass, and low propellant storage volume. The FMMR operates at relatively low stagnation pressure to take advantage of the high storage density of liquid and solid propellants. By operating on the vapor pressure of the stored propellant, the FMMR reduces the amount of power required over thrusters that prevaporize the propellant to create high stagnation pressures. The simple design of the FMMR allows for low-cost manufacturing and testing. The FMMR heater chip allows for large ranges of thrust levels without a significant loss in performance by varying the number and dimensions of the expansion slots.

Previous work has described the fabrication and heat-transfer characteristics of the FMMR concept.[5] Proof-of-principle designs, which showed the utility of the FMMR system for nanosatellite operations, were investigated. Analytical expressions were developed to estimate the overall propulsive efficiency of the design. Recently, the propulsive performance of the FMMR has been determined experimentally.[6] Comparison of the experimental performance data with the analytical results showed that the design of the FMMR based on these free-molecule analytical expressions has met with limited success. The range of operating pressures of the FMMR propulsion system extends into the transitional flow regime where the free-molecule analytical expressions are not completely valid. In Ref. 6, the analytically predicted specific impulse is shown to be up to 20% lower than experimental measurements. Therefore, the need for higher accuracy performance predictions for designing future iterations of the FMMR is evident. In this work, a FMMR is examined numerically. Because typical plenum pressures

---

Presented as Paper 2005-4262 at the AIAA/ASME/SAE/ASEE 41st Joint Propulsion Conference and Exhibit, Tucson, AZ, 10–13 July 2005; received 19 August 2005; revision received 9 December 2005; accepted for publication 12 January 2006. Copyright © 2006 by the authors. Published by the American Institute of Aeronautics and Astronautics, Inc., with permission. Copies of this paper may be made for personal or internal use, on condition that the copier pay the $10.00 per-copy fee to the Copyright Clearance Center, Inc., 222 Rosewood Drive, Danvers, MA 01923; include the code 0748-4658/06 $10.00 in correspondence with the CCC.

*Undergraduate Student.

†Research Assistant Professor.

‡Group Leader, Nonequilibrium Flows Group, Propulsion Directorate.

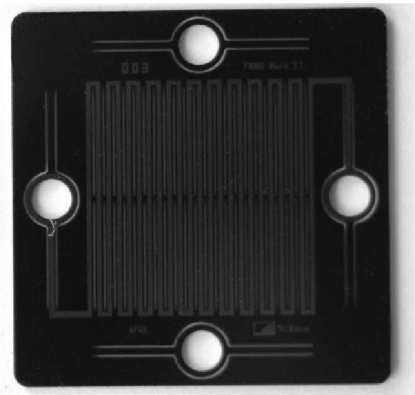

a)

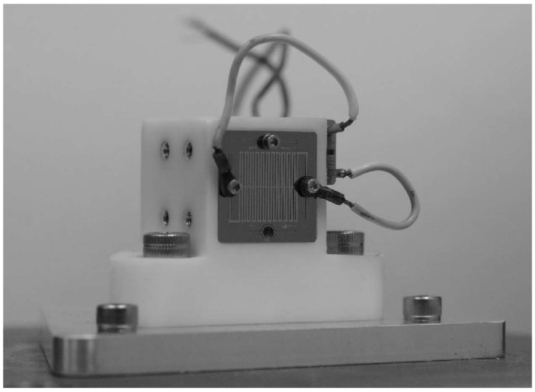

b)

Fig. 1 MEMS fabricated resistojet: a) FMMR heater chip and b) the plenum with the mounted heater chip.

are relatively low (below 1000 Pa) and the Knudsen number based on the slot thickness is on the order of unity, the direct simulation Monte Carlo (DSMC) method has been used in all computations in this study.

The main objectives of this work were threefold. First, the performance of the FMMR was compared to experimental data for different test gases to validate the use of the numerical model and provide a level of confidence in extending the model to simulate performance on the TAM nanosatellite. The second objective was to use the validated code to estimate the level of contamination of a typical spacecraft surface by propellant molecules. Because experimental contamination data are not available, DSMC provides the only means to predict the contamination potential on the TAM nanosatellite. Finally, an analysis of the importance of geometrical and operational parameters, such as plenum pressures and heater chip temperatures, was performed. This final objective was used to investigate the potential of the DSMC technique as a design tool for future iterations of the FMMR system. For initial design criteria, the derived free-molecule analytical expressions given in previous studies[5,6] were utilized. The analytical expressions are valid for low-pressure (high Knudsen number) operation of the thruster but are not expected to be accurate for the higher operating pressure range. Furthermore, future design iterations of the FMMR system will require higher accuracy performance predictions, which might eventually couple the heat-transfer and gas dynamic effects. DSMC offers the opportunity to accurately predict FMMR performance throughout the design process over a wide range of operating parameters.

II. Geometry and Flow Conditions

The current iteration of the FMMR heater chip, shown in Fig. 1a, was designed specifically for the TAM nanosatellite mission. This iteration of the FMMR chip is an 19.2×19.2 mm square with a thickness L of 500 μm. There are 44 interior expansion slots formed in two rows. Each slot is 100 μm wide by 5.375 mm long and is etched completely through the FMMR. The expansion slots are outlined by a serpentine heater pattern consisting of a gold current carrying layer.

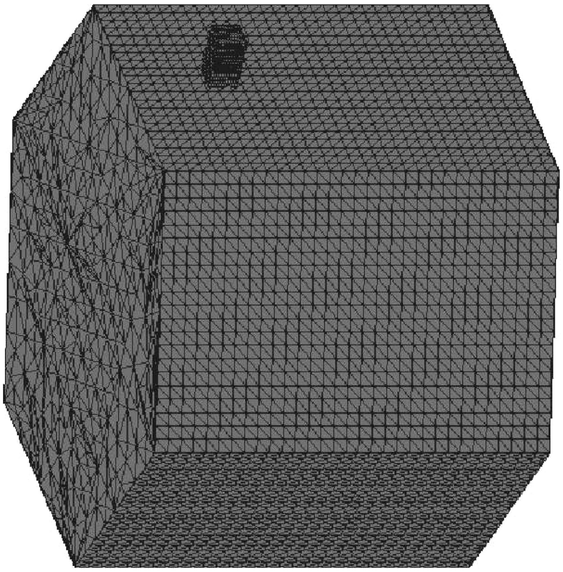

Fig. 2 Satellite geometry.

The plenum is designed as a rectangular box as shown in Fig. 1b. The internal dimensions of the plenum are $11 \times 11 \times 22$ mm. The propellant gas is flowing through the attached tube of 6.35 mm diam, and the plenum pressure can vary from tens to hundreds of Pascals. Although the heater chip temperature will be kept at about 573 K, the temperature of other walls of the plenum will be close to room temperature.

The current design of the satellite represents a 316-mm-long hexagonal cylinder with a side width of 216 mm. The FMMR thruster is mounted on one of the plates of the hexagonal cylinder surface as shown in Fig. 2. The figure also illustrates the triangulated geometry used in the computations.

III. Numerical Approach

The DSMC-based software system SMILE[7] was used in computations. The majorant frequency scheme[8] was used to calculate intermolecular interactions. The intermolecular potential was assumed to be a variable hard sphere.[9] Energy redistribution between the rotational and translational modes was performed in accordance with the Larsen–Borgnakke model. A temperature-dependent rotational relaxation number was used. The reflection of molecules on the surface was assumed to be diffuse with complete energy accommodation.

To examine the flow details inside the plenum, near the expansion slots, as well as in the plume interacting with the spacecraft surface, the computations have been performed in three steps. The first step is the DSMC modeling of a two-dimensional flow through a single expansion slot. The etching technology used in FMMR manufacturing results in a slot geometry that is not rectangular. Therefore, the actual geometry of the slot was evaluated from the scanning electron microscope (SEM) data. (The schematic of the geometry is shown in Fig. 3.) The detailed modeling of the gas flow through a single slot allows for comparison of computed mass flow and thrust with available experimental data[10] for helium and nitrogen propellants. The computations are also performed for water vapor. The second step includes three-dimensional modeling of the water vapor flow inside the plenum and in a small region outside of the FMMR (near field of the plume). The complex geometry of the slots is replaced by rectangular openings described in the preceding section. The third step is the modeling of the plume flow and plume impingement on spacecraft surfaces. A starting surface is generated using the macroparameters obtained at the previous step. The starting surface specifies inflow boundary conditions used for the

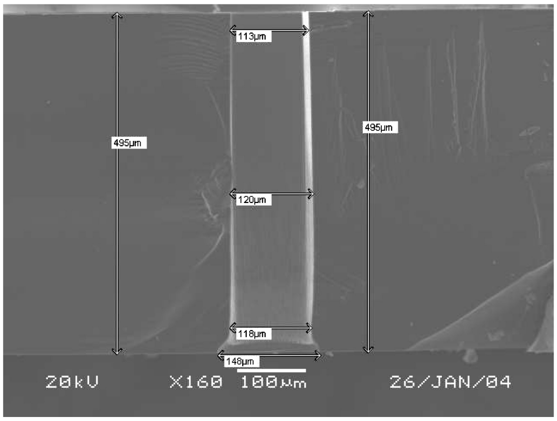

Fig. 3 SEM image of a single slot of FMMR (right).

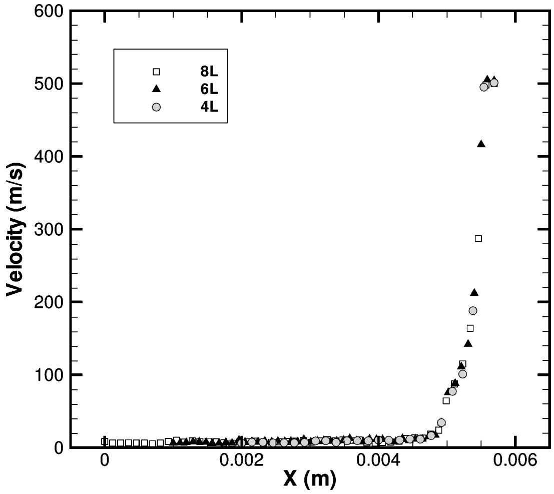

Fig. 4 Axial-velocity profile along the axis of symmetry for different computational domains.

plume impingement modeling step. The surface is 2×2 cm and is located 0.5 mm downstream from the heater chip plane. The inflow molecules are introduced from the starting surface with parameters calculated at the second step; the molecules are sampled from the corresponding ellipsoidal[11] distribution functions. The use of the ellipsoidal distribution function is important because there is a significant, up to a factor of two, difference in temperatures in the directions parallel and perpendicular to the plume.

The DSMC method is conventionally used to model supersonic and hypersonic flows where the boundary conditions are either supersonic inflow or vacuum outflow. For subsonic flows, such as the flow inside the plenum, the application of the DSMC method is more complicated. In the present study, the convergence study has been conducted in order to establish the minimum necessary size of the computational domain. Note that for all two-dimensional computations zero flow velocity was assumed at the inflow boundaries, with the constant pressure and temperature corresponding to given stagnation conditions. Vacuum outflow conditions were used in all of the computations shown next.

The convergence study has been performed for a nitrogen flow and the length of the plenum portion of the computational domain varying from 4 to $8L$. Comparison of the axial velocity and pressure profiles along the slot centerline are shown in Figs. 4 and 5, respectively. The slot entrance is located at $X = 0.005$ m. The difference between the three cases is within the statistical uncertainty of the computations, which was a few percent for flowfields and less than a percent for integral properties, such as mass flow and thrust. Because no visible influence of the computational domain size was observed when the subsonic chamber length was increased from $4L$ to $8L$, the value of $4L$ was used thereafter. A sensitivity study has also been performed with the downstream domain size varied several times to obtain solutions free of the influence of the downstream domain. The downstream domain length of $18L$ was used in the computations discussed in the next section. The typical numbers of collision cells and simulated molecules are 50,000 and one million, respectively.

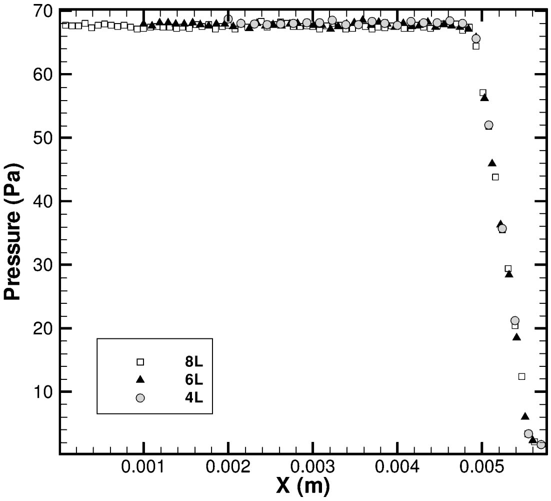

Fig. 5 Pressure profile along the axis of symmetry for different computational domains.

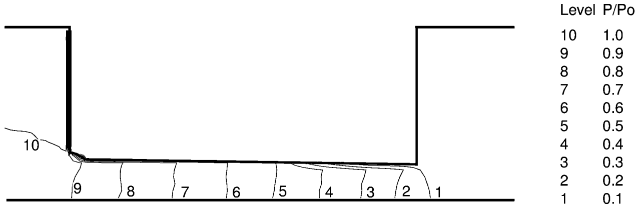

Fig. 6 Normalized pressure fields for $P_0 = 49$ Pa and the heater chip temperature of 300 K, area shown 750 × 250 μm.

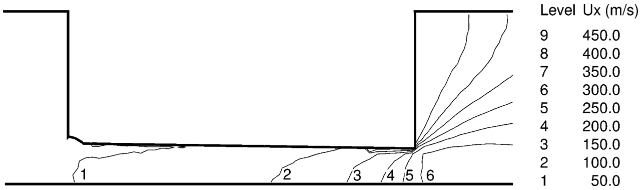

Fig. 7 Axial-velocity (m/s) fields for $P_0 = 49$ Pa and the heater chip temperature of 300 K, area shown 750 × 250 μm.

IV. Effects of Heater Chip Temperature and Stagnation Pressure on Flowfields

The FMMR will operate at an elevated heater chip temperature of about 573 K in order to achieve acceptable efficiency of the thruster. Because the Knudsen number will be about unity based on the slot width, the molecule exit velocity will be primarily determined by the surface temperature and is expected to be proportional to the square root of this temperature T_w. The mass flow is therefore expected to be proportional to the product of the gas density near the slot exit n_e and $\sqrt{T_w}$, whereas the thrust is proportional to $n_e T_w$.

The structure of the flow inside a single slot is shown in Fig. 6 for nitrogen propellant. The pressure values here are normalized by the plenum value. The computations showed that the impact of surface temperature on pressure is negligible—the variation is within 1%. The gas temperature near and inside the slot was found to be close to the surface temperature both for 300 and 573 K, whereas the gas density inside the slot normalized by the plenum value is not affected by the surface temperature.

However, the flow velocity changes significantly with temperature, as illustrated in Figs. 7 and 8. The velocity reaches 50 m/s

Table 1 FMMR performance in nitrogen: two-dimensional computations

P_0, Pa	T_w, K	Mass flow, kg/s	Thrust, N	Isp, s
49	300	$6.7975 \cdot 10^{-7}$	$3.0201 \cdot 10^{-4}$	45.29
49	400	$5.9912 \cdot 10^{-7}$	$3.0287 \cdot 10^{-4}$	51.53
49	500	$5.4257 \cdot 10^{-7}$	$3.0235 \cdot 10^{-4}$	56.80
49	573	$5.1239 \cdot 10^{-7}$	$3.0346 \cdot 10^{-4}$	60.37
69	300	$9.6524 \cdot 10^{-7}$	$4.3337 \cdot 10^{-4}$	45.77
69	400	$8.3901 \cdot 10^{-7}$	$4.2863 \cdot 10^{-4}$	52.08
69	500	$7.5192 \cdot 10^{-7}$	$4.2418 \cdot 10^{-4}$	57.51
69	573	$7.0806 \cdot 10^{-7}$	$4.2421 \cdot 10^{-4}$	61.07
95	300	$1.3343 \cdot 10^{-6}$	$6.0446 \cdot 10^{-4}$	46.18
95	400	$1.1502 \cdot 10^{-6}$	$5.9265 \cdot 10^{-4}$	52.52
95	500	$1.0299 \cdot 10^{-6}$	$5.8689 \cdot 10^{-4}$	58.09
95	573	$9.6222 \cdot 10^{-7}$	$5.8319 \cdot 10^{-4}$	61.78
139	300	$1.9982 \cdot 10^{-6}$	$9.1677 \cdot 10^{-4}$	46.77
139	400	$1.7075 \cdot 10^{-6}$	$8.9177 \cdot 10^{-4}$	53.24
139	500	$1.5112 \cdot 10^{-6}$	$8.7141 \cdot 10^{-4}$	58.78
139	573	$1.4081 \cdot 10^{-6}$	$8.6446 \cdot 10^{-4}$	62.58
185	300	$2.7053 \cdot 10^{-6}$	$1.2521 \cdot 10^{-3}$	47.18
185	400	$2.2717 \cdot 10^{-6}$	$1.1970 \cdot 10^{-3}$	53.71
185	500	$2.0041 \cdot 10^{-6}$	$1.1677 \cdot 10^{-3}$	59.39
185	573	$1.8527 \cdot 10^{-6}$	$1.1473 \cdot 10^{-3}$	63.12

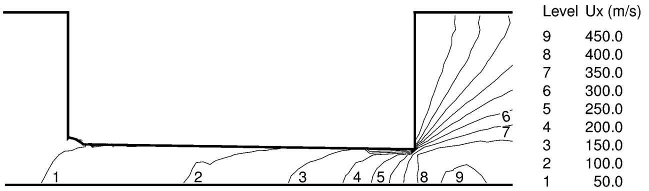

Fig. 8 Axial-velocity (m/s) fields for $P_0 = 49$ Pa and the heater chip temperature of 573 K, area shown 750 × 250 μm.

inside the slot for 300 K case and upstream from the slot entrance for 573 K. The magnitude of the difference increases toward the slot exit and reaches over 100 m/s for the gas that leaves the slot (280 m/s for 300 K and almost 400 m/s for 573 K). This increase is nearly proportional to $\sqrt{T_w}$. Note that this proportionality can be expected for a long channel and near free-molecule flow; it is not obvious however for a slot with a finite length-to-thickness ratio of five, a Knudsen number of one, and $T = 300$ K. In the latter case there are two more contributing sources that complicate the analysis. First, molecules that come directly from the plenum without interacting with the slot walls increase the average velocity. Second, molecules that collide with other molecules generally decrease the velocity. If these sources are small compared to the main surface-generated source, or if they compensate each other, the velocity will be proportional to $\sqrt{T_w}$.

The computations performed for a stagnation pressure of 185 Pa have shown that an almost four-fold increase in pressure does not change the flow pattern. Although the molecular collisions inside the slot become likely as the mean free path becomes one-fourth of the slot width, the length of the slot is still sufficient to increase velocities of most particles coming through it. Also, the average exit velocities are almost identical for 49 and 185 Pa.

V. FMMR Performance and Comparison with Experimental Data

Consider now the performance characteristics of a single FMMR slot for various gas pressures and surface temperatures. The mass flow, thrust, and specific impulse are listed in Table 1 for a nitrogen flow. For all cases, the mass flow is nearly inversely proportional to $\sqrt{T_w}$. Some deviation from the proportionality is related primarily to the effect of gas-gas collisions inside the slot. There is also some finite number of molecules, especially for lower pressures, that come directly from the plenum without interacting with heated slot walls.

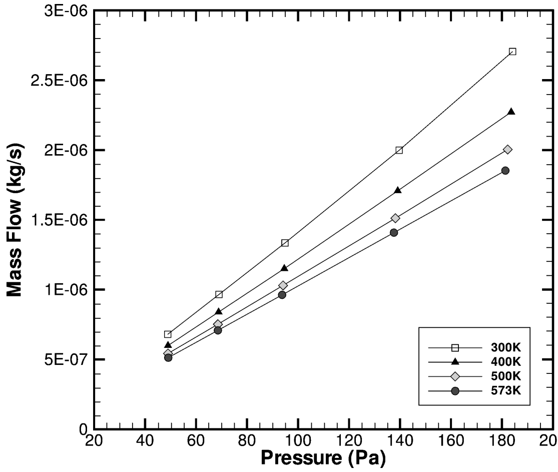

Fig. 9 Mass flow of nitrogen vs computed plenum pressure for different heater chip temperatures.

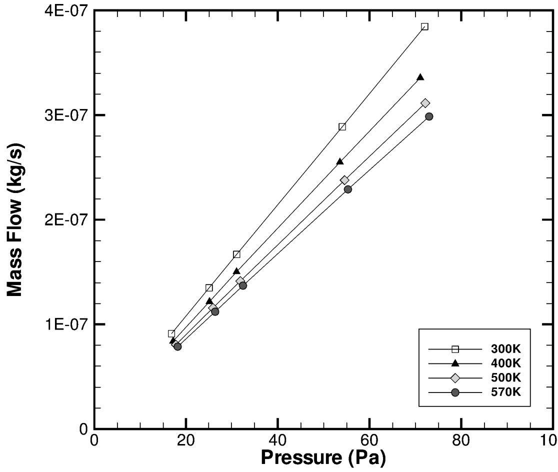

Fig. 10 Mass flow of helium vs computed plenum pressure for different heater chip temperatures.

There is a relatively weak dependence of thrust on surface temperature because the gas density is inversely proportional to T_w throughout the slot, whereas the velocity squared is proportional to T_w. The thrust does not change with T_w for $P_0 = 49$ Pa. At $P_0 = 185$ Pa, however, there is a 10% thrust degradation between heater chip temperatures of 300 and 573 K. The specific impulse slightly increases with pressure, with I_{sp} for $P_0 = 185$ Pa about 4% higher than for $P_0 = 49$ Pa. The ratio of specific impulse values for 573 K to that for 300 K does not depend on pressure and is equal to about 1.34. This is somewhat lower than the theoretical free-molecular value of 1.38.

The numerical results for the mass flow as a function of pressure at different heater chip temperatures are presented in Figs. 9 and 10 for two propellants, nitrogen and helium. The DSMC values of stagnation pressure are used here, obtained as an average over all plenum cells. It is clearly seen that in the considered range of pressures the mass flow is nearly linear for all surface temperatures, $\dot{m} \approx Cp_0$. The proportionality coefficient C is in turn inversely proportional to T_w.

At a fixed pressure, the mass flow strongly depends on the geometry of the heater chip. Although the shape of the FMMR slot cross sections is known qualitatively, the uncertainty in the actual dimensions, primarily entrance and exit width, is no better than 10%. Moreover, the dimensions can differ for different slots. These uncertainties prevent direct comparison of mass flow and thrust computed as functions of pressure with the corresponding experimental data. They are however expected to be a minor issue for comparison of thrust vs mass flow because the pressure dependence is weak in this case.

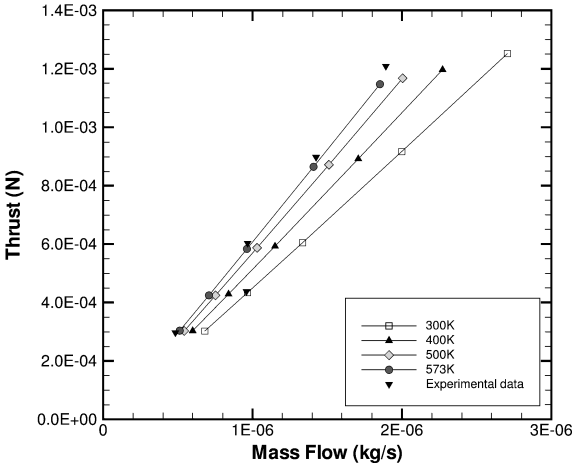

Fig. 11 Thrust force in nitrogen vs mass flow rate for different heater chip temperatures: comparison with experimental data.

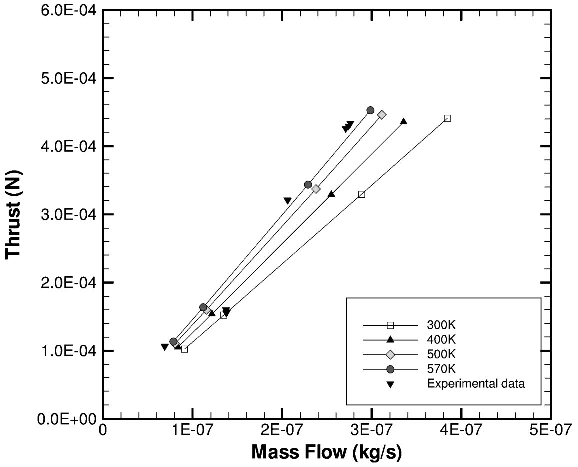

Fig. 12 Thrust force in helium vs mass flow rate for different heater chip temperatures: comparison with experimental data.

Comparison of the calculated force with the experimental data[10] at 573 K for nitrogen and 300 and 573 K for helium is given in Figs. 11 and 12. As expected, both experimental and numerical thrust values exhibit nearly linear dependence vs mass flow. For nitrogen, the computed thrust is about 2% lower than the experimental values. This is attributed primarily to the impact of the plume molecules backscattered to the outer surface of the heater chip. Such molecules increase the total thrust force, and such an impact is underestimated because of the limitations of the two-dimensional numerical statement of the problem. The impact of the backscattered molecules is larger for helium because of its lower mass and larger backscattering; as a result, the difference between the computed and measured thrust values is somewhat larger for this gas.

VI. Three-Dimensional Modeling of the Plenum Flow

The modeling of the FMMR plume flow was performed in two steps. First, the flow inside the plenum and in the near field of the plume was calculated. The numbers of simulated molecules and collision cells in these computations were about 3 million and 0.6 million, respectively. The results were used to specify gas parameters at a starting surface parallel to the outer heater chip plane and 0.5 mm downstream. The starting surface is utilized in the subsequent modeling of the plume interaction and impingement. Because water vapor has been identified as the ideal FMMR propellant, it was used in these computations.

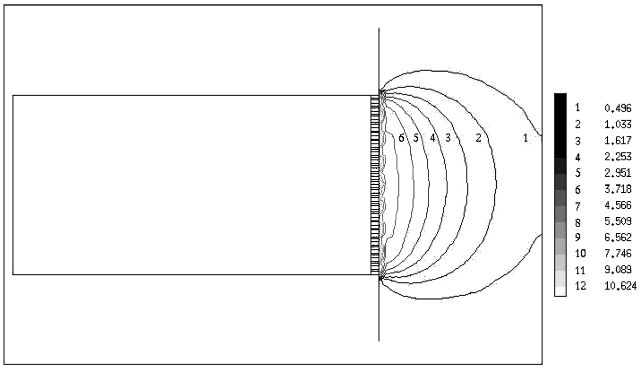

Fig. 13 Pressure (Pa) field inside the plenum for $P_0 = 306.5$ Pa and $T_w = 573$ K, area shown 33 × 23 mm.

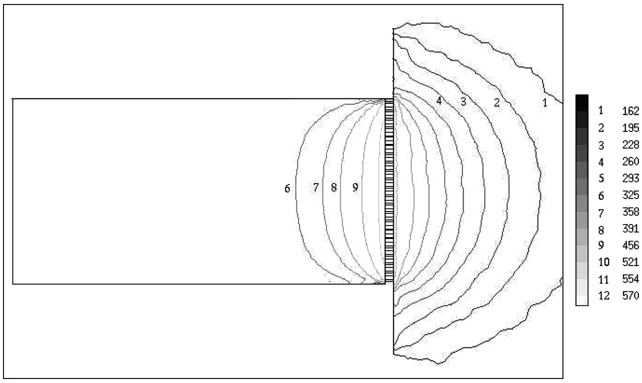

Fig. 14 Translational temperature field inside the plenum for $P_0 = 306.5$ Pa and $T_w = 573$ K, area shown 33 × 23 mm.

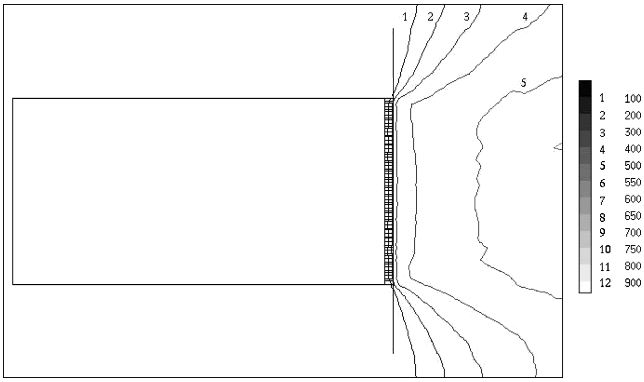

Fig. 15 Flow velocity for $P_0 = 306.5$ Pa and $T_w = 300$ K, area shown 33 × 23 mm.

The results of plenum flow modeling are presented in Figs. 13 and 14, where the pressure and temperature fields are shown respectively for $P_0 = 306.5$ Pa and heater chip temperature of 573 K at the symmetry plane. The figure also illustrates the geometry of the plenum. The gas is supplied through a 6.35-mm tube located at the top left part of the plenum. No significant pressure gradients were observed inside the plenum, with pressure decreasing by less than 1% from the inflow tube to the heater chip. The gas temperature increases from the inflow value of 300 to 573 K in the heated slot region. Note that the increase occurs in the downstream quarter of the plenum, and the gas temperature is significantly less in the regions close to the top and bottom plenum walls that are kept at 300 K. The gas temperature is constant inside the slots and decreases rapidly in the expansion region.

The flow velocity in the direction perpendicular to the heater chip is shown in Figs. 15 and 16 for two heater chip temperatures. Similar to the two-dimensional case, the velocity is higher for 573 K; however, the difference is somewhat smaller for the three-dimensional flow. Note also that multiple jets result in velocity isolines being parallel to the heater chip plane outside the chip; this flow pattern propagates more than 2 cm downstream.

Table 2 FMMR performance for water vapor: three- and two-dimensional simulations

P_0, N/m^2	Wall temperature, K	Case	Mass flow, kg/s	Thrust, N	Isp, s
61.3	300	Three-dimensional	$4.9124 \cdot 10^{-7}$	$2.5970 \cdot 10^{-4}$	53.89
61.3	300	Analytic	$4.2869 \cdot 10^{-7}$	$2.7607 \cdot 10^{-4}$	65.71
61.3	570	Two-dimensional	$4.3984 \cdot 10^{-7}$	$3.1847 \cdot 10^{-4}$	73.81
61.3	570	Three-dimensional	$4.0872 \cdot 10^{-7}$	$2.8756 \cdot 10^{-4}$	71.72
306.5	300	Three-dimensional	$4.0872 \cdot 10^{-6}$	$1.0957 \cdot 10^{-3}$	54.40
306.5	300	Analytic	$2.1435 \cdot 10^{-6}$	$1.3804 \cdot 10^{-3}$	65.71
306.5	570	Two-dimensional	$2.0655 \cdot 10^{-6}$	$1.5605 \cdot 10^{-3}$	77.01
306.5	570	Three-dimensional	$1.8112 \cdot 10^{-6}$	$1.3034 \cdot 10^{-3}$	73.35

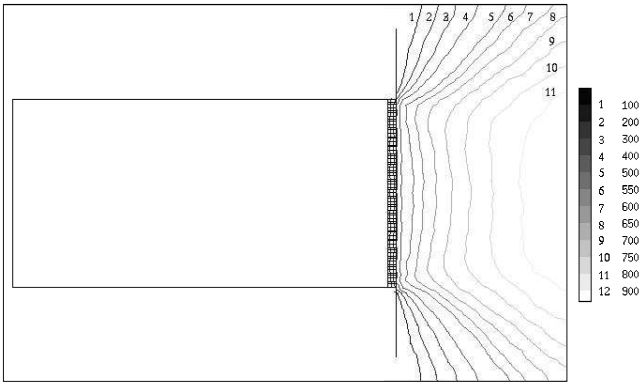

Fig. 16 Flow velocity for $P_0 = 306.5$ Pa and $T_w = 573$ K, area shown 33 × 23 mm.

Let us now examine the impact of heater chip temperature on the FMMR performance. The performance properties are listed in Table 2 for two plenum pressures and two heater temperatures using a water propellant. In contrast to the previous two-dimensional runs, the full three-dimensional modeling results in a simultaneous decrease in the mass flow and increase in thrust when the temperature increases from 300 to 573 K. Note that the decrease in the mass flow is lower than the the square root of the temperature ratio. This behavior is attributed to the impact of the cold plenum walls. The gas is colder than T_w in the downstream corners of the plenum, which in turn causes the larger number density and mass flows at these locations.

Comparison of three-dimensional results with the corresponding two-dimensional parameters (rectangular slots were used in these two-dimensional computations to make comparison meaningful) shows that the complex three-dimensional flow in the plenum results in significantly, about 10%, lower values of both mass flow and thrust. The specific impulse however is close in two- and three-dimensional computations. Generally, it increased by a factor of 1.34 when the heater chip temperature was increased from 300 to 573 K, which is the same as in two-dimensional modeling for helium and nitrogen propellants.

Analytic predictions obtained using the free-molecular analysis of Ref. 10 are also given in Table 2. These estimates were calculated using the assumption that the gas pressure near the FMMR slot entrances is close to the stagnation value, whereas the gas temperature is close to the slot temperature of 573 K. This assumption is reasonable at the range of pressures considered, although it will fail for lower stagnation pressures. The analytic mass flows are within 4% of the corresponding two-dimensional DSMC values, whereas the analytic values of thrust are closer to the three-dimensional DSMC values. As the result, the analytic specific impulse is over 10% lower than that computed with the DSMC method, both two- and three-dimensional.

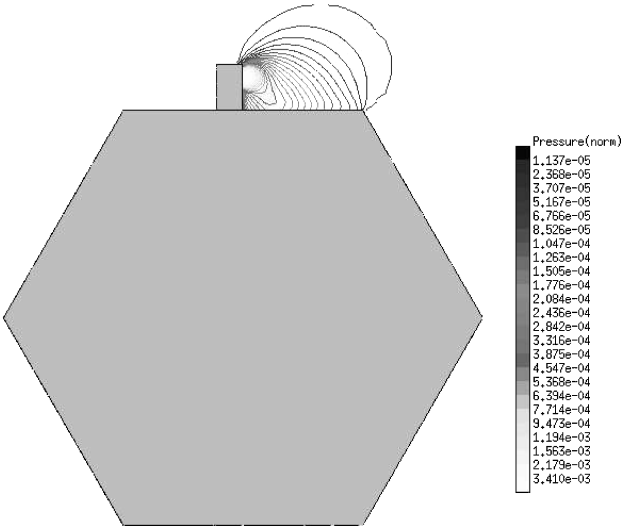

Fig. 17 Normalized pressure field for $P_0 = 306.5$ Pa and $T_w = 573$ K.

VII. Modeling of the Plume Expansion Flow

The modeling of the plume expansion and impingement on the spacecraft surface has been performed for the four three-dimensional cases shown in Table 2. The preceding computations were used to determine parameters for the ellipsoidal distribution function at a starting surface located immediately downstream of the heater chip. Two possible locations of the FMMR were examined, the one shown in Fig. 2 and another one with the FMMR positioned close to the edge of the cylinder panel. The numbers of molecules and cells in these computations were about 5 million and 1.2 million, respectively.

The general flowfield structure for the first location is shown in Fig. 17, where the pressure field normalized by the stagnation value is presented in the plane perpendicular to the heater chip surface and coming through the chip center. Note that the normalized pressure only weakly depends on the plenum pressure when decreased from 306.5 to 61.3 Pa and heater chip temperature when changed from 573 to 300 K. There is a clearly visible interaction region between the plume and the top surface of the satellite approximately 3 cm downstream from the heater chip plane. The pressure there is about 50 times higher than that in the corresponding region above the FMMR.

Figure 18 presents the mass flux of water molecules on the surface of the spacecraft. The important conclusion here is that the plume molecules interact only with the top panel of the spacecraft. No molecular flux was registered on the other panels. This means that molecular flux from the plume will be smaller on these surfaces than that from the freestream in low Earth orbit. The mass flux on the top surface is significant both for contamination and thrust degradation.

The distribution of the mass flux over the spacecraft surface for the second tested location of the FMMR is shown in Fig. 19. There are still water molecules that collide with the cylinder panel where the FMMR is attached, mostly near the panel edge; however, this number is 98% smaller than that for the first considered location. Molecules also reach the adjacent panel of the hexagonal cylinder, and their flux is 85% higher than that for the panel where the FMMR is attached.

Table 3 Thrust degradation of FMMR located on center of panel

P_0, Pa	Wall temperature, K	Surface mass flow, kg/s	Surface force x, N	Surface force y, N	Net thrust x	Net moment, N · m
61.3	300	$1.6628 \cdot 10^{-7}$	$-8.7785 \cdot 10^{-5}$	$-5.6008 \cdot 10^{-5}$	$1.7191 \cdot 10^{-4}$	$2.91 \cdot 10^{-5}$
61.3	573	$1.3623 \cdot 10^{-7}$	$-9.7307 \cdot 10^{-5}$	$-6.0045 \cdot 10^{-5}$	$1.9026 \cdot 10^{-4}$	$3.24 \cdot 10^{-5}$
306.5	300	$7.5071 \cdot 10^{-7}$	$-3.8529 \cdot 10^{-4}$	$-2.7352 \cdot 10^{-4}$	$7.1046 \cdot 10^{-4}$	$1.18 \cdot 10^{-4}$
306.5	573	$6.4807 \cdot 10^{-7}$	$-4.5280 \cdot 10^{-4}$	$-3.0385 \cdot 10^{-4}$	$8.5057 \cdot 10^{-4}$	$1.14 \cdot 10^{-4}$

Table 4 Thrust degradation of FMMR located at edge of panel

P_0, Pa	Wall temperature, K	Surface mass flow, kg/s	Surface force x, N	Surface force y, N	Net thrust x	Net moment, N · m
61.3	300	$4.7786 \cdot 10^{-9}$	$-2.6883 \cdot 10^{-6}$	$-8.5304 \cdot 10^{-6}$	$2.5701 \cdot 10^{-4}$	$4.72 \cdot 10^{-5}$
61.3	573	$2.9353 \cdot 10^{-9}$	$-2.7986 \cdot 10^{-6}$	$-8.4020 \cdot 10^{-6}$	$2.8476 \cdot 10^{-4}$	$5.24 \cdot 10^{-5}$
306.5	300	$3.5330 \cdot 10^{-8}$	$-1.4756 \cdot 10^{-5}$	$-5.4401 \cdot 10^{-5}$	$1.0810 \cdot 10^{-3}$	$1.96 \cdot 10^{-4}$
306.5	573	$2.4430 \cdot 10^{-8}$	$-1.5821 \cdot 10^{-5}$	$-5.3402 \cdot 10^{-5}$	$1.2876 \cdot 10^{-3}$	$2.35 \cdot 10^{-4}$

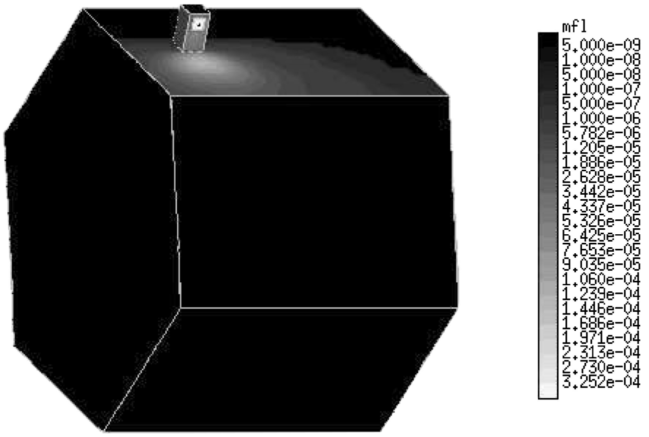

Fig. 18 Surface mass flux (kg/m^2) for $P_0 = 306.5$ Pa and $T_w = 573$ K.

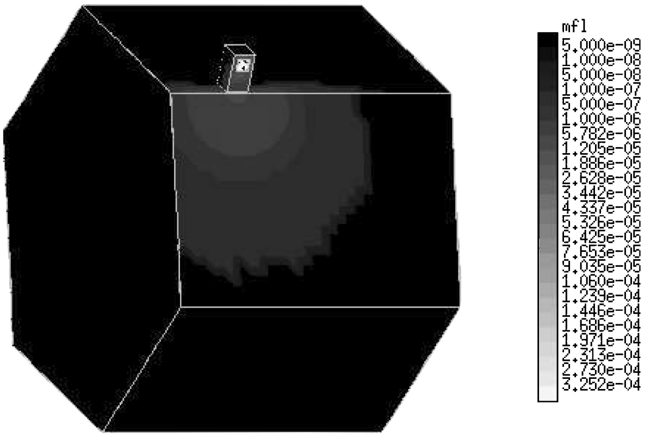

Fig. 19 Surface mass flux (kg/m^2) (right) for $P_0 = 306.5$ Pa and $T_w = 573$ K.

Consider now the impact of the FMMR parameters and location on the integral surface parameters. Tables 3 and 4 show the values of the total surface mass flow for different flow cases. Generally, the amount of plume molecules that hit the surface is nearly proportional to the plenum pressure. Because the mass flow through the heater chip decreases with temperature at fixed pressures, the potential for surface contamination by plume molecules is also lower in this case. This decrease is especially significant for the second location of the FMMR.

Tables 3 and 4 also give the total surface forces in X direction (the direction of the FMMR thrust) and Y direction. For the first location of the FMMR, both X and Y components of the surface forces decrease with the FMMR temperature, thus degrading the net force. The net force column of the table represents the X component of the total force during the operation of FMMR, obtained as a sum of the thrust force (see Table 2) and the surface force. The important conclusion here is that for the first FMMR location the surface force is comparable in magnitude with the thrust force, which results in about 30% thrust degradation as a result of the plume-surface interaction.

When the FMMR is located at the edge of the cylinder panel, the surface force is only about 1% of the thrust force, and the primary factors that contribute to the despinning capability of the FMMR are the thrust force, the direction of the plume, and the arm length. The net despinning moment values are presented in the last column of Tables 3 and 4. For both FMMR locations, the temperature increase from 300 to 570 K results in the net moment increase of 10% for lower pressure and 20% for higher pressure, at a significantly lower mass flow. Most importantly, the second FMMR location is characterized by a 60% higher net moment than the first location. Note that tilting the FMMR clockwise in the second location will increase the contribution of the thrust force to the despinning moment, but at the same time is expected to significantly increase the moment degrading surface forces.

VIII. Conclusions

The gas flow in a free-molecule microresistojet is studied numerically with the direct-simulation Monte Carlo method. A two-dimensional flow of nitrogen and helium is modeled through a single heater slot for a qualitatively accurate slot geometry. The results were obtained for a range of plenum pressures from 50 to 200 Pa and heater chip temperatures from 300 to 573 K.

The thrust was found to be a weak function of the surface temperature, whereas the mass flow was inversely proportional to the square root of the temperature. The results were compared with available experimental data for thrust vs mass flow. A reasonable agreement of numerical and experimental data was observed. The computed specific impulse was about 2% lower than that of experimental data for nitrogen and about 4% for helium. The difference is attributed to the impact of the backscattered plume molecules that act toward increasing thrust; this impact is not properly accounted for in the two-dimensional modeling.

A full three-dimensional modeling of the FMMR geometry has been performed for water vapor in two steps. First, the flow in the plenum was modeled. A significant impact of the cold side walls was found on the FMMR performance parameters compared to the two-dimensional computations. In three-dimensions, the thrust significantly increases with temperature. The mass flow decreases with temperature, but the decrease is less significant than in two-dimensions. At the same time, the specific impulse increases with temperature by a factor of 1.34 when the wall temperature increases from 300 to 573 K both for two and three dimensions.

Second, the FMMR plume flow was computed using a starting surface generated from the plenum simulation. Two locations of the

FMMR were examined—the center of a cylinder panel and the edge of the panel. For the first location, the potential for contamination is important only for the panel of the satellite where the FMMR is installed. For the second location, both the FMMR and the adjacent panels are affected by water molecules, but to an order of magnitude smaller extent than for the first location. For the first location, the surface force caused by the plume-surface interaction is large compared to the thrust force, and the thrust degradation can be as large as 30%. For the second location, the surface-related degradation is only about 1% of the thrust force. The despinning moment is over 60% larger for the second location.

Acknowledgment

This work was supported in part by the Propulsion Directorate of the Air Force Research Laboratory at Edwards Air Force Base, California. The authors thank Taylor Lilly and Riki Lee who provided experimental data for comparison.

References

[1] Ketsdever, A. D., "System Considerations and Design Options for Microspacecraft Propulsion Systems," *Micropropulsion for Small Spacecraft*, edited by M. Micci and A. Ketsdever, Progress in Astronautics and Aeronautics, Vol. 187, AIAA, Reston, VA, 2000, Chap. 4.

[2] Reed, B. D., de Groot, W., and Dang, L., "Experimental Evaluation of Cold Flow Micronozzles," AIAA Paper 2001-3521, July 2001.

[3] Hitt, D. L., Zakrzwski, C. M., and Thomas, M. A., "MEMS-Based Satellite Micropropulsion via Catalyzed Hydrogen Peroxide Decomposition," *Smart Materials and Structures*, Vol. 10, No. 6, 2001, pp. 1163–1175.

[4] London, A. P., Epstein, A. H., and Kerrebrock, J. L., "High-Temperature Bipropellant Microrocket Engine," *Journal of Propulsion and Power*, Vol. 17, No. 4, 2001, pp. 780–787.

[5] Ketsdever, A., Green, A., Muntz, E. P., and Vargo, S., "Fabrication and Testing of the Free Molecule Micro- Resistojet: Initial Results," AIAA Paper 2000-3672, July 2000.

[6] Ketsdever, A. D., Lee, R. H., and Lilly, T. C., "Performance Testing of a Microfabricated Propulsion System for Nanosatellite Applications," *Journal of Micromechanics and Microengineering*, Vol. 15, No. 12, 2005, pp. 2254–2263.

[7] Ivanov, M. S., Markelov, G. N., and Gimelshein, S. F., "Statistical Simulation of Reactive Rarefied Flows: Numerical Approach and Applications," AIAA Paper 98-2669, June 1998.

[8] Ivanov, M. S., and Rogasinsky, S. V., "Analysis of the Numerical Techniques of the Direct Simulation Monte Carlo Method in the Rarefied Gas Dynamics," *Soviet Journal of Numerical Analysis and Mathematical Modelling*, Vol. 3, No. 6, 1988, pp. 453–465.

[9] Bird, G. A., *Molecular Gas Dynamics and the Direct Simulation of Gas Flows*, Clarendon Press, Oxford, England, UK, 1994, Chap. 2.

[10] Lee, R. H., Lilly, T. C., Muntz, E. P., and Ketsdever, A. D., "Free Molecule Microresistojet: Nanosatellite Propulsion," AIAA Paper 2005-4073, July 2005.

[11] Cercignani, C., *Rarefied Gas Dynamics: from Basic Concepts to Actual Calculations*, Cambridge Univ. Press, Cambridge, England, UK, 2000, Chap. 4.

IOPscience iopscience.iop.org

Home Search Collections Journals About Contact us My IOPscience

Performance testing of a microfabricated propulsion system for nanosatellite applications

This article has been downloaded from IOPscience. Please scroll down to see the full text article.

2005 J. Micromech. Microeng. 15 2254

(http://iopscience.iop.org/0960-1317/15/12/007)

View the table of contents for this issue, or go to the journal homepage for more

Download details:
IP Address: 129.198.241.47
The article was downloaded on 11/04/2012 at 16:19

Please note that terms and conditions apply.

INSTITUTE OF PHYSICS PUBLISHING JOURNAL OF MICROMECHANICS AND MICROENGINEERING

J. Micromech. Microeng. **15** (2005) 2254–2263 doi:10.1088/0960-1317/15/12/007

Performance testing of a microfabricated propulsion system for nanosatellite applications

Andrew D Ketsdever[1], **Riki H Lee**[2] **and Taylor C Lilly**[2]

[1] Propulsion Directorate, US Air Force Research Laboratory, 10 E Saturn Blvd,
Edwards Air Force Base, CA 93524, USA
[2] Department of Aerospace and Mechanical Engineering, University of Southern California,
854 W 36th Place, RRB 101, Los Angeles, CA 90089-1191, USA

E-mail: ketsdeve@usc.edu

Received 23 May 2005, in final form 10 October 2005
Published 28 October 2005
Online at stacks.iop.org/JMM/15/2254

Abstract
There is a growing interest in the use of micro and nanosatellites within the aerospace community. Constellations of small satellites may eventually replace much larger, single function spacecraft as a cheaper, more flexible alternative. Micro-technologies will be required to enable small satellite missions including efficient, low-cost propulsion systems for maneuvering. A MEMS fabricated propulsion system has been developed for maneuvers on an upcoming University nanosatellite mission. The Free Molecule Micro-Resistojet (FMMR) is an electrothermal propulsion system designed for on-orbit maneuvers of nanosatellites, which are defined as spacecraft with an initial mass less than 10 kg. The FMMR has been tested using a torsion force balance to assess its performance using a variety of propellants including helium, argon, nitrogen and carbon dioxide. The experimental performance results compare favorably with results obtained from gas kinetic theory, which were used in the design phase to estimate the thruster's performance. The measured performance of the FMMR in this study has proven to be adequate to perform attitude control maneuvers for the University nanosatellite mission.

(Some figures in this article are in colour only in the electronic version)

1. Introduction

Recent trends in the space community for smaller, cheaper and more frequent space missions have driven the development of micro and nanosatellites. The use of small spacecraft constellations is an attempt to enhance the overall performance of communication and remote sensing tasks currently done by a relatively small number of large platforms [1, 2]. Because micro-technologies have the advantage of reducing the total resources required on a spacecraft, the continued development of micro-technologies for space applications will further enable small satellite missions [3, 4]. Nanosatellites (mass between 1 and 10 kg) impose significant limitations on mass, power and volume available for all subsystems including propulsion [5]. In general, micropropulsion devices will need to be more efficient, in an overall systems architecture sense, than their large spacecraft counterparts in order to maximize the limited resources available. For micropropulsion systems, MEMS fabrication processes can be used to integrate thrusters, valves and control electronics into a single device in an attempt to provide a high degree of system efficiency. To this end, the Free Molecule Micro-Resistojet (FMMR) has been developed by the Air Force Research Laboratory.

The FMMR is an electrothermal propulsion system [6] designed for on-orbit maneuvers of nanosatellites. As with any resistojet, the propellant flow through the FMMR is heated by passing it over an electrically heated surface. The FMMR consists of three main parts: the heater chip, the plenum and the propellant feed system as shown in figure 1. The thrust generating principle of the FMMR is shown in figure 2.

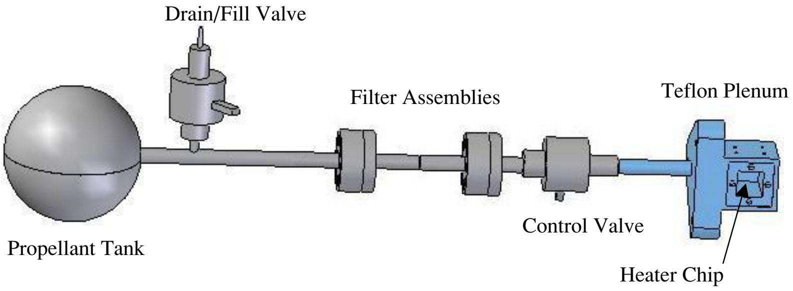

Figure 1. FMMR flight assembly schematic.

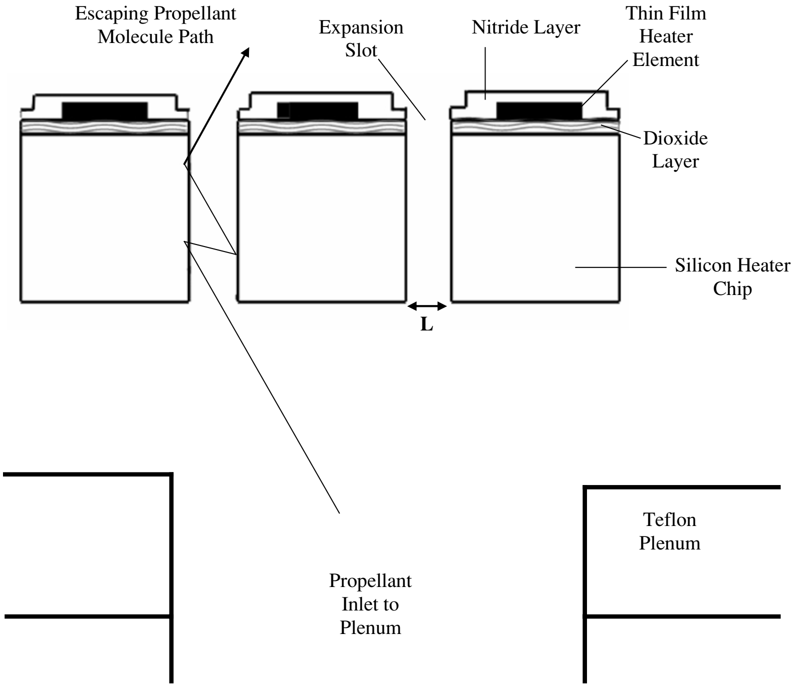

Figure 2. Basic thrust generation principle of the FMMR.

The propellant gas arrives in the plenum after passing from the propellant storage tank through the propellant feed system. The propellant gas escapes the plenum through a series of expansion slots in the MEMS fabricated heater chip, thus generating thrust. The heater chip is designed to operate at temperatures up to 600 K. The propellant molecules gain kinetic energy as they collide with the heated walls of the expansion slots in the heater chip. The transfer of energy from the high temperature expansion slot wall to the propellant molecules is critical to the performance and operation of the FMMR, since the thrust and efficiency, as measured by the specific impulse, of a propulsion system vary linearly with the propellant molecule's velocity at the exit of the thruster.

The FMMR exhibits many system features that are beneficial to nanosatellite operations, such as low-pressure operation, low power consumption, low mass and low propellant storage volume. Low-pressure operation is beneficial for micropropulsion systems for two main reasons. First, valve leak rates are dependent on the operating pressure. Valve leak rate concerns can be reduced for the FMMR over systems that operate at high pressures. This is particularly important when considering MEMS fabricated valves since many state-of-the-art valve designs will not meet nanosatellite mission requirements [7]. Second, the FMMR can be operated on the vapor pressure of a propellant stored as either a liquid or solid at nominal storage temperatures. The storage density of the propellant is important to minimize the volume required for propellant tanks.

Another distinct benefit of the FMMR propulsion system is expansion of propellant gases through many long slots. The expansion slot design leads to a reduction in possible single point failures over the expansion of propellant through a single nozzle configuration, which is a more traditional thruster design. To produce a similar amount of thrust as the FMMR using a high-pressure nozzle expansion, the throat diameter of the nozzle would be relatively small. Plugging of the throat by a contaminant would lead to a failure; however, the plugging of a section of slot in the FMMR device would still leave the remaining slot area available for thrust generation. A potential drawback of the expansion slot design is the loss of propulsive efficiency. However, a previous study has shown that for low-pressure operation, a nozzle does not offer a distinct enhancement in performance over a simple orifice or slot [8].

The aim of this research was to assess the thermal and propulsive performance characteristics of the FMMR

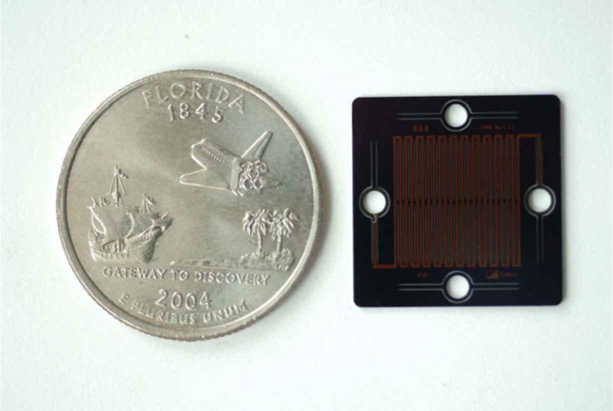

Figure 3. MEMS fabricated heater chip.

Table 1. Nanosatellite propulsion system requirements.

Parameter	Budget/requirement
Power	
Steady state	5 W
Transient	9 W
Propellant mass	90 g
Propellant volume	100 cm^3
Thrust	8×10^{-4} N

Mark 3.1 operating on several different propellants. This version of the FMMR was specifically developed to provide attitude control for an upcoming University nanosatellite mission. The FMMR will provide a de-spin capability for the nanosatellite to allow proper positioning of the satellite. The propulsive requirements for the nanosatellite mission are given in table 1. A slightly different version of the FMMR heater chip was integrated to an Arizona State University nanosatellite that was launched on the inaugural Delta-IV heavy launch vehicle in December 2004. Unfortunately, the 3-Corner Sat nanosatellite did not reach orbit due to a launch vehicle anomaly. In addition to the flight on an upcoming nanosatellite, the current version of the FMMR will be launched on a suborbital flight onboard a newly developed launch vehicle [9].

2. Microfabrication

The FMMR Mark 3.1 heater chip is shown in figure 3. The current iteration of the FMMR heater chip is a 19.2 mm × 19.2 mm square. The heater chip is fabricated using standard MEMS processing techniques. Individual heater chips are fabricated from a 500 μm thick double-sided polished silicon wafer which has been oxidized with a 0.4 μm layer of thermal oxide. The oxide acts as an electrical insulator between the silicon substrate and the subsequently deposited thin-film heater. The fabrication can be divided into the thin-film heater metallization and the deep reactive ion etching (DRIE) steps. Metallization of the heaters begins with a 0.03 μm layer of titanium which acts as an adhesion layer between the oxide layer and the subsequent metal layers. A 0.06 μm layer of platinum is then deposited to act as a diffusion barrier to mobile ions. A final layer of gold is deposited and provides the main current carrying layer of the heating element. The resistance of the gold layer, which is dictated by the layer thickness of 0.075 μm, was selected to allow the heater chip to reach the desired operating temperature while being supplied by the fixed satellite bus voltage for the nanosatellite mission. The heater is patterned to run between each expansion slot in an attempt to keep the heater chip temperature uniform. Once the metallization of the heater is completed, the wafer and patterned metallization is nitride coated in order to encapsulate the heating element, providing an isolation and scratch resistant layer.

The DRIE step was used to fabricate the expansion slots, thermal compensating flexures, attachment holes and was used to pattern the individual heater chips on the wafer. The expansion slots are anisotropically etched using the DRIE technique, which was selected to achieve the desired high aspect ratio. There are 44 expansion slots formed in two rows on each heater chip separated by a small rib to insure structural stability. The FMMR heater chip was specifically designed to survive the expected vibrational and g-force loading expected during the launch of the nanosatellite. The slots are 100 μm wide and 5.375 mm long and etched completely through the 500 μm thick wafer as shown in figure 4. The thrust generated by the FMMR is directly proportional to the collective expansion slot area for a given operating pressure. Therefore, the FMMR can be tailored to meet several different mission requirements by adjusting the expansion slot area.

The DRIE process is also used to fabricate thermal compensator flexures around the attachment holes that are used to attach the heater chip to the plenum. Since the heater chip operates nominally at temperatures of 600 K, the flexures are necessary to account for differential thermal expansion between the heater chip and the cooler plenum. The FMMR is currently packaged by attaching the MEMS fabricated heater chip to a conventionally machined plenum and propellant feed system. Figure 5 shows the heater chip attached to a Teflon plenum assembly that was tested in this study. The Teflon plenum is used to minimize heat transfer and keep the power required for the heater chip as low as possible. In future iterations, integration of the heater chip with other MEMS components and full MEMS packaging techniques must be investigated to improve system efficiency and integration.

3. Theory

The performance of the FMMR is analyzed theoretically as the free molecule flux of mass and momentum through the expansion slots. The amount of rarefaction in a flow is measured by the Knudsen number:

$$Kn = \frac{\lambda}{L} = \frac{1}{\sqrt{2}n\sigma L}, \qquad (1)$$

where λ is the molecular mean free path (the average distance that a molecule travels before colliding with another molecule), L is a characteristic flow dimension (the expansion slot width in this case), n is the number density of the propellant in the plenum and σ is the collision cross-section for the propellant molecules. Free molecule conditions are defined by $Kn \gg 1$ where either the mean free path is very large or the characteristic dimension is very small. Since the FMMR is designed to operate in the transitional flow regime with a

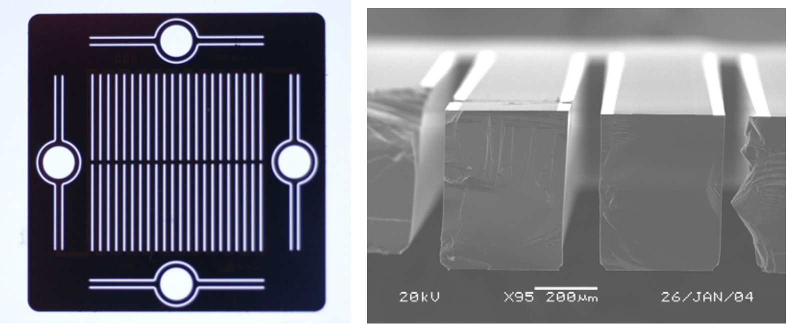

(*a*) (*b*)

Figure 4. (*a*) Expansion slot configuration on the heater chip. (*b*) Scanning electron microscope side image of cleaved expansion slots.

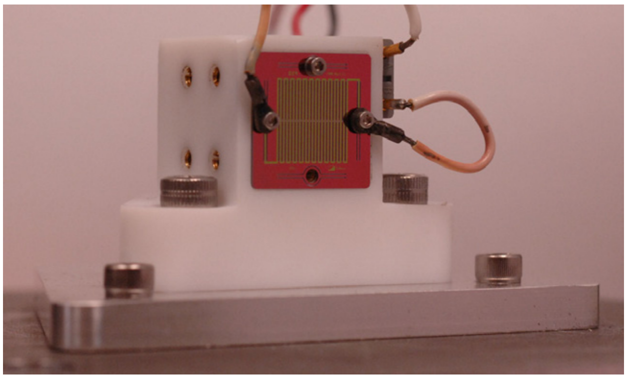

Figure 5. MEMS fabricated heater chip and Teflon flight plenum.

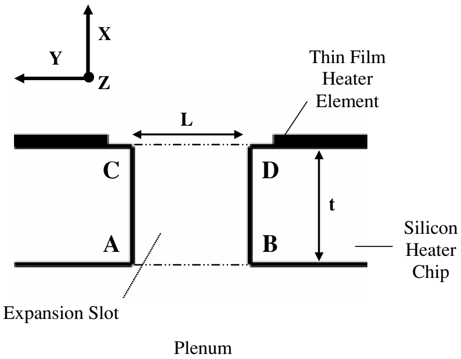

Figure 6. Expansion slot nomenclature and coordinate system.

Knudsen number range between 0.1 and 1, the free molecule analysis that follows is expected to only be approximate. However, the analysis has proven useful in the initial design phase of the FMMR.

The flux per unit area of a molecular parameter Q (either mass, momentum or energy) through a surface is given by

$$\dot{Q} = \int_{-\infty}^{\infty}\int_{-\infty}^{\infty}\int_{0}^{\infty} Q v'_x f(v'_x)\,\mathrm{d}v'_x\,\mathrm{d}v'_y\,\mathrm{d}v'_z, \tag{2}$$

where v'_x is the average thermal speed of the molecule in the x-direction and $f(v'_x)$ is the Maxwellian velocity distribution function for a gas in thermodynamic equilibrium [10]. Equation (2) assumes an orthogonal coordinate system with x in the direction of flow parallel with the expansion slot thickness and the expansion slot entrance and exit in the y–z plane as shown in figure 6.

The mass flux can be derived using equation (2) by setting $Q = \alpha m n$ where m is the mass of the propellant molecules and α is a transmission probability. The transition probability is defined as the probability that a propellant molecule which enters an expansion slot (i.e., crosses line AB in figure 6) will leave the thruster exit plane (i.e., cross line CD in figure 6) and produce thrust. For an infinitely thin expansion slot or for specular wall collisions, the value of the transmission probability would be unity. For the slot thickness to width ratio used in the present FMMR geometry ($t/L = 5$), the transmission probability assuming diffuse wall collisions is approximately 0.38 [11]. This value agrees well with published results for conductance through rectangular slots with similar t/L [12]. The mass flux of propellant molecules through an expansion slot is

$$\dot{m} = \alpha m n \frac{\bar{v}'}{4} A_s, \tag{3}$$

where $\bar{v}'$ is the average thermal speed of the propellant molecules in the plenum and A_s is the expansion slot area. The average thermal speed of the propellant molecules is given by the expression

$$\bar{v}' = \sqrt{\frac{8kT_o}{\pi m}}, \tag{4}$$

where k is Boltzmann's constant and T_o is the temperature of the propellant molecules in the plenum. Combining equations (3) and (4) with the ideal gas law results in

$$\dot{m} = \alpha P_o \sqrt{\frac{m}{2\pi k T_o}} A_s, \tag{5}$$

where P_o is the pressure of the propellant gas in the plenum.

The thrust generated by the propellant gas expanding through the slots can be defined in a high Mach number flow as

$$\Im = \dot{m} u_e, \tag{6}$$

where u_e is the propellant velocity at the exit plane of the expansion slot. The exit velocity can be derived from free molecule flow as

$$u_e = \sqrt{\frac{\pi k T_w}{2m}}, \tag{7}$$

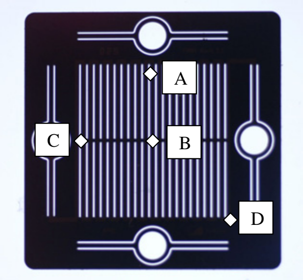

Figure 7. Thermocouple positions on the FMMR heater chip. Unless otherwise noted, the heater chip temperature was measured at position A.

where T_w is the heated wall temperature of the expansion slot. Therefore, the theoretical thrust produced by the FMMR can be written as

$$\Im = \frac{\alpha P_o A_s}{2}\sqrt{\frac{T_w}{T_o}}. \tag{8}$$

The specific impulse or Isp is used as a measure of the propellant utilization efficiency and is defined as

$$\mathrm{Isp} = \frac{\Im}{\dot{m} g_o} = \frac{u_e}{g_o} = \sqrt{\frac{\pi k T_w}{2 m g_o^2}}, \tag{9}$$

where g_o is the Earth's gravitational acceleration. As can be seen in equation (9), the Isp is inversely proportional to the square root of the propellant molecular mass; therefore, lighter propellant molecules will result in increased propellant efficiency. The FMMR has been designed to operate using water propellant with a relatively low molecular weight that can be stored as a liquid or solid. The Isp is also proportional to the square root of the wall temperature; therefore, higher wall temperatures will result in better propellant efficiency. However, the operating heater chip temperature must be weighed against the required power.

The overall efficiency of an electric propulsion system is measured by the product of the thrust and specific impulse per unit input power as given by

$$\eta = \frac{\Im \, \mathrm{Isp}\, g_o}{2\wp} = \frac{\Im^2}{2\dot{m}\wp}, \tag{10}$$

where $\wp$ is the input power to the heater chip. Based on this formulation, large-scale resistojets generally have efficiencies on the order of 25–35% [13].

4. Experimental set-up

After the fabrication of the heater chip and plenum, the FMMR was tested to assess its thermal properties. For nanosatellite operations, the input power to the heater chip will be extremely limited. For efficient operation of the FMMR, the input power must couple efficiently to the propellant gas through collisions with the expansion slot walls. The heat transfer characteristics of the FMMR design were measured using a series of thermocouples attached to various parts of the heater chip and plenum. The locations of the thermocouples on the heater chip are shown in figure 7. The FMMR was placed in a vacuum chamber with an ultimate background pressure capability of 10^{-6} Torr. Transient and steady-state temperature measurements were recorded as a function of input power and propellant mass flow. The final step of this process involved placing the FMMR under a liquid nitrogen shield to simulate temperatures that a nanosatellite might encounter on-orbit. Similar data sets were recorded for background temperatures of 120 K and 300 K.

Table 2. Nominal FMMR operating parameters.

Parameter	Value
Heater chip temperature, T_w	600 K
Mass flow, $\dot{m}$	50 sccm
Plenum pressure, P_o	
Helium	35 Pa
Nitrogen	95 Pa
Argon	112 Pa
Carbon dioxide	120 Pa

The propulsive characteristics of the FMMR were measured using the nano-Newton thrust stand (nNTS) and an electrostatic comb calibration system described in detail elsewhere [14, 15]. The nNTS was placed in a large vacuum chamber, Chamber IV of the Collaborative High Altitude Flow Facility at the University of Southern California, which was capable of maintaining background pressures below 10^{-5} Torr throughout the range of experiments performed in this study. Maintaining low background pressure was critical in obtaining accurate thrust measurements [16]. The mass flow of propellants was measured along with the thrust in order to determine the thruster's specific impulse. Tests were conducted using helium, nitrogen, carbon dioxide and argon propellants. Mass flow rates of the propellants ranged from 1 to 100 sccm, and heater chip temperatures ranged from 300 to 600 K. Unless otherwise noted, the heater chip temperature is measured from the thermocouple at position A (figure 7). For the upcoming nanosatellite mission, the nominal operating characteristics of the FMMR are given in table 2.

5. Results and discussion

The requirements for maximum allowable power draw and minimum allowable thrust generated from the onboard propulsion system make the efficiency of the FMMR a critical design component for this mission. The propulsive efficiency is given by equation (10) and is seen to be a trade-off between higher thrust (with a higher heater chip temperature) and the increased power required to generate that thrust. To establish that the current FMMR design meets both the transient and steady-state power requirements, experiments were performed to measure thermal characteristics of the heater chip and plenum assembly.

The heater chip temperature as a function of input power is shown in figure 8 for various propellants with a constant mass flow rate of 50 sccm. The nominal operating temperature of the FMMR heater chip of 600 K was obtained with an input power of 3.7 W at the nominal propellant mass flow of 50 sccm. The input power required to heat the heater chip to 600 K is shown in figure 8 to be relatively independent of the propellant gas used for a given propellant number flux (mass flow in sccm). An empirical formulation was derived to estimate the input power required to heat the heater chip to a given temperature

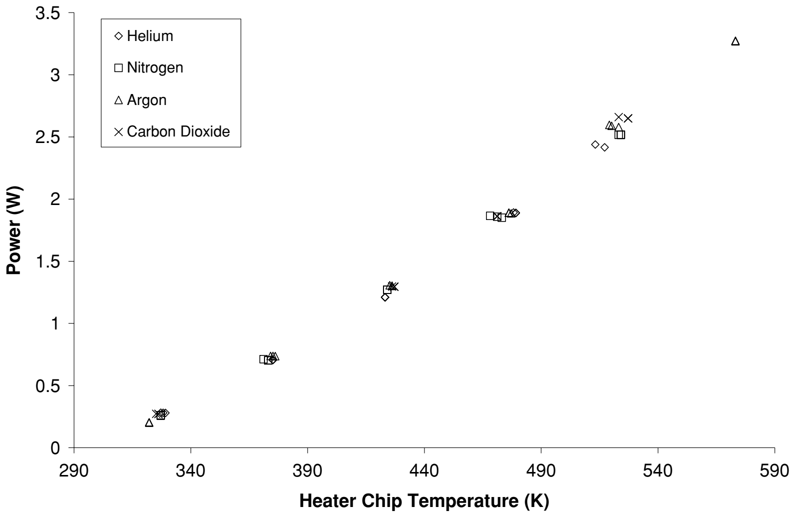

Figure 8. Heater chip temperature as a function of thin-film heater input power.

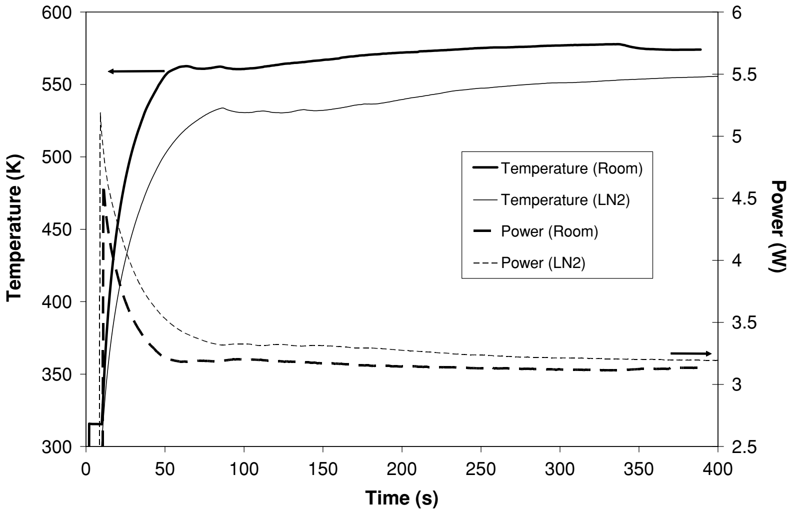

Figure 9. Transient heater chip temperature and input power for the heater chip radiating to the vacuum chamber walls (room temperature, 300 K) and to a liquid nitrogen shield (120 K).

Table 3. Empirical constants for equation (11).

Empirical constant	Value
a_1	1.279×10^{-5}
a_2	8.647×10^{-4}
a_3	-1.401
c_1	2.005×10^{-3}
c_2	0.9003

as a function of the propellant mass flow. The empirical result is given by

$$\wp = \left(a_1 T_w^2 + a_2 T_w + a_3\right)(c_1 \dot{m} + c_2), \qquad (11)$$

where T_w is the heater chip temperature in Kelvin and $\dot{m}$ is the propellant mass flow in sccm. The empirical constants in equation (11) are given in table 3. Equation (11) is valid for all of the propellants used in this study. The transient heat transfer properties of the FMMR are shown in figure 9. The two cases investigated were for the heater chip radiating to a wall at 300 K (room) and a wall at 120 K (LN2). For a constant input voltage applied to the thin-film heater at time $t = 0$, the power draw and corresponding heater chip temperature are shown with no propellant mass flow. For efficient FMMR operation, the heater chip will be brought to steady-state operating temperature before the propellant mass flow is initiated. Based on figure 9, a time between 60 and 100 s is required to bring the FMMR to steady-state operating temperature depending on the initial temperature of the heater chip. Although the nominal steady-state input power is on the order of 3.25 W in figure 9, a transient input power as high as 5.25 W is present for a short time at start-up. This is due to the relatively low thin-film heater resistance at low temperature. The heater resistance increases with temperature, which acts to lower the input power at constant voltage. For a power limited nanosatellite system, the initial spike in the FMMR power draw could be an issue that must be addressed in the power budget. The transient and steady-state power requirements for the nanosatellite mission are given in table 1.

The uniformity of the temperature across the heater chip is important in establishing efficient operation. The nominal

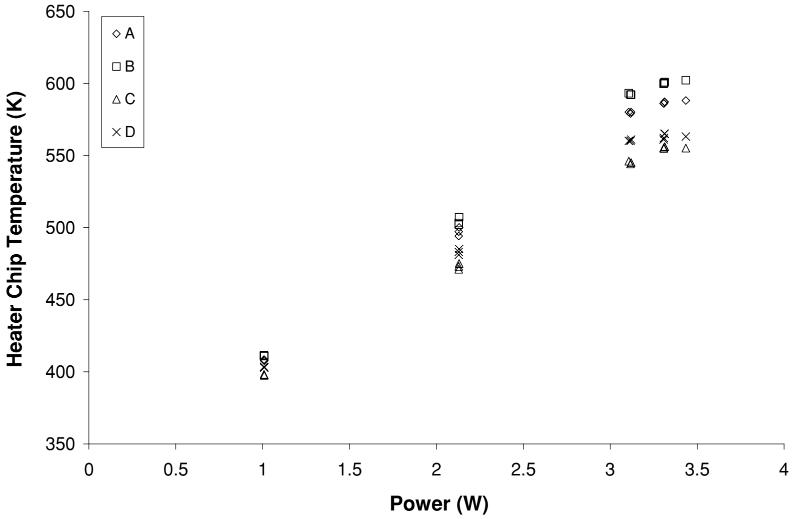

Figure 10. Heater chip temperature as a function of thin-film heater input power at various positions on the heater chip.

operating temperature of the FMMR heater chip is 600 K, which is the desired temperature at the center of the heater chip (position B in figure 7). The design criterion was for the heater chip temperature at any point to be within 10% of the temperature at the center. Figure 10 shows the heater chip temperature as a function of input power for various locations on the heater chip. As seen in figure 10 for an argon propellant with a mass flow of 50 sccm, the heater chip temperature remained within 3% of the center temperature at the lowest power setting and within 8% in the higher power range. Similar results were obtained for all of the propellants and corresponding mass flow rates investigated in this study. The subsequent values of the heater chip temperature, T_w, are given for position A where the temperature was monitored for the thrust testing.

Figure 11(*a*) shows the propellant mass flow as a function of the FMMR plenum pressure for various propellants at a constant $T_w = 575$ K. Figure 11(*b*) shows the data for helium compared to the theoretical line obtained from equation (5). There are several explanations for the differences between theory and experiments. One possibility is the uncertainty of the fabricated expansion slot area. A second possibility is the flow regime of the experiments. As figure 11(*b*) shows, the operating regime of the FMMR provides a higher mass flow rate than the free molecule theory predicts. Recall that the theory developed earlier assumed free molecule flow with $Kn \gg 1$. For the pressure range in figure 11(*b*), the helium Knudsen number ranged from 3 to 40. This is classified as the transitional flow regime [10] for which there are no analytical solutions of the Boltzmann equation. The low Knudsen numbers imply that the FMMR flows for these conditions are not free molecular, and there are a significant number of collisions between propellant molecules. As the FMMR plenum pressure increases even more, a continuum flow regime is approached ($Kn \ll 1$), and the transport of mass through the expansion slots is expected to become more efficient [8]. However for the FMMR, there is expected to be a trade-off between increased mass flow and the overall propulsive efficiency. As the mass flow increases (increased plenum pressure leading to a decrease in flow Knudsen number), intermolecular collisions will increase and a boundary layer will form near the expansion slot wall. The boundary layer will act to decrease the ability of the expansion slot wall to heat the gas outside of the boundary layer. Much of the propellant gas will exit the expansion slot without having increased its kinetic energy through collisions with the heated walls.

Table 4. Curve fit equations for figures 13 and 14(*a*).

Figure	Propellant gas	Curve fit equation	R^2
13	He	$Y = 1.505 \times 10^{-5}\, x^{0.4143}$	0.9992
13	N_2	$y = 2.506 \times 10^{-5}\, x^{0.5046}$	0.9995
13	Ar	$y = 3.185 \times 10^{-5}\, x^{0.4877}$	0.9998
13	CO_2	$y = 4.862 \times 10^{-5}\, x^{0.4335}$	0.9979
14(*a*)	He	$y = 9.395\, x^{0.4431}$	0.9993
14(*a*)	N_2	$y = 3.054\, x^{0.4788}$	0.9990
14(*a*)	Ar	$y = 2.424\, x^{0.4836}$	0.9997
14(*a*)	CO_2	$y = 2.615\, x^{0.4737}$	0.9994

Figure 12 shows the thrust obtained by the nano-Newton thrust stand as a function of the propellant mass flow rate. The results in figure 12 are for various propellants at $T_w = 575$ K. This is expected to be a linear relationship based on equation (6) since the exit velocity should be constant for a constant heater chip temperature. Figure 13 shows the thrust as a function of T_w for a constant $\dot{m} = 50$ sccm. From equation (8), the relationship between thrust and heater chip temperature is expected to vary as $\sqrt{T_w}$. The curve fit (best fit) equations for the data in figure 13 is given in table 4. Figure 14(*a*) shows the specific impulse as a function of T_w for a constant $\dot{m} = 50$ sccm for a variety of propellants. Figure 14(*b*) shows the specific impulse data for helium compared to the free molecule theory result from equation (9). Differences between theory and experiment in figure 14 may stem from a variety of uncertainties and approximations including the assumption of high Mach number flow that stems from the use of equation (6). As with the thrust data, the specific impulse is expected to vary as $\sqrt{T_w}$. The curve fit (best fit) equations for the data in figure 14 are also given in table 4. As expected, the measured specific impulse is greater than that

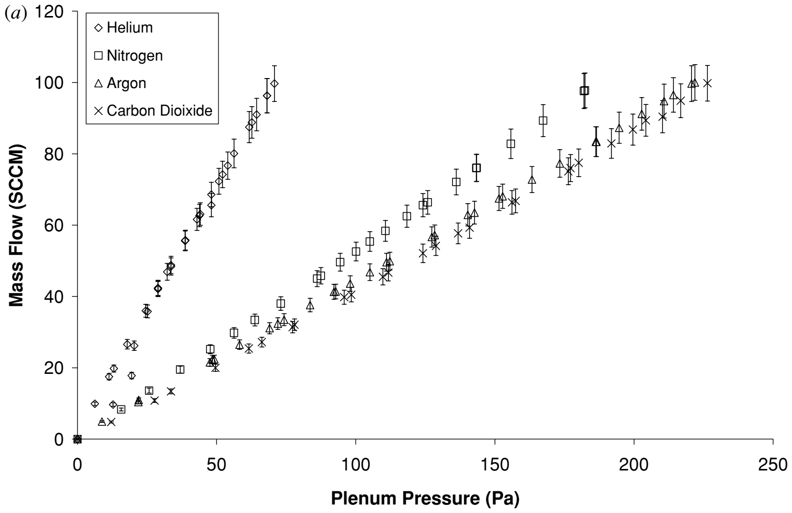

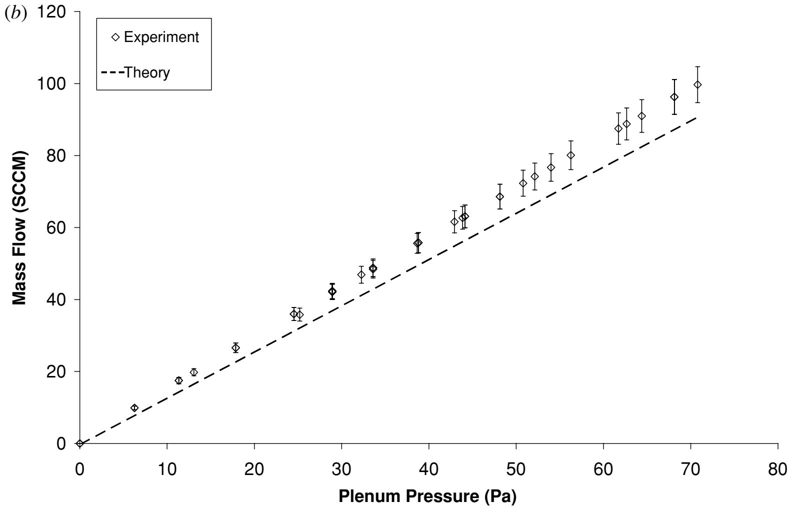

Figure 11. Mass flow versus plenum pressure for (*a*) various propellants. (*b*) Helium compared with free molecule theory.

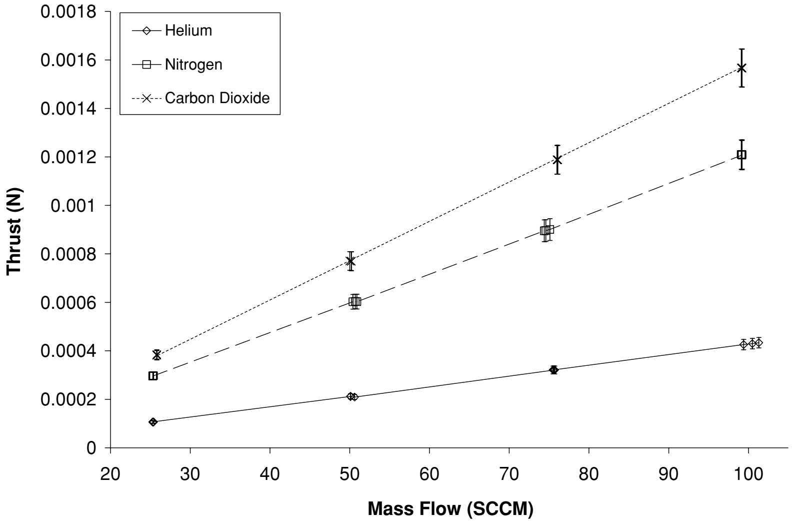

Figure 12. Thrust versus mass flow for various propellants.

predicted by the free molecule theory due to the transitional flow regime selected for FMMR operations. Table 5 gives the current FMMR parameters with the associated requirements for the nanosatellite mission. In its current configuration, the FMMR system will meet all of the mission requirements for the nanosatellite mission.

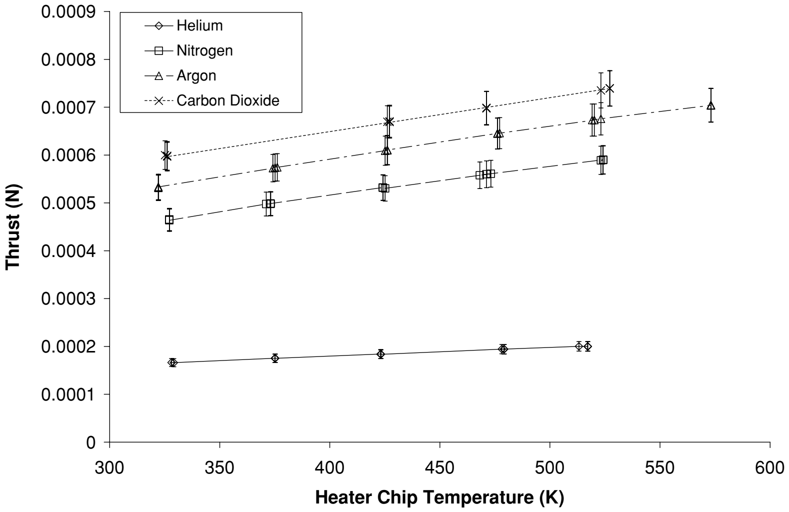

Figure 13. Thrust as a function of heater chip temperature for various propellants.

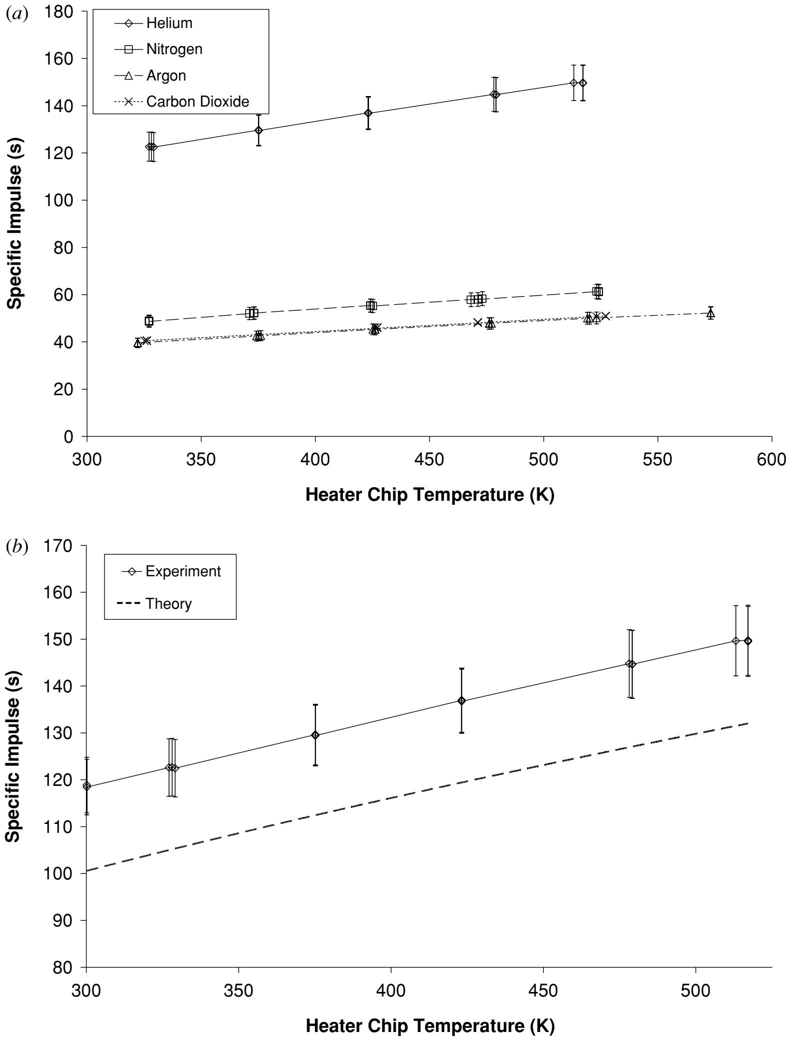

Figure 14. Specific impulse versus heater chip temperature for (*a*) various propellants. (*b*) Helium compared with free molecule theory.

The propulsive efficiency of the FMMR at nominal operating conditions (table 2) is approximately 15%. The efficiency is shown to improve up to 25% for higher mass flow rates at a given input power level. Increased efficiency can come from several different parameters. Minimizing the heat losses from the heater chip to the plenum would lead

Table 5. Comparison of nanosatellite mission requirements with the propulsive characteristics of the FMMR. The margin is the difference between the measured value and the requirement. Positive margin is required to meet (exceed) the requirements.

Parameter	Budget/ requirement	Measured values	Margin
Power			
Steady state (W)	5	3.2	+1.8
Transient (W)	9	5	+4
Propellant mass (g)	90	87	+3
Propellant volume (cm^3)	100	96	+4
Thrust (N)	8×10^{-4}	1.7×10^{-3}	$+9 \times 10^{-4}$

to an overall reduction in the total input power. This can be accomplished by minimizing the contact surface area of the heater chip with the surrounding plenum. The thrust produced by the FMMR can also be improved with the fabrication of more expansion slots per unit area. Efficiencies on the order of 30% could be possible with these relatively minor improvements to the current design.

From equation (9), it is evident that the specific impulse of the FMMR can be improved by using propellants with low molecular mass. Storing high-density propellants (either solid or liquid) also has distinct advantages in reducing the storage volume required over gaseous propellants stored at high pressure. To improve the overall system efficiency of the FMMR, a water vapor propellant is being investigated [17]. Water has many attractive benefits as a propellant such as liquid (or solid) storage on orbit and a relatively low molecular mass. Preliminary measurements and numerical simulation suggest that a specific impulse of approximately 68 s can be attained using water vapor at the FMMR nominal operating conditions. In this configuration, the FMMR would operate on the vapor pressure of the liquid water.

6. Conclusions

A simple method of fabricating a novel MEMS propulsion system has been demonstrated. The effects of propellant species, propellant mass flow and heater chip input power on the thermal and propulsive properties of the FMMR have been investigated. The propulsive properties of the FMMR were tested using a nano-Newton thrust stand. Data for propellant mass flow, thrust and specific impulse follow the trends predicted from free molecule theory. Although the absolute values differ, this was expected since the flows investigated in this study were in the transitional regime and not strictly free molecular. Thrust varied linearly with plenum pressure and mass flow at a constant T_w as expected. For a constant P_o, the thrust was relatively independent of the propellant gas used. For a constant propellant mass flow, the thrust varied approximately as $\sqrt{T_w}$. The specific impulse varied approximately as $\sqrt{T_w/m}$. Higher specific impulse was measured for larger T_w and propellants with a smaller molecular mass. At nominal operating conditions, the overall efficiency of the FMMR was approximately 15%. Optimizing the number of expansion slots per unit heater chip area and optimizing the heat transfer between the heater chip and the plenum can improve the overall efficiency of the FMMR for future nanosatellite missions. However, as shown in table 5, the FMMR system has positive margins for all of the mission requirements for the upcoming nanosatellite flight.

Acknowledgments

This work was supported by the Propulsion Directorate of the Air Force Research Laboratory at Edwards AFB, California. The authors wish to thank Mr Mike Huggins, Mr Jay Levine and Dr Ingrid Wysong for their continued support. The authors are also indebted to Dr Stephen Vargo of SiWave, Inc. for his efforts in assisting with the design and fabrication of the FMMR heater chip.

References

[1] Janson S, Helvajian H and Robinson E 1993 The concept of nanosatellite for revolutionary, low-cost space systems *44th International Astronautics Congress (Graz, Oct. 1993)* IAF Paper 93-U.5.573

[2] Bille M, Kane R and Nowlin M 2002 Military microsatellites: matching requirements and technology *Space 2000 Conference (Long Beach, CA, Sept. 2000)* AIAA Paper 2000-5186

[3] Martinez de Aragon A 1998 Space applications of micro/nano-technologies *J. Micromech. Microeng.* **8** 54–6

[4] Helvajian H 1997 *Microengineering Technology for Space Systems* (Reston, VA: AIAA)

[5] Ketsdever A D 2000 System considerations and design options for microspacecraft propulsion systems *Micropropulsion for Small Spacecraft* (Reston, VA: AIAA)

[6] Jahn R G 1968 *Physics of Electric Propulsion* (New York: McGraw-Hill)

[7] Mueller J 2000 Thruster options for microspacecraft: a review and evaluation of state-of-the-art and emerging technologies *Micropropulsion for Small Spacecraft* (Reston, VA: AIAA)

[8] Ketsdever A D, Clabough M T, Gimelshein S F and Alexeenko A A 2005 Experimental and numerical determination of micropropulsion device efficiencies at low Reynolds number *AIAA J.* **43** 633–41

[9] Ketsdever A D, D'Souza B, Jamison A J, Young M and Chinnery A 2002 Sub-orbital flight demonstration of MEMS technologies for space applications *NanoTech 2002 (Houston, TX, Sept. 2002)* AIAA Paper 2002-5704

[10] Bird G A 1994 *Molecular Gas Dynamics and the Direct Simulation of Gas Flows* (New York: Oxford University Press)

[11] Ketsdever A D, Green A A, Muntz E P and Vargo S E 2000 Fabrication and testing of the Free Molecule Micro-Resistojet: initial results *36th Joint Propulsion Conference (Huntsville, AL, July 2000)* AIAA Paper 2000-3672

[12] Lafferty J 1992 *Foundation of Vacuum Science and Technology* (New York: Wiley)

[13] Filliben J D 1997 *Electric Thruster Systems* CPTR 97-65 (Columbia, MD: Chemical Propulsion Information Agency)

[14] Jamison A J, Ketsdever A D and Muntz E P 2002 Gas dynamic calibration of a nano-Newton thrust stand *Rev. Sci. Instrum.* **73** 3629–37

[15] Selden N P and Ketsdever A D 2003 Comparison of force balance calibration techniques for the nano-Newton range *Rev. Sci. Instrum.* **74** 5249–54

[16] Ketsdever A D 2002 Facility effects on performance measurements of micropropulsion systems that utilize gas expansion *J. Prop. Power* **18** 797–804

[17] Ketsdever A D 2000 Predicted performance and systems analysis of the Free Molecule Micro-Resistojet *Micropropulsion for Small Spacecraft* (Reston, VA: AIAA)

AIP | Review of Scientific Instruments

Investigation of time-dependent forces on a nano-Newton-second impulse balance

Brian C. D'Souza and Andrew D. Ketsdever

Citation: Rev. Sci. Instrum. **76**, 015105 (2005); doi: 10.1063/1.1834707
View online: http://dx.doi.org/10.1063/1.1834707
View Table of Contents: http://rsi.aip.org/resource/1/RSINAK/v76/i1
Published by the American Institute of Physics.

Additional information on Rev. Sci. Instrum.
Journal Homepage: http://rsi.aip.org
Journal Information: http://rsi.aip.org/about/about_the_journal
Top downloads: http://rsi.aip.org/features/most_downloaded
Information for Authors: http://rsi.aip.org/authors

ADVERTISEMENT

HAVE YOU HEARD?
Employers hiring scientists
and engineers trust
physicstoday JOBS
http://careers.physicstoday.org/post.cfm

HTML ABSTRACT * LINKS

REVIEW OF SCIENTIFIC INSTRUMENTS **76**, 015105 (2005)

Investigation of time-dependent forces on a nano-Newton-second impulse balance

Brian C. D'Souza
Department of Aerospace and Mechanical Engineering, University of Southern California, Los Angeles, California 90089-1191

Andrew D. Ketsdever
Air Force Research Laboratory, Propulsion Directorate, Edwards Air Force Base, California 93524

(Received 16 March 2004; accepted 10 September 2004; published online 22 December 2004)

A torsional impulse balance has been developed as a new diagnostic tool to study fundamental physical processes in micropropulsion systems and laser–surface interactions. The impulse balance has been designed and tested with a robust calibration system to measure impulsive forces with resolution as low as several nano-Newton-seconds. The behavior of the impulse balance was thoroughly studied and characterized. A simple analytical model of the balance's motion was developed from the general equation of motion of an underdamped, harmonically oscillating system. Also, two distinct methods of analyzing the experimental data from the nano-impulse balance have been investigated. The first method resolves the total impulse as a function of the balance's maximum deflection. The second method enables the determination of the impulse and/or force applied as a function of time from the balance's time-resolved motion. A calibration scheme employing electrostatic actuation techniques is used to experimentally validate the model and impulse measurement techniques. © *2005 American Institute of Physics.*

[DOI: 10.1063/1.1834707]

I. INTRODUCTION

Several impulse balances have been designed to measure transient forces produced by a variety of processes.[1–3] Generally, the impulse generated by a device is investigated by measuring the maximum deflection of the balance caused by a given impulse.[2,3] There are two major shortcomings of this approach. First, there is no information that can be inferred from this data regarding the pulse width, τ, or the pulse shape. Second, it is only strictly valid for $\tau \ll T$. Since very different pulse widths and shapes can lead to the same maximum deflection on an impulse balance, the simple method of investigating a balance's maximum deflection is not adequate to determining the characteristics of the impulse delivered. A detailed analysis of the impulse balance's equation of motion can lead to a more complete understanding of the complex physical processes which may be driving device operation.

There are a number of applications of current interest where the knowledge of time resolved forces would be beneficial to the basic understanding of physical processes. Two of these applications are spacecraft propulsion and laser ablation. For spacecraft propulsion, fine attitude control requires precise and reproducible impulse delivery from the thruster system. Although total delivered impulse is generally measured and deemed adequate for most mission scenarios, time resolved thrust measurements would be beneficial in understanding the physics of thruster operation and could lead to the development of more precise and efficient thruster systems. For example, pulsed plasma thrusters (PPT) use a spark generated across a Teflon propellant to produce an energetic arc-ablated ionized plume.[4] The total impulse delivery from a PPT involves a relatively low mass of highly energetic ions and a large mass of slow moving molecules and heavier particles as shown schematically in Fig. 1(a). The initially ablated material produces the majority of the thrust. Subsequent heat adsorption by the Teflon produces a late-time ablative plume of relatively massive, slow moving molecules and particles.[5] The late-time ablation does not produce significant thrust; however, a relatively large amount of propellant mass is lost in this process leading to thruster inefficiencies. Although the total impulse, $\mathcal{J}$, obtained from integrating $F(t)$ versus time in Fig. 1(a) and Fig. 1(b) are the same, the detailed physics behind the production of each impulse curve may be quite different. A simple analysis based on the balance maximum deflection would not yield any information about the pulse shape. The investigation of the time-dependent forces produced by a PPT can lead to more efficient thrusters by investigating system changes that maximize the efficient production of ionized propellant and minimize the production of late-time ablation. A measure of propulsive efficiency is the specific impulse, I_{sp} given by

$$I_{\text{sp}} = \frac{1}{M_p g_o} \int_{t=0}^{t=t'} F(t)dt, \tag{1}$$

where $F(t)$ is the time-dependent force produced by the thruster, t' is the thruster's pulse duration, and M_p is the total mass of the propellant lost in the pulse, and g_o is the Earth's gravitational constant. From Eq. (1), it can be seen that details of the impulse delivery in the integral are important for thruster efficiency.

© 2005 American Institute of Physics

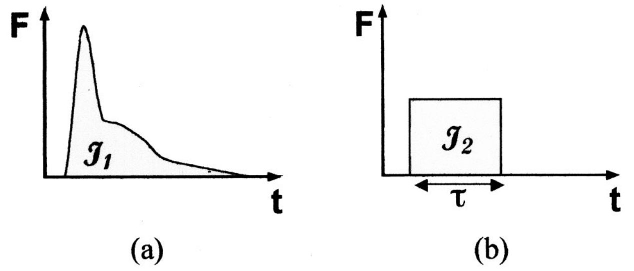

FIG. 1. Schematic of two very different force profiles that result in equivalent total impulses $\mathcal{J}_1 = \mathcal{J}_2$. (a) Large initial force with smaller residuals. (b) Constant force of pulsewidth τ.

Within the scope of laser ablation, investigations of a wide variety of physical processes, which include sputtering, vaporization, ionization, and gas desorption, are of interest.[6] The conditions under which each physical process might occur and the parameters which may control each process can be studied by time resolved force measurements. For example, an investigation of the onset of sputtering as a function of laser energy or pulse duration can be performed. At relatively low laser energy and long pulsewidth, gas desorption, due to the rapid heating of the surface, is expected to be the dominant impulse producing process. As the laser energy increases and/or the pulse duration decreases, material sputtering or ionization may become dominant.[7] Through a careful investigation of the time resolved forces produced in the photon–surface interactions, the energy corresponding to the onset of sputtering for a particular material may be identified.

The scope of this work was three fold. First, a uniquely successful nano-Newton-second impulse balance system (NIBS) capable of resolving total impulse measurements as low as 7 nano-Newton-seconds (nNs) was designed and constructed. Second, an analytical model was developed from the equations of motion for an underdamped, harmonically oscillating system. The model was validated using experimental data obtained from the NIBS. Finally, a data reduction method to accurately time-resolve the applied force from the NIBS deflection data was developed. The developed model and data reduction methods in this study are extended to impulse balance operation for arbitrary pulsewidth (i.e., with no restriction on the pulsewidth duration relative to the natural motion of the stand).

II. NANO-IMPULSE BALANCE SYSTEM

The current version of the NIBS is based upon a torsional thrust stand developed jointly by the Air Force Research Laboratory and the University of Southern California.[8] The NIBS design has been modified to allow for very low impulse measurements, which could not be attained by previous versions of the stand. An electrostatic comb force calibration technique described by Selden and Ketsdever[9] has been employed to accurately calibrate the system for transient impulses.

As shown in Fig. 2, the NIBS is a torsional pendulum with viscous damping. Two flexure pivots provide the restoring force for the system with a combined rotational spring constant of approximately 0.200 Nm/rad (measured). The entire structure is made of aluminum to keep the balance's moment of inertia as low as possible in an attempt to maximize the deflection for a given applied force. The arms were fabricated from square tubing to provide rigidity over long lengths, and channels were cut from the side of the tubing to reduce mass. Propulsion systems or test materials are mounted at the end of the 45.1 cm long arms. The Electrostatics Force Calibration System (EFCS) is mounted on the end of one arm at the same location from the center of rotation as the impulse delivery is expected. The NIBS motion is sensed by a linear variable differential transducer (LVDT). The LVDT senses a linear motion at the end of the balance's arm, which can be transformed into a rotational deflection. The data trace obtained by monitoring the LVDT output over time provides the basis for deriving the impulse imparted to the NIBS. A damping cup is mounted to the bottom of the NIBS and is placed in an oil bath to provide viscous damping, which is essential for damping out the motion of the stand in vacuum.

III. IMPULSE BALANCE MODEL

The motion of an underdamped, harmonically oscillating system can be expressed in rotational or linear terms by the following:

$$I\ddot{\theta}(t) + C\dot{\theta}(t) + K\theta(t) = F(t)r = M(t), \qquad (2)$$

$$I\ddot{x}(t) + C\dot{x}(t) + Kx(t) = F(t)r^2 = M(t)r.$$

The angular solutions can easily be transformed into a linear deflection to correspond to the measurement methods used in the experimental setup. For the general case of forced motion

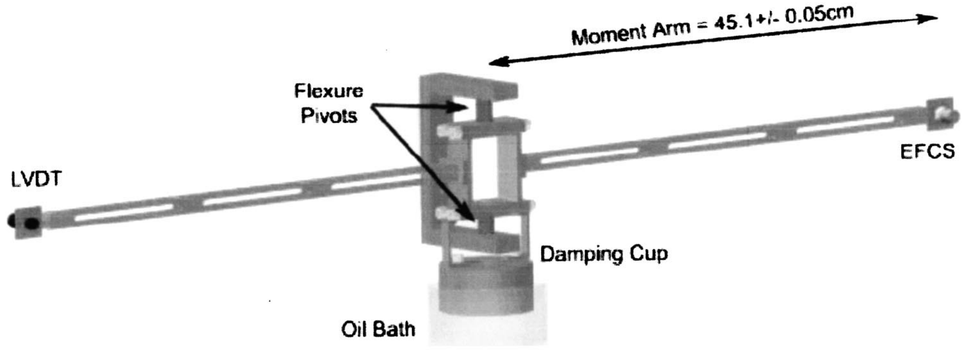

FIG. 2. Schematic of the nano-Newton impulse balance system.

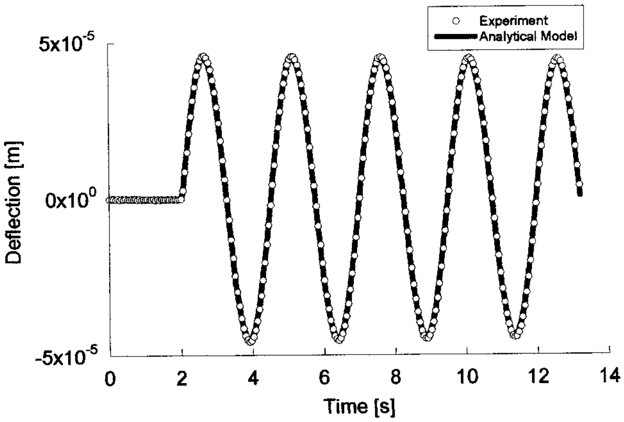

FIG. 3. Time-varying deflection trace for a 242 nNs impulse comparing experimental data and the analytical model.

of an underdamped system, consider $M(t)=M_o$ to be constant over a defined time period (pulse width) τ, as shown in Fig. 1(b). This can be representative of either a constant impulse or steady-state situation, depending on the length of τ. The solution to Eq. (2) for initial conditions of angular displacement θ_o and angular velocity $\dot{\theta}_o$ is[10]

$$\theta(t) = \frac{M_O}{K} + e^{\alpha t}\left[\left\{\theta_O - \frac{M_O}{K}\right\}\cos \beta t + \left\{\frac{\dot{\theta}_O K - \alpha K\theta_O + \alpha M_O}{k\beta}\right\}\sin \beta t\right], \tag{3}$$

$$\dot{\theta}(t) = e^{\alpha t}\left[\dot{\theta}_O \cos \beta t + \left\{\frac{I\alpha\dot{\theta}_O - K\theta_O + M_O}{I\beta}\right\}\sin \beta t\right], \tag{4}$$

$$\ddot{\theta}(t) = e^{\alpha t}\left[\left\{\frac{M_o - C\dot{\theta}_o - K\theta_o}{I}\right\}\cos \beta t + \left\{\frac{\alpha(M_o - C\dot{\theta}_o - K\theta_o) - K\dot{\theta}_o}{I\beta}\right\}\sin \beta t\right], \tag{5}$$

where $\alpha=-C/2I=-\delta/T$ and $\beta=[K/I-\alpha^2]^{1/2}$. Note that by removing the damping term, the expected natural frequency $\omega_n=[K/I]^{1/2}$ for a simple torsional spring is obtained.

A closed-form analytical solution of the equation of motion in Eq. (2) is not possible for any arbitrary applied moment, $M(t)$. However, the problem may be broken up into segments. Any arbitrary or irregular force can be reasonably approximated using a series of constant force segments of small time widths $d\tau$. The initial conditions of any given segment are simply the end state of the displacement and velocity terms from the previous segment.

Equations (3)–(5) have been used to develop a simple software tool that has been validated using experimental data. The software has been used to examine the expected behavior of the NIBS for impulses of varying pulse widths and for steady state operations. Figure 3 shows a comparison of NIBS experimental data for a 242 nNs impulse with the analytical model. Figure 3 shows good agreement between the model and experimental data for the magnitude and frequency of the balance's motion.

IV. SIGNAL PROCESSING AND DATA REDUCTION

A. Wavelet and Fourier transform denoising

The ability to obtain reliable and repeatable force measurements from NIBS depends on the time-varying deflection traces provided by the LVDT. The LVDT sensor provides an analog output, which commonly exhibits significant high frequency noise components. The noise can mostly be attributed to electrical sources (primarily in the 15 Hz, 50 Hz, and 60 Hz ranges). Two signal analysis techniques have been employed in this study to perform denoising of the LVDT signal: Fourier and wavelet transforms.

First, the Fourier transform $F(\omega)$ of a given signal $f(t)$ deconstructs the signal into constituent sinusoidal components. Fourier signal analysis techniques are fairly common and numerous tools exist to facilitate the transform of a given signal into a frequency spectrum. The denoising technique employed was a simple frequency thresholding, whereby all components higher than a specified frequency are filtered out. This technique essentially functions as an ideal low-pass filter (LPF).[11] The signal can then be transformed back from the frequency domain into the time domain for further data reduction and analysis.

While the principal frequency of interest is the effective frequency of the NIBS, care must be taken in choosing a threshold frequency. Selecting too low of a threshold frequency may result in the loss of actual signal, which would typically result in the undervaluing of the derived impulse. For sets of data that were analyzed using the Fourier techniques, the threshold frequency used was 10 Hz.

Alternately, the wavelet transform has also proved to be a valuable tool for denoising and smoothing of the raw experiment data. The wavelet transform is analogous to Fourier transforms in that it decomposes a signal into coefficients of constituent waveforms. However, Fourier analysis depends entirely on decomposition by sinusoids across the frequency spectrum. Wavelet analysis allows for the waveform to be of any arbitrary shape and decomposes the signal across the time domain. The coefficients of the wavelet transform are a function of scale and position (shift in time).[12]

The decomposition by scale and position allows for the isolation of successive levels of small scale structure or detail, leaving the remaining portion as an approximation of the original signal. Applying thresholding settings to these detail coefficients can result in removing general noise components while leaving actual fine structure intact. Such a deconstruction into scale and time domains can provide valuable information about the signal through inspection of the coefficients, as anomalous points and localized events are often clearly evident. Also, since the transform remains in the time domain, it is also possible to perform wavelet analysis on finite or shifting segments of a data set. This can be an extremely useful in handling large data sets. The major drawback of the wavelet process is that it can be extremely computationally intensive.

Both transform methods have been demonstrated to be quite reliable for deriving the total impulse from the deflection data. In either case, attention must be paid to not filter out more than just the noise from the signals. Figure 4 shows

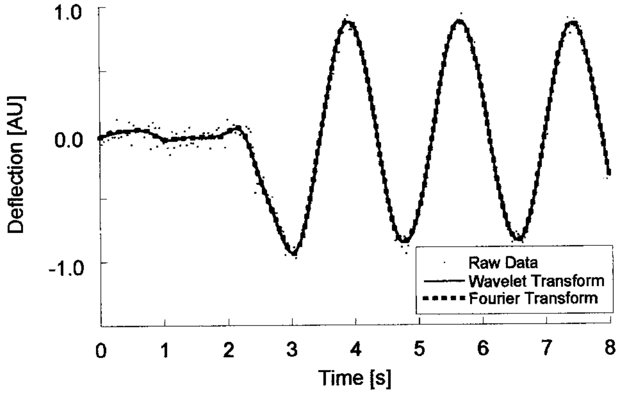

FIG. 4. Denoising of LVDT experimental data using wavelet transform and Fourier transform techniques.

a comparison between the Fourier and wavelet denoising techniques for a typical deflection trace. Agreement between the Fourier and wavelet processed signals is excellent. Furthermore, the comparison of the derived impulse from such traces processed with Fourier and wavelet techniques resulted in differences less than 1%.

B. Time resolved impulse measurement process

Once the raw data has been denoised through either the Fourier and/or wavelet transform methods, it can be used to derive the total impulse that was imparted to the NIBS. In the simplest case, for $\tau \ll T$, the total impulse may be derived from the maximum deflection. Calibration curves for this method can readily be derived, as will be shown in Sec. VI. However, the real interesting details of the impulse or force applied are the time resolved characteristics. The time resolved impulse measurement (TRIM) process is derived from Eq. (2). The equation of motion for the NIBS indicates that the force applied (as a function of time) is simply related to the addition of the position, velocity and acceleration components, which are scaled by the spring constant K, damping coefficient C, and the moment of inertia I, respectively, as shown in Fig. 5.

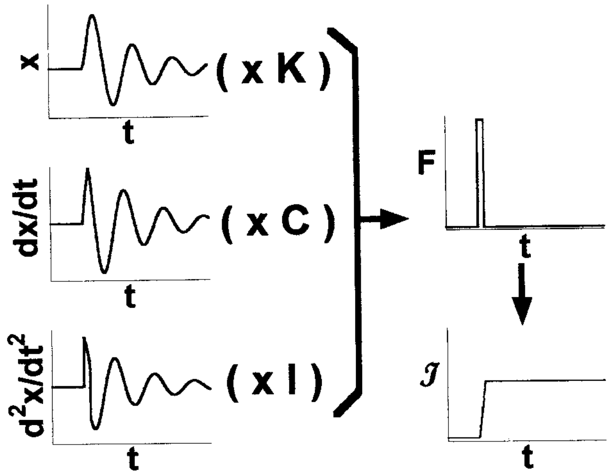

FIG. 5. Schematic representation of the TRIM process for deriving the time-varying impulse or force from the balance's deflection and its derivatives.

Since the position (deflection) as a function of time is measured in the experiments, the derivative of the data must simply be taken once to obtain the velocity and twice for the acceleration. The major problem here is resolving the derivatives for a signal with noise. Using the signal processing methods previously described, the raw position data can be cleaned up significantly. In addition, a Savitzky–Golay algorithm is used to take the derivatives. This algorithm employs a moving window over which the points are fitted for a line. The slope of the line represents the derivative of the point at the center of the window. This method results in artifacts at the beginning and end of a data trace. This method also tends to introduce slight aliasing effects, depending on the size of the window. However, it reliably maintains the content under the curve, which is essential for calculating the total impulse.

To complete the process, we need to determine I, C, and K. The moment of inertia of the NIBS can be determined through a combination of physical measurement and CAD analysis. The spring constant and damping coefficient can then be determined from the position data by extracting the period of the oscillations T and the damping ratio δ, which is obtained from the natural logarithm of the ratio of successive peaks in the displacement data, $\delta = \ln[x_{\max 1}/x_{\max 2}]$. For completeness, it is also necessary to remember to include the term for the moment arm in Eq. (2). Finally, from the derived force $F(t)$, the total impulse $\mathcal{J}(t)$ is given by integrating $F(t)$.

V. EXPERIMENTAL SETUP AND PROCEDURE

The NIBS was installed in a 41 cm diameter × 122 cm long, stainless steel vacuum chamber fitted with a 450 l/s turbomolecular pump capable of maintaining pressures of approximately 2×10^{-6} Torr. For this study, impulse delivery to the NIBS is accomplished by supplying a potential difference to the EFCS. The EFCS consisted of either an aluminum parallel plate assembly[2] or an aluminum comb assembly[9] with one side of the EFCS assembly attached directly to the NIBS. As shown in the experimental setup in Fig. 6, the power supply for the EFCS was attached to a pulse generator capable of delivering ±3500 V with a 20 ns risetime and a variable dc pulse width (minimum of 60 ns). The output of the pulse generator was sent directly to the EFCS assembly in the chamber through a high voltage vacuum feedthrough and was monitored by a 16-bit data acquisition (DAQ) system with a maximum sample rate of 333 kHz. The applied (and monitored) voltage to the EFCS was used to calculate the actual time-dependent force applied to the NIBS.[9]

The actual forces applied were later compared to the force derived from the NIBS deflection data through the TRIM process described in Sec. IV B. The motion of the NIBS was measured using a LVDT, which was connected to either a 16 or 24-bit data acquisition system. The 24-bit system used was limited to a sampling rate of 60 Hz, and the 16-bit system was capable of sampling at 333 kHz. In some of the tests, a simple low-pass filter (LPF) was used on the LVDT signal to minimize electrical noise. The analog filtering serves to complement the signal processing techniques discussed in Sec. IV A. The raw data was filtered to reduce

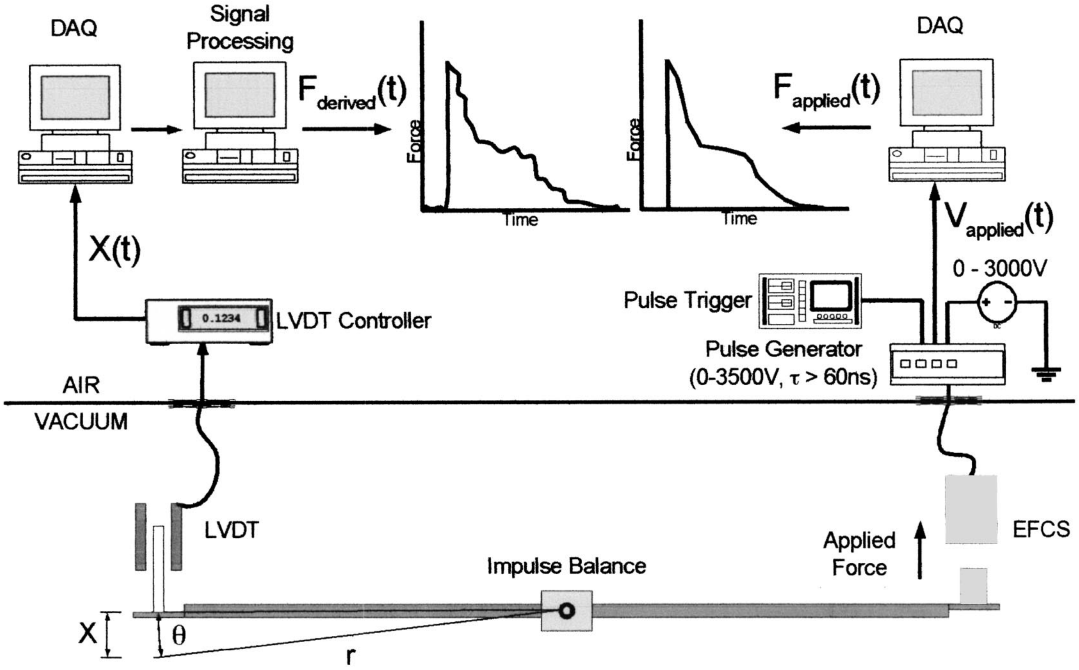

FIG. 6. Schematic of NIBS experimental setup and TRIM process for obtaining the derived and applied forces imparted to the impulse balance as a function of time.

the noise in the experimental data, and the de-noised data was differentiated to provide NIBS velocity and acceleration information, which was used to determine the characteristics of the delivered impulse as described in the previous section. Values of T and δ were obtained using NIBS displacement data. From these parameters and the measured moment of inertia, the values of the damping (C) and spring (K) coefficients were calculated. Table I shows the characteristic values for the NIBS in this study.

VI. RESULTS

A. Calibration

Calibration of the NIBS was a critical element of this study. The application of a variety of known impulses of different magnitudes and pulsewidths were tested to demonstrate the stability and repeatability of the NIBS. From these tests, a process has been developed which allows the balance to be well characterized under any configuration.

In order to use the LVDT voltage output to obtain a derived impulse, a calibration factor is required that converts the analog voltage signals into appropriate displacement measurements. The LVDT was independently calibrated from repeated measurements in a staged micrometer configuration that spanned the full range of the LVDT. The conversion factor was determined to be 1453.366 V/m for the tested configuration, which included the use of a LPF for analog signal conditioning. For test configurations without the use of a LPF, an additional scaling factor of 1.0902 was necessary to compensate for the signal attenuation caused by the LPF.

TABLE I. General NIBS characteristics.

Parameter	Value	Error (+/−)
Moment of inertia, I	0.03184 kg m^2	0.00010 kg m^2
Damping coefficient, C	0.00023 kg m^2/s	0.00002 kg m^2/s
Spring constant, K	0.020034 N/m	0.00150 N/m
Period, T	2.49 s	0.01 s
Angular frequency, ω_{eff}	2.523 s^{-1}	0.010 s^{-1}
Damping ratio, δ	0.0090	0.0009
Moment arm, r	0.4510 m	0.0005 m

The applied impulse is the known impulse delivered to the stand using the EFCS. The voltage applied to the EFCS is typically greater than 100 V and is monitored and known to within 0.1 V. The actual force produced by the EFCS was independently calibrated by the microbalance method described by Selden and Ketsdever.[9] The microbalance method requires that the EFCS is mounted vertically on a precision microbalance. One element of the EFCS assembly rests grounded on the microbalance, while the other element is suspended by a known distance above. An attractive force is created by charging the suspended EFCS element, resulting in a measurable change in weight. The EFCS assembly is extensively characterized in a steady state condition over a large range of applied potential differences (0–3000 V) and separation distances (1–15 mm). The error for a given applied force was found to be less than 2%. For all results presented in this paper, this error is understood to be present in all applied forces and impulses, whether or not it is visible in the figures or explicitly stated in the values.

Figure 7 shows three sets of dissimilar calibration data that was analyzed using appropriate calibration factors. One set of data was originally sampled at 9000 Hz, the next was 1000 Hz data, and the third was 1000 Hz with the use of an analog LPF. Each of the sets show reasonable agreement with expected results as the derived impulses are consistently within 4.5% of the applied impulse. Each calibration data set

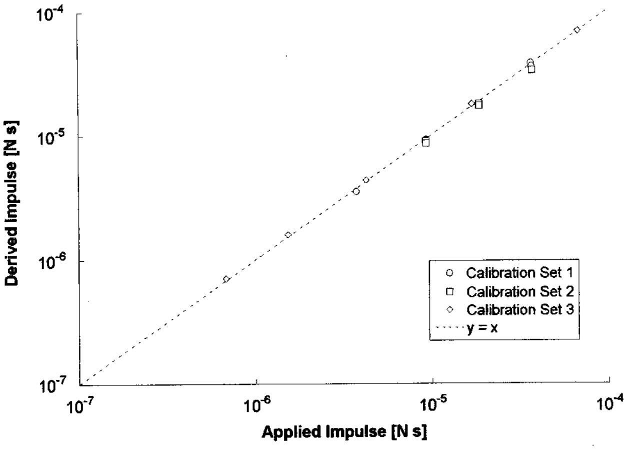

FIG. 7. TRIM derived impulse versus applied impulse for three dissimilar sets of calibration data.

also shows trends of being consistently slightly high or low, which would be consistent with filtering variations for each of the sets of data. This suggests that for any configuration of the NIBS, a consistent set of calibration data could be used with a consistent signal processing parameter to obtain appropriate calibration factors for an unknown impulse, which could minimize error in the derived impulse. Nevertheless, without any additional correction factors, the results for derived impulse throughout the paper repeatedly fall within 4.5% of the applied impulse.

B. Maximum deflection analysis

Figure 8 shows the NIBS maximum linear deflection as a function of applied impulse. The analytical model is in good agreement with the experimental data as shown in Fig. 8. For the cases presented in Fig. 8, the impulse pulsewidths (τ) were shorter than approximately one-tenth of the period (T) of the NIBS. Typically, impulse balances are operated using the assumption that the maximum deflection is linearly dependent on the delivered impulse.[2,3] The assumption is only strictly valid for $\tau \ll T$. Figure 9 shows the maximum NIBS deflection as a function of τ/T for various total impulses. The analytical model captures not only the trend of the experimental data, but is also in excellent agreement with the magnitude of the data. As seen in Fig. 9 for $\tau > 0.1$ T, the direct correlation between the maximum balance displacement and the delivered impulse is no longer valid. For $\tau \ll T$, the maximum deflection has a linear relationship with the total impulse as shown in Fig. 8. For larger τ, there are two possible scenarios. First, two different total impulses (say one with $\tau \ll T$ and one with $\tau \sim T$) can lead to the same maximum deflection; second, two identical total impulses with different pulsewidth can result in different maximum deflection. Examples of these two scenarios will be shown in Sec. VI C. Therefore, another means by which to analyze the data is necessary if the pulsewidth is not known *a priori*.

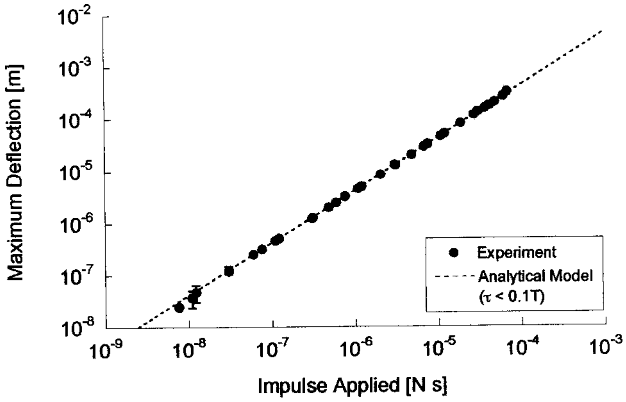

FIG. 8. Comparison of maximum deflection versus applied impulse of the analytical model and experimental deflection data. Error bars represent the standard deviation of at least 10 repeated tests, and are typically smaller than the symbol used.

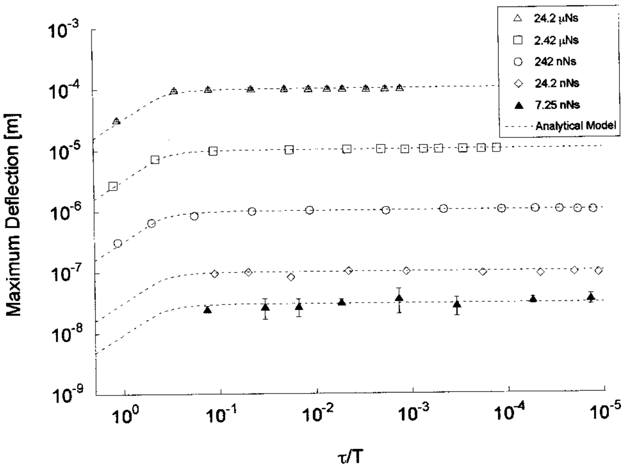

FIG. 9. NIBS maximum deflection as a function of normalized impulse pulsewidth compared to the analytical model results. For $\tau \ll$T, the maximum deflection is constant. The data points represent experimental measurements with error bars showing the standard deviation of at least 10 repeated tests.

C. Derived impulse analysis

It may be noted that for Figs. 10–14, the pulsewidth used in these figures is significantly larger than that typically expected of laser ablative processes or many pulsed electric thruster systems (<10 ms). However, these time scales are still appropriate for many other pulsed propulsion systems that could benefit from such analytical techniques. For the cases presented here, the longer pulsewidths were chosen to clearly demonstrate the principle of derived impulse analysis through the TRIM process, and ensure that the test cases would not be complicated by aliasing effects or hardware-related time-response limitations, which will be discussed in Sec. VII.

Figure 10(a) shows the impulse balance deflection as a function of time for two impulses of the same total magnitude (integrated force with time). The maximum deflection from the NIBS is not the same even though the total impulse is identical for both cases. The actual time varying force applied is shown by the dashed line in Fig. 10(b). As shown, the pulsewidth of the two traces was different by an order of magnitude. The TRIM process described in Sec. IV B was used to obtain the derived time varying force also shown in Fig. 10(b). Figure 10(c) shows the total impulse delivered to the balance obtained by the integral under the curves in Fig.

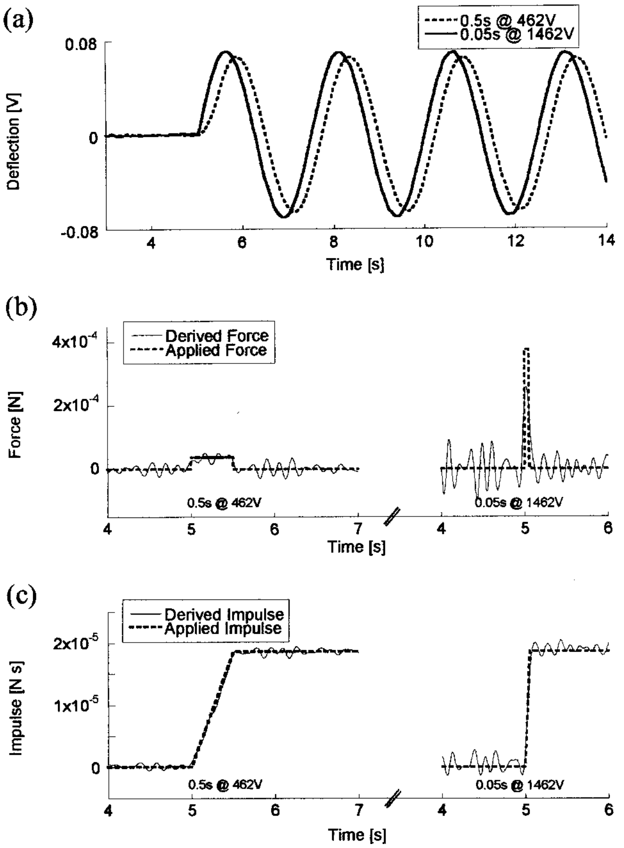

FIG. 10. Two test cases of equivalent total impulse, with different applied force and pulsewidth. (a) Shows that equivalent total impulses can result in different maximum displacements. (b) Shows the shape of the applied force for each impulse. (c) Shows that the two total impulses are in fact equivalent.

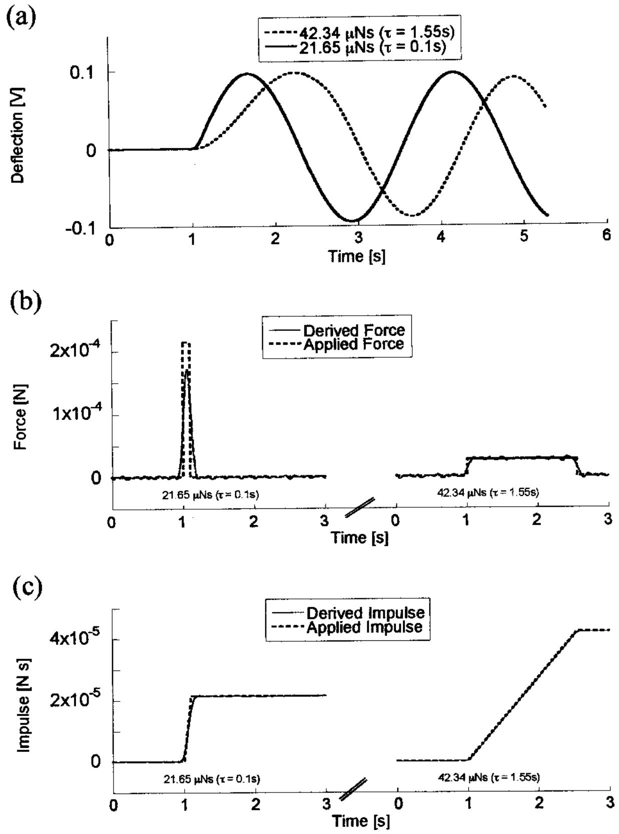

FIG. 11. Two test cases of different total impulses that result in the same maximum deflection of the balance as shown in (a). (b) Shows the shape of the applied force for each impulse (c) Shows that the two total impulses are in fact different by about a factor of 2.

10(b). Although the maximum deflection for the two pulses was not the same, Fig. 10(c) shows that the total impulse delivered were in fact identical.

Figure 11(a) shows the NIBS linear displacement versus time for impulses of 42.34 μNs and 21.65 μNs. The pulsewidths for these impulses was 1.55 s and 0.1 s, respectively. As seen in Fig. 11(a), the maximum NIBS deflection is the same for both impulses even though the total impulses are different by a factor of 2. Figure 11(b) shows the impulse shape for both cases. The dashed lines are from the signal delivered by the pulse generator, and the solid lines are derived from the filtered NIBS deflection data using the TRIM data reduction technique described in Sec. IV B. As Fig. 11(b) indicates, there are system time response issues that would not allow better resolution of the impulse shape with faster data acquisition sampling. The time response of the LVDT signal-conditioning unit was seen to be less than 100 Hz, which was generally not fast enough to adequately resolve the impulse shape for very short pulsewidths due to aliasing. However, the total impulse taken as the integral under both curves (pulse generator, LVDT derived) is the same to within 4.5% as shown in Fig. 11(c). Although the maximum displacement of the NIBS was the same for the two impulses [as shown in Fig. 11(a)], the total impulse was indeed a factor of 2 different as shown in Fig. 11(c).

Figure 12(a) shows the experimentally derived force

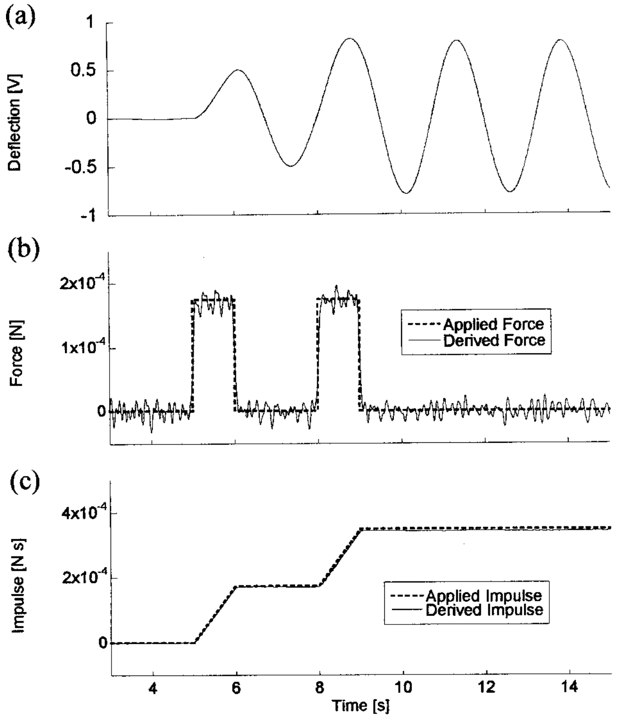

FIG. 12. The TRIM process can be used to resolve discrete forces applied to the NIBS. (a) Shows the deflection trace corresponding to (b) the time-varying force traces for 2 discrete impulses of 170 mN for 1 s each. (c) Shows the resulting total impulse as a function of time.

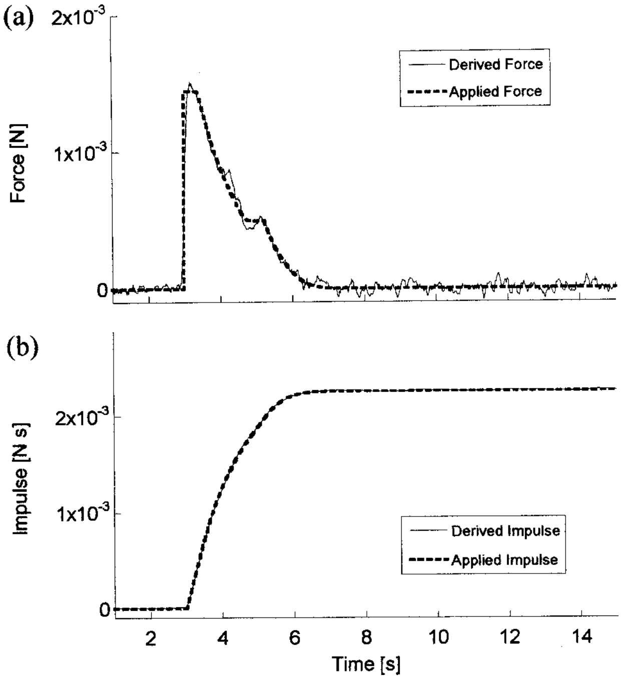

FIG. 13. Plots of (a) the applied and derived forces as a function of time for an arbitrary impulse, and (b) the corresponding applied and derived total impulses.

from the NIBS as a function of time for an impulse comprised of two square waves from the pulse generator. The pulses each represent a force of 170.7 μN over a 1.0 s pulsewidth and are separated by 2.0 s. As seen in Fig. 12(a), there is good agreement between the measured impulses delivered by the pulse generator to the EFCS and the derived impulses from the NIBS deflection data. Figure 12(b) shows the delivered impulse as a function of time. As Fig. 12 shows, the data analysis method developed in this study is adequate to resolve discrete forces applied to the impulse balance.

Although attention has been paid to only square-wave impulses to this point, arbitrary impulse shapes can also be investigated. Figure 13(a) shows a time varying force applied to the thrust stand which might resemble that produced by a PPT or laser ablation mechanism. The derived force obtained from the NIBS position versus time data reproduced the actual applied force reasonably well. Many of the differences in the time varying force have been linked to limitations in the time resolution of the LVDT conditioning unit. Although a factor of perhaps 10 improvements in the LVDT can be reasonably expected, other methods of time resolving the NIBS deflection are being investigated. As shown in Fig. 13(b), the applied and derived impulses are nearly identical and compare to within 1.9%.

D. Model comparison

Figure 14 shows the comparison of the developed model with experimental data for a relatively complicated case of four square-wave impulses applied over a 25 s time period. In Fig. 14(a) the model is able to capture the motion of the NIBS for a series of impulses delivered to the balance. The model used the measured and calculated characteristics of the NIBS given in Table I as input parameters. Figures 14(b) and 14(c) show the calculated values of the NIBS velocity and acceleration as a function of time. Again, the model compares well with the experimentally derived data obtained from differentiating the NIBS time varying position data. Figure 14(d) shows the actual time varying forces applied to the NIBS compared to the experimentally derived data. The first pulse was 98.39 μN with a 0.2 s pulsewidth with the second pulse of the same magnitude separated by 0.3 s. The second and third pulses were separated by 8.606 s. The third and fourth pulses were also 98.39 μN with a 0.4 s pulsewidth separated by 7.055 s. The integrals under the time varying force curves are shown in Fig. 14(e). Again, the experimental data was able to time resolve the impulse delivery to the NIBS, and the total impulse derived from the NIBS data is within 2.2% of the actual applied impulse.

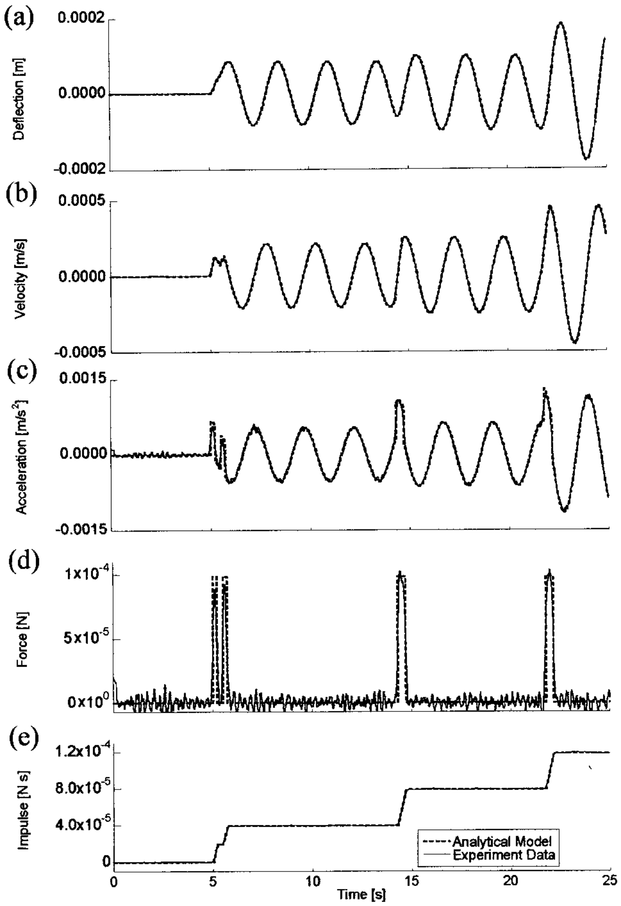

FIG. 14. Comparison of the analytical model with the experimental measurements for multiple pulses of varying pulsewidth. The plots show the sequence of steps in the TRIM process. (a) The balance's deflection, (b) velocity, and (c) acceleration. (d) The time varying force, and (e) the total impulse as a function of time.

VII. DISCUSSION

The extension of operating conditions of impulse balances to arbitrary impulse pulsewidth, shape, and magnitude (down to 7 nNs) has been demonstrated with the NIBS using a combination of an analytical code and a data analysis method. Previous studies[2,3] have been limited to data analysis based on the assumption that $\tau \ll T$. For basic research involving new propulsion systems and photon–surface interactions, the characteristic time dependence of the impulse of a particular process may not be known *a priori*, making a generalized scheme necessary to time-resolve the impulse delivery to the balance. Also, a torsional impulse balance can deflect the same amount for different total impulses (e.g., see Fig. 9), particularly where the assumption of $\tau \ll T$ is no longer valid. Under similar pulsewidth conditions, an impulse balance can also deflect differently for equivalent total impulses. Therefore, a generalized τ-independent data analysis tool is required.

The NIBS has already demonstrated that it can be used to time-resolve impulses. The real issues now become that of performance. The common measure of an impulse balance's performance is typically that of impulse magnitude resolution. The NIBS has repeatably measured impulses as low as 7 nNs and as high as hundreds of micro-Newton-seconds, and has consistently derived results that fall within 4.5% (worst case) of the applied impulse. However, when time resolving the forces, it becomes apparent that there are more performance related issues than just the magnitude of the impulse. Qualitatively, the accuracy of the shape of the time-varying force is of interest. In other words, how closely the derived force matches the applied force over time is important in determining the overall effectiveness of both the TRIM technique and the NIBS itself. Noise and time response of the whole system then become significant issues.

Noise in the measured signal from the NIBS is one of the largest sources of error in the TRIM process. Excessive noise affects the derivatives of the deflection trace and results in noisy time-resolved forces or impulses. There are several sources of noise including external physical vibrations, temperature variations, and electronic noise directly from the LVDT and its signal conditioner. The simplest way to eliminate a significant portion of the electronic noise is the use of a well-tuned LPF. However, LPFs introduce significant time response problems, as they attenuate high frequency components that may actually be part of the signal. Only when time-resolving the forces is not necessary, the LPF provides the best method to obtaining clean signals for basic maximum deflection measurements. In all other cases, the LPF should not be utilized, and the signal processing discussed in Sec. IV becomes the critical noise reduction method.

In terms of system time response, each component of the NIBS system must be examined. First, the DAQs components play an important role. Often there is a trade-off between resolution and speed. The NIBS system is equipped with both a 16-bit resolution system that samples up to 333 kSamples/s and a 24-bit resolution system that samples up to 60 samples/s. Ideally, a high-speed, 24-bit resolution system would be optimal, but has yet to be identified.

Next, the impulse balance itself must be considered for time response issues. The NIBS has been extensively tested with impulses of pulsewidth τ as low as 10^{-7} s up to minutes in length. Due to time response limitations from the LVDT, the TRIM process only currently provides accurate results for pulsewidths as low as 0.05 s. Below this point, aliasing effects make it difficult to discern whether the time resolution problems are due to the impulse balance or just signal processing artifacts, though the latter is suspected to be the most likely. The current time response limitations of the NIBS have been determined to be primarily hardware related. As such, it is possible that other time resolution limitations may exist, related to the acoustic time of the system. Further study on other possible time response limitations would be warranted once the hardware limitations are alleviated. However, from extensive maximum deflection results, the NIBS behaves as expected across the entire range of pulsewidths tested. This suggests that the impulse balance is behaving well according to the ideal equations of motion, and may not have any significant time response problems, at least on the order of 10^{-7} s.

The last system component to examine for time response issues is the LVDT and its signal conditioner. The time response of a LVDT is typically considered to be at best one-tenth of the excitation frequency of the LVDT. For the NIBS, the LVDT is driven at an excitation frequency of 2.5 kHz. However, the signal conditioning provided within the controller unit limits the response characteristics further.[13] This accounts for the current time-resolution limitations of the TRIM process. Improvement of the technique described here would be easily achieved through improvements of the overall system time response. While providing excellent displacement resolution, the LVDT signal conditioner was found to have the slowest time response of the entire system, making its replacement desirable. Optical interferometry may offer improved time response over the LVDT system and has been previously investigated, although not for these particular impulse derivation methods. Alternatively, capacitive and other electromagnetic sensors could also be considered.

For actual operation of the NIBS, the error in the TRIM process can be reduced significantly by using a consistent calibration scheme. Since any modification to the impulse balance can change its fundamental characteristics (i.e., I, C, and K), it is necessary to calibrate in the actual test configuration. Using a robust set of calibration tests that maintains a set sampling frequency and covers a wide range of impulses, forces and pulsewidth variations, a correction factor could be determined that would minimize the error. Ideally, calibration sets will be taken before and after any experimental measurements to ensure that the impulse balance remains consistent.

Ultimately, the performance of the impulse balance comes down to repeatability. For the maximum deflection analysis, the experimental error was taken as the standard deviation of between five and ten data points and was typically less than ±2% (i.e., smaller than the symbol size in Figs. 8 and 9 unless otherwise indicated). For the time-resolved impulse analysis, all derivations of total impulse from the deflection measurements have resulted in errors less than ±4.5%, which encapsulates all sources of error including from the applied force. The repeatability of the NIBS data suggests that it is a viable diagnostic tool for the investigation of arbitrarily produced impulses from a variety of devices.

Nomenclature

α = damping term in equations of motion (s^{-1})
β = frequency term in equations of motion (s^{-1})
δ = damping ratio, $\ln[x_{\max 1}/x_{\max 2}]$
$\mathcal{J}$ = impulse, $\int F(t)dt$(N s)
τ = pulsewidth (s)
θ = angular displacement or deflection (rad)
$\dot{\theta}$ = angular velocity (rad/s)
$\ddot{\theta}$ = angular acceleration ($\mathrm{rad/s^2}$)
ω_{eff} = effective (angular) frequency (s^{-1})
ω_n = natural (angular) frequency (s^{-1})
C = viscous damping coefficient ($\mathrm{kg\,m^2/s}$)
F = force (N)
I = moment of inertia ($\mathrm{kg\,m^2}$)
K = spring constant (N/m)
M = moment or torque, $F \cdot r$ (N m)
r = moment arm (m)
T = period (s)
t = time (s)
x = linear displacement of deflection (m)
$\dot{x}$ or v = linear velocity (m/s)
$\ddot{x}$ or a = linear acceleration ($\mathrm{m/s^2}$)

ACKNOWLEDGMENTS

This work was supported by the Air Force Research Laboratory, Propulsion Directorate, Space and Missile Propulsion Division (AFRL/PRSA), Edwards AFB, California. One of the authors (B.D.) was also supported in part by a graduate assistantship from the Department of Aerospace and Mechanical Engineering at the University of Southern California.

[1] E. Cubbin, J. Ziemer, E. Choueiri, and R. Jahn, Rev. Sci. Instrum. **68**, 2339 (1997).
[2] M. Gamero-Castano, Rev. Sci. Instrum. **74**, 4509 (2003).
[3] T. Haag, Rev. Sci. Instrum. **68**, 2060 (1997).
[4] R. G. Jahn, *Physics of Electric Propulsion* (McGraw–Hill, New York, 1968).
[5] G. Spanjers, K. McFall, F. Gulczinski, and R. Spores, AIAA Paper No. 1996–2723, 32nd Joint Propulsion Conference, July 1996.
[6] R. F. Haglund, *Laser Ablation and Desorption*, *Experimental Methods in the Physical Sciences*, edited by J. Miller and R. Haglund (Academic, San Diego, 1998), Vol. 30, pp. 15–138.
[7] J. Millard, M. Yang, and J. Reilly, J. Phys. Chem. **95**, 4045 (1991).
[8] A. Jamison, A. Ketsdever, and E. P. Muntz, Rev. Sci. Instrum. **73**, 3629 (2002).
[9] N. Selden and A. Ketsdever, Rev. Sci. Instrum. **74**, 5249 (2003).
[10] R. K. Vierck, *Vibration Analysis* (Thomas Y. Crowell, New York, 1979).
[11] C. Gasquet and P. Witomski, *Fourier Analysis and Applications: Filtering, Numerical Computation, Wavelets* (Springer, New York, 1999).
[12] L. M. Jameson, *Wavelets Theory and Applications*, edited by G. Erlebacher, M. Y. Hussaini, and L. M. Jameson (Oxford University Press, New York, 1996), pp. 1–37.
[13] E. O. Doebelin, *Measurement Systems: Application and Design* (McGraw–Hill, New York, 1966).

AIP | Conference Proceedings

Experimental and Numerical Study of Nozzle Plume Impingement on Spacecraft Surfaces

A. D. Ketsdever, T. C. Lilly, S. F. Gimelshein, and A. A. Alexeenko

Citation: AIP Conf. Proc. **762**, 367 (2005); doi: 10.1063/1.1941564

View online: http://dx.doi.org/10.1063/1.1941564

View Table of Contents: http://proceedings.aip.org/dbt/dbt.jsp?KEY=APCPCS&Volume=762&Issue=1

Published by the American Institute of Physics.

Related Articles

Simulation of the flow around an upstream transversely oscillating cylinder and a stationary cylinder in tandem
Phys. Fluids 24, 023603 (2012)

Stability and breakup of confined threads
Phys. Fluids 24, 012102 (2012)

Sedimentation of a charged colloidal sphere in a charged cavity
J. Chem. Phys. 135, 214706 (2011)

Non-axisymmetric impact creates pineapple-shaped cavity
Phys. Fluids 23, 091106 (2011)

Effect of central slotted screen with a high solidity ratio on the secondary resonance phenomenon for liquid sloshing in a rectangular tank
Phys. Fluids 23, 062106 (2011)

Additional information on AIP Conf. Proc.

Journal Homepage: http://proceedings.aip.org/

Journal Information: http://proceedings.aip.org/about/about_the_proceedings

Top downloads: http://proceedings.aip.org/dbt/most_downloaded.jsp?KEY=APCPCS

Information for Authors: http://proceedings.aip.org/authors/information_for_authors

ADVERTISEMENT

AIPAdvances
Submit Now
Explore AIP's new open-access journal
• Article-level metrics now available
• Join the conversation! Rate & comment on articles

Downloaded 11 Apr 2012 to 129.198.241.47. Redistribution subject to AIP license or copyright; see http://proceedings.aip.org/about/rights_permissions

Experimental and Numerical Study of Nozzle Plume Impingement on Spacecraft Surfaces

A.D. Ketsdever[1], T.C. Lilly[2], S.F. Gimelshein[2], and A.A. Alexeenko[2]

[1] *US Air Force Research Laboratory, Propulsion Directorate, Edwards AFB, CA 93524 USA*
[2] *University of Southern California, Dept. of Aerospace and Mechanical Eng. Los Angeles, CA 90089 USA*

Abstract. An experimental and numerical effort was undertaken to assess the effects of a cold gas (T_o=300K) nozzle plume impinging on a simulated spacecraft surface. The nozzle flow impingement is investigated experimentally using a nano-Newton resolution force balance and numerically using the Direct Simulation Monte Carlo (DSMC) numerical technique. The Reynolds number range investigated in this study is from 0.5 to approximately 900 using helium and nitrogen propellants. The thrust produced by the nozzle was first assessed on a force balance to provide a baseline case. Subsequently, an aluminum plate was attached to the same force balance at various angles from 0° (parallel to the plume flow) to 10°. For low Reynolds number helium flow, a 16.5% decrease in thrust was measured for the plate at 0° relative to the free plume expansion case. For low Reynolds number nitrogen flow, the difference was found to be 12%. The thrust degradation was found to decrease at higher Reynolds numbers and larger plate angles.

INTRODUCTION

When in orbit, spacecraft require on-board or secondary propulsion systems to perform orbit transfer, orbit maintenance, and attitude control maneuvers. An important issue in the use of any spacecraft propulsion system involves the assessment and reduction of effects caused by the interaction between the thruster plume and spacecraft surfaces [1]. Direct impingement of a thruster plume on surfaces can generate unwanted torques, localized surface heating, and surface contamination. Self impingement (i.e. the impingement of a thruster plume on a host satellite surface) generally occurs for small surface angles with respect to the propulsion system's thrust vector or occurs in the thruster backflow. Cross impingement (i.e. the impingement of one spacecraft's thruster plume onto another spacecraft) can occur at essentially any angle and is becoming increasingly important with the advent of microsatellite constellations. Many studies, both nuermical [2-4] and experimental [5-6], have been performed by various investigators to assess the impingement of plumes onto surfaces.

In recent years, micropropulsion systems have been developed to address the need for highly mobile microspacecraft. A wide array of concepts will require the expansion of propellant gases through microscale nozzles. Because many micropropulsion systems will also operate at relatively low pressures, the investigation of low Reynolds number flow has become increasingly important. [7] The Reynolds number at a nozzle throat is given by

$$\mathrm{Re}^* = \frac{\rho^* a^* d_t}{\mu^*} \tag{1}$$

An experimental and numerical effort has been developed to assess the effects of a nozzle plume impinging on a simulated spacecraft surface. The nozzle flow impingement is investigated experimentally using a nano-Newton resolution force balance and numerically using the Direct Simulation Monte Carlo (DSMC) numerical technique. The purpose of this work is to extend previous nozzle plume impingement results [5] to the low Reynolds number flow range for application to micropropulsion systems. The Reynolds number range investigated in this study is from 0.5 to approximately 900.

CP762, *Rarefied Gas Dynamics: 24th International Symposium,* edited by M. Capitelli
© 2005 American Institute of Physics 0-7354-0247-7/05/$22.50

Downloaded 11 Apr 2012 to 129.198.241.47. Redistribution subject to AIP license or copyright; see http://proceedings.aip.org/about/rights_permissions

EXPERIMENTAL SET UP

The DeLaval nozzle used in this study had a throat diameter of d_t = 1.0 mm and an expansion ratio of ε = 62.42 and has been described in previous work. [8] The thrust produced by the nozzle configuration, in the absence of any surfaces, was measured on the nano-Newton Thrust Stand (nNTS), which has been described in detail by Jamison, et. al. [9] The nNTS was installed in Chamber-IV of the Collaborative High Altitude Flow Facility (CHAFF-IV). CHAFF-IV is a 3 m diameter by 6 m long stainless steel vacuum chamber that was pumped by a 1 m diameter diffusion pump with a pumping speed of 25,000 L/s for nitrogen and 42,000 L/s for helium. The ultimate facility pressure was approximately 10^{-6} Torr with operational pressures up to 2×10^{-4} Torr. After the free expansion thrust was measured, an electropolished aluminum engineering surface (length=width=2.54cm) was attached to the thrust stand in the configuration shown in Fig. 1. The total force measured on the nNTS for this configuration is given by

$$F_t = \Im_p - F_s + F_b \qquad (2)$$

where $\Im_p$ is the thrust produced by the nozzle in the absence of the plate, F_s is the incident shear force on the plate (acting in the opposite direction as the thrust force), and F_b is the force exerted on the plenum wall due to gas pressure in the backflow. The angle α was varied from 0° to 10°. The surface temperature was held constant throughout at T_S=300K.

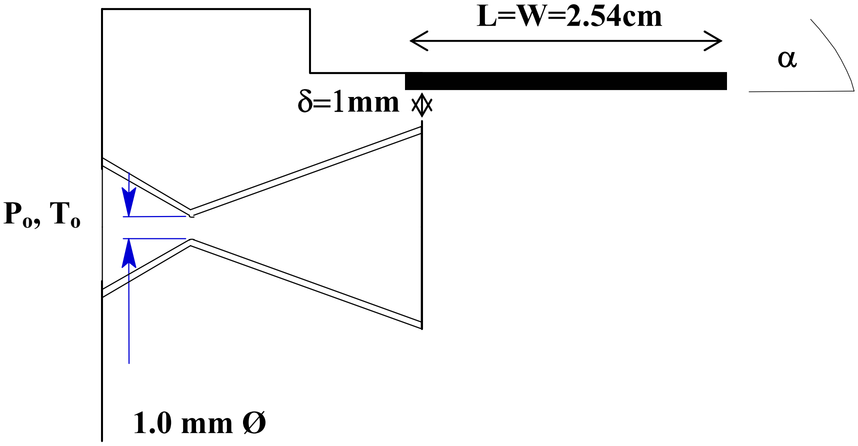

FIGURE 1. Nozzle-surface configuration.

The propellant was introduced into the nozzle plenum through an adjustable needle valve located downstream of an MKS® mass flow meter. The propellant gas temperature was held constant at T_o=300K. Nitrogen and helium were used as propellant gases in this study.

NUMERICAL METHOD

The DSMC-based software system SMILE [10] was used in all DSMC computations. The important features of SMILE that are relevant to this work are parallel capability, different collision and macroparameter grids with manual and automatic adaptations, and spatial weighting for axisymmetric flows. The majorant frequency scheme was used to calculate intermolecular interactions. The intermolecular potential was assumed to be a variable hard sphere. Energy redistribution between the rotational and translational modes was performed in accordance with the Larsen-Borgnakke model. A temperature-dependent rotational relaxation number was used. The reflection of molecules on the surface was assumed to be diffuse with complete energy and momentum accommodation.

The three-dimensional plume-surface interaction was modeled using a starting surface at the nozzle exit, generated using an axisymmetric solution (also obtained with SMILE). An elliptic distribution function was used for inflow molecules. The number of simulated molecules and cells was about 40 million and 3 million, respectively. The computational geometry included the nozzle with the external side of the plenum and the plate which size and location correspond to the experimental setup.

Downloaded 11 Apr 2012 to 129.198.241.47. Redistribution subject to AIP license or copyright; see http://proceedings.aip.org/about/rights_permissions

RESULTS

Figure 2 shows the thrust obtained in the experiments by the nNTS for a helium flow. Figure 2(A) shows a decrease in the measured thrust when the engineering surface is attached to the nozzle (as in Fig. 1) due to the shear force produced by the plume impingement. For the surface at $\alpha=0^\circ$, the thrust decrease is approximately 16.5% compared to the free expansion nozzle thrust. Larger α increases the measured thrust due to decreased plume impingement on the surface. For $\alpha=10^\circ$, the thrust degradation is only 7.0% compared to the free expansion case. Presumably, the measured thrust would approach the free expansion limit as α tends to 90°. As the Reynolds number (mass flow) increases, the difference becomes less pronounced as shown in Fig. 2(B). Figure 3 shows similar results for a nitrogen flow. In the low mass flow cases, the thrust decrease is 12.0% and 4.9% for $\alpha=0^\circ$ and $\alpha=10^\circ$, respectively. Note that the thrust for the surface impingement cases begins to approach the free expansion case beginning at a mass flow of 80 SCCM for nitrogen. Figure 3(B) shows that that the thrust measured for the $\alpha=10^\circ$ case is approximately equivalent to the free expansion thrust at mass flows above 200 SCCM. At higher Reynolds numbers, the nozzle plume becomes less divergent due to higher axial velocities and the reduction of the viscous interaction layer inside the nozzle geometry. Therefore, the plume impingement on the engineering surface decreases as the Reynolds number increases. It should be noted that for a given stagnation pressure, the Reynolds number for nitrogen is roughly a factor of 3 larger than helium leading to the transition to the free expansion case at lower mass flow rates for nitrogen as shown in the differences between Fig. 2(A) and Fig. 3(A).

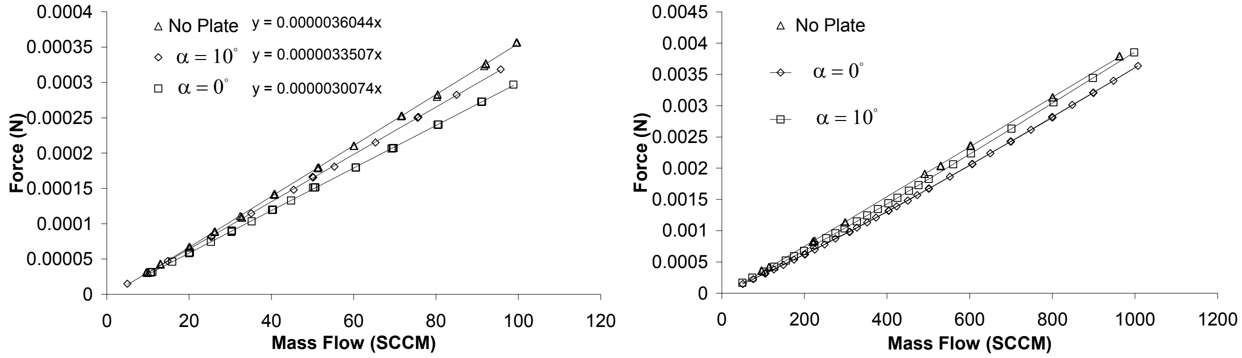

(A) **(B)**

FIGURE 2. Thrust versus mass flow for helium propellant. Measurements for free expansion, and engineering surface at $\alpha=0^\circ$ and 10° (A) Mass flow from 0 to 100 SCCM, (B) Mass flow from 100 to 1000 SCCM.

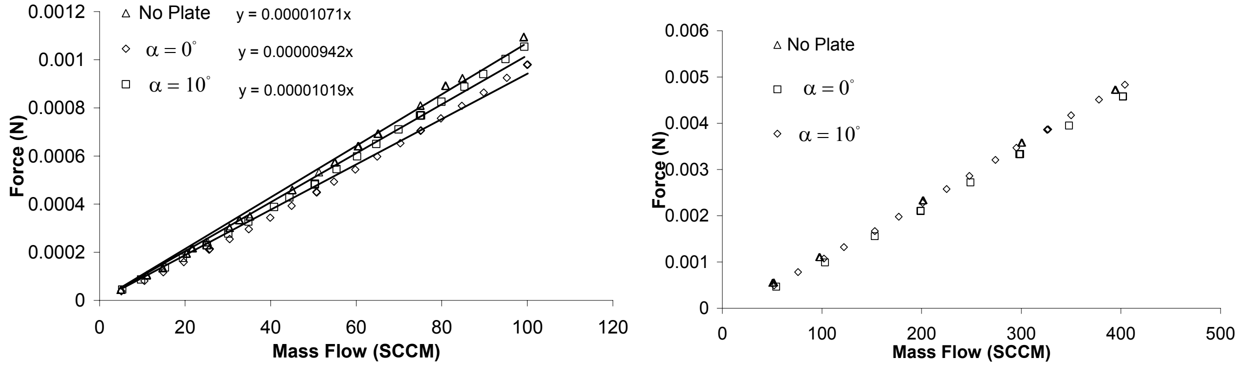

(A) **(B)**

FIGURE 3. Thrust versus mass flow for nitrogen propellant. Measurements for free expansion, and engineering surface at $\alpha=0^\circ$ and 10° (A) Mass flow from 0 to 100 SCCM, (B) Mass flow from 50 to 400 SCCM.

Downloaded 11 Apr 2012 to 129.198.241.47. Redistribution subject to AIP license or copyright; see http://proceedings.aip.org/about/rights_permissions

DSMC Results

The pressure flow field, normalized by the stagnation pressure, is given in Fig. 4 for a nitrogen flow at Re=60. The interaction region between the plume and the plate is clearly seen in Fig. 4, with the local pressure maximum located near the plate surface about 7mm downstream from the nozzle exit plane. The pressure values in that region are over an order of magnitude larger than those at the corresponding location in the bottom half of the plume. There is significant backflow observed as the result of the plume-surface interaction. A strong backflow will result in a noticeable contribution of backflow molecules interacting with the plenum surface (F_b) to the total force. This contribution increases the total force in x-direction. The increase in α from 0 to 10° significantly weakens the plume-surface interaction, as shown in Fig. 4(B). The pressure maximum is more than two times smaller for 10° than it was for 0°, and the plate no longer has a noticeable effect on the flowfield in the immediate vicinity of the nozzle exit. The backflow pressure is also reduced and is only slightly higher than the corresponding pressure at the bottom half of the plume backflow.

As mentioned earlier, the increase in the stagnation pressure causes a less divergent plume. This is illustrated in Fig. 5, where the pressure field is given for nitrogen flow at Re=270. As a result, the difference between the pressures near the surface and the corresponding undisturbed values (bottom half of the plume) is smaller than for Re=60. The local pressure maximum near the plate shifts downstream to about 12mm from the nozzle exit plane. The plume backflow formed due to the plume-surface interaction is lower than the Re=60 case. The increase in the plate angle further decreases the backflow as seen in Fig. 5(B).

The quantitative impact of the plume on the plate surface is shown in Fig. 6 where the force in axial direction (shear force) is given. The force maximum is located at about 10mm from the exit plane. The negative force at the upstream part of the plate is due to the influence of backflow molecules. The force is negative even at small axial distances, which means that the force there is governed by molecules that come from the main plume and not the boundary layer of the nozzle. These molecules come primarily from the plume scattering and those molecules reflected from the surface. The region of negative force in x-direction increases with the plate angle as shown in Fig. 6(B). The location of the maximum force is close for both $\alpha=0^\circ$ and 10°, whereas the magnitude of the maximum is over a factor of two lower for $\alpha=10^\circ$. Increasing the Reynolds number shifts the maximum shear force location downstream and stretches the force islolines in the axial direction.

The contribution of the plume force ($\Im_p$), plate shear force (F_s), and the backflow force (F_b) that acts on the plenum to the total force (F_t) is given in Table 1 for nitrogen. For lower Reynolds number, the plate shear force amounts to about 20% of the plume force for $\alpha=0^\circ$ and over 8% for $\alpha=10^\circ$, while the backflow force is about 3% and 1.5%, respectively. These contributions are reduced almost two times for the higher Reynolds number case. The results for a helium flow are qualitatively similar to those for nitrogen. In addition, the computations were performed for a 80% diffuse and 20% specular surface using the Maxwell gas-surface interaction model. These computations showed that plate shear force and the backflow force are proportional to the percent of molecules reflected diffusely, which implies a relatively small impact of plume-surface interaction region (or, more accurately, molecules reflected from the surface), on plume molecules impinging on the surface.

Result Comparison

Figure 7 shows the comparison of the DSMC results with the experimental data for the total force (F_t) as a function of mass flow for the engineering surface at $\alpha=0^\circ$ and 10°. The DSMC results are within 2% of the experimental results at Re=60. The greater disagreement between the two results at Re=270 is most likely caused by the finite background pressure in the facility at the higher flow rates. As discussed by Ketsdever [11], the background gas pressure can cause a thrust degradation on the order of a few percent in the thrust range considered in this work. Similar agreement between the DSMC and experimental results has also been found for helium flows.

CONCLUSIONS

DSMC results have compared to within a few percent of experimental measurements of the total system force for a nozzle plume impinging on an engineering surface with nitrogen and helium cold gas propellants. For low Reynolds number, the plate shear force was found to be approximately 20% of the nozzle's free expansion thrust when the plate was parallel to the flow. For larger angles (α) and Reynolds number, both the surface shear force

Downloaded 11 Apr 2012 to 129.198.241.47. Redistribution subject to AIP license or copyright; see http://proceedings.aip.org/about/rights_permissions

and the backflow force on the plenum decreased. As a result, the total force measured tended towards the free expansion thrust. The DSMC results have also shown that the surface shear force and the backflow force are proportional to the percent of molecules that reflect diffusely. For the cases investigated in this study of cold gas (T_o=300K) impinging on a cold surface (T_s=300K), the momentum accommodation coefficient is near unity.

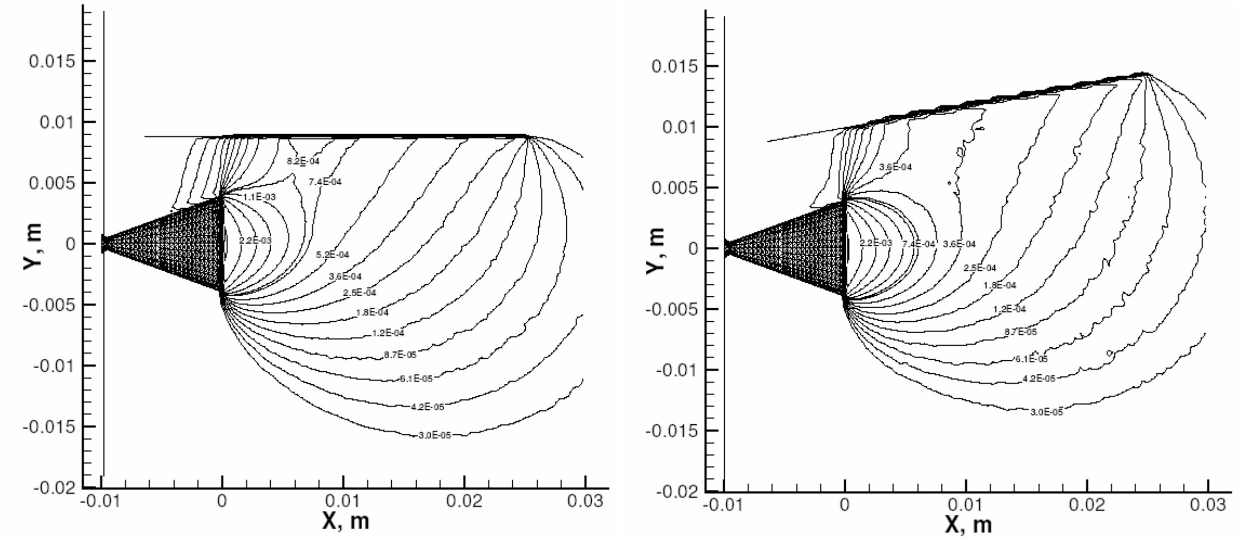

(A) **(B)**

FIGURE 4. Pressure profiles for Re=60 nitrogen flow. (A) α=0°, (B) α=10°.

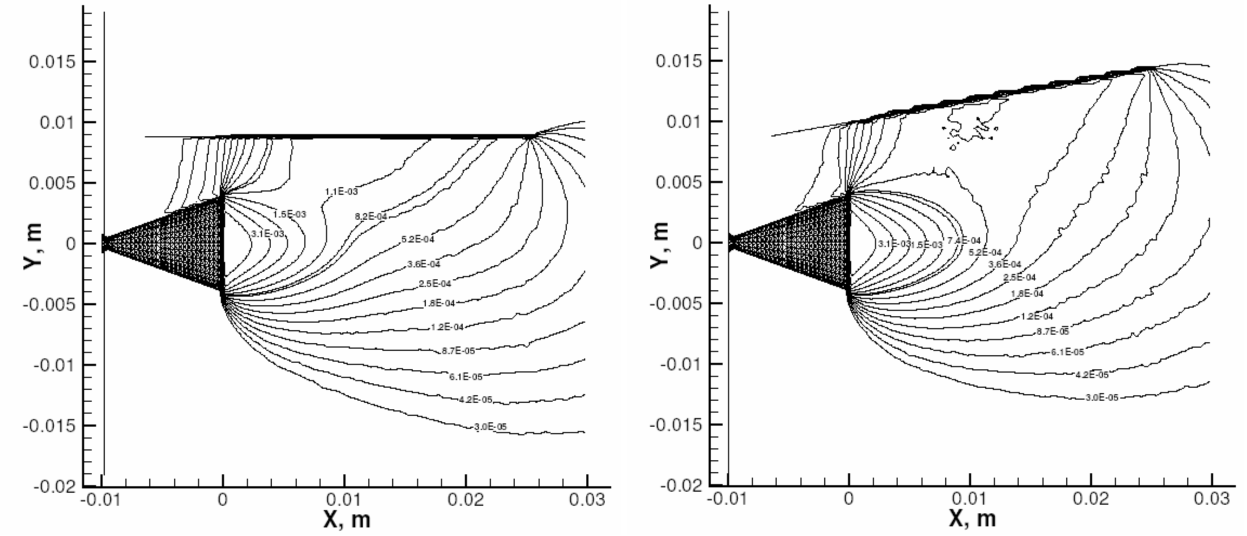

(A) **(B)**

FIGURE 5. Pressure profiles for Re=270 nitrogen flow. (A) α=0°, (B) α=10°.

REFERENCES

1. Boyd, I. and Ketsdever, A., J. Spacecraft and Rockets, 38, 380 (2001).
2. Lengrand, J-C., Allegre, J., Bisch, D., Skovorodko, P., "Impingement of a Simulated Rocket Exhaust Plume onto a Surface," in Rarefied Gas Dynamics – Proceedings of the 20th International Symposium, edited by C. Shen, Bejing University Press, Beijing, 1997, pp. 537-542.
3. Ivanov, M., Markelov, G., Kaskhovsky, A., Giordano, D., "Numerical Analysis of Thurster Plume Interaction Problems," in Proceedings of Second European Spacecraft Propulsion Conference, ESA SP-38, 1997, pp. 603-610.
4. Hyakutake, T., Nishida, M., "Numerical Simulation of Rarefied Nozzle Plume Impingements," in Rarefied Gas Dynamics, Proceedings of the 22nd International Symposium, edited by T. Bartel and M. Gallis, AIP Conference Proceedings 585, American Institute of Physics, New York, 2001, pp. 806-811.

Downloaded 11 Apr 2012 to 129.198.241.47. Redistribution subject to AIP license or copyright; see http://proceedings.aip.org/about/rights_permissions

5. Leege, H., "Plume Impingement Forces on Inclined Flat Plates," in Rarefied Gas Dynamics, Proceedings of the 17th International Symposium, edited by A. Beylich, VCH, Aachen, 1991, pp. 955-962.
6. Deependran, B., Sujith, R., Kurian, J., "Impingement of Low Density Freejets on a Flat Plate," in Rarefied Gas Dynamics – Proceedings of the 20th International Symposium, edited by C. Shen, Bejing University Press, Beijing, 1997, pp. 465-466.
7. Ketsdever, A., Micropropulsion for Small Spacecraft, AIAA Progress Series in Astronautics and Aeronautics, eds. Micci and Ketsdever, Vol. 187, 2000, pp. 139-166.
8. Jamison, A. and Ketsdever, A., "Low Reynolds Number Performance Comparison of an Underexpanded Orifice and a DeLaval Nozzle," in Rarefied Gas Dynamics - Proceedings of the 23nd International Symposium, edited by A. Ketsdever and E.P.Muntz, AIP Conference Proceedings 663, American Institute of Physics, New York, 2003, pp. 557-564.
9. A. Jamison, A. Ketsdever, and E.P. Muntz, Rev. Sci. Instrum., 73, 3629-3637 (2002).
10. Ivanov, M.S., Markelov, G.N., Gimelshein, S.F. "Statistical Simulation of Reactive Rarefied Flows: Numerical Approach and Applications," AIAA Paper 98-2669, 31st AIAA Thermophysics Conference, Albuquerque, NM, June 1998.
11. Ketsdever, A., J. Propulsion and Power, 18, 797-804 (2002).

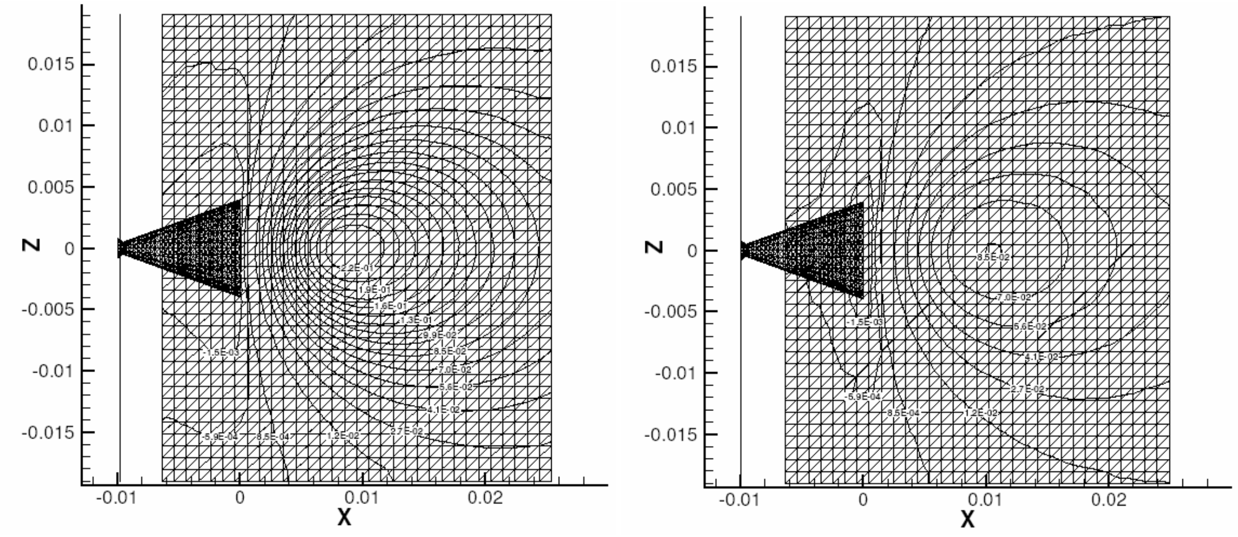

(A) **(B)**

FIGURE 6. Shear force isolines for Re=60 nitrogen flow. (A) α=0°, (B) α=10°.

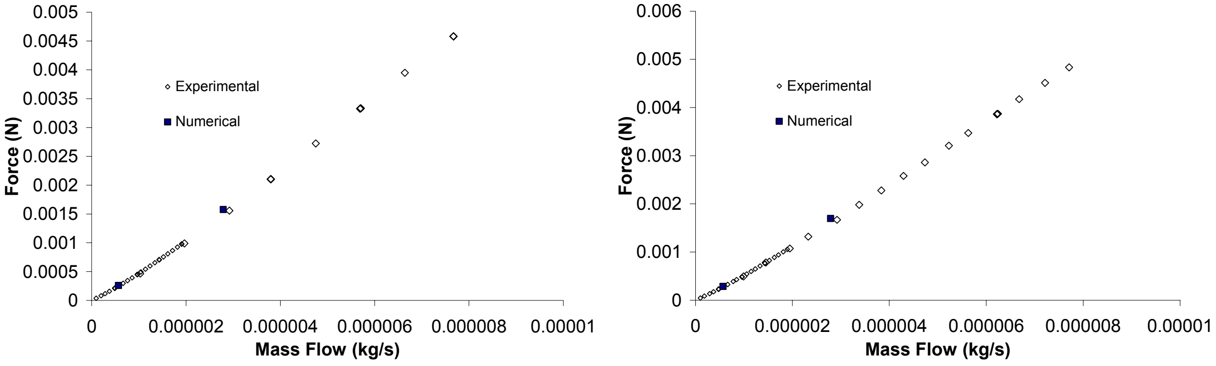

(A) **(B)**

FIGURE 7. Comparison of experimental and numerical results for nitrogen flow. (A) α=0°, (B) α=10°.

TABLE 1. DSMC data for nitrogen flow.

Re*	Mass Flow (kg/sec)	α (deg.)	$\Im_p$ (N)	F_s (N)	F_b (N)	F_t (N)	$F_t/\Im_p$
60	5.67E-7	0	3.076E-4	5.889E-5	1.119E-5	2.599E-4	0.845
60	5.67E-7	10	3.076E-4	2.611E-5	4.850E-6	2.863E-4	0.931
270	2.79E-6	0	1.771E-3	2.277E-4	3.414E-5	1.577E-3	0.890
270	2.79E-6	10	1.771E-3	8.906E-5	1.384E-5	1.696E-3	0.958

Downloaded 11 Apr 2012 to 129.198.241.47. Redistribution subject to AIP license or copyright; see http://proceedings.aip.org/about/rights_permissions

AFRL-RZ-ED-TR-2012-0016
Primary Distribution of this Report:

AFRL/RZSA (1 CD)
Andrew Ketsdever
10 E. Saturn Blvd
Edwards AFB CA 93524-7680

AFRL/RZSA (Electronic)
Record Custodian
10 E. Saturn Blvd
Edwards AFB CA 93524-7680

AFRL/RZ Technical Library (2 CD + 1 HC)
6 Draco Drive
Edwards AFB CA 93524-7130

Chemical Propulsion Information Analysis Center
Attn: Tech Lib (Mary Gannaway) (1 CD)
10630 Little Patuxent Parkway, Suite 202
Columbia MD 21044-3200

Defense Technical Information Center
(1 Electronic Submission via STINT)
Attn: DTIC-ACQS
8725 John J. Kingman Road, Suite 94
Ft. Belvoir VA 22060-6218